Springer ThesesRecognizing Outstanding Ph.D. Research

Roser Juanola-Parramon

A Far-Infrared Spectro-Spatial Space Interferometer

Instrument Simulator and Testbed Implementation



Springer Theses

Recognizing Outstanding Ph.D. Research

Aims and Scope

The series "Springer Theses" brings together a selection of the very best Ph.D. theses from around the world and across the physical sciences. Nominated and endorsed by two recognized specialists, each published volume has been selected for its scientific excellence and the high impact of its contents for the pertinent field of research. For greater accessibility to non-specialists, the published versions include an extended introduction, as well as a foreword by the student's supervisor explaining the special relevance of the work for the field. As a whole, the series will provide a valuable resource both for newcomers to the research fields described, and for other scientists seeking detailed background information on special questions. Finally, it provides an accredited documentation of the valuable contributions made by today's younger generation of scientists.

Theses are accepted into the series by invited nomination only and must fulfill all of the following criteria

- They must be written in good English.
- The topic should fall within the confines of Chemistry, Physics, Earth Sciences, Engineering and related interdisciplinary fields such as Materials, Nanoscience, Chemical Engineering, Complex Systems and Biophysics.
- The work reported in the thesis must represent a significant scientific advance.
- If the thesis includes previously published material, permission to reproduce this must be gained from the respective copyright holder.
- They must have been examined and passed during the 12 months prior to nomination.
- Each thesis should include a foreword by the supervisor outlining the significance of its content.
- The theses should have a clearly defined structure including an introduction accessible to scientists not expert in that particular field.

More information about this series at http://www.springer.com/series/8790

Roser Juanola-Parramon

A Far-Infrared Spectro-Spatial Space Interferometer

Instrument Simulator and Testbed Implementation

Doctoral Thesis accepted by the University College London, UK



Author
Dr. Roser Juanola-Parramon
University College London
Department of Physics and Astronomy
London
UK

Supervisor
Dr. Giorgio Savini
University College London
Department of Physics and Astronomy
London
UK

ISSN 2190-5053 ISSN 2190-5061 (electronic) Springer Theses ISBN 978-3-319-29399-8 ISBN 978-3-319-29400-1 (eBook) DOI 10.1007/978-3-319-29400-1

Library of Congress Control Number: 2016936983

© Springer International Publishing Switzerland 2016

This work is subject to copyright. All rights are reserved by the Publisher, whether the whole or part of the material is concerned, specifically the rights of translation, reprinting, reuse of illustrations, recitation, broadcasting, reproduction on microfilms or in any other physical way, and transmission or information storage and retrieval, electronic adaptation, computer software, or by similar or dissimilar methodology now known or hereafter developed.

The use of general descriptive names, registered names, trademarks, service marks, etc. in this publication does not imply, even in the absence of a specific statement, that such names are exempt from the relevant protective laws and regulations and therefore free for general use.

The publisher, the authors and the editors are safe to assume that the advice and information in this book are believed to be true and accurate at the date of publication. Neither the publisher nor the authors or the editors give a warranty, express or implied, with respect to the material contained herein or for any errors or omissions that may have been made.

Printed on acid-free paper

This Springer imprint is published by Springer Nature
The registered company is Springer International Publishing AG Switzerland



Supervisor's Foreword

After the recent successes of the far-IR missions IRAS, ISO and the Herschel Space Observatory, the era of space interferometry beckons. Indeed interferometry is indicated as the way forward in many fields and at all wavelengths with far-infrared having the possibility of leading the way, thanks to the reduced metrology requirements. Interferometry in space is on the other hand extremely challenging and many attempts to jump-start studies and mission concepts have proven in many cases ahead of their time or in dire need of technology development to raise the feasibility of the proposed concepts.

One technique which has been proposed as an optimal candidate for future far-infrared interferometry is double-Fourier-modulated spectral-spatial interferometry, with preliminary concepts being studied in both the US and Europe and testbed demonstrators explored at both the relevant wavelengths and the to-scale optical wavelengths. This technique, unlike standard photometry or spectroscopy that are mainstream techniques, has to conquer an additional challenge which is to be understood and adopted by a larger community that is often sceptical of new techniques until data is produced robustly and in a reproducible manner. To achieve the latter, an end-to-end physical simulator was coded to allow the astronomer who is not familiar with this technique, as well as the instrumentation community to visualize the potential of a mission concept adopting this technique, as well as the implications of systematic effects introduced by given elements of such a payload on the recovered data, in order to both plan the science capabilities and parametrically test different configurations and observation modes.

This thesis describes the physics and the computational aspects of an end-to-end simulator aimed at predicting the performance of a space-based far-infrared interferometer, including the science capabilities and instrumental state of the art. It outlines the requirements involved in such a mission and describes this most promising technique to capture most of the astrophysical information by combining spectroscopy with spatial interferometry.

The simulation of such a system is extremely complex requiring multiple Fourier transforms each of which is subject to instrument non-idealities and appropriate

optimization techniques. As a conclusion, the thesis provides an example of the basic performance achievable with such an instrument when targeting a young star formation region by running the simulator with a previously generated datacube and recovering the astrophysical scene.

London February 2016 Dr. Giorgio Savini

Preface

A large and growing number of astronomers recognize the importance of high spatial and spectral resolution observations in the far-infrared. Half of the energy emitted by stars and accreting objects comes to us in the far-infrared waveband and has yet to be explored in detail. On the one side, to study the far-infrared wavelength range there is a need for space observatories due to one main reason: the Earth's atmosphere. On the other side, to achieve high angular resolution there are two options: a very large aperture single dish telescope, or an array of smaller telescopes, that is, an interferometer. It is possible for ground-based systems to consist of very large apertures, but for space observatories there are launch requirements that limit both the size and the weight of the telescopes. Hence, to satisfy the community's sensitivity requirements in the far-infrared and in order to improve the existing resolution in space, a space-based interferometer is the most practical solution.

Far-infrared interferometer (FIRI) is a concept for a spatial and spectral space interferometer with an operating wavelength range 25–400 µm and sub-arcsecond angular resolution, and is based on the combination of two well-known techniques, stellar interferometry and Fourier transform spectroscopy, to achieve high spectral and spatial resolution in the far infrared. The resulting technique is called Double Fourier Spatio-Spectral Interferometry (Mariotti and Ridgway 1988) or Double Fourier Modulation. With an increased spatial and spectral resolution, a number of interesting science cases such as the formation and the evolution of active galactic nuclei and the characterization of gas, ice and dust in disks undergoing planetary formation, among others, can be investigated.

In Chap.1 I give an introduction to far-infrared astronomy and the science cases that could be studied with a double Fourier interferometer from space. An overview of past, current and future instruments is given and the scope of this thesis is presented. In Chap.2 the theoretical background needed to understand the principles of Double Fourier Modulation is presented. Starting with the basics of Fourier transform spectroscopy, where the generation and sampling of interferograms is shown, and stellar interferometry, with an emphasis on the *uv*-map generation, the link is

x Preface

made to explain analytically Double Fourier Modulation. The state-of-the-art data synthesis techniques are also summarized.

In this thesis I present two approaches to study the feasibility of a FIRI system:

- (a) An experimental approach via the Cardiff University-UCL FIRI testbed, a laboratory prototype spectral-spatial interferometer to demonstrate the feasibility of the double Fourier technique at the far-infrared regime, including the Wide-Filed Imaging Interferometry Testbed at the Optical and Near-infrared regime located at NASA's Goddard Space Flight Center, both presented in Chap.3. My contribution has been to the characterization of the system, data analysis and forward modelling for the Cardiff–UCL FIRI testbed, and in the data analysis and verification for the WIIT. Both systems are operational and ongoing, and the current issues and next steps are shown.
- (b) The Far-Infrared Interferometer Instrument Simulator (FIInS) to assess the performance of a space-based system. The main goal of this software is to simulate both the input and the output of such a system, which is the core of my research and is described in Chap.4. With a modular design, the different components of the software are explained, from the sky generator to the interferograms readout. The modules will allow future instrument artifacts to be added to the simulator. It is also capable of simulating different instrument configurations, i.e. boom-based or formation flying interferometers.

In Chap.5 the interferograms generated by FIInS are processed and synthesized to obtain the source information and to compare with the input sky map. In order to verify the performance of FIInS, the parameters are tuned to simulate the Cardiff-UCL FIRI testbed and the results obtained are shown.

FIInS is intended to be a tool available to the scientific community to test the performance of such an instrument for the different science cases. In Chap.6 a description and simulation of a selected science case, a circumstellar disk, is presented for both an ideal instrument (noise-free) and a more realistic instrument. Finally, in Chap.7 a summary of the conclusions of the work in this thesis is presented, as well as future work possibilities regarding the Cardiff-UCL FIRI testbed and the possible extensions of the instrument simulator FIInS.

The work described here is the result of my Ph.D. research, which was started in October 2010, defended in 2014. Dr. Giorgio Savini then suggested the nomination of this thesis for publication in the Springer Theses series, and thanks to the endorsement of Dr. David Leisawitz (NASA Goddard Space Flight Center) it was accepted by Springer in July 2015. I would like to thank both of them for their encouragement and support.

Washington, D.C. February 2016

Dr. Roser Juanola-Parramon

Acknowledgements

First and foremost, I would like to thank my supervisor, Dr. Giorgio Savini, for giving me the incredible opportunity to do this Ph.D. It is due to his support, knowledge and enthusiasm that this work has been possible, and I would have to write another thesis to express my gratitude. It has been an absolute pleasure to work with him and I am looking forward to many years to come.

I also want to thank my second supervisor, Dr. Enzo Pascale, for his advice and discussions, as well as the rest of the Cardiff University—UCL testbed team for all their help and contributions, specifically to Prof. Peter Ade and Prof. Matt Griffin. I would like to thank Dr. Simon Doyle for the crash course on LeKID devices.

I owe a special thanks to Dr. David Leisawitz, Dr. Stephen Rinehart and the WIIT team at NASA's Goddard Space Flight Center for giving me the opportunity to visit their centre and to work with them on WIIT; their expertise has been a tremendous contribution to this work.

I want to thank my two examiners, Dr. David Leisawitz and Prof. Mathew Page for taking the time out of their busy schedules to read this work and for their valuable input.

Last but certainly not least, I want to thank my family and friends. First of all, I want to thank my mother, for 29 years of love and support and for making me believe that I could do whatever I wanted to do. I also want to thank Rafel, for encouraging me and challenging me to do my best. Without them I would have never made it this far. Special thanks to my friends, you know who you are: the ones in Barcelona for leaving everything to come to meet me on my flash trips back home; my Kiver Road family, for making London a home and for being there all the way through this Ph.D.; and the UCL Ph.D. crowd for making me truly enjoy these past 3 years.

Contents

1	Intr	oduction	1	1		
	1.1	Far Infi	rared Astronomy	2		
		1.1.1	The FIR Gap	3		
		1.1.2	FIR Science Cases	4		
	1.2	Far Infi	rared Astronomy Instruments	6		
		1.2.1	Past and Present FIR Instruments	7		
		1.2.2	Ongoing and Future FIR Instruments	8		
	1.3	The Su	b-arcsecond Space-Based FIR Interferometer	11		
		1.3.1	Mission Concepts	11		
		1.3.2	FIRIT—Direct Imaging Interferometry	12		
	Refe	rences.		14		
2	The	oretical	Background	17		
_	2.1		Transform Spectroscopy	18		
		2.1.1	The Michelson Interferometer	18		
		2.1.2	Generating the Interferogram	20		
		2.1.3	Sampling the Interferogram	22		
		2.1.4	Recovering the Spectrum	24		
	2.2	Interferometry	27			
		2.2.1	Basic Principles	27		
		2.2.2	Observability and UV-Coverage	33		
		2.2.3	Data Synthesis	35		
	2.3 Multi-Fourier Transform Interferometry					
		2.3.1	Basic Principles	36		
		2.3.2	Data Analysis and Synthesis	38		
	2.4	Chapter	r Summary	39		
	Refe	-		39		
3	Sneo	rtro-Spa	tial Interferometry Testbeds	41		
	3.1	_	RI Laboratory Testbed	41		
	J.1	3.1.1	Experimental Set-Up	42		
		3.1.2	Characterization of the System	44		

xiv Contents

		3.1.3	Initial Results	46
		3.1.4	Forward Modelling	48
		3.1.5	Current Issues and Next Steps	53
	3.2		Field Imaging Interferometry Testbed (WIIT)	54
		3.2.1	The Testbed	54
		3.2.2	Data Analysis	59
		3.2.3	Data Synthesis and Simulation	69
		3.2.4	Current Issues and Next Steps	69
	3.3	-	r Summary	70
	Refe	rences.		70
4			I Interferometer Instrument Simulator (FIInS)	73
	4.1		Overview	73
	4.2		Architecture	75
	4.3		Parameters	75
		4.3.1	Control Flags	76
	4.4		mulator	77
		4.4.1	Sky Generator Module	77
		4.4.2	Sky Photon Noise Module	78
	4.5		nent Model	79
		4.5.1	uv-Map Generator Module	79
		4.5.2	FTS Drive Module	81
		4.5.3	Beam Calculator Module	82
		4.5.4	Pointing Errors Module	84
		4.5.5	Instrument Thermal System	86
		4.5.6	Background Power Module	89
		4.5.7	Double Fourier Module	90
		4.5.8	Detector Noise Module	91
		4.5.9	Add Noise Module	95
		4.5.10	Detector Module	96
		4.5.11	Sampling and Readout Module	97
	4.6		vity	97
	4.7	_	r Summary	98
				98
5			Processing and Verification	101
	5.1		be Reconstruction from Detected Interferograms	101
		5.1.1	Noise Reduction and Time Domain Interpolation	103
		5.1.2	Extracting the Spectra	105
		5.1.3	Interferometric Image Synthesis:	
	_	_	The Dirty Data Cube	106
	5.2		ynthesis Algorithms	109
		5.2.1	Blind Deconvolution	109
		5.2.2	Interferometic CLEAN Algorithm	112

Contents xv

	5.3	FIInS Validation via FIRI Testbed	118			
		5.3.1 Input Sky Map	118			
		5.3.2 Instrument Parameters and Generation				
		of Interferograms	119			
		5.3.3 Recovering the Spectral and Spatial Information	120			
	5.4	Chapter Summary	125			
	Refe	erences	126			
6	Sim	ulated Observations with FIInS	127			
	6.1	Protoplanetary Disks—Birthplaces of Planets	127			
		6.1.1 Protoplanetary Disk Evolution	128			
		6.1.2 Protoplanetary Disk Structure	129			
		6.1.3 Far Infrared Interferometry for the Observation				
		of Disks	130			
	6.2	Numerical Simulation of a Circumstellar Disk	130			
	6.3	A Circumstellar Disk as Seen by a Spectro-Spatial Space				
		Interferometer	131			
		6.3.1 Ideal Instrument	132			
		6.3.2 Realistic Instrument	134			
	6.4	Chapter Summary	140			
	Refe	References				
7	Con	iclusions and Future Work	143			
	7.1	=	145			
		7.1.1 About the Cardiff-UCL FIRI Testbed	145			
		7.1.2 About the Instrument Simulator FIInS	146			
		7.1.3 About the Synthesis of DFM Data	147			
	7.2	Closing Remarks	148			
	Refe	erences	148			
			1.40			
Aļ	ppend	lix A: Telescope Beam Profiles Calculation	149			
۸.	mand	lix B: FIInS Quick Start Guide	152			
∠]	JULIU	na D. Prino Zuick Duit Guiuc	100			

Chapter 1 Introduction

"What makes the desert beautiful," said the little prince, "is that somewhere it hides a well..."

Antoine de Saint-Exupéry, The Little Prince

1

The astronomical community is showing a growing interest in the observation of sub-millimeter waves with high angular resolution (sub-arcsecond) and sensitivity in both spatial and spectral domain, because half of the energy emitted by stars and accreting objects comes to us in the Far Infrared waveband and has yet to be explored in detail.

To achieve such angular resolution there are two options: a very large aperture single dish telescope, or an array of telescopes, this is, an interferometer. It is possible for ground based systems to consist of very large apertures, but for space observatories there are launch requirements that limit both the size and the weight of the telescopes. In order to improve on the existing resolution in space, interferometry is therefore the most plausible solution.

To study the Far Infrared wavelength range there is a need for space observatories due to one main reason: the Earth's atmosphere. The atmosphere presents a high attenuation of the signal due to the absorption by water vapour, and the level of atmospheric attenuation is a function of the line-of-sight water vapour concentration. For this reason most of the ground based observatories are located at high altitude sites. However, the only way to eliminate the atmosphere effect is to go to space.

There is another advantage about having a Far Infrared observatory in space. When observing from the ground, both the telescope and the atmosphere are emitting at around 300 K with non-negligible values of emissivity, which represents a very strong signal in the FIR region usually many orders of magnitude greater than the target. This causes a degraded sensitivity, which can only be avoided by having a space observatory, and even improved by cooling the optics to cryogenic temperatures. However, it is technologically challenging to cool large apertures in space to cryogenic temperatures, which gives us an extra reason for the use of multi aperture configurations.

© Springer International Publishing Switzerland 2016 R. Juanola-Parramon, *A Far-Infrared Spectro-Spatial Space Interferometer*, Springer Theses, DOI 10.1007/978-3-319-29400-1_1

In this Thesis an instrument simulator for a Far Infrared space interferometer is presented, as well as a test bed implementation of the technique intended to be used to achieve high spectral and spatial resolutions from space. In this Introduction the motivation for this system is given: from a general view of the Far Infrared astronomy and the possible science cases, through the past and present Far Infrared instruments, to FIRI, the concept of a space based Far Infrared Interferometer.

1.1 Far Infrared Astronomy

The Far Infrared and submillimeter wavelength range, which spans from $25 \,\mu m$ up to 1 mm, is of significant importance to astronomy. Its potential is most clearly illustrated by considering the three main components that dominate the electromagnetic energy content of the Universe shown in Fig. 1.1.

The dominant component is the microwave background produced by the primordial Universe at recombination (z \sim 1089). The second most important is the FIR background, produced by galaxies in the young Universe. The third is the optical background dominated by evolved stars/galaxies and AGN (Dole et al. 2006). The first and third of these components have now been mapped in detail over the entire sky, while virtually no sky has been imaged in the FIR to any reasonable depth.

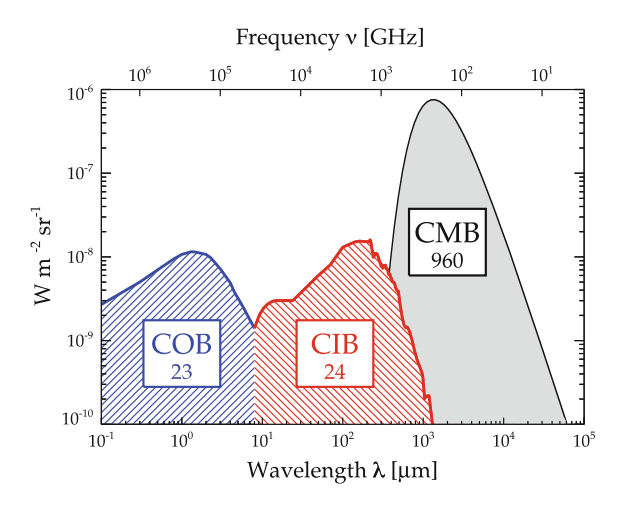


Fig. 1.1 Schematic Spectral Energy Distributions (SED) of the most important (by intensity) backgrounds in the Universe, and their approximate brightness in nW m⁻² sr⁻¹ written in the *boxes*. From *right* to *left* the Cosmic Microwave Background (CMB), the Cosmic Infrared Background (CIB) and the Cosmic Optical Background (COB) [*Credit* Dole et al. A&A, 451(2), 417–429, 2006, reproduced with permission ©ESO]

1.1.1 The FIR Gap

The FIR wavelength region is the least explored part of the electro-magnetic spectrum yet it provides uniquely powerful tools to study material associated with the earliest evolutionary stages of galaxies, stars and planets. So with increased spatial and spectral information, a number of interesting science cases can be investigated as proposed by Helmich and Ivison in the ESA's Cosmic Vision 2015–25 program (Helmich and Ivison 2009).

Figure 1.2 shows the 'FIR gap'. With interferometric angular resolution of the order of 0.02 arcsec at 100 μm , as well as sufficient sensitivity to allow photon-starved spectroscopy across an arcmin field of view in the 25–400 μm band, a Far Infrared Interferometer would allow the study of objects from nearby planetary systems to the highest red-shift galaxies. For example, in the Far infrared, such an instrument could, but would not be limited to (a) characterise gas, ice and dust in disks undergoing planetary formation, (b) resolve the Cosmic Infrared Background, (c) investigate the formation and evolution of AGN, (d) trace Milky Way type galaxy formation, (e) investigate Star Formation and (f) characterise exoplanets.

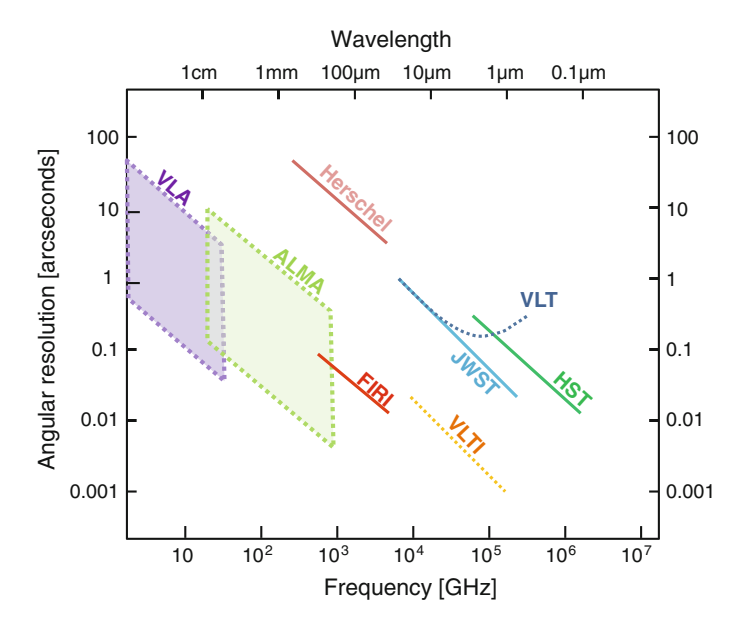


Fig. 1.2 Resolution parameter space as a function of wavelength/frequency for existing and inconstruction facilities. The FIRI expected angular resolution is compared to other current and future facilities. *Dashed lines* are to indicate ground-based facilities

1.1.2 FIR Science Cases

Being able to access the FIR gap would mean the capacity to perform high resolution observations at the Far Infrared wavelength range where a wide variety of science cases can be studied, such as observations of nearby massive star formation regions, the study of galaxy formation and evolution, and even the resolution of the FIR background at the high red-shift Universe.

Basically this wavelength range allows a unique probe into objects during their formation as it provides direct access to the peak of the lower temperature blackbody emission from the dust which enshrouds them and to a wealth of atomic and molecular spectral lines critical in understanding their energy balance and chemical evolution.

Separated in four general groups, the science cases the astronomical community is currently more interested in are presented below according to the White Paper submitted in response to the European Space Agency's call for the L2 and L3 L-class missions (Sauvage et al. 2013).

1.1.2.1 Protoplanetary Disks and Planet Formation

Most planetary systems are pervaded by dust due to the planet formation process, where through coagulation of dust and gas accretion in the disks that develop during the collapse and infall of massive protostar envelopes planets are formed. By studying the structure and dynamics of this dust, which is very bright at the Far Infrared wavelengths, one can gain information on how such systems were formed. Once the planets are formed, as their motion influence the distribution of the dust, planetary orbits can be traced.

Figure 1.3 (left) shows an artist's impression of the disk of gas and cosmic dust around the young star HD142527. The ALMA interferometer has allowed the observation of vast streams of gas flowing across the gap in the disk, expected to be created by giant planets accreting gas as they grow.

The emission of organic molecules that could be the building blocks of life in the Universe, such as ammonia and water, can be observed at the FIR region of the spectrum as well. Understanding the contents and chemistry of the Inter Stellar Medium (ISM) can be beneficial to asses the potential for life in these planetary systems.

1.1.2.2 Star Formation

Studies of single stars in low-mass star forming regions have provided a general picture of star formation starting with the collapse of dense cores in interstellar molecular clouds, moving through the protostellar classes and ending with a main sequence star (McKee and Ostriker 2007) as explained in the Young Stellar Objects

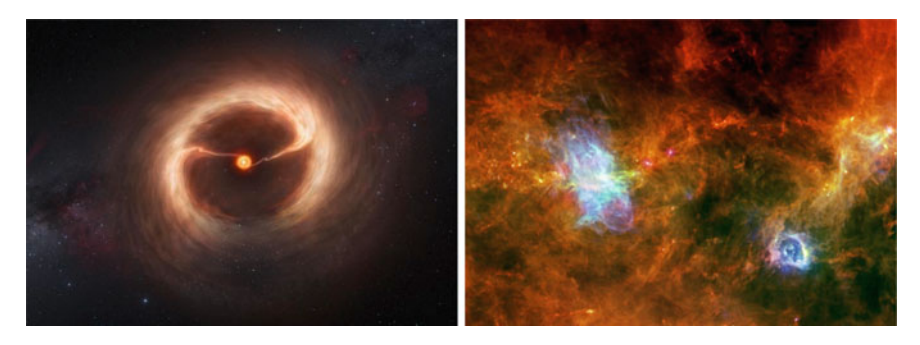


Fig. 1.3 (*Left*) Artist's impression of the disc and gas streams around HD 142527 [*Credit* ALMA (ESO/NAOJ/NRAO)/M. Kornmesser (ESO)]. (*Right*) A Herschel PACS and SPIRE false colour map of Vela C (red = 250 μ m, green = 160 μ m, blue = 70 μ m), highlighting regions of intense feedback (e.g. butterfly shaped RCW 36 in *blue*), the filamentary network, with the massive Vela ridge in the RCW 36 region, and cores forming stars [*Credit* ESA/PACS and SPIRE Consortia, T. Hill, F. Motte, Laboratoire AIM Paris-Saclay, CEA/IRFU CNRS/INSU Uni. Paris Diderot, HOBYS Key Programme Consortium]

(YSO) classification (Lada 1987). However, there is not as much knowledge on the formation of higher mass stars ($>8M_{\odot}$) because they are rare and distant, and it is the formation of the latter which controls the chemical and dynamical evolution of galaxies. Also the initial mass function (IMF), the distribution of stellar masses at birth which is one of the fundamentally important parameters in astrophysics, is not well constrained because of the lack of sufficiently resolved regions on which to study its emergence.

Herschel observations of high-mass star forming regions have shown additional structural properties, this is the presence of very dense filaments, called 'ridges', together with a network of smaller filaments connected to the ridge (Hill et al. 2011; Hennemann et al. 2012; Minier et al. 2013). Figure 1.3 shows Vega C (PACS and SPIRE false colour map) where it can be observed the filamentary network and a ridge, and cores forming stars. These ridges are not properly understood yet, and unfortunately Herschel could not resolve the high-density regions in high-mass star forming clouds due to their distance. However, having access to 1 arcsecond resolution at $100~\mu m$ from space to avoid studies through a variable atmosphere would potentially clarify the process of mass accretion through ridges.

1.1.2.3 The Nearby Universe

When access to the smallest physical scales is available the Galaxy is the target of choice. However, there are a number of fundamental limits to these observations, such as distance ambiguities and line-of-sight pile up. In order to expand the current studies only performed in the Galaxy, one needs to have access to high angular resolution to observe objects in different evolutionary or energetic stages.

For example, one could use FIR spectroscopy at high angular resolution to disentangle emission from Active Galactic Nuclei (AGN) and starburst within the nuclei of the galaxies. AGNs are of fundamental importance in astrophysics, because by converting gravitational energy into radiation they are the most powerful objects in the Universe. It is thus important to study the AGN feeding and feedback as well as the accretion physics.

There are two main reasons why there is a need for MIR/FIR observations for disentangling the complex interactions accruing near AGNs. First, the regions are often heavily obscured at shorter wavelengths and second, this spectral region contains a large amount of atomic and molecular lines covering a wide physical parameter space.

Herschel provided unprecedented sensitivity for FIR spectroscopy and improved the angular resolution over ISO, but it was not enough to differentiate spatially the AGN and starburst components. With 0.1–1 arcsecond angular resolution almost all the components of nearby AGNs (Cen A, NGC 1068, Circinus) could be resolved, from the molecular torus (10pc) out to the outflow and jet structure (1kpc).

1.1.2.4 The Evolving Universe

The most dramatic phase of evolution for AGNs and their host galaxies occurred between $z \sim 3$ and the present day, which represents a period of 11.5 Gyr (84% of the age of the Universe).

The first luminous objects in the Universe appear at around 100 Myr after the Big Bang. At these epochs, due to the Lyman opacity of hydrogen observations at optical or NIR wavelengths are impossible. The bulk of galaxy formation is thought to occur after reionization, between 500 Myr and 6 Gyr after the Big Bang, but nearly all of the stellar and black hole mass build-up in these galaxies occurs while shrouded in dust. For this reason, FIR observations are essential to understand how these galaxies are forming.

It is also essential to reach arcsecond to sub-arcsecond resolution because it will break free the confusion limit that marred the Herschel survey. Moreover, such spatial resolution would sample sub-kpc structure at any redshift (\sim 0.8 arcsecond at z=1 to z=3, and even better at z<1).

In summary, there is an obvious need for sub-arcsecond angular resolution at the FIR wavelength regime to observe astronomical targets that can unveil unprecedented knowledge.

1.2 Far Infrared Astronomy Instruments

Currently there is a lack of observational capability in the Far Infrared. ALMA (Wootten and Thompson 2009) will explore a number of wide atmospheric windows at millimeter wavelengths, and at longer wavelengths in the radio region astronomers

have made use of large interferometry arrays to produce high spatial resolution information, and will continue with LOFAR (Röttgering 2003), e-MERLIN (Garrington et al. 2004) and SKA (Dewdney et al. 2009). With JWST (Gardner et al. 2006) near and mid infrared wavelengths astrophysics will be covered with high sensitivity and high angular resolution data up to 28.5 μm . In the Far Infrared region instruments such as SPIRE, HIFI and PACS on the Herschel (Pilbratt et al. 2010) space Observatory provided unprecedented data and further improvements will occur with SAFARI on SPICA (Swinyard and Nakagawa 2009) thanks to the reduced thermal emission of a 4K-cooled primary mirror, but there is still one drawback: the spatial resolution.

To achieve high angular resolution one needs to use interferometry, and to operate at the Far Infrared the best scenario is a space based system, where there is no attenuation from the atmosphere. With this requirements the Far Infrared Interferometer concept, FIRI, is defined.

1.2.1 Past and Present FIR Instruments

IRAS (Neugebauer et al. 1984) is often credited for opening our window on the dusty Universe. Over the course of 300 days in 1983 it surveyed 96% of the sky at 12, 25, 60 and 100 μ m, discovering not only Vega-type debris disks and thousands of hot, dense, star-forming cores in our Galaxy, but also a new class of dusty, gas-rich starbursts, which is now known to be the tail end of a more numerous population of luminous, dusty starbursts at higher redshift: submm-selected galaxies (SMGs, Smail et al. 1997).

In 1995, ESA's cryogenic Infrared Space Observatory (Kessler et al. 1996) (ISO) was an unprecedented success, with almost 1000 high-impact refereed papers describing major scientific insights, particularly the discovery of crystalline features in objects ranging from comets to proto-stellar disks, the first detection of FIR water lines, the confirmation of evolution in the LIRG ($\sim\!10^{11}~L_{\odot}$) population from z = 0 to 1 via deep 15 μm imaging, the discovery of cold ($\sim\!20~K$) dust components in normal, inactive spirals at 175–200 μm , and the development of diagnostic ratios via spectroscopy of cooling lines and PAHs (Genzel and Cesarsky 2000). Despite pioneering breakthroughs in the FIR regime, IRAS, ISO and Spitzer have provided only a glimpse of what is to come. Their angular resolution, around 60 arcsec at 200 μm , makes source confusion a major issue at only moderate depths at the wavelength where the energy density from galaxies is greatest.

NASA's Spitzer space telescope (Werner et al. 2004), and more recently ESA's Herschel space observatory, both provide large area survey atlases across this FIR wavelength range. However, for most science cases, neither telescope has sufficient angular resolution to probe individual targets of interest in detail, and thereby study the physical processes which govern these sources.

ESA's Herschel, launched in 2009, has yielded a major breakthrough for FIR astronomy. Its spatial resolution at 200 μm is five times better than ISO and this has allowed imaging photometric and spectroscopic observations of the interstellar



Fig. 1.4 FIR instruments in chronological order from *left* to *right* IRAS (1983), 0.6-m dish cooled at 2 K and operating at 12, 25, 60 and 100 μ m; ISO (1995), 0.6-m dish cooled at 2–3 K operating in the band 3–200 μ m; Spitzer (2003), 0.85 m dish cooled at 4 K operating in the band 3–180 μ m; Herschel (2009), 3.5-m dish cooled at 80 K operating in the band 55–670 μ m. [*Credit*, respectively: NASA/JPL; ESA; NASA/JPL-Caltech; ESA/AOES Medialab, background from Hubble Space Telescope image (NASA/ESA/STScI)]

medium (ISM) in our Galaxy and its neighbours. Herschel has also extended the wavelength coverage into the short wavelength sub-mm waveband (200–670 μ m) for the first time. Source confusion, however remains an issue. In even relatively short integrations there are unresolved sources which limit the depth of an observation. This is true for both extragalactic and Galactic observations, with distant galaxies dominating the noise even in moderately luminous regions of the plane of the Galaxy, an effect already noted by researchers searching for debris disks in Spitzer images.

Figure 1.4 shows, in chronological order, the satellites just presented. IRAS (1983) was provided with a 0.6 m telescope cooled at 2 K, operating at 12, 25, 60 and 100 μm . ISO (1995) had only a single dish telescope of 0.6 m cooled at 2–3 K but operating in the band 3–200 μm . Spitzer (2003) increased the dish size to 0.85 m and was cooled to 4 K, still operating in a similar band as ISO (3–180 μm). Finally Herschel (2009) represented a huge increase of spatial resolution due to its 3.5 m telescope diameter cooled at 80 K. Its band of operation was from 55 to 670 μm .

1.2.2 Ongoing and Future FIR Instruments

On the ground, the Atacama Large Millimeter/submillimeter Array (ALMA) is located in the Chile's Atacama desert. Its initial configuration is composed of 66 antennas with a possible extension in the future. ALMA is entering operation Cycle 2 in June 2014 (with 6 of its 10 spectral bands) and has already shown enormous potential in exploring the high-spatial resolution FIR-mm wave window in its early test runs. In Cycle 2 thirty four 12-m antennas in the main array (12-m Array), and nine 7-m antennas (7-m Array, for short baselines) and two 12-m antennas (Total

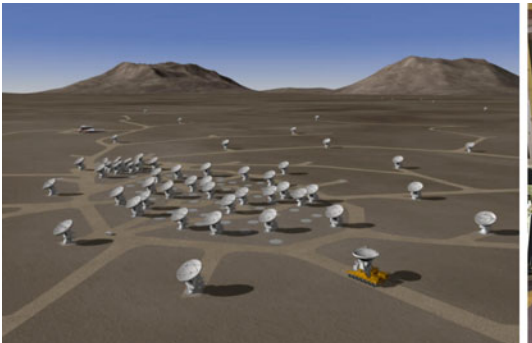
Power Array or TP Array, for making single-dish maps), which together constitute the Atacama Compact Array will be available.

The James Webb Space Telescope (JWST) will be a large infrared telescope with a 6.5-m primary mirror. With its Mid-Infrared Instrument (MIRI) is expected to enter routine operation after 2018–20. It will also contain three more science instruments, the Near InfraRed Camera (NIRCam), the Near InfraRed Spectrograph (NIRSpec), and the Fine Guidance Sensor/Near InfraRed Imager and Slitless Spectrograph (FGSNIRISS), designed to work primarily in the infrared range of the electromagnetic spectrum, with some capability in the visible range. It will be sensitive to light from 0.6 to 28 μm .

Both these facilities shown in Fig. 1.5 will represent a significant improvement in angular resolution in the sub-mm to mm wavelength ranges and in the mid-infrared respectively, but a gap will be left in the important FIR window, wherein the best resolution possible will be 2–3 orders of magnitude worse than the surrounding spectral ranges.

The SPICA FIR space mission, project initially led by JAXA and the successor of AKARI, is intended to become operational within the next decade, around 2026. With a 3.5 m diameter telescope cooled to 4.5 K it is designed to also observe at longer wavelengths (3.5–210 μm) than the JWST. It will be a key technical and scientific precursor to FIRI, although it will have an angular resolution similar to that of Herschel and will fail to close this FIR resolution gap. Currently there are major changes in roles of international partners, and there is a plan for re-entering the open competition in the ESA Cosmic Vision program for an M-class mission.

A large, single aperture in space would provide unprecedented increases in sensitivity and mapping speed over any existing or planned facility, particularly if actively cooled. However, it is clear that to make significant advances on Herschel and SPICA in all areas of astronomy, from nearby planetary systems to the highest red-shift galaxies, even the largest conceivable dish would be inadequate. These fields of



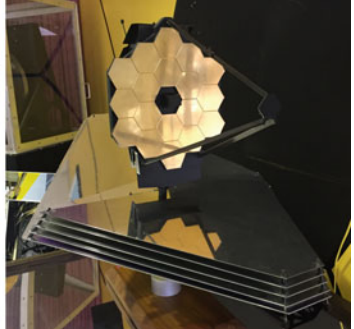


Fig. 1.5 (*Left*) Artist conception of the ALMA array with roads, in the extended configuration. *Credit* ALMA (ESO/NAOJ/NRAO). (*Right*) Model of the James Webb Space Telescope, located at NASA Goddard Space Flight Center

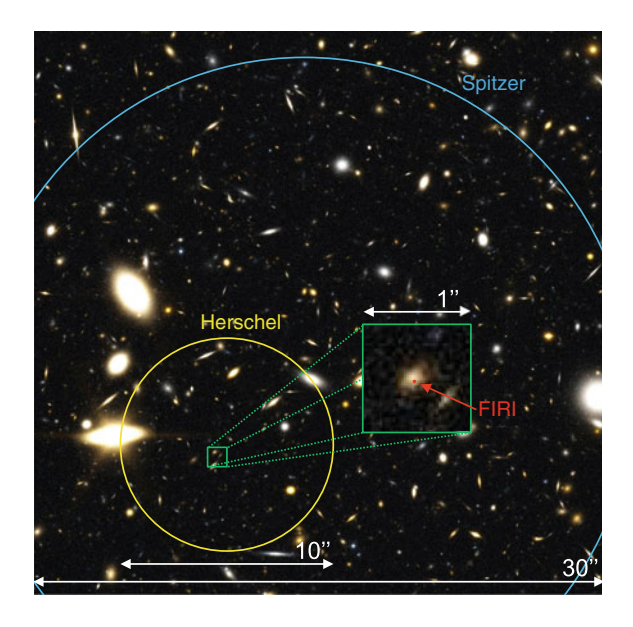
study call for exquisite angular resolution of the order of 0.02 arcseconds at 100 μ m, as well as sufficient sensitivity to allow photon-starved spectroscopy across an arcminute field of view in the 25–400 μ m band.

An example of this achievable spatial resolution is portrayed in Fig. 1.6 where a comparison with Herschel and Spitzer beam footprints is made on a simulated JWST deep field. Here the study of single galaxies would be possible beating the current confusion limit.

Two instruments have been extensively studied and proposed so far regarding space interferometry: the Space Infrared Interferometric Telescope (Leisawitz et al. 2007) (SPIRIT), as a practical step towards the more ambitious Submillimeter Probe of the Evolution of Cosmic Structure (Harwit et al. 2007) (SPECS), and the Far Infrared Interferometer (FIRI).

In 2007, NASA's SPIRIT was proposed as a Far Infrared observatory from space for high-resolution imaging and spectroscopy operating at the 25–400 μm range. The concept consists in a two 1-m telescopes boom-based interferometer providing a 0.3 arcsecond resolution at 100 μm and a spectral resolution of R=3000. With this characteristics, some of the science cases presented earlier in this chapter could be addressed. During the past decade technology and mission concept development has been reported, and SPIRIT was selected by NASA for study as a candidate Origins Probe mission. During the next decade technology development is expected to meet the requirements for such a mission, from technology maturation to telescope and instrument tested buildup, integration and testing.

Fig. 1.6 Simulated 30 arcsecond JWST deep field, illustrating FIRI's ability to distinguish the emission from individual galaxies. For comparison, the Spitzer resolution at 160 μm is shown, as well as the Herschel beam. FIRI's subarcsecond synthesised beam, *red dot*, is barely visible even in the blown-up arcsecond² image



In 2006, as part of the ESA's Cosmic Vision 2015–25 program, FIRI was proposed to carry out high-resolution imaging spectroscopy in the FIR range of wavelengths. The FIRI mission concept consisted in three cold 3.5-m apertures orbiting a beam-combining module with a separation of up to 1 km (free flying or tethered) operating in the range 25–385 μm . The technique selected was direct detection interferometry to ensure μJy sensitivity and 0.02 arcsecond angular resolution at 100 μm and a spectral resolution >3000. Unfortunately, FIRI was not selected because to enable a mission as complex as FIRI substantial technology development effort is still required, specifically in the field of cooling, optics and detector technology, and metrology.

1.3 The Sub-arcsecond Space-Based FIR Interferometer

Earlier in 2013, as a response to the call for White Papers for the definition of the L2 and L3 missions in the ESA Science Programme, and following the steps of the 2006 proposal a new sub-arcsecond far-infrared space observatory was presented. This White Paper was the result of an European collaboration lead by Ivison, Helmich and Sauvage.

1.3.1 Mission Concepts

Focusing in the science cases presented before which all require a 0.1-1 arcsecond angular resolution at $100\,\mu$ m, three straw-man concepts were proposed and are shown in Fig. 1.7: TALC (left), FIRIT (centre) and ESPRIT (right).

The TALC (Thinned Aperture Light Collector) concept consists of a 20 m diameter deployable aperture. It explores some unconventional optical solutions between the single dish and the interferometer in order to achieve a very large aperture by



Fig. 1.7 Straw-man concepts proposed in the White Paper for the definition of the L2 and L3 missions in the ESA Science Programme presented by Ivison, Helmich and Sauvage. A deployable large aperture telescope TALC (*left*), a direct imaging interferometer FIRIT (*centre*) [*Credit* NASA/GSFC] and a heterodyne interferometer for the FIR, ESPRIT (*right*)

overcoming the constraints of launching a big single dish aperture to space. However, an unconventional optical design requires to combine data acquisition with unconventional data processing techniques, which are currently under development. The TALC mirror is a segmented ring of 20-m diameter and 3-m width, reaching a 0.9 arcsecond angular resolution at 100 μ m. It is intended to be cooled at 80 K, and simulations show that a 0.1 mJy 5σ -1h can be achieved.

FIRIT is a concept for a conservative design of a direct imaging interferometer. With sub-arcsecond spatial resolution, this option is based on the pre-existing ESA CDF study (2006) for FIRI and the SPIRIT concept. This design consists of the combination of input beams from two telescopes, moving along an unfolding or telescopic boom, in a third hub unit with the detecting part of the payload. A promising option for the payload is the Double Fourier Modulation technique, which allows spectral and spatial interferometry to be performed simultaneously in a single instrument. With two 1-m dishes on a 36-m boom, or potentially more depending on the mission time frame, a band from 25–400 μm would allow a spatial resolution of 0.18 and 2.8 arcseconds, respectively. In the next Section more details regarding this instrument concept are given.

Finally, ESPRIT (Wild et al. 2008) is a concept for a heterodyne interferometer for the Far Infrared. The design would consist in four 3.5-m diameter dishes separated up to 50 m in a free flying configuration in order to achieve $\sim\!1$ arcsecond resolutions at 200 μm (for comparison with FIRIT, 0.13 arcseconds at 25 μm ; 2.01 arcseconds at 400 μm , although current technology is now reaching 2.7 THz, this is $\sim\!110\,\mu m$). The uv-plane would be filled by letting the dishes drift with respect to each other, and to guarantee optimal image quality phase-closure and self-calibration would have to be employed. The main advantage of this system is that the heterodyne principle creates a long coherence length allowing for relaxed positioning requirements.

1.3.2 FIRIT—Direct Imaging Interferometry

As presented before, the work described in this Thesis is related to the FIRIT concept regarding the detection technique. However, different instrument scenarios are considered.

Recent developments for a balloon based experiment, BETTII (Rinehart et al. 2009; Rinehart 2010a, b, 2011; Rinehart and BETTII Team 2010; Leisawitz 2008), and space based spectral-spatial interferometers such as SPIRIT (Leisawitz et al. 2007, 2008; Leisawitz 2008), SPECS, FIRI have identified that some technology needs to be developed and demonstrated, for example high sensitivity detectors (NEPs $\sim 10^{-20}$ W/Hz $^{1/2}$), cooled apertures, beam combination and data processing algorithms. In all these proposals, the common point is the technique employed to perform observations, the Double Fourier Modulation.

1.3.2.1 Double Fourier Modulation

To achieve the angular resolution and sensitivity required for FIRI, one can use the so-called Spectral-Spatial Interferometry, Double Fourier Modulation, multi-Fourier Transform Spectroscopy or Double Interferometry (Mariotti and Ridgway 1988; Ohta et al. 2006, 2007), as a result of a combination of two well-known techniques: Stellar Interferometry and Fourier Transform Spectroscopy.

Stellar Interferometry Interferometric techniques in astronomy are based on the Michelson interferometer. Two telescopes mounted on a baseline are separated by a distance *d*, and the light collected is combined on a beam splitter. By using a delay line the geometrical delay introduced by the sidereal motion of a star across the sky is compensated. At the detector plane the fringes are measured. Changing the baseline corresponds to being sensitive to different spatial frequencies.

Fourier Transform Spectroscopy Based on the Michelson interferometer, this technique allows determination of a source spectral distribution. The light of a source is divided and recombined after introducing a variable delay on one of the optical paths. At the detector an interferogram is recorded, and by Fourier transforming it, the source spectral distribution can be obtained.

For the combination of these two techniques, instead of dividing the light from the source with a beam splitter, one uses two apertures and recombines the incoming light from these two apertures. More theoretical details are given in Chap. 2, and the testbed demonstration of this technique in the Far Infrared is presented in Chap. 3.

1.3.2.2 Designs Under Consideration

Three different designs have been identified as possible candidates for a future Far Infrared space-based interferometer operating in the 25–400 μm wavelength range.

The first one is a boom-based system. Based on NASA's SPIRIT, it consists of two 1-m apertures separated up to 36 m on a boom. By using a boom the metrology requirements are more relaxed, but it also limits the maximum baseline of the interferometric system. In this case, one would be able to observe with an angular resolution of 0.3 arcseconds at $100~\mu m$. This is the most conservative design.

Going one step further, a tethered version is under consideration. For example, if using two 2-m apertures and a tether of up to $100\,m$ in length an angular resolution of 0.1 arcseconds could be achievable at $100\,\mu m$. This concept is similar to a reduced version of SPECS, which consists of a tethered interferometer with 3-m apertures separated up to 1 km, providing an angular resolution of 0.01 arcseconds at $100\,\mu m$.

Finally, the most ambitious concept is the free flying configuration. This would allow kilometric baselines which would provide an angular resolution of 0.01 arcseconds at 100 μ m. However, the metrology requirements for the positioning of the telescopes is more restrictive than in the previous concepts due to the fact that there would be no rigid structure holding the different elements together.

In the ESA's CDF Study Report one can find a full description of the optics involving the configurations just presented including the identification of the critical technologies.

1.3.2.3 Current Efforts

Recently the Research Executive Agency (REA) has started sponsoring two activities: the FP7-SPACEKIDS and FP7-FISICA.

The three-year SPACEKIDS project is working on the development of a new detector technology, Kinetic Inductance Detectors (KIDs), to be used in future space missions. The new detectors will be capable of working at extremely low temperatures and will be designed for use in future satellites for astronomy and for the study of the Earth's atmosphere.

FISICA (Far Infrared Space Interferometer Critical Assessment) is also a three year project for the definition and technology development for the next generation THz space interferometry, more specifically to advance beam-combination, cryogenic delay lines, position metrology and to create a representative instrument simulator for a direct detection interferometer. The instrument simulator presented in this Thesis will form the basis of the first version of the FISICA simulator.

References

- P.E. Dewdney, P.J. Hall, R.T. Schilizzi, T.J.L.W. Lazio, The square kilometre array. Proc. IEEE **97**(8), 1482–1496 (2009). ISSN 0018-9219. doi:10.1109/JPROC.2009.2021005
- H. Dole, G. Lagache, J.-L. Puget, K.I. Caputi, N. Fernández-Conde, E. Le Floc'h, C. Papovich, P.G. Pérez-González, G.H. Rieke, M. Blaylock, The cosmic infrared background resolved by Spitzer. Astron. Astrophys. 451(2), 417–429 (2006). doi:10.1051/0004-6361:20054446
- ESA Concurrent Design Facility. Far Infrared Interferometer—CDF Study Report. CDF-49(A): 1–294, (2006). http://sci.esa.int/future-missions-office/40738-firi-cdf-study-report/
- J.P. Gardner, J.C. Mather, M. Clampin, R. Doyon, M.A. Greenhouse, H.B. Hammel, J.B. Hutchings, P. Jakobsen, S.J. Lilly, K.S. Long, J.I. Lunine, M.J. McCaughrean, M. Mountain, J. Nella, G.H. Rieke, M.J. Rieke, H.-W. Rix, E.P. Smith, G. Sonneborn, M. Stiavelli, H.S. Stockman, R.A. Windhorst, G.S. Wright, The James Webb space telescope. Space Sci. Rev. 123, 485–606 (2006). doi:10.1007/s11214-006-8315-7
- S.T. Garrington, B. Anderson, C. Baines, J.A. Battilana, M.N. Bentley, D. Brown, P. Burgess, P.J. Diamond, G.J. Kitching, R. McCool, T.W. Muxlow, R.G. Noble, N. Roddis, R.E. Spencer, P. Thomasson. e-MERLIN, ed. by J.M. Oschmann, Jr. *Ground-based Telescopes*, volume 5489 of Society of Photo-Optical Instrumentation Engineers (SPIE) Conference Series, pp. 332–343, Oct 2004. doi:10.1117/12.553235
- R. Genzel, C.J. Cesarsky, Extragalactic results from the infrared space observatory. Annu. Rev. Astron. & Astr. 38, 761–814 (2000). doi:10.1146/annurev.astro.38.1.761
- M. Harwit, D. Leisawitz, Rinehart, D.S., Benford, J. Budinoff, R. Chalmers, C. Cottingham, W. Danchi, M.J. DiPirro, R. Farley, T.T. Hyde, A.L. Jones, M.J. Kuchner, A. Liu, R. Lyon, J.C. Mather, C.T. Marx, A.J. Martino, S.H. Moseley, S. Ollendorf, D.A. Quinn, R.F. Silverberg, P. Whitehouse, M. Wilson, J.C. Pearson, C. Lawrence, E. Serabyn, M. Shao, R. Smythe, H.W. Yorke, L.G. Mundy, E. Lorenzini, C. Bombardelli, R.J. Allen, D. Calcetti, A. Blain, W. Doggett,

A. Labeyrie, T. Nakagawa, D.A. Neufeld, S. Satyapal, G. Stacey, E.L. Wright, N.M. Elias, D. Fischer, J. Leitch, M.C. Noecker, T. Espero, E.J. Friedman, R.A. Woodruff, C. Lillie, A kilometerbaseline far-infrared submillimeter interferometer in space. SPECS Vision Mission Study Final Report. *AIAA*, (2007)

- F.P. Helmich, R.J. Ivison, FIRI A far-infrared interferometer. Exp. Astron. 23, 245–276 (2009). doi:10.1007/s10686-008-9100-2
- M. Hennemann, F. Motte, N. Schneider, P. Didelon, T. Hill, D. Arzoumanian, S. Bontemps, T. Csengeri, P. André, V. Konyves, F. Louvet, A. Marston, A. Men'shchikov, V. Minier, Q. Nguyen, Luong, P. Palmeirim, N. Peretto, M. Sauvage, A. Zavagno, L. D. Anderson, J.-P. Bernard, J. Di Francesco, D. Elia, J. Z. Li, P. G. Martin, S. Molinari, S. Pezzuto, D. Russeil, K. L. J. Rygl, E. Schisano, L. Spinoglio, T. Sousbie, D. Ward-Thompson, G.J. White. The spine of the swan: a Herschel study of the DR21 ridge and filaments in Cygnus X. Astron. Astrophys. 543, L3 (2012). doi:10.1051/0004-6361/201219429
- T. Hill, F. Motte, P. Didelon, S. Bontemps, V. Minier, M. Hennemann, N. Schneider, P. André, A. Men'shchikov, L.D. Anderson, D. Arzoumanian, J.-P. Bernard, J. di Francesco, D. Elia, T. Giannini, M.J. Griffin, V. Könyves, J. Kirk, A.P. Marston, P.G. Martin, S. Molinari, Q. Nguyen, Luong, N. Peretto, S. Pezzuto, H. Roussel, M. Sauvage, T. Sousbie, L. Testi, D. Ward-Thompson, G.J. White, C.D. Wilson, A. Zavagno. Filaments and ridges in Vela C revealed by Herschel: from low-mass to high-mass star-forming sites. Astron. Astrophys. 533, A94 (2011). doi:10.1051/0004-6361/201117315
- M.F. Kessler, J.A. Steinz, M.E. Anderegg, J. Clavel, G. Drechsel, P. Estaria, J. Faelker, J.R. Riedinger, A. Robson, B.G. Taylor, S. Ximénez de Ferrán, The Infrared Space Observatory (ISO) mission. Astron. Astrophys. **315**, L27–L31 (1996)
- C.J. Lada, Star formation-from ob associations to protostars, in *Star Forming Regions*, vol. 115, pp. 1–17 (1987)
- D. Leisawitz, The Space Infrared Interferometric Telescope (SPIRIT): A Far-IR Observatory for High-resolution Imaging and Spectroscopy, in 37th COSPAR Scientific Assembly, volume 37 of COSPAR, Plenary Meeting, p. 1740 (2008)
- D. Leisawitz, C. Baker, A. Barger, D. Benford, A. Blain, R. Boyle, R. Broderick, J. Budinoff, J. Carpenter, R. Caverly, P. Chen, S. Cooley, C. Cottingham, J. Crooke, D. Dipietro, M. Dipirro, M. Femiano, A. Ferrer, J. Fischer, J.P. Gardner, L. Hallock, K. Harris, K. Hartman, M. Harwit, L. Hillenbrand, T. Hyde, D. Jones, J. Kellogg, A. Kogut, M. Kuchner, B. Lawson, J. Lecha, M. Lecha, A. Mainzer, J. Mannion, A. Martino, P. Mason, J. Mather, G. McDonald, R. Mills, L. Mundy, S. Ollendorf, J. Pellicciotti, D. Quinn, K. Rhee, S. Rinehart, T. Sauerwine, R. Silverberg, T. Smith, G. Stacey, H.P. Stahl, J. Staguhn, S. Tompkins, J. Tveekrem, S. Wall, M. Wilson, The space infrared interferometric telescope (SPIRIT): high-resolution imaging and spectroscopy in the far-infrared. Adv. Space Res. 40, 689–703 (2007). doi:10.1016/j.asr.2007.05.081
- D. Leisawitz, T.T. Hyde, S.A. Rinehart, M. Weiss, The Space Infrared Interferometric Telescope (SPIRIT): the mission design solution space and the art of the possible, in *Society of Photo-Optical Instrumentation Engineers (SPIE) Conference Series*, volume 7010 of Society of Photo-Optical Instrumentation Engineers (SPIE) Conference Series, Aug 2008. doi:10.1117/12.789952
- J.-M. Mariotti, S.T. Ridgway, Double Fourier spatio-spectral interferometry—combining high spectral and high spatial resolution in the near infrared. Astron. Astrophys. 195, 350–363 (1988)
- F.C. McKee, E.C. Ostriker, Theory of star formation. Annu. Rev. Astron. Astrophys. **45**, 565–687 (2007)
- V. Minier, P. Tremblin, T. Hill, F. Motte, N. Ph André, N.Schneider Lo, E. Audit, G.J. White, M. Hennemann et al., Ionisation impact of high-mass stars on interstellar filaments. Astron. Astrophys. 550 (2013)
- G. Neugebauer, H.J. Habing, R. van Duinen, H.H. Aumann, B. Baud, C.A. Beichman, D.A. Beintema, N. Boggess, P.E. Clegg, T. de Jong, J.P. Emerson, T.N. Gautier, F.C. Gillett, S. Harris, M.G. Hauser, J.R. Houck, R.E. Jennings, F.J. Low, P.L. Marsden, G. Miley, F.M. Olnon, S.R. Pottasch, E. Raimond, M. Rowan-Robinson, B.T. Soifer, R.G. Walker, P.R. Wesselius, E. Young,

The Infrared Astronomical Satellite (IRAS) mission. Astrophys. J. Lett. 278, L1–L6 (1984). doi:10.1086/184209

- I.S. Ohta, M. Hattori, H. Matsuo, Development of a multi-Fourier-transform interferometer: fundamentals. Appl. Opt. 45, 2576–2585 (2006). doi:10.1364/AO.45.002576
- I.S. Ohta, M. Hattori, H. Matsuo, Development of a multi-Fourier-transform interferometer: imaging experiments in millimeter and submillimeter wave bands. Appl. Opt. 46, 2881–2892 (2007). doi:10.1364/AO.46.002881
- G.L. Pilbratt, J.R. Riedinger, T. Passvogel, G. Crone, D. Doyle, U. Gageur, A.M. Heras, C. Jewell, L. Metcalfe, S. Ott, M. Schmidt, Herschel space observatory. Astron. Astrophys. 518, L1 (2010). doi:10.1051/0004-6361/201014759
- S. Rinehart, The Balloon Experimental Twin Telescope for Infrared Interferometry (BETTII): Spatially-Resolved Spectroscopy in the Far-Infrared, in *American Astronomical Society Meeting Abstracts #215*, volume 42 of Bulletin of the American Astronomical Society, p. 441.01, Jan 2010a
- S. Rinehart, The Balloon Experimental Twin Telescope for Infrared Interferometry (BETTII), in *Society of Photo-Optical Instrumentation Engineers (SPIE) Conference Series*, volume 7734 of Society of Photo-Optical Instrumentation Engineers (SPIE) Conference Series, July 2010b. doi:10.1117/12.855476
- S.A. Rinehart, BETTII Team, The Balloon Experimental Twin Telescope for Infrared Interferometry, eds. by V. Coudé Du Foresto, D.M. Gelino, I. Ribas, Astronomical Society of the Pacific Conference Series, volume 430 of Astronomical Society of the Pacific Conference Series, p. 524, Oct 2010
- S. Rinehart, The Balloon Experimental Twin Telescope for Infrared Interferometry (BETTII): High Angular Resolution in the Far-Infrared, in *American Astronomical Society Meeting Abstracts* #217, volume 43 of Bulletin of the American Astronomical Society, p. 157.08, Jan 2011
- S. Rinehart, C. Allen, R. Barry, D. Benford, W. Danchi, D. Fixsen, D. Leisawitz, L. Mundy, R. Silverberg, J. Staguhn, The Balloon Experimental Twin Telescope for Infrared Interferometry (BETTII): High Angular Resolution Astronomy at Far-Infrared Wavelengths, in *American Astronomical Society Meeting Abstracts #213*, volume 41 of Bulletin of the American Astronomical Society, p. 475.19, Jan 2009
- H. Röttgering, Lofar, a new low frequency radio telescope. New Astron. Rev. 47(4), 405–409 (2003)
 M. Sauvage, R.J. Ivison, F. Helmich, Sub-arcsecond far-infrared space observatory: a science imperative (2013). submitted in response to the European Space Agency's call for Science White Papers
- I. Smail, R.J. Ivison, A.W. Blain, A deep sub-millimeter survey of lensing clusters: a new window on galaxy formation and evolution. Astrophys. J. Lett. 490, L5 (1997). doi:10.1086/311017

for the L2 and L3 L-class missions

- B. Swinyard, T. Nakagawa, The space infrared telescope for cosmology and astrophysics: SPICA a joint mission between JAXA and ESA. Exp. Astron. **23**(1), 193–219 (2009). ISSN 0922-6435. doi:10.1007/s10686-008-9090-0
- M.W. Werner, T.L. Roellig, F.J. Low, G.H. Rieke, M. Rieke, W.F. Hoffmann, E. Young, J.R. Houck, B. Brandl, G.G. Fazio, J.L. Hora, R.D. Gehrz, G. Helou, B.T. Soifer, J. Stauffer, J. Keene, P. Eisenhardt, D. Gallagher, T.N. Gautier, W. Irace, C.R. Lawrence, L. Simmons, J.E. Van Cleve, M. Jura, E.L. Wright, D.P. Cruikshank. The Spitzer space telescope mission. Astrophys. J. Suppl. Ser. 154(1), 1 (2004). http://stacks.iop.org/0067-0049/154/i=1/a=1
- W. Wild, T. de Graauw, F. Helmich, A. Baryshev, J. Cernicharo, J.R. Gao, A. Gunst, A. Bos, J.-W. den Herder, B. Jackson, V. Koshelets, H.-J. Langevelde, P. Maat, J. Martin-Pintado, J. Noordam, P. Roelfsema, L. Venema, P. Wesselius, P. Yagoubo, ESPRIT: a study concept for a farinfrared interferometer in space, in *Society of Photo-Optical Instrumentation Engineers (SPIE) Conference Series*, volume 7013 of Society of Photo-Optical Instrumentation Engineers (SPIE) Conference Series, July 2008. doi:10.1117/12.789603
- A. Wootten, A.R. Thompson, The atacama large millimeter/submillimeter array. Proc. IEEE 97(8), 1463–1471 (2009). ISSN 0018-9219. doi:10.1109/JPROC.2009.2020572

Chapter 2 Theoretical Background

The fundamentals of Spectro-Spatial Interferometry (Mariotti and Ridgway 1988), also called Double Fourier Modulation (DFM) or Multi-Fourier Transform Spectroscopy (Ohta et al. 2007, 2006), are presented here and provide the background for the understanding of the following chapters.

The goal of Double Fourier Modulation is to measure the spectral and spatial characteristics of an object simultaneously and it can be understood as the combination of two well known techniques: Fourier transform spectroscopy (FTS) and Stellar Interferometry. The literature regarding both FTS and Stellar Interferometry is extensive, and the concepts presented here are the ones related to the work of this Thesis.

In Sect. 2.1 the theoretical background of Fourier Transform Spectroscopy is presented. The starting point is the Michelson Interferometer, as the design of many interferometers used today are based on the Michelson original design from 1891. Special emphasis is after given to the generation and sampling of the interferograms, as a correct measurement of a source spectrum is strongly related to the selection of the instrument parameters. Finally the procedure for the recovery of the spectrum is described.

In Sect. 2.2 the fundamentals of Stellar Interferometry are shown. Starting with the Young's double slit experiment the interferometric observables are explained, this is, the complex visibility function. The data synthesis relevant to the work of this thesis is then presented. Finally, in Sect. 2.3 the concept of Multi-Fourier Transform Interferometry is developed.

2.1 Fourier Transform Spectroscopy

Fourier Transform Spectroscopy (FTS) is a widely used technique (Griffiths and de Haseth 2007) based on the Michelson interferometer for the determination of the spectral distribution of a source. The light of a source is divided and recombined after delaying one of the optical paths as a function of time to generate an interferogram recorded with a detector. This interferogram is consequently Fourier transformed to obtain the source spectral distribution. In this section the principles of operation of the Fourier transform spectrograph are presented, with emphasis on the sampling of the interferogram and the spectrum reconstruction algorithms.

2.1.1 The Michelson Interferometer

The design of many interferometers used for infrared spectrometry today is based on that of the two-beam interferometer originally designed by Michelson (1891a, b, 1903) in 1891. The Michelson interferometer is a device that generates an interference pattern by splitting a beam of light into two paths and recombining them. The introduced spatial delay of one of the optical paths causes the appearance of fringes by forcing constructive or destructive interference. By recording the power at different spatial positions an interferogram is acquired.

Figure 2.1 shows the simplest form of a Michelson interferometer. It consists of two perpendicular plane mirrors, one fixed and one movable to introduce the required

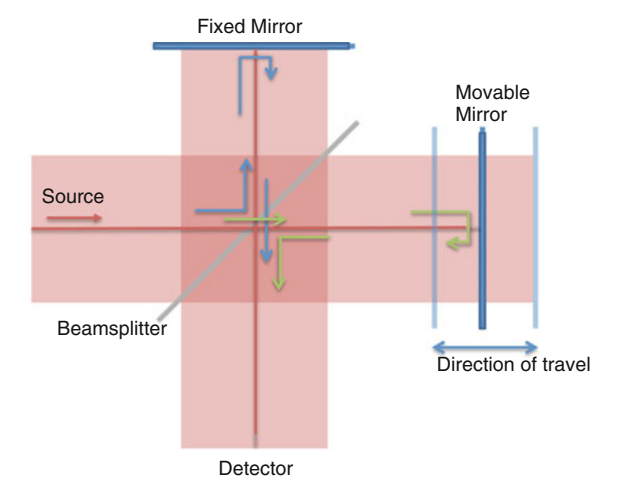


Fig. 2.1 The simplest Michelson interferometer, consisting of two mutually perpendicular plane mirrors, one of which can move along an axis that is perpendicular to its plane. A collimated light source (*red*) reaches the beamsplitter, which splits the light in two paths: reflected (*blue arrow*) and transmitted (*green arrow*). The fixed mirror reflects the light back to the beamsplitter, and the movable mirror reflects the transmitted light to the beamsplitter, where they interfere

delay, and a beamsplitter. The beamsplitter partially reflects and partially transmits a collimated beam of radiation from an external source. The beams then return to the beamsplitter where they interfere and are again partially reflected and partially transmitted.

The optical path difference (OPD) between the beams that travel to the fixed and movable mirror and back to the beamsplitter is called retardation, δ . When the path length on both arms of the interferometer are equal, the position of the moving mirrors is referred to as the position of zero retardation or zero path difference (ZPD). The two beams are perfectly in phase on recombination at the beamsplitter, where the beams interfere constructively and the intensity of the beam passing to the detector is the sum of the intensities of the beams passing to the fixed and movable mirrors. Therefore, all the light from the source reaches the detector at this point and none returns to the source. To understand why no radiation returns to the source at ZPD one has to consider the phases on the beam splitter.

2.1.1.1 Phases on the Beam Splitter

A beam that is reflected by a mirror at normal incidence undergoes a phase change of π . However, the phase difference between the reflected and the transmitted beams from a beam splitter is $\pi/2$: the beam that is reflected undergoes a phase change of $\pi/2$ while the phase of the transmitted beam remains unchanged (Lawson 2000). In this section this statement is proved.

First consider an ideal, thin and symmetric beam splitter. The relative amplitude and phase shift of the reflected wavefront are r and δ_r , and the relative amplitude and phase shift of the transmitted wavefront are t and δ_t , respectively.

The source emits a beam with amplitude E_0 which is split into a reflected complex amplitude $re^{i\delta_r}$ and a transmitted complex amplitude $te^{i\delta_t}$. Each beam is reflected by a perfectly reflecting mirror and returned to the beam splitter, where the beams each split again. The output or emerging amplitudes towards the detector (E_d) and towards the source (E_s) are

$$E_{d} = E_{0}re^{i\delta_{r}}te^{i\delta_{t}} + E_{0}te^{i\delta_{t}}re^{i\delta_{r}}$$

$$= 2rtE_{0}e^{i(\delta_{r}+\delta_{t})}$$

$$E_{s} = E_{0}re^{i\delta_{r}}re^{i\delta_{r}} + E_{0}te^{i\delta_{t}}te^{i\delta_{t}}$$
(2.1)

$$=E_0\left[r^2e^{i2\delta_r}+t^2e^{i2\delta_t}\right] \tag{2.2}$$

The corresponding intensities of the incident beam (I_0) and the emerging beam $(I_d \text{ and } I_s)$ are

$$I_0 = E_0 E_0^* = |E_0|^2 (2.3)$$

$$I_d = E_d E_d^* = |E_0|^2 4RT (2.4)$$

$$I_s = E_s E_s^* = |E_0|^2 \left[(R - T)^2 + 4RT \cos^2(\delta_r - \delta_t) \right]$$
 (2.5)

where $R = |r^2|$ and $T = |t^2|$. Conservation of energy requires that $I_0 = I_d + I_s$. In this scenario, the phase shift is

$$\cos^{2}(\delta_{r} - \delta_{t}) = 0$$

$$|\delta_{r} - \delta_{t}| = \pi/2$$
(2.6)

Thus the reflected and transmitted beam from a thin beam splitter will present a $\pi/2$ phase shift between them.

The overall phases of the system are as follow: the beam to the detector that travels to the fixed mirror undergoes a $\pi/2$ phase change on the beam splitter, a π phase change on the fixed mirror, and no phase change at the beam splitter, $3\pi/2$ in total. The transmitted beam to the detector undergoes no phase change when transmitted through the beam splitter, π phase change on the movable mirror and $\pi/2$ phase change when reflected by the beam splitter, again $3\pi/2$ in total. Therefore, the beams are in phase and interfere constructively. The beam travelling back to the source from the fixed mirror undergoes a $\pi/2$ at the beam splitter, a π phase change at the fixed mirror and a second $\pi/2$ phase change on the beam splitter, 2π phase change in total. From the movable mirror, the beam undergoes only the mirror phase change, π . Thus, the two beams are π radiants out of phase and interfere destructively. For this reason, at the ZPD the entire power of the incident beam is transmitted to the detector and no light returns to the source.

2.1.2 Generating the Interferogram

By displacing the movable mirror one alters the retardation between the beams. If the mirror is displaced a distance $\lambda/4$, the optical path difference between the beams on the beamsplitter is $\lambda/2$ and the beams interfere destructively as they are out of phase. In this situation, all the light returns to the source. Likewise, if the retardation is λ (corresponding to a mirror displacement of $\lambda/2$), the beams interfere constructively on the beam splitter, and all the light travels to the detector.

In the case of monochromatic light of wavelength λ_0 (or wavenumber $\nu_0=1/\lambda_0$), as shown in Fig. 2.2, the intensity of the beam at the detector measured as a function of retardation has a cosine shape, where the maximums correspond to retardation intervals multiple of λ_0 . At other wavenumbers ν , the intensity of the beam at the detector is

$$I_d(\delta) = 2RTI_0(\nu)(1 + \cos 2\pi \nu \delta) \tag{2.7}$$

As seen in Eq. 2.4, for the particular case of the ZPD where $\delta = 0$, the intensity of the beam at the detector is $I_d(\delta) = 4RTI_0(\nu)$. Considering an ideal beam splitter (R = T = 1/2) this equation becomes

$$I_d(\delta) = \frac{1}{2}I_0(\nu)(1 + \cos 2\pi \nu \delta)$$
 (2.8)

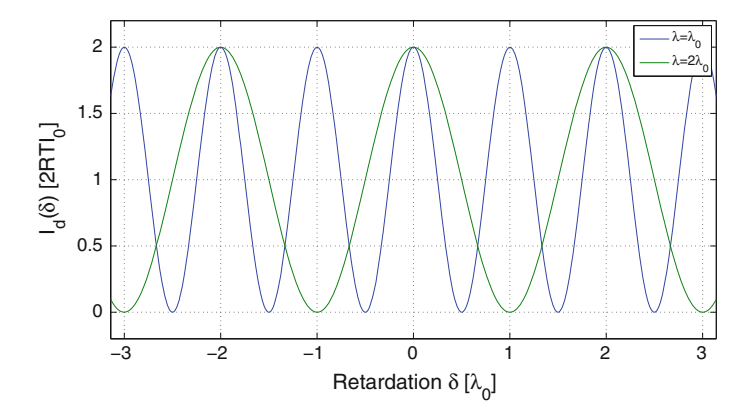


Fig. 2.2 Interference pattern for monochromatic light of wavelength λ_0 (*blue*) and $2\lambda_0$ (*green*) as a function of the retardation δ (in units of λ_0). The maxima corresponds to retardation intervals multiple of λ_0 and $2\lambda_0$, respectively

where a dc component equal to $\frac{I_0(\nu)}{2}$ and a modulated component $\frac{I_0(\nu)}{2}\cos 2\pi\nu\delta$ can be observed. In spectroscopy only the ac component is used in general, and is referred to as the interferogram.

For a broadband source $B(\nu)$, where radiation of more than one wavelength is emitted by the source, the measured interferogram is the result of the sum of the cosines contributions corresponding to each wavenumber, in other words, a measure of the interference of all the spectral components of $B(\nu)$ as the retardation is varied. In this situation the measured interferogram is

$$I_d(\delta) = \int_{-\infty}^{\infty} B(\nu) \cos(2\pi \nu \delta) d\nu$$
 (2.9)

which is the cosine Fourier transform (or the real part of the Fourier transform). By performing the inverse cosine Fourier transform, one can recover the spectral information of the source, this is

$$B(\nu) = \int_{-\infty}^{\infty} I_d(\delta) \cos(2\pi \nu \delta) d\delta$$
 (2.10)

B(v) is an even function and it can be written as

$$B(\nu) = 2 \int_0^\infty I_d(\delta) \cos(2\pi \nu \delta) d\delta \tag{2.11}$$

which means that in theory one could measure the complete spectrum from 0 to ∞ at infinitely high spectral resolution.

Figure 2.3 shows a representation of the generation of an interferogram for a broadband source with a flat spectrum.

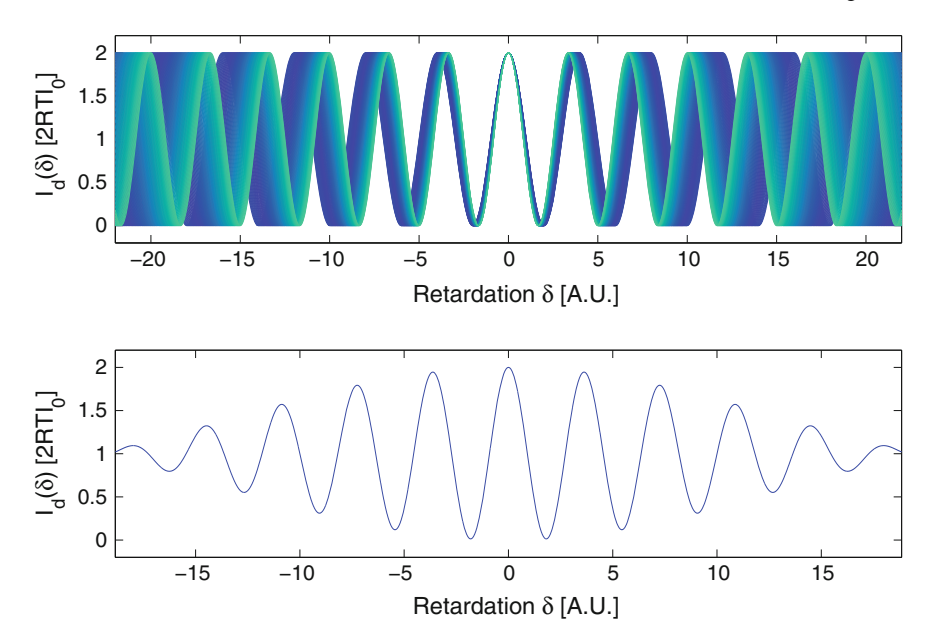


Fig. 2.3 Individual monochromatic responses (*top*) and the resulting interferogram (*bottom*) for a broadband (or polychromatic) source

In theory, by scanning an infinite distance one could recover the spectrum at infinitely high resolution. In practice one selects a maximum optical path difference to be scanned, limiting the spectral resolution of the measurement.

2.1.3 Sampling the Interferogram

Interferograms are sampled at equal intervals of retardation x, which mathematically is the multiplication of an analog interferogram by a repetitive impulse function, the Dirac comb, given by

$$III(x) = \sum_{n = -\infty}^{\infty} \delta(x - n\Delta x)$$
 (2.12)

where Δx is the sampling interval. The Fourier transform of the Dirac delta comb is another Dirac delta comb of period $1/\Delta x$, that is

$$III(\nu) = \sum_{n = -\infty}^{\infty} \delta(\nu - \frac{n}{\Delta x})$$
 (2.13)

In the Fourier domain, the spectra are convolved with the Dirac delta comb (Eq. 2.13), which means the spectrum will be infinitely repeated. To avoid aliasing, if the spectrum covers a bandwidth from 0 to v_{max} , the transformed Dirac delta comb must have a period of at least $2v_{max}$, this is

$$\Delta x \le \frac{1}{2\nu_{max}} \tag{2.14}$$

Under this condition, which is known as the *Nyquist criterion*, the analog signal may be digitised without any loss of information.

2.1.3.1 Effect of Finite Path Difference

By sampling a finite path difference Δ another instrumental effect is introduced to the interferogram. Effectively, the complete interferogram (from $-\infty$ to ∞) is multiplied by a boxcar truncation function, D(x), which is

$$D(x) = \begin{cases} 1 & \text{if } -\Delta \le x \le \Delta \\ 0 & \text{if } x > |\Delta| \end{cases}$$

In the spectral domain, it is equivalent to the convolution of the spectra B(v) with the Fourier transform of D(x), which is

$$f(\nu) = 2\Delta \frac{\sin 2\pi \nu \Delta}{2\pi \nu \Delta}$$

= $2\Delta \operatorname{sinc} 2\pi \nu \Delta$ (2.15)

and it is also called the *Instrument Line Shape* function (ILS). For any spectrometer, the ILS defines the shape of a spectral line given a monochromatic input.

2.1.3.2 Spectrometer Resolution

When the spectrum to be measured corresponds to a single spectral line of wavenumber ν_1 , this is $B_1(\nu) = \delta(\nu - \nu_1)$ the recovered spectrum is

$$B(\nu) = B_1(\nu) * f(\nu) = 2\Delta \operatorname{sinc} 2\pi (\nu - \nu_1) \Delta$$
 (2.16)

Figure 2.4 shows the instrumental line shape, f(v) (top), and B(v) (bottom) for $v_1 = 2/\Delta$. Looking at the ILS, it can be observed that the curve intersects the wavenumber axis at $\pm 1/2\Delta$, and for B(v) the intersection happens at $v_1 \pm 1/2\Delta$. In this situation, two spectral lines separated by twice this amount $(1/\Delta)$ will be completely resolved.

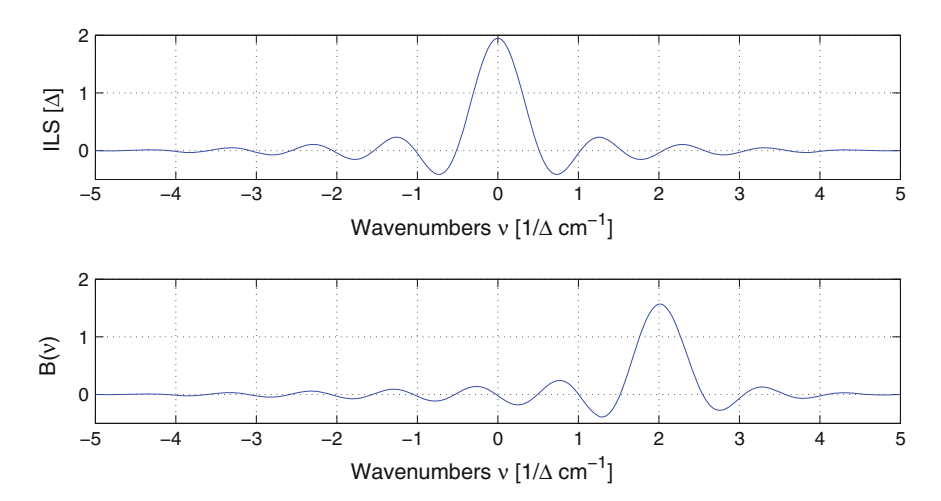


Fig. 2.4 Instrumental Line Shape ILS(v) (top), which is the Fourier transform of a boxcar function of unit amplitude extending from $+\Delta$ to $-\Delta$. Fourier transform of an interferogram generated by a monochromatic line at $v_1 = 2/\Delta$ (bottom)

However, the practical resolution is better than this value. Considering the full width at half maximum (FWHM) criterion, two spectral lines will be resolved if the spacing between lines is greater than the FWHM of either line, this is

$$\Delta v = \frac{1.207}{2\Delta} \tag{2.17}$$

which is valid for a sinc-like ILS. The ILS can be modified through *apodization*, which can be useful to reduce the side lobes of the ILS by weighting the interferogram but can also affect the photometric accuracy.

2.1.4 Recovering the Spectrum

The relationship between an interferogram and the corresponding spectrum is the Fourier transform (or cosine transform, as the interferogram is real). However, the interferogram is discretely sampled and finite. For this reason, a *discrete Fourier transform* (DFT) needs to be performed.

The general definition of the DFT is

$$B(\mathbf{v}) = \sum_{n=0}^{N-1} I_d(\delta_n) e^{-2\pi \mathbf{v} \delta_n / N}$$
 (2.18)

where v is the wavenumber vector and N the number of elements of the interferogram $I_d(\delta)$. Given the maximum wavenumber defined by the Nyquist criterion, v_{max} , the spectral resolution is

$$\Delta v = \frac{v_{max}}{N} \tag{2.19}$$

and as the sampling interval is $\Delta \delta = \Delta/N$, combining both expressions the spectral resolution can be written as

$$\Delta v = \frac{1}{2\Delta} \tag{2.20}$$

which is only valid if the ILS is not being considered.

2.1.4.1 Apodization

The convolution theorem (Goodman 2005) states that the Fourier transform of the multiplication of two functions in one domain is equivalent to the convolution in the other, as given by

$$\mathscr{F}^{-1}\{F(v)\cdot G(v)\} = f(x) * g(x) = \int_{-\infty}^{\infty} f(t)g(x-t)dt$$
 (2.21)

where t is a dummy variable and f(x) * g(x) denotes the convolution of f(x) and g(x).

Apodization is the modification of the interferogram by multiplication with an apodization function (Griffiths and de Haseth 2007). If the interferogram is unweighted, the shape of a spectral line is the convolution of the spectrum with a sinc function, which is the Fourier transform of the boxcar truncation function.

A sinc function introduces ringing in the spectrum because of the side lobes. By selecting a different apodization function, the side lobes can be reduced but at the cost of a loss of spectral resolution.

The most common apodization functions are those proposed by Norton and Beer (1976) and the triangle function (Griffiths and de Haseth 2007). Norton and Beer tested over 1000 functions of the general form

$$A(\delta) = \sum_{i=0}^{n} C_i \left[1 - \left(\frac{\delta}{\Delta} \right)^2 \right]^i$$
 (2.22)

and concluded that there is a distinct empirical boundary relation between the FWHM and the relative magnitude of the strongest side lobe to the central lobe. Three preferred functions are Norton-Beer weak, medium and strong apodization function.

Figure 2.5 shows three examples of apodization functions and the corresponding ILS. It can be observed that the triangular and squared triangular apodization functions (green and red, respectively) present a reduced side lobe intensity. However,

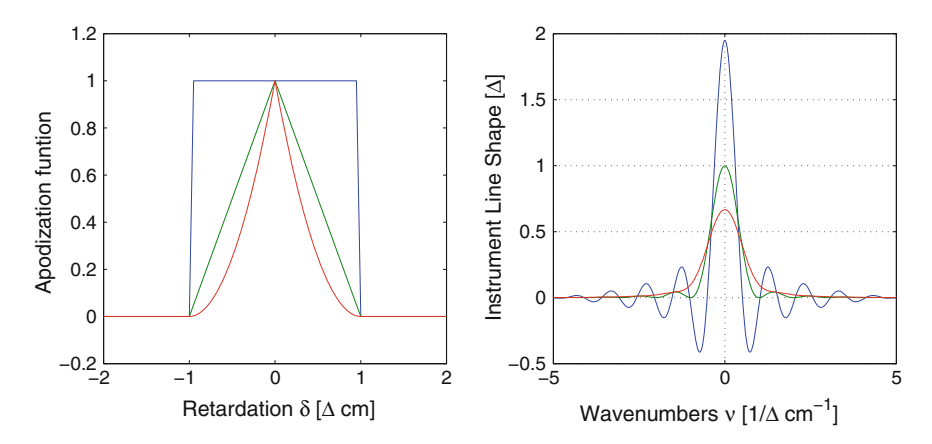


Fig. 2.5 Apodization functions (*left*) and corresponding Instrumental Line Shape (*right*) boxcar (*blue*), triangular (*green*) and squared triangular (*red*)

the spectral resolution is being decreased with respect to the boxcar apodization function.

2.1.4.2 Phase Effects

Until now, it has been assumed the interferogram to be perfectly symmetric or even. However, in practice an additional term often has to be added to the phase angle $2\pi \nu \delta$ to describe the measured interferogram.

Phase effects $\varphi(\nu)$ in the interferogram mainly appear because the zero path difference point is not accurately known or sampled, some dispersive phenomena exist in optical elements, and/or due to electronic filters used to reduce the bandwidth of the detector, which induce a wavenumber dependent phase lag. Under these circumstances, the interferogram can be written as

$$I(\delta) = 2 \int_0^\infty B(\nu) \cos[2\pi \nu \delta + \varphi(\nu)] d\nu$$
 (2.23)

$$= \int_{-\infty}^{\infty} B(\nu) e^{-i\varphi(\nu)} e^{-i2\pi\nu\delta} d\nu \tag{2.24}$$

where $\varphi(-\nu) = -\varphi(\nu)$ and the interferogram is no longer symmetric. The interferogram is now the Fourier transform of $S(\nu) = B(\nu)e^{-i\varphi(\nu)}$, which can also be written as

$$S(\nu) = B_r(\nu) \cos[\varphi(\nu)] - B_i(\nu) \sin[\varphi(\nu)]$$
 (2.25)

where $B_r(\nu)$ and $B_i(\nu)$ represent the real and imaginary parts of $B(\nu)$.

2.1.4.3 Phase Correction

The process of phase correction consists of determining $\varphi(\nu)$ experimentally from the imaginary and the real parts of $S(\nu)$ and then multiplying through by $e^{i\varphi(\nu)}$ to recover $B(\nu)$, by using the fact that the phase error $\varphi(\nu)$ is a smooth function and does not vary rapidly with ν .

The Forman phase correction method (Forman et al. 1966) is one of the most used methods. Given an interferogram unequally sided by sampling from $-\Delta_1$ to Δ_2 (in order to increase the spectral resolution by increasing the total optical path difference), the Forman method first finds the ZPD and selects a region where the interferogram is double sided and the signal exceeds the noise, ZPD $\pm x$. This interferogram is then apodized with a triangular apodization function and by performing the Fourier transform the phase can be extracted. Once the phase is known, it is inverted and inverse Fourier transformed to create the convolution kernel. Next, the measured interferogram and the kernel are convolved. This process can be iterative, and eventually the convolution kernel resembles a delta function. This process is illustrated in Fig. 2.6.

2.2 Stellar Interferometry

An interferometer can be basically described as an instrument that measures the interference of an electromagnetic field. The advantage of interferometers over other instruments when measuring astronomical sources is the angular resolution achievable, providing means to address certain scientific questions not available to single aperture telescopes. In this Section the basic principles and characteristics of an ideal stellar interferometer are presented, as well as the interferometric observables and its synthesis (Born and Wolf 1999; Monnier 2003; Quirrenbach 2001).

2.2.1 Basic Principles

When using an interferometer one is measuring coherence functions (Haniff 2007). In this section the focus is on the spatial coherence function, which is the case associated with measuring the electric field from a source at two locations but at the same time. This is equivalent to the Young's two slit experiment.

2.2.1.1 The Young Experiment

The first experiment for demonstrating the interference of light is due to Young (1804). In his experiment, light from a monochromatic point source S falls on two pinholes, P_1 and P_2 which are close together on a screen and equidistant from S. The

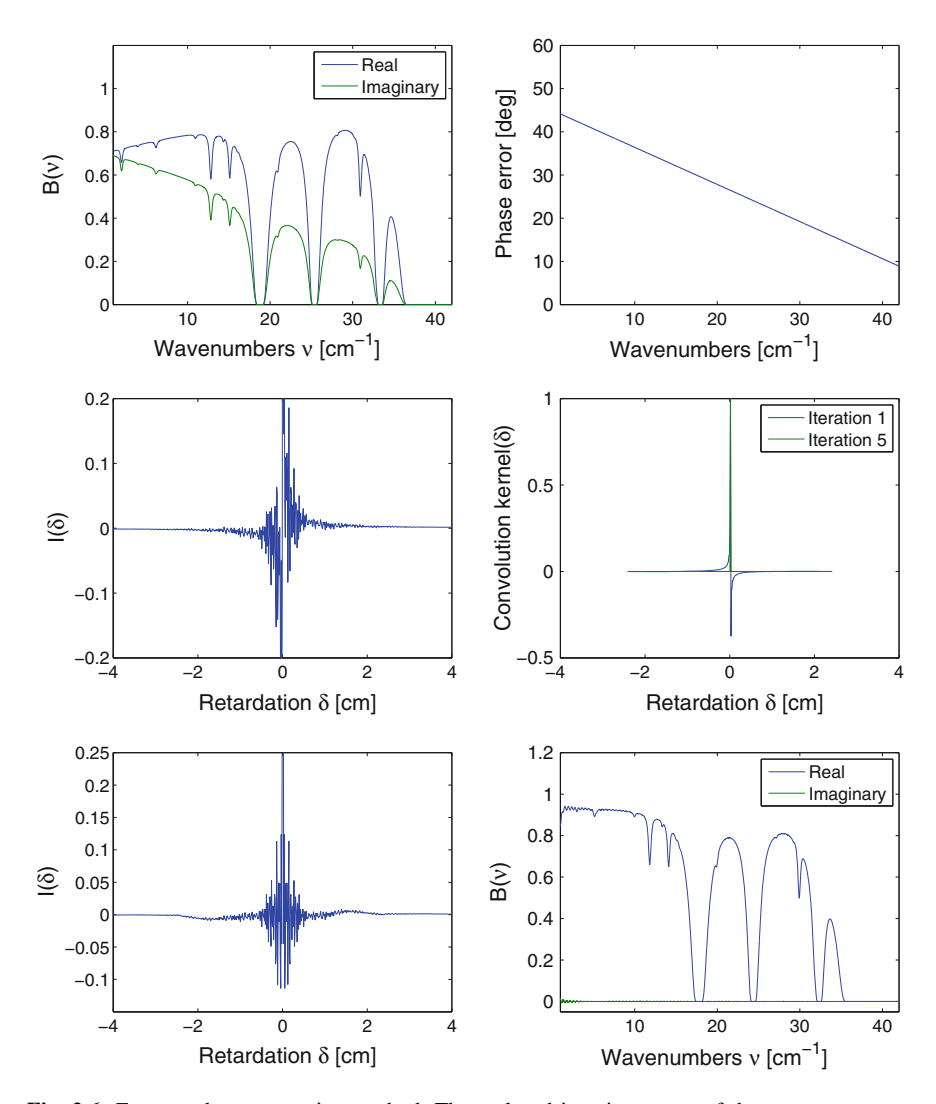


Fig. 2.6 Forman phase correction method. The real and imaginary part of the spectrum corresponding to the transmission of the atmosphere from 0 to 42 cm⁻¹ has been distorted (*top-left*) with a linear phase error (*top-right*). The measured interferogram is not symmetric anymore (*centre-left*). After extracting the convolution kernel (*centre-right*) and applying the correction method 5 times, the interferogram symmetry is improved (*bottom-left*). Fourier transforming the corrected interferogram, the spectrum is recovered (*bottom-right*) and is real

separation between the two pinholes is the baseline, *b*. The pinholes act as secondary monochromatic point sources which are in phase, and the light is projected onto a screen beyond the pinholes screen and a pattern of fringes is observed.

The interference is due to the wave nature of light: the electric field at each slit is propagating to the screen with different relative path lengths, hence interfering constructively and destructively at different points along the screen. Figure 2.7 (left) shows a simple Young's two-slit interferometer response to a point source, where the interference fringe can be characterised by an amplitude and phase. For constructive interference, the fringe spacing $\Delta\Theta$ is proportional to the projected slit separation b in units of wavelength λ , this is

$$\Delta\Theta = \frac{\lambda}{h} \operatorname{rad}$$
 (2.26)

and the fringe spatial frequency is

$$u = \frac{b}{\lambda} \operatorname{rad}^{-1} \tag{2.27}$$

If a second point source is located at an angle of $\lambda/(2b)$ from the first source, as in Fig. 2.7 (right) the two interference patterns are out of phase with one another by π rad and they cancel each other, as the fringe phase depends on the angle of the incoming wavefront: the measurement of fine phase is equivalent to a measurement of stellar position on the sky. On the screen, one would see a uniform illumination. The Young's experiment is a simple illustration of an interferometer having two telescopes in place of pinholes and subsequently combining the two beams for interference.

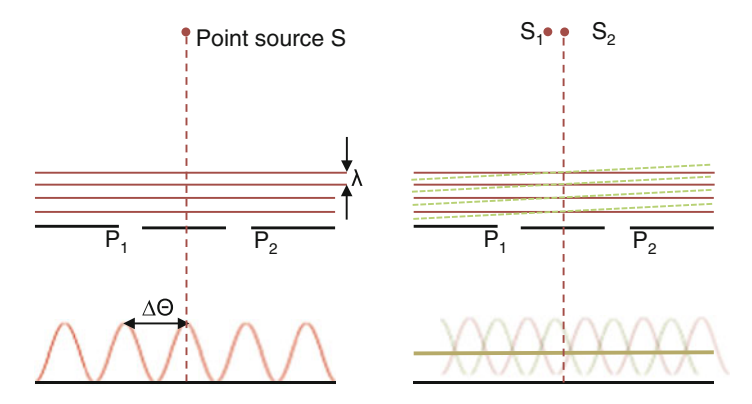


Fig. 2.7 The Young's two-slit interferometer response to a point source (*left*) is a pattern of fringes characterised by an amplitude and a phase. If a second point source is positioned at a distance $\lambda/(2b)$ from the initial source (*right*), the two interference patters are out of phase and cancel each other, allowing the measurement of the stellar position on the sky

Fig. 2.8 Schematic of an interferometer. Two telescopes collect the light that then travels along the delay lines DL1 and DL2 and interferes at the beam combiner. The geometrical delay δ is compensated with the delay lines in order to find maximum fringe coherence to measure stellar positions. θ is the view angle

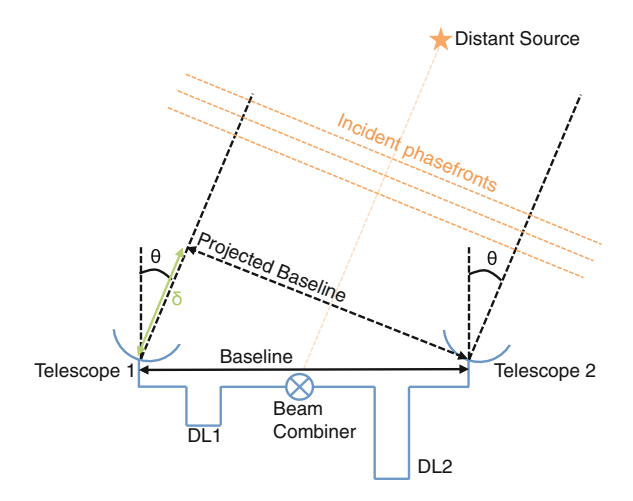


Figure 2.8 shows a basic representation of a 2 element interferometer. Two telescopes are separated by a physical distance, the baseline, and pointing towards a distant source at an angle θ from the meridian. By measuring the delay line required to find stellar fringes, the incoming angle of the wavefronts can be calculated and thus the stellar position on the sky.

2.2.1.2 Angular Resolution and Fringe Visibility

The angular (or spatial) resolution, is defined as the ability to discern two objects with an image-forming device. For an astronomical instrument the ability to distinguish the two components of a binary star is often used. Classical diffraction theory established the Rayleigh criterion for the definition of the diffraction limited resolution (Hecht 2001). According to the Rayleigh criterion, two sources will be resolved when one component is centred on the first null in the diffraction pattern of the other. In this case, given a circular aperture of diameter D, the angular resolution is

$$\Delta\theta_{Tel} = 1.220 \frac{\lambda}{D} \,\text{rad} \tag{2.28}$$

If instead of the Rayleigh criterion the full width at half maximum (FWHM) criterium is considered, the angular resolution is $\Delta\theta_{Tel}=1.02\lambda/D\approx\lambda/D$. For an interferometer, two equal brightness sources will be resolved when the fringe contrast goes to zero at the longest baseline b, this is

$$\Delta\theta_{Int} = \frac{\lambda}{2b} \, \text{rad} \tag{2.29}$$

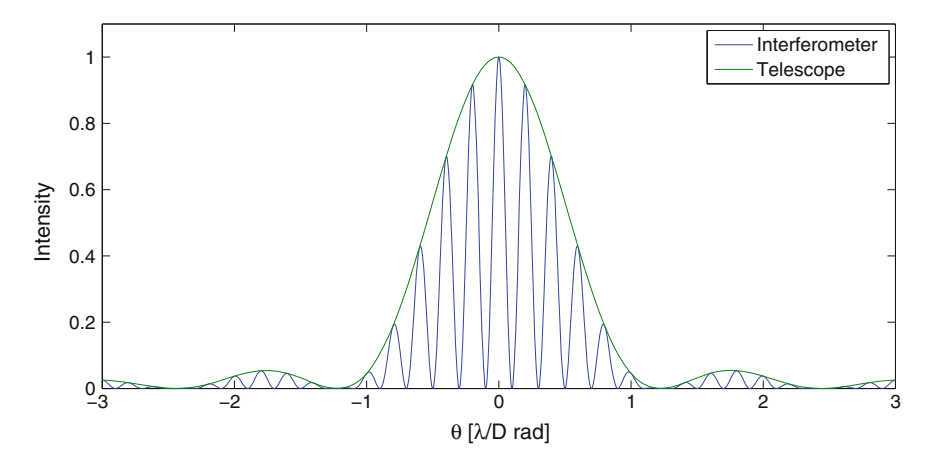


Fig. 2.9 Measured interferogram for a single telescope (*green*) and a two aperture interferometer (*blue*) for a point source. The interferometer fringe pattern is equivalent to the single telescope one multiplied by a cosine given by the baseline separation

Figure 2.9 shows the fringe pattern for a single telescope and an interferometer for a point source, where the baseline separation is b = 5D. It can be observed that the resolution of the interferometer is 12 times higher than the resolution of the single aperture if the Rayleigh criterion is used. In interferometry, the resolution of the single aperture is the field of view of the interferometer.

However, if the radiation is not monochromatic one has to consider each frequency separately and add the resulting fringe patterns, which have different separation (λ/b) between maxima. In this situation, the visibility fringes 'wash out', limiting the field of view of the interferometer. If the bandwidth is $\Delta\lambda$, the field of view is given by

$$\Delta\theta = \frac{\lambda}{b} \frac{\lambda}{\Delta\lambda} \tag{2.30}$$

which is the product of the angular (or spatial) resolution and the resolving power $R = \lambda/\Delta\lambda$.

Another quantitative parameter is the fringe contrast, which historically is called *visibility amplitude*. For a 2 telescope interferometer it is calculated as

$$V = \frac{I_{max} - I_{min}}{I_{max} + I_{min}} \tag{2.31}$$

where I_{max} and I_{min} are the maximum and minimum intensity of the fringes, respectively. This value will approach zero if the two beams are incoherent.

2.2.1.3 Complex Visibility

The output of an interferometer are the so-called *complex visibilities*, also called spatial coherence function. When observing an object with an interferometer, the light intensity I is the result of the superposition of electromagnetic waves coming from the apertures. Considering an instrument with two apertures P_1 and P_2 , the corresponding electric fields at the apertures are $E_1(t)$ and $E_2(t)$, respectively. At the recombination point Q, the intensity of the recombined signal is

$$I(Q,\tau) = \langle |E_1(t) + E_2(t+\tau)|^2 \rangle_t$$
 (2.32)

where the time lag τ is caused by the internal light path length difference from each aperture to Q and $\langle \rangle_t$ denotes time average. If one defines the mutual coherence function $\Gamma_{1,2}(\tau)$ as

$$\Gamma_{1,2}(\tau) = \langle E_1(t)E_2^*(t+\tau)\rangle_t \tag{2.33}$$

at recombination point the intensity can be written as

$$I(Q,\tau) = \Gamma_{1,1}(0) + \Gamma_{2,2}(0) + \Gamma_{1,2}(\tau) + \Gamma_{1,2}^*(\tau)$$

= $\Gamma_{1,1}(0) + \Gamma_{2,2}(0) + 2\Gamma_{1,2}^{(r)}(\tau)$ (2.34)

where $\Gamma_{1,2}^{(r)}(\tau)$ is the real part of $\Gamma_{1,2}(\tau)$, $\Gamma_{1,1}(0) = I_1$ and $\Gamma_{2,2}(0) = I_2$. The interferogram is contained in $\Gamma_{1,2}(\tau)$, and for $\tau = 0$, this is the complex visibility, which is basically the quantity that a Young's double slit experiment measures.

The Van-Cittert-Zernike theorem describes the relation between the complex visibility of an object and its brightness distribution on the plane of the sky. It states that for sources in the far field the normalised value of the spatial coherence function (or complex visibility) is equal to the Fourier transform of the normalised sky brightness distribution. If a source with a brightness distribution $I(\theta)$, where $\theta = (\theta_x, \theta_y)$ are the coordinates on the sky plane Ω , illuminates the two apertures connected with the baseline vector $\mathbf{b} = (b_x, b_y)$, the wavenumber dependent spatial coherence function is

$$\frac{V(\mathbf{b})}{V(0)} = \frac{\Gamma_{1,2}(\mathbf{b}, \nu)}{\Gamma_{1,2}(0, \nu)} = \frac{\int_{\Omega} I(\mathbf{\theta}, \nu) \exp[-i2\pi\nu\mathbf{\theta} \cdot \mathbf{b}]d\theta^2}{\int_{\Omega} I(\mathbf{\theta}, \nu)d\theta^2}$$
(2.35)

where $\theta \cdot b$ is the projection of the baseline vector on the sky plane. Using spatial frequency notation, this is $u = b_x/\lambda$ and $v = b_y/\lambda$, the normalised complex visibility is

$$V_{norm}(u, v) = \frac{\int_{\Omega} I(\boldsymbol{\theta}, v) \exp[-i2\pi (u\theta_x + v\theta_y)]d\theta^2}{\int_{\Omega} I(\boldsymbol{\theta}, v)d\theta^2}$$
(2.36)

The components u and v are the components of the baseline vector between two sampling points projected onto a plane perpendicular to the source direction and measured in wavelengths. It can be observed that by inverse Fourier transforming one can retrieve the source spatial structure if the uv-plane (the Fourier space) has been sampled suitably.

2.2.2 Observability and UV-Coverage

When observing with a stellar interferometer, the efficiency and quality of an observation depends on the sampling of the *uv*-plane, which is defined by the baseline range and position, the quantity of interest being the projected baseline vector on the sky (Ségransan 2007). For ground based interferometers, two parameters are usually taken into account for the filling of the *uv*-plane: the Earth rotation and the number of telescopes of the interferometer (Thompson et al. 1986; Millour 2008). By taking advantage of the Earth rotation the *uv*-tracks become ellipses. The link between the baseline position and its projection on the sky is given by

$$\begin{pmatrix} u \\ v \\ w \end{pmatrix} = \frac{1}{\lambda} \begin{pmatrix} \sin(h) & \cos(h) & 0 \\ -\sin(\delta)\cos(h) & \sin(\delta)\cos(h) & \cos(\delta) \\ \cos(\delta)\cos(h) & -\cos(\delta)\sin(h) & \sin(\delta) \end{pmatrix} \begin{pmatrix} X \\ Y \\ Z \end{pmatrix}$$
(2.37)

where (X, Y, Z) represent the terrestrial coordinate system for the antenna position as described in Thompson et al. (1986), and δ and h are the declination and hour angle of the phase reference position. Then the elliptical uv-tracks when observing an object of declination δ are

$$u^{2} + \left(\frac{v - (Z/\lambda)^{2} \cos(\delta)}{\sin(\delta)}\right)^{2} = \frac{1}{\lambda^{2}} (X^{2} + Y^{2})$$
 (2.38)

By increasing the number of telescopes N_t , although this is a more expensive solution, the number of available baselines N_b is increased and is given by

$$N_b = \frac{1}{2} N_t (N_t - 1) \tag{2.39}$$

To further increase the *uv*-sampling one can use multiple spectral bands. Assuming that an object's shape is achromatic with regards to the wavelength, the *uv*-coverage is increased simply because different wavelengths represent different spatial frequencies for a given baseline (Millour 2008).

As presented before, the measurement of an interferometer is related to the Fourier transform of the object brightness. In order to maximise the efficiency of

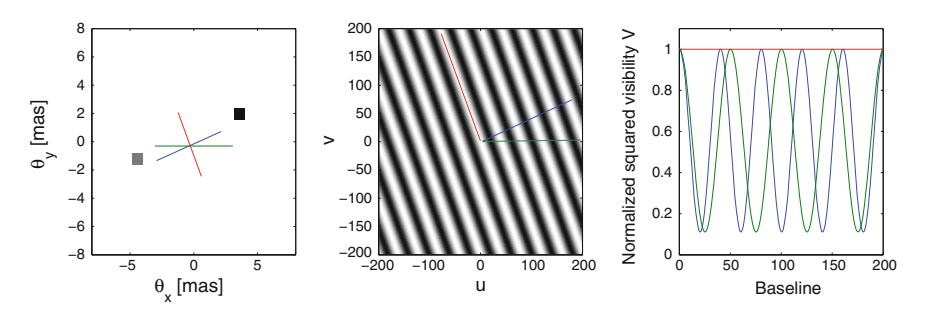


Fig. 2.10 Simulation of an observation of a binary system consisting of 2 unresolved monochromatic point sources separated approximately 9 mas (*left*) and f = 0.5. The normalised squared visibility amplitude in units of spatial frequency $1/\lambda$ (*centre*) has a cosine shape given by the source separation. Three baselines have been simulated: aligned with the point sources (*blue*), perpendicular to the line connecting the point sources (*red*), and in an angle between *red* and *blue* (*green*)

an observation, it is important to know the shape and size of the object under study and use it for the selection of the baselines as well as for introducing model fitting to the measured visibilities (Berger and Segransan 2007). For example, if the object is a resolved binary, the brightness can be written as

$$I(\theta_x, \theta_y) = F_1 \delta(\theta_x - \theta_{x,1}, \theta_y - \theta_{y,1}) + F_2 \delta(\theta_x - \theta_{x,2}, \theta_y - \theta_{y,2})$$
(2.40)

where F_1 and F_2 are the fluxes and $(\theta_{x,1}, \theta_{y,1})$ and $(\theta_{x,2}, \theta_{y,2})$ are the angular coordinates of the stars S_1 and S_2 . This is sum of two unresolved point sources. In this case, the normalised squared visibility amplitude is

$$|V(u,v)|^2 = \frac{1+f^2+2f\cos[2\pi v(\boldsymbol{\theta} \cdot \boldsymbol{b})]}{(1+f)^2}$$
 (2.41)

where $f = F_2/F_1$. Figure 2.10 shows a simulation of an observation of a binary with a separation of approximately 9 mas. Three projected baselines have been considered: blue, aligned with the point sources; red, perpendicular to the line connecting the two point sources; and green, a baseline in between blue and red. It can be observed that the visibility remains constant for the red baseline, because the interferometer 'sees' only one point source. For the blue baseline, the visibility has its maximum frequency. The green baseline presents also a cosine modulation but at a lower frequency. This illustrates the fact than when observing a given object, one has to select the baselines orientation and range accordingly.

2.2.3 Data Synthesis

Once the *uv*-plane has been sampled and so the complex visibilities measured, one could apply the fundamental relationship between the visibility function for a given frequency and the normalised sky brightness distribution, this is

$$I(\theta_x, \theta_y) = \int \int V(u, v) \exp[i2\pi (u\theta_x + v\theta_y)] dudv$$
 (2.42)

However, in order to extract the source brightness the uv-plane should be fully sampled, which is not the case. In practice, one has a sampled version of V(u, v). By performing the inverse Fourier transform of the sampled complex visibility function one obtains the $dirty\ image$ or dirty map

$$I_{dirty}(\theta_x, \theta_y) = \int \int V(u, v)S(u, v) \exp[i2\pi(u\theta_x + v\theta_y)]dudv$$
 (2.43)

$$= B_{dirty}(\theta_x, \theta_y) * I_{norm}(\theta_x, \theta_y)$$
 (2.44)

where S(u, v) is the sampling function, which is 1 where the uv-plane is sampled and zero otherwise. In this equation, $B_{dirty}(\theta_x, \theta_y)$ is the $dirty\ beam$ and is simply the PSF of the interferometer, which is the Fourier transform of the sampling function

$$B_{dirty}(\theta_x, \theta_y) = \int \int S(u, v) \exp[i2\pi (u\theta_x + v\theta_y)] dudv$$
 (2.45)

Since the $B_{dirty}(\theta_x, \theta_y)$ is known because it depends on the telescopes positions, recovering the image $I(\theta_x, \theta_y)$ can be accomplished via deconvolution.

Different deconvolution algorithms have been developed for interferometry (Thiébaut 2009). The most popular ones are CLEAN (Högbom 1974) and the Maximum Entropy Method, MEM (Bryan and Skilling 1980; Gull and Skilling 1984), initially developed for radiointerferometric observations but applicable to the optical/IR domain.

In this thesis the CLEAN algorithm is used for the data synthesis of Double Fourier Modulation data and is described in detail in Chap. 5. In general terms, it is basically a numerical deconvolving process applied in the (θ_x, θ_y) domain. It is an iterative process, which consist of breaking down the intensity distribution into point source responses, and then replacing each one with the corresponding response to a 'clean' beam, this is, a beam free of side lobes.

In conclusion, when performing interferometric imaging it is crucial to define the optimal *uv*-sampling for the object to be measured, as the number of baselines is limited. In any case, a more populated *uv*-space will increase the angular resolution of the reconstructed image. As presented before, if the object's shape is achromatic with regards to the wavelength, one way to increase the *uv*-sampling is using multiple spectral bands.

2.3 Multi-Fourier Transform Interferometry

Double Fourier Spatio-Spectral Interferometry is the application of a Fourier-transform spectrometer (FTS) to aperture synthesis interferometry. This technique was proposed for the near IR regime by Itoh and Ohtsuka (1986) with a single-pupil interferometry approach, and by Mariotti and Ridgway (1988) with multi-pupil interferometry for high spatial resolution.

Leisawitz et al. (2003) proposed an extension of the FOV by using a focal plane detector array for optical wavelengths, technique called Wide-Field Imaging Interferometry. However, direct detector arrays in the Far Infrared are still expensive and a similar approach is not straightforward.

Ohta et al. (2006) theoretically proposed to apply a Martin-Puplett-type Fourier-transform spectrometer to the aperture synthesis system in millimeter and submillimeter waves. They succeeded in proving that this system is capable of performing broadband imaging observations (Ohta et al. 2007). Also a laboratory prototype spectral-spatial interferometer (Chap. 3) has been constructed to demonstrate the feasibility of the double-Fourier technique at far infrared (FIR) wavelengths (0.15–1 THz) by Grainger et al. (2012).

2.3.1 Basic Principles

Double Fourier Modulation (DFM) is based on the combination of spatial interferometry and Fourier transform spectroscopy simultaneously. As presented earlier in this chapter, a Fourier transform spectrograph is based on the Michelson interferometer, where the light of a source is divided and recombined while delaying one of the optical paths to generate an interferogram. To combine this technique with spatial interferometry, instead of dividing the light from a single telescope one uses two apertures and recombines the incoming light from these two apertures.

Figure 2.11 shows a classical FTS (left) and a spectro-spatial interferometer (right). In the FTS the incoming light is divided at the beamsplitter (BS) and with the movable mirror an optical path difference is introduced. In the spectro-spatial interferometer, by using two telescopes an extra path difference due to the baseline is introduced when the source is not on the line of sight perpendicular to the baseline. When using the two telescope interferometer, due to the division of the spatial wavefront outside the instrument, one has to take into account all the phase changes of the optical elements (Mariotti and Ridgway 1988). Considering that all mirrors introduce a π phase delay and that the beam splitter is ideal and symmetric, this is the phase delay between the transmitted and reflected beam is $\pi/2$, at the detector one measures sine interferograms due to the extra $\pi/2$ phase shift. Because this is the result of the addition of the beam splitter phase ϕ_{BS} , throughout this thesis this value is left as parameter in order to account for beam splitter non-symmetries.

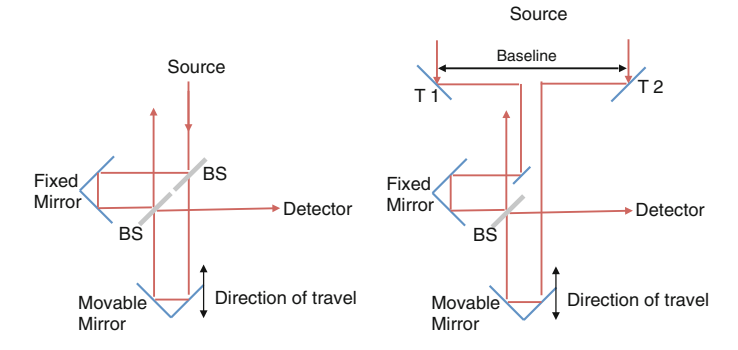
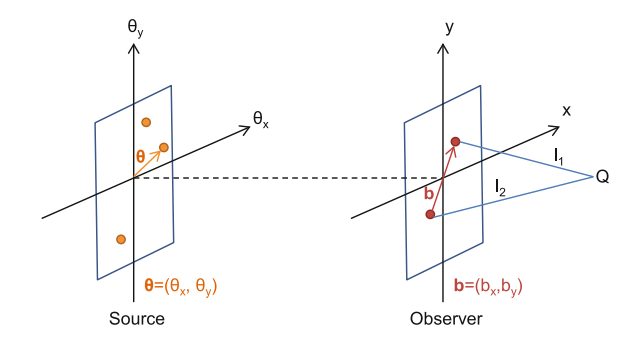


Fig. 2.11 Schematic of a classical FTS (*left*) and a spectro-spatial interferometer (*right*). For the FTS, the incoming light is divided in the first beam splitter and half of it is delayed with the movable mirror before arriving to the second beam splitter where interference occurs. The spectro-spatial interferometer receives light from two telescopes (T1 and T2), and the light travelling from T2 is delayed at the movable mirror before interfering with the light travelling from T1 at the beam splitter, where interference occurs

Fig. 2.12 Coordinate system used. The source plane (or sky map in later sections) is assumed to be very far away from the observer plane



Initially one must define the coordinate system, shown in Fig. 2.12 and following the notation of Born and Wolf. The origin of the coordinate system on the source plane is the center of the FOV. The viewer angle of the source from the observer plane is $\theta = (\theta_x, \theta_y)$. The origin of the coordinate system on the observer plane is the center of the baseline ($\boldsymbol{b} = (b_x, b_y)$) that separates the two apertures.

Going back to Eq. 2.34, the complex visibility or spatial coherence function was defined as the mutual coherence function when $\tau=0$. According to the van-Cittert-Zernike theorem, the normalised spatial coherence function is the Fourier transform of the normalised sky brightness distribution (Eq. 2.35). The temporal coherence function is defined as the mutual coherence function for b=0, and according to the Weiner-Khinchin theorem, the normalised value of the temporal coherence function is equal to the Fourier transform of the normalised spectral energy distribution of the source, this is

$$V(\tau) = \frac{\int B(\omega) \exp(-i\omega\tau) d\omega}{\int B(\omega) d\omega}$$
 (2.46)

where $\omega = 2\pi f = 2\pi c/\lambda$. With DFM one takes advantage of both aspects of the mutual coherence function.

Considering that $f\tau = \nu \delta$, where δ is the spectroscopical optical path difference due to the movable mirror (as in Eq. 2.9), the measurement of the mutual coherence function by a Multi-Fourier Transform Interferometer of the waves obtained by two apertures for a given baseline and measuring a specific source intensity $I(\theta, \nu)$ is

$$\Gamma(\boldsymbol{b}, \delta) = \int_{\Omega} \left\{ \int I(\boldsymbol{\theta}, \nu) \exp[-i2\pi\nu(\boldsymbol{b} \cdot \boldsymbol{\theta}) + i2\pi\nu\delta + i\phi_{BS}] d\nu \right\} d^2\theta \qquad (2.47)$$

and its real part is

$$\Gamma^{(r)}(\boldsymbol{b}, \delta) = \int_{\Omega} \left\{ \int I(\boldsymbol{\theta}, \nu) \cos[-2\pi\nu(\boldsymbol{b} \cdot \boldsymbol{\theta}) + 2\pi\nu\delta + \phi_{BS}] d\nu \right\} d^{2}\theta \qquad (2.48)$$

where Ω is the solid angle subtended by the source, ν is the wavenumber, and δ is the optical path difference between apertures. In this equation the interferometric phase shift $2\pi \nu (\boldsymbol{b} \cdot \boldsymbol{\theta})$ and the spectroscopic modulation $2\pi \nu \delta$ can be easily distinguished.

With Eq. 2.48 one obtains a set of interferograms corresponding to an interferogram per baseline, this is, a spectroscopic measurement for each sampled point in the *uv*-space. It must be noticed that in this situation, the concept of a spectroscopic zero path difference is not applicable anymore. For example, if the source is a binary consisting of two unresolved point sources, the interferometric phase shift will cause the separation of the two spectroscopic interferograms. This case is similar to the testbed implementation presented in the next chapter.

2.3.2 Data Analysis and Synthesis

To recover the information from the source, a two step process needs to be performed. First, to obtain the spectroscopy-resolved source image one has to perform a Fourier integration of the obtained $\Gamma^{(r)}$ in δ to obtain first the spectrally resolved mutual coherence function, $\hat{\Gamma}(u, v, v)$, which in interferometer notation is

$$\hat{\Gamma}(u, v, v) = \int_{\Omega} \tilde{I}(\boldsymbol{\theta}, v) \exp[-i2\pi(u\theta_x + v\theta_y)]d^2\theta]$$
 (2.49)

where $u = b_x v$, $v = b_y v$ and \tilde{I} is a spectrally convolved source intensity distribution, defined as

$$\tilde{I}(\boldsymbol{\theta}, \nu) = \int I(\boldsymbol{\theta}, \nu') 2\delta_0 \operatorname{sinc}[2\pi(\nu' - \nu)\delta_0] d\nu'$$
(2.50)

The convolution kernel depends on the apodization function, in this case a top-hat function has been used. By Fourier transforming the data in u and v, one obtains source images for various frequencies.

In summary, a DFM system is capable of performing simultaneous measurements of the source brightness distribution and spectrum. In the interferograms, however, the ZPD position is lost, which means that spectroscopy data processing techniques like mathematical apodization and phase correction are not straightforward. Depending on the observation, one can correct the instrumental phase errors by selecting a ZPD for each interferogram separately and computing the slope of the phase from the Fourier transform of a short section around the central fringe area.

2.4 Chapter Summary

In this Chapter the theoretical background that led to the Double Fourier Modulation technique has been presented, this is Fourier Transform Spectroscopy and Stellar Interferometry.

Fourier Transform spectroscopy is based on the Michelson interferometer, with which one can generate and interferogram by dividing the light from a source and recombining it on a beam splitter after delaying one of the optical paths. To obtain the spectra of the source, one has to Fourier transform the interferogram. For a correct detection of the spectral information the sampling of the interferogram is of great importance, because it defines the spectral resolution and the spectral band coverage.

Stellar Interferometry is based on the Young's two slit experiment, where incoming light from a source falls on two apertures (or telescopes) which then are made to interfere onto a screen. The measured quantity is the complex visibility V(u, v). By selecting the position of the telescopes the uv-map is sampled. The brightness distribution on the plane of the source is recovered by Fourier transforming the complex visibility. The aperture separation, or baseline, defines the angular resolution of the interferometer.

The Double Fourier Modulation technique is the combination of Fourier Transform Spectroscopy with Stellar Interferometry: for a given interferometric baseline, one performs an FTS scan. With this technique measurements of the source brightness distribution and spectrum are performed simultaneously.

References

J.P. Berger, D. Segransan, An introduction to visibility modeling. New Astron. Rev. 51(8), 576–582 (2007)

M. Born, E. Wolf, *Principles of Optics* (1999)

R.K. Bryan, J. Skilling, Deconvolution by maximum entropy, as illustrated by application to the jet of M87. Mon. Not. RAS **191**, 69–79 (1980)

M.L. Forman, W.H. Steel, G.A. Vanasse, Correction of asymmetric interferograms obtained in fourier spectroscopy. J. Opt. Soc. Am. 56(1), 59–61 (1966). doi:10.1364/JOSA.56.000059. http:// www.opticsinfobase.org/abstract.cfm?URI=josa-56-1-59

- J.W. Goodman, Introduction to Fourier optics (2005)
- W.F. Grainger, R. Juanola-Parramon, P.A.R. Ade, M. Griffin, F. Liggins, E. Pascale, G. Savini, B. Swinyard, Demonstration of spectral and spatial interferometry at THz frequencies. Appl. Opt. 51(12), 2202–2211 (2012). doi:10.1364/AO.51.002202. http://ao.osa.org/abstract.cfm?URI=ao-51-12-2202
- P.R. Griffiths, J.A. de Haseth, Fourier Transform Infrared Spectrometry, 2nd edn. (Wiley, 2007)
- S.F. Gull, J. Skilling, Maximum entropy method in image processing. Commun. Radar Signal Process. IEE Proc. F 131(6), 646–659 (1984). ISSN 0143-7070. doi:10.1049/ip-f-1:19840099
- C. Haniff, An introduction to the theory of interferometry. New Astron. Rev. **51**(8), 565–575 (2007) E. Hecht, *Optics*, 4th edn. (2001)
- J.A. Högbom, Aperture synthesis with a non-regular distribution of interferometer baselines. Astron. Astrophys. Suppl. 15(1974), 417–426 (1974)
- K. Itoh, Y. Ohtsuka, Fourier-transform spectral imaging: retrieval of source information from three-dimensional spatial coherence. J. Opt. Soc. Am. A 3(1), 94–100 (1986). doi:10.1364/JOSAA.3. 000094. http://josaa.osa.org/abstract.cfm?URI=josaa-3-1-94
- P.R. Lawson (ed.), Principles of Long Baseline Stellar Interferometry (2000)
- D.T. Leisawitz, B.J. Frey, D.B. Leviton, A.J. Martino, W.L. Maynard, L.G. Mundy, S.A. Rinehart, S.H. Teng, X. Zhang, in *Wide-field imaging interferometry testbed I: purpose, testbed design, data, and synthesis algorithms*, ed. by M. Shao. Society of Photo-Optical Instrumentation Engineers (SPIE) Conference Series, vol. 4852 of Society of Photo-Optical Instrumentation Engineers (SPIE) Conference Series (2003), pp. 255–267. doi:10.1117/12.460704
- J.-M. Mariotti, S.T. Ridgway, Double Fourier spatio-spectral interferometry—combining high spectral and high spatial resolution in the near infrared. Astron. Astrophys. 195, 350–363 (1988)
- A.A. Michelson, Light Waves and Their Uses, vol. 3 (The University of Chicago Press, 1903)
- A.A. Michelson, XXVIII. Visibility of interference-fringes in the focus of a telescope. Philos. Mag. Ser. 5 31(190), 256–259 (1891a). doi:10.1080/14786449108620101. http://www.tandfonline.com/doi/abs/10.1080/14786449108620101
- A.A. Michelson, XXXVIII. On the application of interference-methods to spectroscopic measurements. Philos. Mag. Ser. 5 31(191), 338–346 (1891b). doi:10.1080/14786449108620117. http://www.tandfonline.com/doi/abs/10.1080/14786449108620117
- F. Millour, All you ever wanted to know about optical long baseline stellar interferometry, but were too shy to ask your adviser. New Astron. Rev. **52**(2), 177–185 (2008)
- J.D. Monnier, Optical interferometry in astronomy. Rep. Prog. Phys. 66(5), 789 (2003). http://stacks.iop.org/0034-4885/66/i=5/a=203
- R.H. Norton, R. Beer, New apodizing functions for fourier spectrometry. J. Opt. Soc. Am. **66**(3), 259–264 (1976). doi:10.1364/JOSA.66.000259. http://www.opticsinfobase.org/abstract.cfm?URI=josa-66-3-259
- I.S. Ohta, M. Hattori, H. Matsuo, Development of a multi-Fourier-transform interferometer: fundamentals. Appl. Opt. 45, 2576–2585 (2006). doi:10.1364/AO.45.002576
- I.S. Ohta, M. Hattori, H. Matsuo, Development of a multi-Fourier-transform interferometer: imaging experiments in millimeter and submillimeter wave bands. Appl. Opt. 46, 2881–2892 (2007). doi:10.1364/AO.46.002881
- A. Quirrenbach, Optical interferometry. Ann. Rev. Astron. Astrophys. **39**, 353–401 (2001). doi:10. 1146/annurev.astro.39.1.353
- D. Ségransan, Observability and UV coverage. New Astron. Rev. 51(8), 597-603 (2007)
- É. Thiébaut, Image reconstruction with optical interferometers. New Astron. Rev. **53**(11), 312–328 (2009)
- A.R. Thompson, J.M. Moran, G.W. Swenson, *Interferometry and Synthesis in Radio Astronomy* (1986)
- T. Young, The bakerian lecture: experiments and calculations relative to physical optics. Philos. Trans. R. Soc. Lond. **94**, 1–16 (1804). ISSN 02610523. http://www.jstor.org/stable/107135

Chapter 3 Spectro-Spatial Interferometry Testbeds

In this chapter the two Spectro-Spatial Interferometry Testbeds in which I have been involved during my programme are presented: the FIRI laboratory testbed and WIIT, the Wide-field Imaging Interferometry Testbed. Both testbeds are intended to demonstrate the theory of Double Fourier Spatio-Spectral Interferometry or the application of a Fourier-transform spectrometer (FTS) to aperture synthesis interferometry which was presented in the previous chapter. The difference between the two experimental approaches is the wavelength range of operation: the FIRI laboratory testbed operates at Far Infrared wavelengths, while the WIIT is designed to operate at Optical wavelengths. A second difference resides in the detection scheme: by operating at optical wavelengths, WIIT approach consists in an extension of the FOV by using a focal plane detector array (Leisawitz et al. 2003). However, because direct detector arrays in the Far Infrared are still expensive, single pixel detection is the only viable option which can be explored with modest funding and a detector system contained in size for the FIRI laboratory testbed (Grainger et al. 2012).

3.1 The FIRI Laboratory Testbed

The FIRI laboratory testbed is the the result of an effort by Cardiff University, the Rutherford Appleton Laboratory (RAL) and UCL to develop an instrument to demonstrate the feasibility of the Double-Fourier technique at Far Infrared (FIR) wavelengths, which in a long term basis is expected to be the precursor of the space-based Far Infrared Interferometer (Helmich and Ivison 2009). It is currently located at the Physics and Astronomy Department of Cardiff University. This system is in constant development, and here the current design and issues, the latest results and the future planned improvements are presented.

3.1.1 Experimental Set-Up

A Spectro-Spatial Interferometer operating in the waveband 5–35 cm⁻¹ has been developed. This laboratory test-bed consists of two parts, a source simulator and a spectral-spatial interferometer. The source simulator, detailed below, is intended to provide, with a point-like source, a flat wavefront for the interferometer, allowing the test-bed to assume the source is at infinity. The test-bed is intended to be a verification tool of the physics included in the Instrument Simulator described in Chap. 5, not viceversa: the model must be applicable to different instruments.

3.1.1.1 Source Simulator

The source is a water cooled mercury arc lamp (MAL). The lamp is a 10 mm diameter quartz cylinder with a wall thickness of 0.9 mm, and provides a black-body spectrum with a temperature of \sim 1800 K. A taut-band resonant chopper oscillates at 28 Hz close to the MAL to modulate the light beam to enhance the signal-to-noise ratio of the detected signal. An aperture, 1 mm from the chopper, then provides a well defined extended source. A 60° segment of a 1-m radius gold-plated carbon-fibre spherical mirror, kindly loaned from the BLAST team (Pascale et al. 2008) is situated 2.1 m away from the source (the focal length of the reflector) to generate a flat wavefront for the interferometer. Zemax modelling gives a focal plane scale of 0.027 deg/mm.

Three apertures are used: (i) a single slit 1.5 mm wide; (ii) a double slit, each slit 1.5 mm wide, with the centres separated by 5.5 mm; (iii) a third aperture being identical to the second with one of the slits covered with a low-pass filter (edge at 21 cm⁻¹). The third aperture is used to have a different source not only spatially, but also spectrally. As the interferometer is only sensitive in one spatial dimension, the slits are arranged perpendicular to the projected scanning direction to increase the overall signal available.

3.1.1.2 Interferometer

The light path in the interferometer is shown in Fig. 3.1. There are two input telescopes with 100 mm diameter apertures, each configured as a 3:1 beam condenser (to reduce the diameter of the beam by a factor of 3). All the mirrors on the optical bench other than the beam condensing input telescopes and the final parabolic condenser are 50 mm square optical quality flats. To achieve different spatial baselines, one of the input telescopes and reflecting mirror are attached to a Thorlabs Long Travel Stage which allows 300 mm of mechanical travel. Hereafter we will refer to this 'arm' of the interferometer as 'spatial'. The same model drive is used for translating the spectral rooftop mirror. The rooftop mirror is used to minimise the effect of tilt by returning the beam along a path that is parallel to that of the incident beam. Hereafter we will refer to this 'arm' of the interferometer as 'spectral'. The beam combiner is

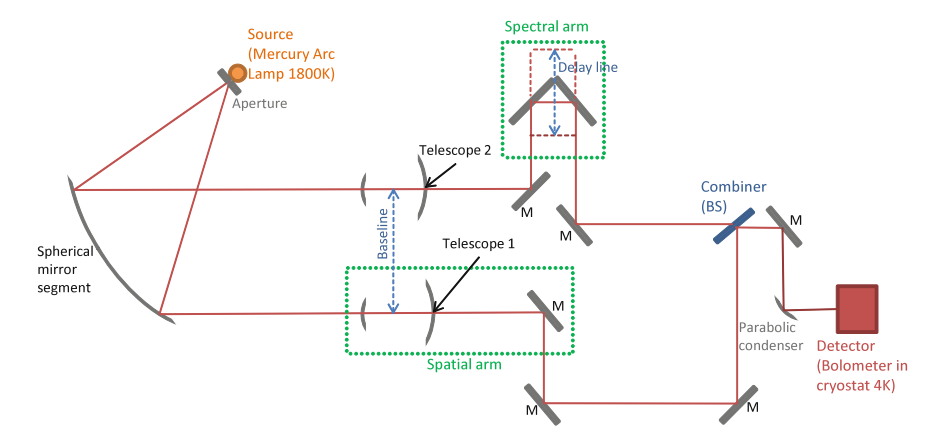


Fig. 3.1 Schematic of the interferometer. Dashed lines indicate moving parts

a 63 mm diameter 50:50 metal-mesh intensity beam splitter originally used for the SCUBA project (Naylor and Gom 2003).

The detector is a single pixel silicon bolometer, operating at a temperature of 4.2 K in a standard OMCI cryostat (OMC Instruments Ltd 2005). Coupling to radiation is done via a f/4 Winston cone (Harper et al. 1976), an off-axis parabola designed to maximise collection of incoming rays within a given field of view. Winston cones are nonimaging light concentrators intended to funnel all wavelengths passing through the entrance aperture out through the exit aperture. They maximise the collection of incoming rays by allowing off-axis rays to make multiple bounces and reach the exit aperture. Spectral filtering of the radiation of interest is achieved with multiple metal mesh filters. Rejection of NIR and visible light is also achieved with similar technology. The bolometer is AC coupled (to reject DC and low-frequency signal components) to a low-noise preamplifier (gain 1000) mounted on the outside wall of the cryostat, followed by a Stanford Research Systems amplifier-filter bank and finally a Stanford Research Systems lock-in amplifier. A lock-in amplifier is used to extract a signal with a known carrier frequency from a noisy environment. In our case, the known carrier is the frequency of the chopper, so the TTL reference signal for the lock-in is acquired from the chopper. The analog output from the lock-in amplifier, configured to be proportional to the amplitude of the signal, is digitised with a National Instruments PCI-MIO-16XE-IO ADC card. Drives and data acquisition system are controlled with a Labview program.

When running the spectral arm, data is acquired every $16\,\mu\text{m}$ of travel, or $32\,\mu\text{m}$ of optical path difference (OPD), which corresponds to a Nyquist sampling of 4.7 THz. The data presented corresponds to a scanning of the spectral arm from the nominal zero path difference along $3.2\,\text{cm}$, at $0.005\,\text{cm/s}$.

One would generally prefer to operate in a fast scan mode without a chopper, as it allows monitoring of the source variability, atmospheric variability and noise spikes, and also faster operation. However, depending on the detector time of response,

faster scans cause asymmetry in the resulting interferogram due to the integration time constant of the bolometer.

Initial alignment of the testbed was achieved with a continuous wave green laser mounted on the optical axis between the beam combiner and the detector, pointing in the direction of the source. The detector position was then set to provide maximum signal with the MAL source with the spectral arm a long way from the ZPD.

3.1.2 Characterization of the System

After performing the optical alignment, the alignment with the millimetre beam can be investigated, and the illumination response evaluated.

3.1.2.1 Vignetting at the Spectral Arm

The effect of spatial filtering due to the physical dimensions of the optical elements is the vignetting. The result is a gradual decrease in light intensity towards the image periphery. When referring to the spectral arm, it means the distortion and/or attenuation due to the motion of the mirrors along the optical path. Figure 3.2 (right) shows a set of interferograms, both forwards (sample 0–2000) and backwards (sample 2001–4000). The position corresponding to the sample 0 refers to the longest optical path length (the rooftop mirror is situated at the far end of the mechanical stage), sample 2000 refers to the shortest optical path length (the rooftop mirror is situated at the near end of the mechanical stage). The observed 38 % variation of amplitude along the length of the spectral arm (between sample 0 and sample 2000) is the vignetting. This effect can be removed during the data processing through polynomial fitting. Figure 3.2 (left) shows a detail of this signal variation and its polynomial fit.

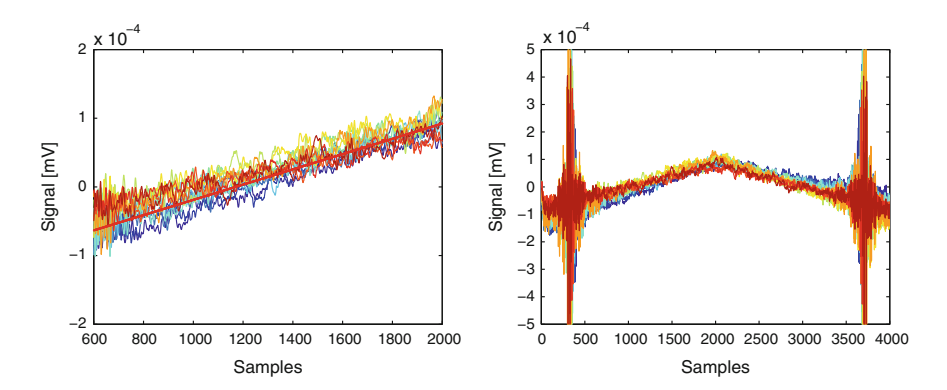
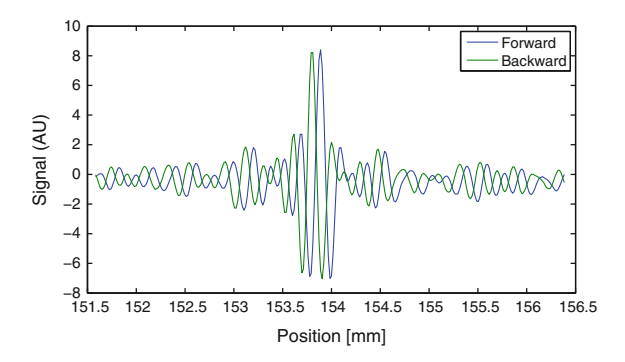


Fig. 3.2 Forward (samples 0–2000) and backward (samples 2001–4000) interferograms (*right*) presenting vignetting effect and detail of the signal variation and polynomial fit (*left*). Different colours indicate different baseline separations

Fig. 3.3 Single slit interferogram. Forward and backward data acquisition



3.1.2.2 Positional Accuracy of the Drive

Figure 3.3 shows an interferogram plotted against position as reported by the drive, for both a forward and backward scan (4.8 mm span, 1 sample per $16\,\mu$ m that corresponds to 300 samples), showing a clear offset between the forward and backward scans. This is a potential indicator of backlash in the system or delay in the acquisition system. The reported position is calculated internally in the Thorlabs Long Travel Stage either from an incremental encoder mounted to the ballscrew or by counting pulses sent to the encoder. Also in this test setup, the rooftop mirror is mounted on a standard Thorlabs right angle mount, which interfaces to the drive via an aluminium tube. This places the majority of the mass on the end of a lever arm. When accelerating the drive up to $10\,\text{mm/s}$ (for fast-scanning mode), at $10\,\text{mm/s}^2$, this starts to oscillate, adding noticeable fringing to the resulting interferogram.

3.1.2.3 Optical Efficiency of the System

From the source to the detector, infrared light covers an optical path of more than 8 m, which means that a considerable amount of power is lost during travel due to vignetting by the optical components of the system (mirrors, filters, among others). Atmospheric attenuation is also present at these wavelengths, meaning the so-called water-lines mask part of the spectra. For these reasons the optical efficiency has to be modelled and understood, to overcome as much as possible or to discriminate signal from environmental/system noise.

Detector system: bolometer, filters and Winston cone in a liquid helium cryostat The detector system is a QMC Instruments Ltd (QMC Instruments Ltd 2005). detector system type QSIB/2 which incorporates a composite structure silicon thermal bolometer. The detector is mounted in an optical integrating cavity behind Winston cone optics and low pass blocking filters. These components are mounted in a type TK1813 liquid helium cryostat. The active absorbing area of the detector is 2 mm diameter, and it is designed for operation around 4.2K. Multimesh filter technology (Pisano et al. 2008; Ade et al. 2006) allows high in-band

transmission efficiency and good out-of-band rejection in order to generate the right conditions for ultra-sensitive detection, i.e. by reducing the radiative heat load incident on the liquid helium cooled stage of the cryostat. The detector feedhorn is a Winston cone (Harper et al. 1976), whose circular aperture is 10 mm diameter, designed to maximise the collection of incoming radiation within a given field of view: all the rays passing through the entrance aperture go through the exit aperture due to multiple reflections. Waveguide theory (David 2005) shows that the exit diameter of this cone defines the cut-off wavenumber of the system, which for the dominant mode TE_{11} is

$$v_c = \frac{1.8142}{\pi d_{exit}} \tag{3.1}$$

For the FIRI testbed $d_{exit} = 2 \text{ mm}$ and the cut-off wavenumber is $v_c = 2.89 \text{ cm}^{-1}$.

Beam-splitter

The beams from the two arms are combined at a metal mesh photolithographic structure designed as a beam splitter built from capacitive and inductive meshes (Ade et al. 2006) to achieve a nearly constant equal transmission and reflection over a broad band.

Vignetting

The effect of geometric filtering by the limiting size of optical elements is the vignetting. This means that the power is modulated by the point spread function of the optical elements. In the case of a circular aperture, the modulation function has a sinc like profile; for squared apertures, the modulation function has a Bessel profile in both x and y directions of the signal. This effect can be simulated and understood, and can be reduced by re-designing the system to accommodate larger optical elements.

Atmospheric attenuation

The main problem of Far-Infrared ground based interferometers is the atmospheric attenuation at these frequencies. This effect can only be removed if the interferometer is space-based. However, water lines can be useful as a first instrument approach to calibrate the test-bed. Figure 3.4 (left) shows the atmospheric attenuation and the Winston cone filtering in the 0– $40\,\mathrm{cm}^{-1}$ wavenumber range.

3.1.3 Initial Results

Shown in Fig. 3.4 (right) are the resultant spectra from interferograms corresponding to different spatial baselines with the single slit in front of the MAL. Comparing with Fig. 3.4 (left), the water absorption lines at 18.6, 25.1 and 32.9 cm⁻¹ are clearly visible. The loss of power at high frequencies appears due to the finite size of the source being spatially resolved, as the wavelength is comparable to the size of the aperture.

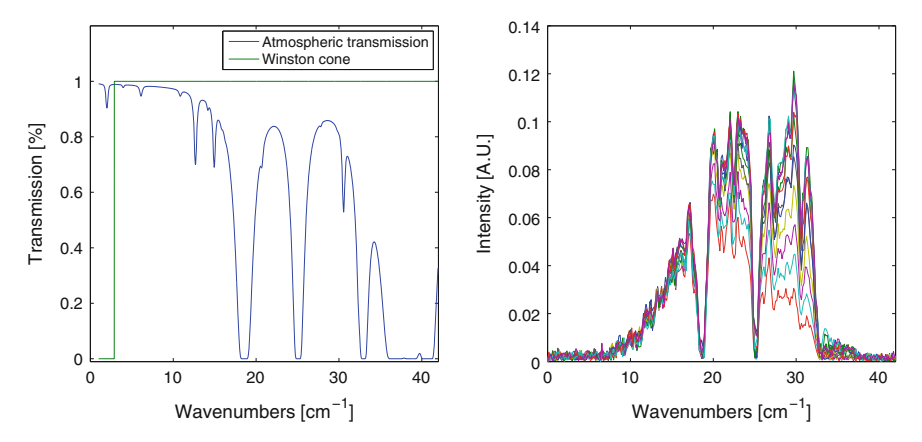


Fig. 3.4 (*Left*) Atmospheric transmission (*blue line*) and cut-off wavenumber due to the Winston cone (*green line*). (*Right*) Spectra for different spatial baselines with a single slit (1 mm wide) source

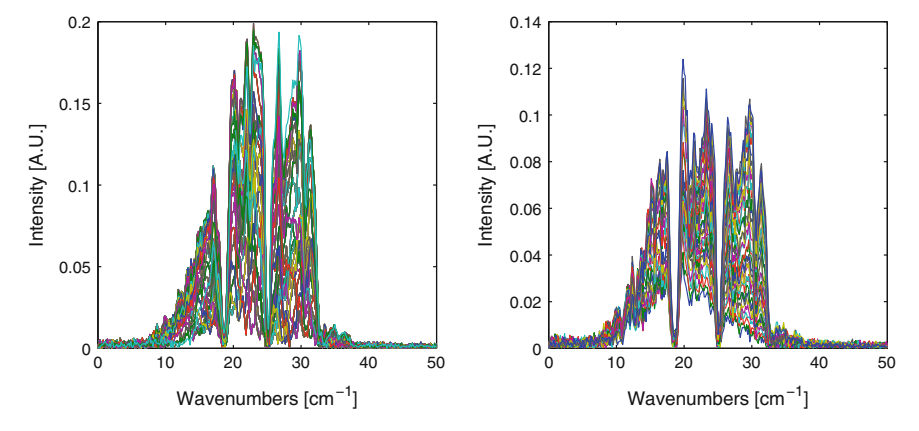


Fig. 3.5 Spectra for different spatial baselines with a double slit aperture in front of the MAL (*left*) and with a double slit aperture in front of the MAL with one of the slits covered with a low pass filter (*right*)

Some other measurements were taken with different source configurations. Figure 3.5 (left) shows the spectra obtained when a double slit aperture is positioned in front of the MAL. The last measurement shown in Fig. 3.5 (right) corresponds to the spectra measured when one of the two slits is 'blocked' with a low-pass frequency edge filter.

From these measurements one can extract information about the sources being measured. For the single slit aperture, we can actually distinguish the contribution of the two described techniques: for low frequency measurements, the interferometric beam for any baseline length is spatially bigger than the source and by performing an FTS scan the spectra of the source is recorded. However, at higher frequencies the source is being spatially resolved as the baseline length increases, and the interferometric modulation due to this baseline separation appears, which corresponds to the Stellar Interferometer contribution.

For a double slit source, the modulation due to the source being spatially resolved appears at lower frequencies, as expected, because the source is spatially bigger than the interferometric beam for any baseline length. In this particular case, this modulation due to the Stellar Interferometer almost reaches zero intensity, because we are interfering two almost identical sources and therefore destructive interference is achieved. The destructive interference is not complete due to the different optical elements in the system (i.e. transmissions of the optical elements, the 'spectral' arm contains one extra mirror compared to the 'spatial' arm).

For the double slit source when one of the slits is covered with a low pass filter, destructive interference is not achieved. In order to extract more information about the filter contribution to the modulation, the low pass filter should be fully characterised.

3.1.3.1 Phase Correction

The Forman phase correction algorithm, presented in Chap. 2, is shown in Fig. 3.6. Initially, the raw interferogram is cropped around the zero path difference (ZPD) to get a symmetric interferogram called subset. This subset is multiplied by a triangular apodization function and Fourier transformed. With the complex phase obtained from the FFT a convolution Kernel is obtained, which is used to filter the original interferogram and correct the phase. Finally the result of the last operation is Fourier transformed to get the phase corrected spectrum. This process is repeated until the convolution Kernel approximates to a Dirac delta function.

Note that the phase correction algorithm has not been applied in the previous spectra, as we are interested in the modulation present due to the slit separation, because it is the contribution of the stellar interferometer. The phase correction algorithm is necessary and recommended when performing FTS-only measurements, this is, splitting the incoming light after the 'spectral' arm telescope (Telescope 2 in Fig. 3.1) and recombining the two beams on the beam splitter after one of them has been delayed with the delay line.

3.1.4 Forward Modelling

The interferogram acquired when a single slit is used to cover the source is known, and the spectrum of the source can be recovered by Fourier transforming and phase correcting the data. However, when more complex sources (i.e. extended sources) are used, it is difficult to discern if the final spectrum is actually the one desired. Moreover, the final goal of the system is to detect unknown sources, so previous spectral data will not be available.

In order to analyze the interferogram recorded with a double slit source we adopted the following approach. Initially, we record the interferogram from a single slit source and the shortest baseline available (IG_{single}). As we know the new source is a double slit source, we can assume that the resultant interferogram (IG_{double}) is a linear

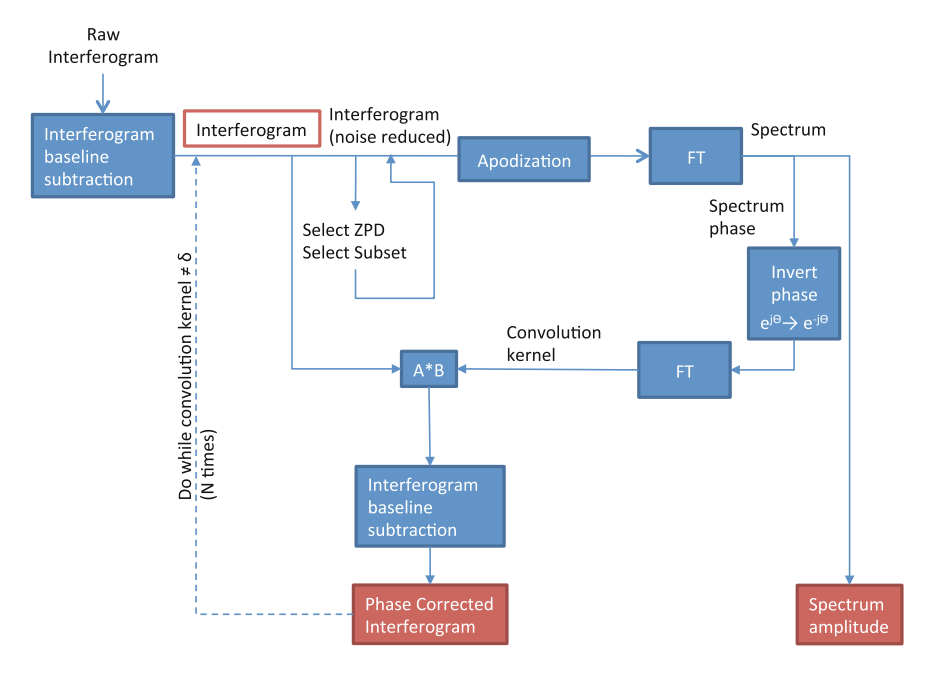


Fig. 3.6 Phase correction algorithm flux diagram

combination of two single slit interferograms. These two single slit interferograms are weighted (c_1, c_2) and shifted (S) relatively (r) and absolutely (a).

$$IG_{double} = S\{a, c_1 \cdot IG_{single} + c_2 \cdot S\{r, IG_{single}\}\}$$
(3.2)

Figure 3.7 shows an example of the measured spectral interferograms for spatial baselines 217, 292 and 367 mm and the approach described above.

To compute the coefficients listed above we use a least squares fitting method. Figure 3.8 left shows the evolution of the shift parameters as a function of the baseline. As expected, while the absolute shift a does not present a baseline dependence, the relative shift increases linearly as a function of the baseline: as the distance between the two antennas increases, the optical path difference between signals increase and a higher shift is required. Figure 3.8 right shows the evolution of the weight coefficients. c_1 remains close to 1 while c_2 slightly decreases as a function of the baseline, which can be explained by the antenna response and the vignetting effects.

These coefficients can be used to test the physical system, as the slit separation of the source can be extracted from the relative shift coefficients. From one side Zemax modelling allows us to calculate the Focal Plane Scale (FPS), which gives us information of the deviation of angle $\Delta\theta$ of incidence of the rays on the antenna when the source position is shifted a distance d in the way

$$\Delta\theta = d \cdot FPS \tag{3.3}$$

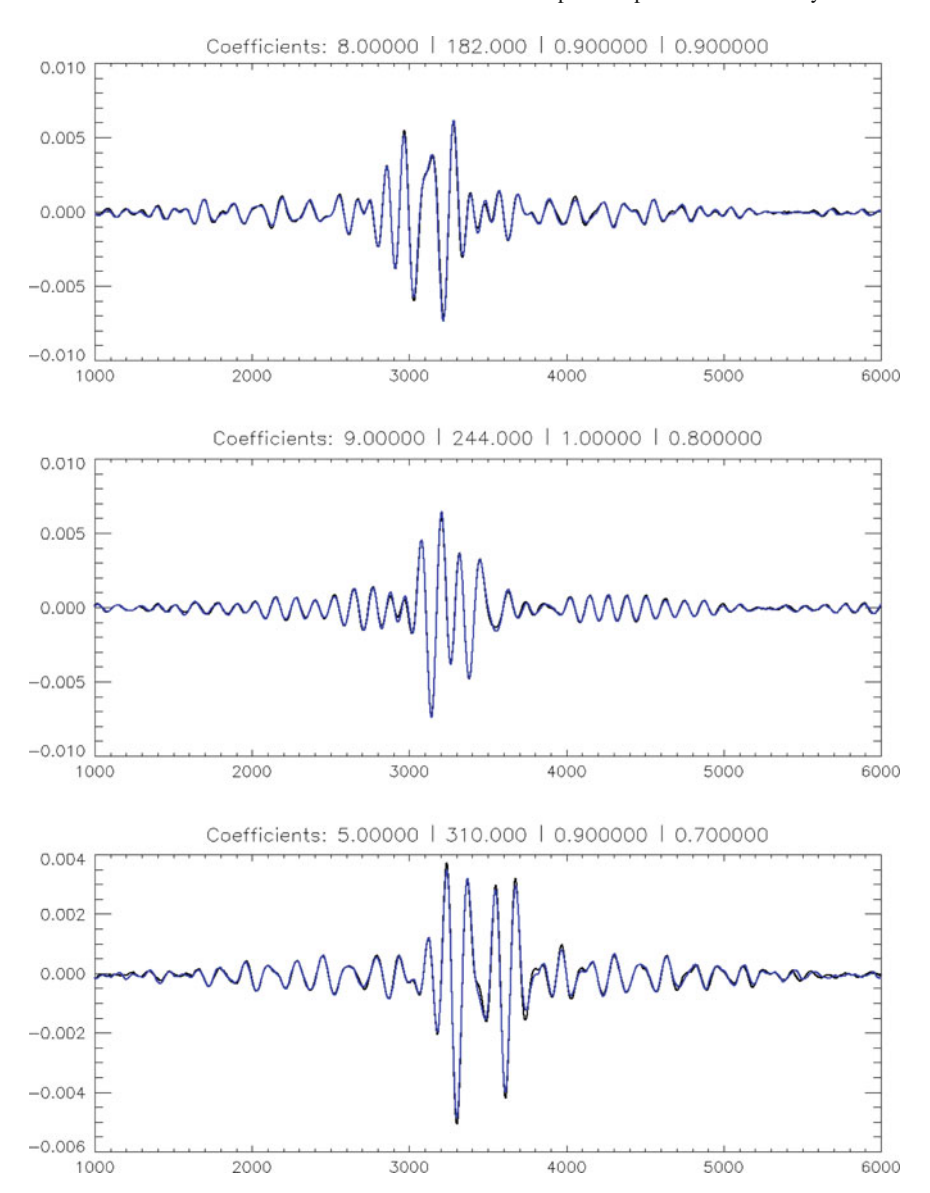


Fig. 3.7 Measured spectral interferograms (*black*) and model fit (*blue*) for spatial baselines 217 mm (*top*), 292 mm (*middle*) and 367 mm (*bottom*) for a double slit source. (Coefficients: absolute shift *a*lrelative shift rlc_1lc_2)

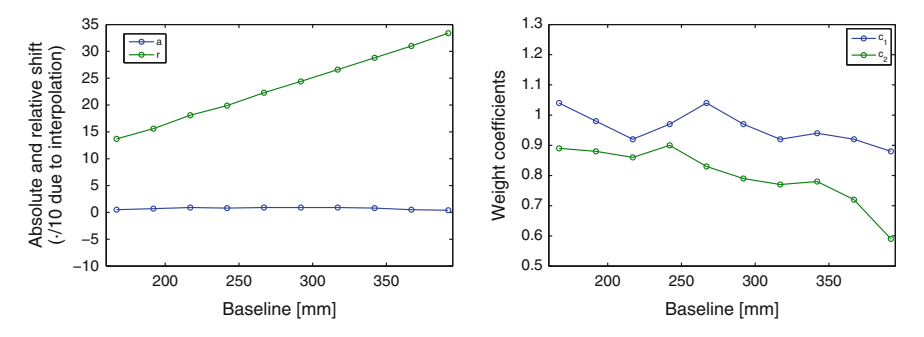


Fig. 3.8 The absolute shift and relative shift (*left*), and scaling parameters (*right*) as a function of the baseline

When $\Delta\theta$ is known, we can compute the optical path difference Δ_{OP} as

$$\Delta_{OP} = \Delta_{ant2} - \Delta_{ant1} = b \cdot (\sin \theta_2 - \sin \theta_1) \simeq b \cdot \sin \Delta\theta \tag{3.4}$$

As shown in Fig. 3.9, Δ_{OP} increases as the baseline increases. On the other side, as the forward modelling combines two single interferograms separated by a distance d, the optical path difference between the rays on each antenna can be extracted from the relative shift r between interferograms as

$$\Delta_{OP} = \frac{r}{N} 32 \left[\mu m \right] \tag{3.5}$$

where N is the interpolation rate, in this case N = 10, and 32 μ m is the optical path displacement per sampling point.

In conclusion, the distance between the two slits can be calculated and compared to the test-bed measurement. In this case, as shown in Fig. 3.10, comparing the optical path difference from the Zemax modelling and the optical path difference from the forward data modelling as a function of the baseline gives us a slit distance of 5.7 mm. The distance measured on the source is 5.5 mm, which means a difference of 3.5 %.

Once the method has been tested for a simple double slit source representing two identical point sources, the next step is to apply this method for different sources. To achieve this, we use again a double slit source but one of the apertures being covered with a low-pass spectral filter (LPF) with cut-off wavenumber at 21 cm⁻¹, to simulate two different sources in the sky and increase the complexity of the procedure. The new forward modelling method to compute the new source from the single slit data is

$$IG_{double} = S\{a, c_1 \cdot IG_{single} + c_2 \cdot S\{r, IG_{LPF}\}\}$$
(3.6)

In this situation the weight coefficient c_2 is expected to be substantially lower, as a considerably amount of power is filtered. Applying the previous least squares algorithm for different coefficient values and different cut-off wavenumbers (but

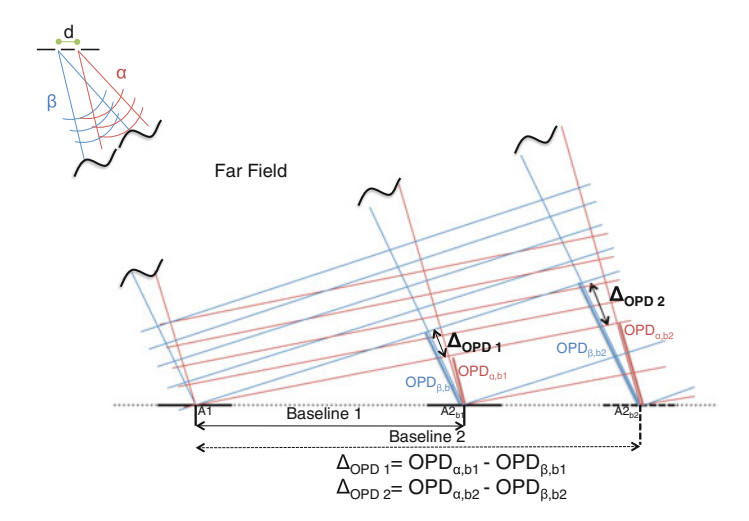
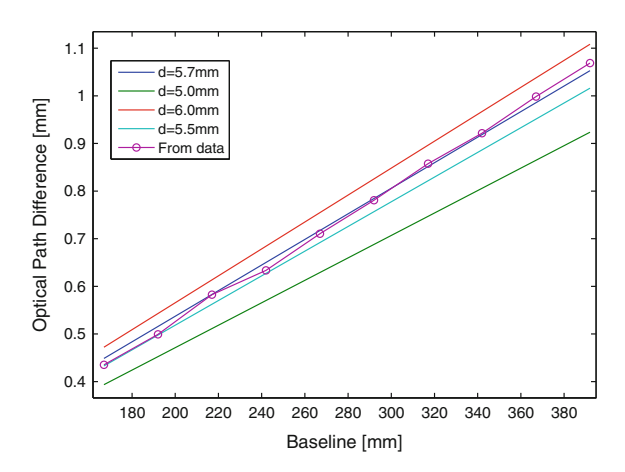


Fig. 3.9 Sketch to show how optical path difference increments with baseline, allowing the extraction of the distance between the two slits. Δ_{OPD1} is the distance between the optical path difference corresponding to the source α and the optical path difference corresponding to the source β in the baseline 1 configuration (from antenna A1 to antenna $A2_{b1}$). Δ_{OPD2} is the distance between the optical path difference corresponding to the source α and the optical path difference corresponding to the source β in the baseline 2 configuration (from antenna A1 to antenna $A2_{b2}$)

Fig. 3.10 Optical path difference computed for different slit distances *d*. The *dotted line* corresponds to the distance extracted from the data



assuming from the previous case that the absolute shift is constant and the relative shift varies as a function of the baseline) we compute the partially-simulated interferograms for different values of the low-pass filter, more specifically, for cut-off wavenumbers of 11, 14, 17, 20, 23 and $26 \, \mathrm{cm}^{-1}$.

Figure 3.11 (left) shows the reduced χ^2 distribution of the fit of the real interferogram with the simulated interferogram for different cut-off wavenumbers. It can be observed that a minimum peak appears around $20 \, \text{cm}^{-1}$. Figure 3.11 (right) presents

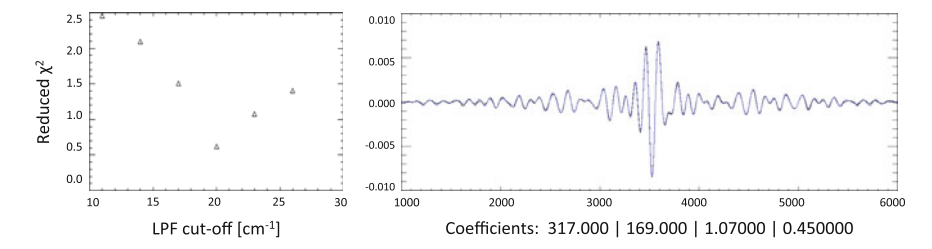


Fig. 3.11 Reduced χ^2 distribution of the fit of the real interferogram with the simulated interferogram for different cut-off wavenumbers (*left*). Real interferogram (*black*) and the computed one (*blue*) when a 21 cm⁻¹ filter is introduced (*right*). The weight coefficients are $c_1 = 1.07$ and $c_2 = 0.45$

the real interferogram and the computed one when a $21\,\mathrm{cm}^{-1}$ filter is introduced. The weight coefficients suggest the method is working properly, because as expected, c_2 is lower than c_1 . The low value of the reduced χ^2 is due to an overestimation of the uncertainty.

Even though these results are promising and help to understand the overall system features, the fact that a previous knowledge of the source is needed in order to be identified is constraining. For this reason a test-bed simulator with ZEMAX is being built, which will allow characterisation of the system, and to understand and minimize errors such as vignetting and misalignment. Also, the instrument simulator FIInS described in Chap. 5 is capable of performing an analytical demonstration of the spectro-spatial interferometry, and more specifically to validate the testbed results.

3.1.5 Current Issues and Next Steps

A number of features still can be improved in the system, which can be addressed both with improved modelling and hardware changes. Regarding the hardware, the beam walk-off or vignetting in the spectral arm of the interferometer, as illustrated in Fig. 3.2 (left), should be reduced by using beam focusing optics. Also, the mechanical construction of the aperture mask is not robust, and if we are to move to higher frequencies, then the uniformity of the slit edges and parallelism need to be more carefully controlled by utilising photolithographic-made aperture masks. In further work, more robust scenes will be used, as well as tunable sources. Finally, there exists the possibility of unbalanced spectral throughput in each interferometer arm, which can lead to spectral phase errors. This can be monitored by examining both output ports at the beam splitter.

The use of a step and sample scan method is inefficient compared with rapid scan techniques for the spectral drive. A future upgrade involves the installation of a rapid scan drive with improved metrology to increase the overall observing efficiency and provide absolute phase measurement.

As we explore more complex scenes, more sophisticated data-processing techniques must be considered. The current forward modelling is limited to the knowledge of the single slit spectral information. These requirements include observations of known point-like sources to calibrate the instrument or taking advantage of techniques such as self-calibration, where a known point source in a complex scene is used to calibrate the system.

3.2 Wide-Field Imaging Interferometry Testbed (WIIT)

The Wide-Field Imaging Interferometry Testbed (Leisawitz et al. 2003) (WIIT) is located at NASA's Goddard Space Flight Center, specifically at the Goddard Advanced Interferometry and Metrology Laboratory (AIM Lab). The AIM Lab is a world-class facility, which was developed with the requirements of this particular experiment in mind. A combination of thermal stability, acoustic isolation, passive and active vibration control, and gentle, laminar air flow in a clean room allow the data obtained with WIIT in the AIM Lab to be practically free of environmentally induced errors. In the summer of 2012 I spent five weeks at NASA's Goddard Space Flight Center to understand the data acquisition process, and the data analysis and synthesis of WIIT. My main contribution has been in the data analysis detailed in this chapter.

The design and assembly of the testbed took place over a two-year period beginning in May 1999, and culminated in detection of the first white light fringes in 2001, but major improvements have been implemented since (Rinehart et al. 2010). It is designed to develop and validate the dual-Michelson interferometric technique. By combining Michelson stellar interferometry with Fourier-transform spectroscopy, and using a detector array instead of a single-pixel detector, the WIIT is capable of measuring high-resolution spatial-spectral data over a large field-of-view, which will be detailed in the next section.

3.2.1 The Testbed

WIIT is a 1:150 functional scale model of the space far-IR interferometer SPIRIT, and is designed to observe complex scenes representative of far-IR astronomical fields. It provides full *uv*-plane coverage and a wide FOV, operating at visible rather than far-IR wavelengths for several practical reasons (Leisawitz et al. 2012): (a) the optical apertures and the delay line are scaled down from those intended for a far-IR instrument in proportion to the wavelength; (b) a CCD detector with sensitivity

limited by photon noise (as expected in a cold far-IR space interferometer) was commercially available and affordable; (c) many other parts, such as translation and rotation stages, were available off-the shelf and inexpensive; and (d) a commercial optical metrology system accurate to 10 nm was affordable.

The novel aspect of WIIT is the use of a detector array (a CCD camera) instead of the single-pixel detector used in a traditional Michelson interferometer (as in the Cardiff University Testbed). Each pixel on the detector records light arriving from different parts of the sky (test scene). As the delay line is scanned, each pixel records an interferogram unique to the field angle corresponding to the pixel. By using observations at a wide range of uv-positions, obtained by rotating the source and increasing/decreasing the interferometric baseline length, reconstructed images can be produced for each pixel; these images can then be mosaiced together, producing a wide field-of-view image with the full interferometric angular resolution. In reality, a more sophisticated algorithm is used to generate a spatial-spectral data cube covering the wide field of view (Lyon et al. 2008). By providing a long delay line scan, spectral information for the observed sources is obtained. To obtain a spectral resolution R requires an optical path delay (OPD) scan range of $\delta = R\lambda$.

To understand how WIIT images a wide field of view next consider a source located at an angle θ relative to the optical axis, as illustrated in Fig. 3.12. If the angular offset is in a direction parallel to the baseline vector established by the antennas (or collector mirrors), and we define this as the 'x' direction, then light from the off-axis source will be brought to a focus on a pixel $(x_0 - \delta_x, y_0)$ with

$$\delta_x = f\theta \tag{3.7}$$

and where f is the focal length of the re-imaging lens. In other words the re-imaging lens is performing an optical Fourier transform of the input plane waves. The signal

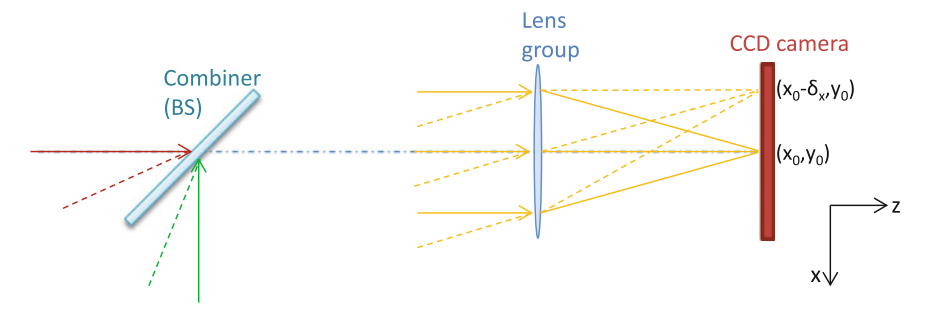


Fig. 3.12 Light rays from a source located on the optical axis of the collimating mirror (*solid lines*), after passing along opposite arms of the interferometer, reach the beam combiner at right angles. A lens images those rays onto pixel (x_0, y_0) . As the optical delay line is scanned the pixels record an interferogram. Light rays from an off-axis source (dashed lines) strike the beam combiner symmetrically but at an acute or obtuse angle. These rays are imaged onto pixel $(x_0 - \delta_x, y_0)$, which records an interferogram whose ZPD is displaced δ_x relative to the ZPD for an on-axis source. (Figure adapted from Leisawitz et al. 2003)

recorded as a function of time by a camera pixel located at $(x_0 - \delta_x, y_0)$ will be an interferogram whose Fourier transform is the spectrum of the off-axis source at the spatial frequency sampled by the baseline $b = b_0 cos(\theta)$ which is the projection of the source on the baseline and the zero path difference (ZPD) will be displaced relative to its location for the on-axis source by an amount $d_{ZPD} = b_0 \sin \theta$. Therefore, by stroking the delay line through a distance greater than the required for spectroscopy, one can allow for the ZPD shift and obtain useful interferometric data for off-axis sources.

Figure 3.13 shows a schematic of the WIIT experimental setup. Light from the test scene, generated by the Calibrated Hyperspectral Image Projector (Bolcar et al. 2012) (CHIP) and located at the focus of the collimating mirror, is projected into the interferometer. The two collector mirrors feed the two arms of the interferometer. One of these arms consists solely of fixed flat mirrors (fixed arm), while the other includes a pair of mirrors mounted on the delay line stage in a rooftop configuration (delay arm). The delay line scans a range of optical path difference between the two arms of the interferometer. The beams from the two arms are recombined within the beam splitter, and the output from one of the two output ports is focused onto a CCD camera by a lens group. The source scene is rotated via software, providing access to all possible baseline orientations. The collector mirrors can be moved along a straight

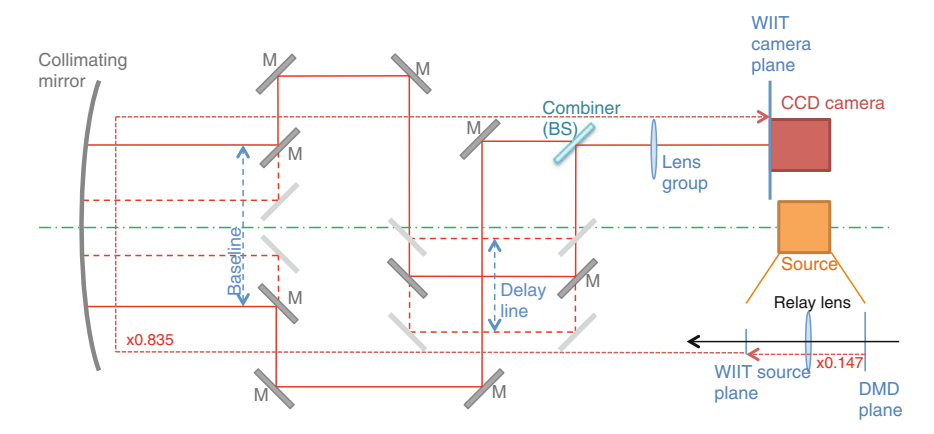


Fig. 3.13 Schematic of the WIIT experimental setup. Light from the test scene (source) located at the focus of the collimating mirror is projected into the interferometer. The two collector mirrors separated by the baseline length feed the two arms of the interferometer. One of these arms consists solely of fixed flat mirrors (lower arm, fixed), while the other includes a pair of mirrors mounted on the delay line stage in a rooftop configuration (upper arm, delay arm). The delay line scans a range of optical path difference between the two arms of the interferometer. The beams from the two arms are recombined at the combiner (beam splitter), and the output from one of the two output ports is focused onto a CCD camera by a lens group. The demagnification of the DMD plane is also shown: a relay lens system images the DMD plane to the WIIT source plane while demagnifying the DMD by a factor 0.147. The testbed provides an additional demagnification of 0.835 due to the WIIT collimator and lens system

rail to vary baseline length. Compared to the testbed set in Cardiff University, WIIT moves both collector mirrors instead of just one arm.

3.2.1.1 The Calibrated Hyperspectral Image Projector (CHIP)

The Calibrated Hyperspectral Image Projector (CHIP), located at the focus of the collimating mirror, generates the scene to be measured. It is based on an instrument first pioneered by the Optical Technologies Division at the National Institute of Standards and Technology (NIST). The basic design uses a combination of Digital Light Processing (DLP) projectors to produce complex spectra and complex scenes, similarly to commercially available video projectors. In DLP projectors, the image is created by microscopically small mirrors laid out in a matrix on a semiconductor chip, known as a Digital Micromirror Device (DMD). When the micromirrors of the DMD are 'on' the light is reflected to create the desired image.

In CHIP there are two DLP projectors to create custom, spectrally diverse and spatially complex scenes. The two DLP engines (a spectral engine and a spatial engine) operate in series to produce the scene to be measured. First, a broadband source is dispersed onto the DMD of the spectral engine such that individual columns of the mirror are mapped to individual wavelengths. By turning the mirrors in a single column 'on', the user includes that specific wavelength in the output. The number of 'on' mirrors in a column determines the relative intensity of the spectral component. By selecting numerous columns and appropriately weighting the various spectral components, the user generates a 'basis spectrum' of the hyperspectral scene to be projected. CHIP is capable of producing arbitrary spectra in the band between 380 and 780 nm with a spectral resolution of 5 nm.

The spatial engine works very much like a basic video projector. A 2-dimensional binary scene is generated on the DMD by turning the appropriate pixels 'on' or 'off'. Alternatively, an 8-bit grey scale image can be generated using pulse-width modulation to vary the amount of time a particular pixel is 'on' relative to the others. Pixels within the DMD array are individually addressed, meaning that arbitrarily complex scenes can be constructed with relative ease.

The spatial and spectral engines are synchronised to produce a hyperspectral scene. Basis spectra are matched with image frames where the intensity of each pixel in the frame determines how much of that basis spectrum is present in the pixel. By cycling through a complete set of frames and their corresponding basis spectra in a period of time that is short compared to the WIIT's integration time, a hyperspectral scene is produced.

The CHIP image format is a 1024×768 pixel array (the pixel size being $10.6 \,\mu\text{m}$). As shown in Fig. 3.13 a commercial photography lens relays the DMD plane to the WIIT source plane while demagnifying the DMD by a factor 0.147 (WIIT source plane pixel size is $1.6 \,\mu\text{m}$). The testbed provides an additional demagnification of 0.835 due to the WIIT collimator and lens system, therefore the DMD pixels appear to be $1.3 \,\mu\text{m}$ pixels at the WIIT camera plane, or about 1/12 of a WIIT camera pixel.

The angle that a single WIIT pixel subtends is called the WIIT plate scale, and it is 7.88×10^{-6} radiants or 1.63 arcsec. A CHIP pixel appears to subtend 0.135 arcsec (1.63 arcsec/12). The highest spatial resolution of the WIIT corresponds to the maximum baseline separation (230 mm) and minimum wavelength (400 nm), and it is 0.18 arcsec. Therefore a single CHIP pixel remains unresolved by WIIT, allowing for calibration of the interferograms collected by the WIIT. The CHIP scene is computer generated and synchronised with the WIIT CCD camera exposure and optical delay line motion, synchronisation that also enables simulation of interferometer rotation and motion smearing associated with on-the-fly observing.

To summarise, the 1024×768 pixel CHIP scene corresponds to 2.30×1.73 arcmin FOV or approximately 85×64 pixels of the CCD camera. However, on the data acquisition process only the relevant CCD area is recorded to minimise the volume of data to be stored.

3.2.1.2 Data Acquisition with WIIT

Raw data from the WIIT consists of a series of CCD camera frames corresponding to the sampled optical path lengths and baselines and ancillary data (Leviton et al. 2003; Leisawitz et al. 2003). To facilitate data reduction and analysis the science data and synchronously collected ancillary data (Leviton et al. 2003) (such as environmental, optical and electro-mechanical metrology) are recorded in the astronomical standard FITS (Flexible Image Transport System) format. All of the data from a single delay line scan and fixed rotation baseline (length and angle) are recorded in a single FITS file. The header and housekeeping data records in the file include all the information needed to calculate the baseline vector.

At a given baseline position and rotation a data cube is collected. Each plane of the cube is a 85×64 pixel image if the full FOV is recorded. Typically a 70×50 pixel image is recorded. Each cube contains a number of planes or frames proportional to the total optical path range to be scanned and the delay line increments, with the finest step size measured with the metrology system being $9.89\,\mathrm{nm}$. For example, if the desired optical path range is $60\,\mu\mathrm{m}$ this corresponds to approximately 6000 steps of the delay line and thus this number of frames to each baseline cube.

3.2.1.3 Expected Results

The main goals of WIIT are to observe astronomically representative test scenes with a Double Fourier interferometer that is equivalent in functionality and performance to a space far-IR interferometer, and compare observed interferograms with those predicted by a high-fidelity computer model of the testbed in which error terms associated with individual hardware components are modelled and can be switched on or off. This comparison can be performed by visibility analysis.

Different sources of errors will lead to a fringe visibility loss, for example imperfect optical components and detectors, undersampling of the spatial Fourier

components, photon noise, motion smearing, and artifacts associated with image construction. Specifically for WIIT, imperfect surfaces and alignment are the dominant contributors to a net 16% loss of fringe visibility relative to a perfect interferometer (Leisawitz et al. 2012). In other words, when an unresolved source (V = 1) is observed with WIIT, the measured visibility is about 0.84.

3.2.2 Data Analysis

For each measurement, the data consist of a series of FITS files. Each FITS file consist of a series of CCD camera frames corresponding to the sampled optical path lengths for a given baseline separation and rotation of the scene and the metrology data for each delay line position. The delay line moves approximate increments of 9.89 nm.

3.2.2.1 Data Format

The best way to understand how the data is structured is looking at actual data. One of the first data sets obtained by WIIT with CHIP as the scene projector on June 2012 measured a 5×5 point sources array. The baseline separations range from 30 to 220 mm with 10 mm steps. For each baseline separation the CHIP scene is rotated to simulate the rotation of the sky and span the uv-coverage. For example, for a baseline separation of 30 mm the rotations of the scene are 0, 45, 90-45 and -90° . As the centre of the baseline is aligned with the centre of the source scene, a rotation of 90° is equivalent to a rotation of -90° . For longer baselines, smaller rotation steps need to be recorded for a better coverage of the scene, i.e. for a 220 mm baseline 35 different rotations are recorded.

Figure 3.14 (left) shows the position of the antennas for the different baselines and rotations. Each colour represents a baseline separation. The uv-coverage (right) is obtained by dividing the baseline separations by the wavelength. Different wavelengths generate different coverages: in the figure, the red coverage corresponds to $\lambda = 780 \,\mathrm{nm}$ and the blue coverage has been calculated at $\lambda = 380 \,\mathrm{nm}$.

3.2.2.2 Data Processing

Every FITS file consists of the Image data and the Table data. In this particular data set the Image consists of 1830 frames, every frame being a 64×66 pixels image. The first 30 frames are dark frames, the 1800 other frames (corresponding to a optical path scan of approximately $60\,\mu m$) are the actual raw data cube containing the interferograms. Thus the first step to reduce the data is to average the dark frames and subtract the result (DF) to the raw data cube (IG).

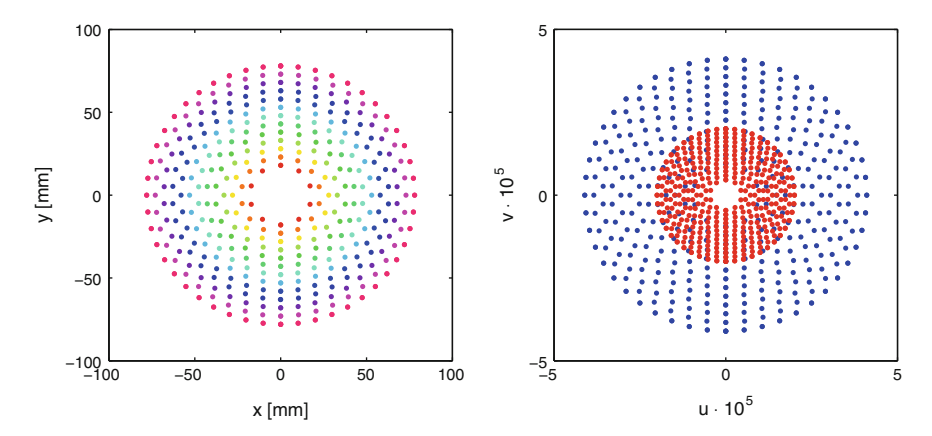


Fig. 3.14 (*Left*) For a given data set, position of the antennas for the different baseline lengths and rotations. Each color represents a baseline separation. (*Right*) Corresponding uv-coverage at $\lambda = 780 \, \text{nm}$ (*red*) and $\lambda = 380 \, \text{nm}$ (*blue*)

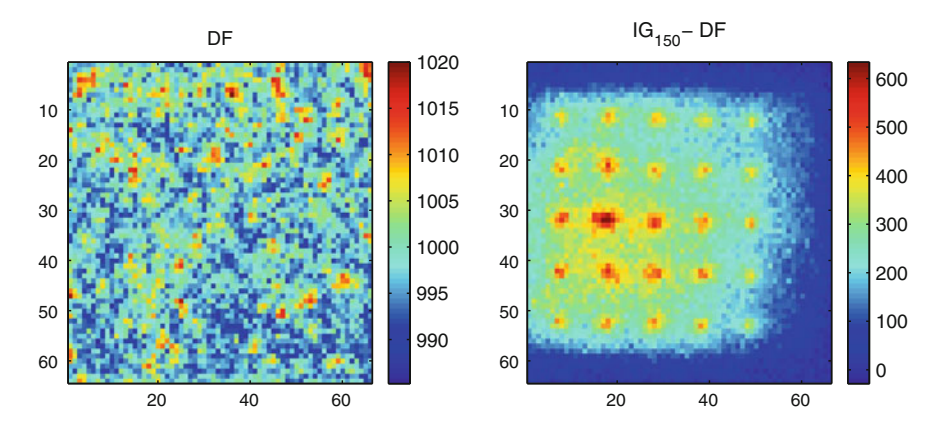


Fig. 3.15 For the 5×5 point sources array scene, averaged dark frame (*left*) and the data after the dark frame subtraction (*right*)

Figure 3.15 shows the averaged dark frame (left) and the data after the dark frame subtraction (right). However, looking at the data it can be observed that there is a residual or background illumination. After this data set was acquired it was discovered that the background was because of the CHIP itself and it will be discussed later in this chapter.

To correct the background illumination Mathematical Morphology (Serra 1983) techniques are applied. Mathematical Morphology was born in 1964 from the collaborative work of Georges Matheron and Jean Serra, at the École des Mines de Paris, France. It provides an approach to the processing of digital images which is based on shape.

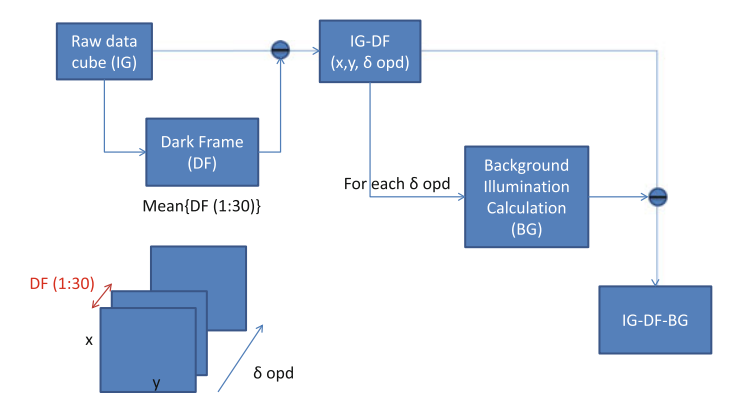


Fig. 3.16 Flow diagram of the data processing operations. First the averaged dark frame (DF) is subtracted from the raw data (IG). Then the background illumination is calculated (BG) and extracted for every frame (IG-DF-BG)

The function used to perform the background illumination subtraction is Opening, the Dilation of the Erosion of an image by a structuring element. Together with closing, the opening serves in computer vision and image processing as a basic workhorse of morphological noise removal. Opening removes small objects from the foreground of an image, placing them in the background. However, in this situation the small objects are the objects of interest, the sources being measured. Therefore, by selecting an appropriate structuring element (circle of radius bigger than the point source, but smaller not to contain 2 sources), the sources are removed and the background illumination is extracted. Then the background illumination (BG) is subtracted from the data (IG-DF-BG).

Figure 3.16 presents a complete flow diagram of the operations performed. Background Illumination Calculation is where the Morphological Opening is performed. It is performed for each frame or optical path step. It is a computationally heavy process, but the calculation of a single background for the average of the data frames resulted in unreal interferogram visibilities greater than 1. Figure 3.17 (left) shows the extracted background illumination by Mathematical Morphology using as a structuring element a disc or radius 5 pixel, and the resulting data after the extraction of the background illumination (right).

3.2.2.3 Visibility Analysis

Once the data has been 'cleaned' a study of the interferogram can be performed. However, the first step consist in the reduction of the noise of the interferograms. To do this, a 3×3 binning is performed so the signal-to-noise ratio is increased. In this situation the loss of resolution is not an issue as we are not trying to resolve point source next to each other.

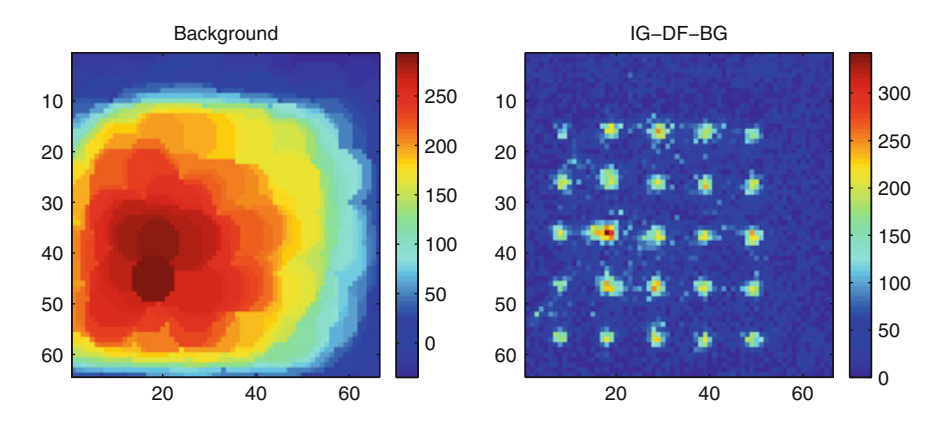


Fig. 3.17 Background illumination calculated with Mathematical Morphology algorithms using as a structuring element a disc or radius 5 pixel (left), and the resulting data after the extraction of the background illumination (right)

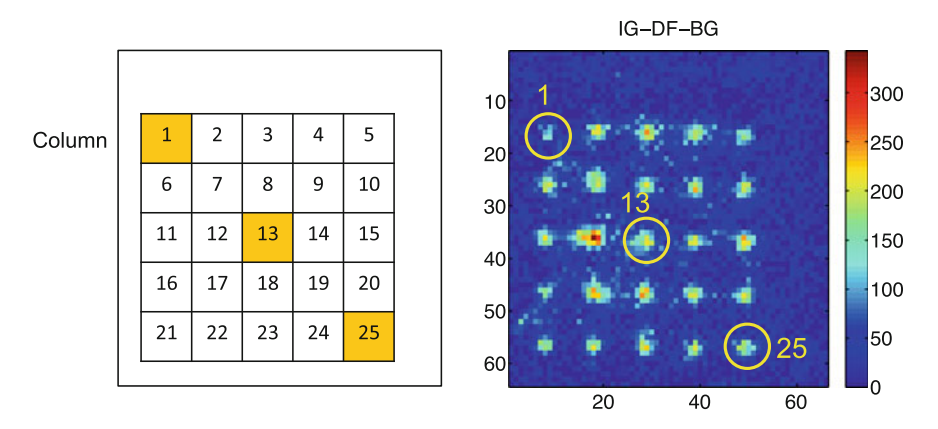


Fig. 3.18 Number assigned to every source of the 5×5 point source array (*left*) and real data where the 3 reference sources 1, 13 and 25 are indicated (*right*)

Figure 3.18 shows how the sources are coded from now on. Each of the 5×5 sources is numbered from 1 to 25, and sources 1, 13 and 25 are used for reference.

Figure 3.19 shows interferograms for the reference sources 1 (blue), 13 (green) and 25 (red) for baselines of 30, 50, 70, 90 110 and 130 mm. First of all, if we look at the level of continuum signal for this 3 sources we can observe that sources 1 and 25 have a similar level of approximately 125 counts while source 13 has a level of approximately 160 counts. This difference is due to a residual background illumination. Looking at the plot for the baseline 30 mm, it can be observed that the distance between the zero path difference (ZPD) of the source 1 and 13 is equal to the distance of ZPD between sources 13 and 25, approximately 10 µm. As the baseline is increased, this distance also increases. It can be observed that at baseline 130 mm

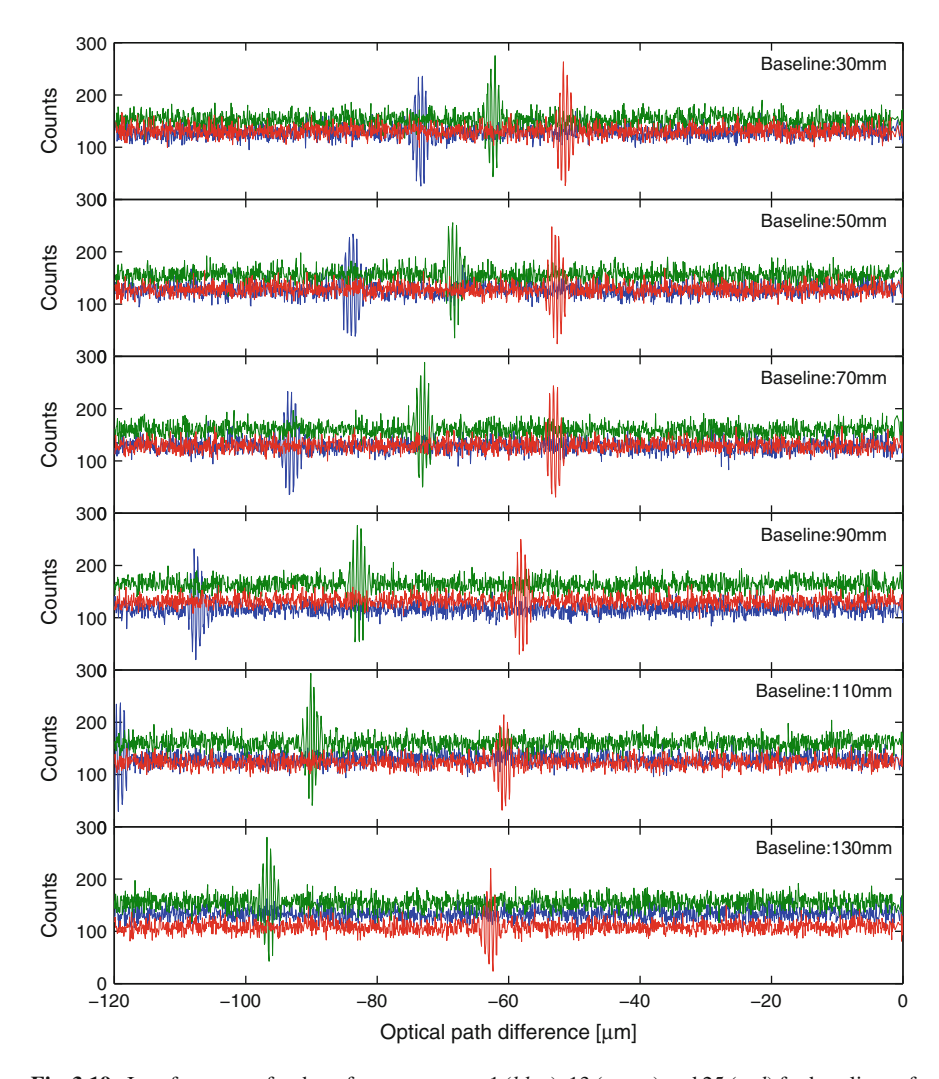
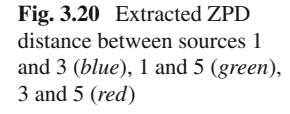


Fig. 3.19 Interferograms for the reference sources 1 (*blue*), 13 (*green*) and 25 (*red*) for baselines of 30, 50, 70, 90 110 and 130 mm. The infterferogram of source 1 (*blue*) is lost after baseline 110 mm because the ZPD is not being scanned

there is no interferogram for the source 1. This is because the ZPD is not being scanned. The use of wide-field interferometry requires to expand the optical path difference scanning, as the ZPD of off-axis sources is shifted a distance proportional to the baseline and the position angle on the sky or source simulator, this is $d_{ZPD} = b_0 \sin \theta$. Sources 1 and 13 are separated approximately 20 pixels on the CCD frame. Using the WIIT plate scale introduced early in this chapter, the shift of ZPD should be approximately 5 μ m for a baseline of 30 mm, which disagrees from the recorded data.



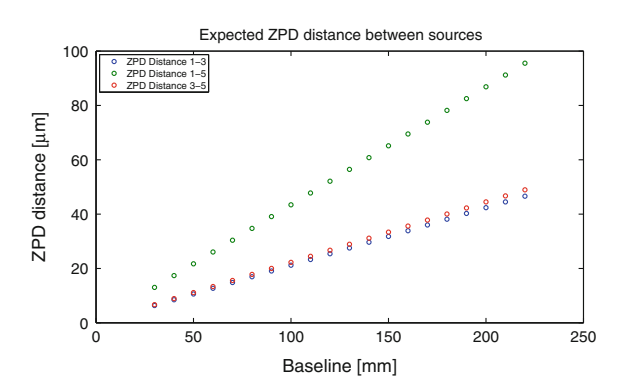


Figure 3.20 shows the expected ZPD distance between sources 1 and 3, 1 and 5, and 3 and 5. It is important to know the expected ZPD evolution as the baseline is increased to ensure recording interferograms for all the sources within the FOV.

Currently the possible factors for this disagreement are being studied, but it seems there might be a malposition of the re-focusing lens system previous to the CCD camera. In any case, this disagreement on the WIIT plate scale is not relevant to the visibility analysis.

The visibility quantifies the contrast of interference referring to the amplitude of the envelope of the interference fringe pattern and is approximately

$$V = \frac{I_{max} - I_{min}}{I_{max} + I_{min}} \tag{3.8}$$

where I_{max} and I_{min} are the maximum (constructive interference) and minimum (destructive interference) intensities.

Figure 3.21 shows the calculated visibilities for the point sources of the 5×5 array as a function of the baseline separation. For the sources situated at column 1 (top-left image) the visibilities are approximately 0.8, meaning a drop of visibility of around 20%, a value that is consistent with the predictions. From the baseline 120 mm there is a drop of visibility. This is because the ZPD of the corresponding interferogram is not being scanned. However, for the sources situated at column 2 (top-right image), and more specifically for source number 12 there is a 50% drop of visibility. The reason for this situation is the background illumination peaking at that position, as the image processing algorithm used has subtracted part of the signal. The ZPD of the sources situated at column 2 is not scanned from a baseline of 150 mm, and hence a 20% visibility from that baseline. The same occurs for the sources of column 3 (centre-left image) from a baseline of 190 mm. The ZPD of the sources located at column 4 (centre-right image) and 5 (bottom-left) is scanned for every baseline, and the visibility remains around 0.8. Figure 3.21 bottom-right shows a direct comparison of the visibilities for the reference sources 1, 13 and 25.

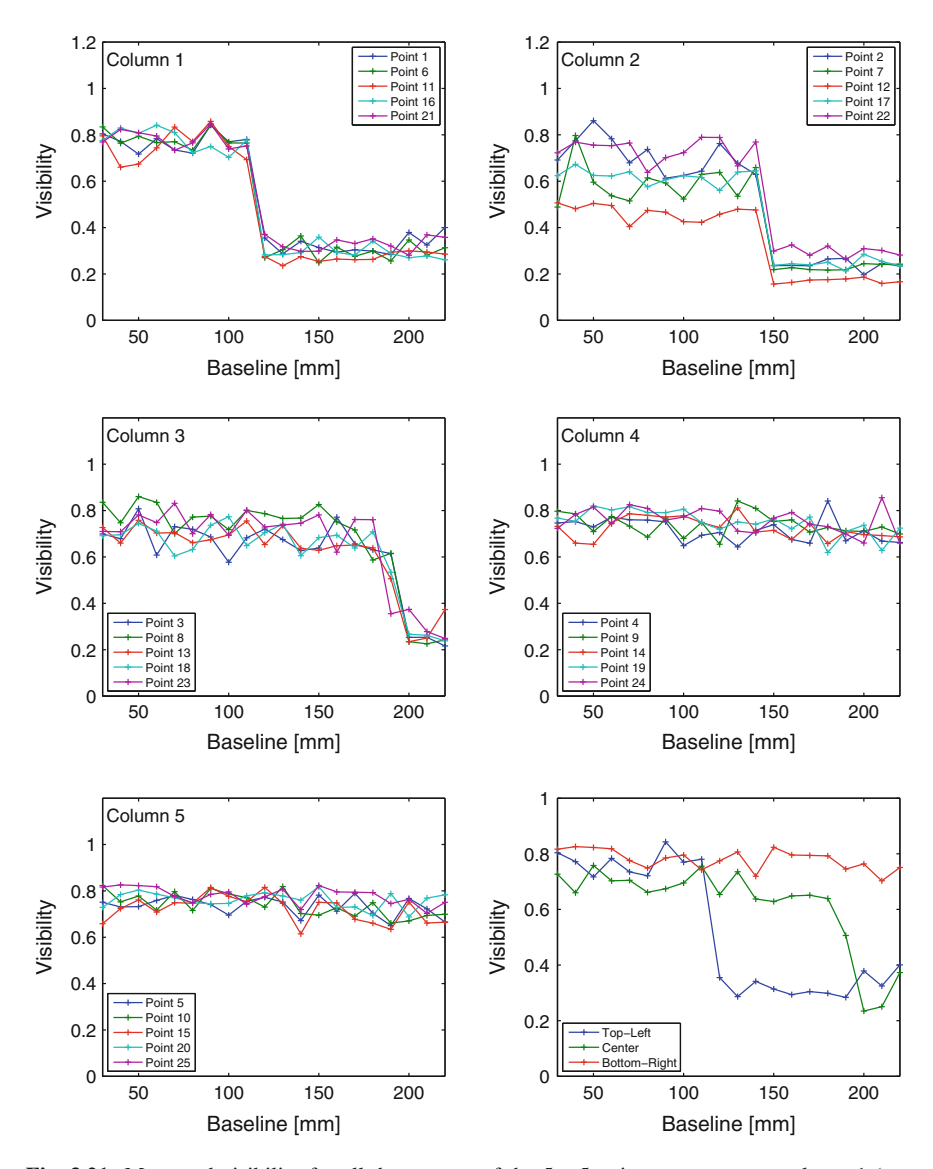


Fig. 3.21 Measured visibility for all the sources of the 5×5 point source scene: column 1 (top left), column 2 (top right), column 3 (centre left), column 4 (centre right) and column 5 (bottom left), and comparison of the visibilities of the 3 reference sources (bottom right)

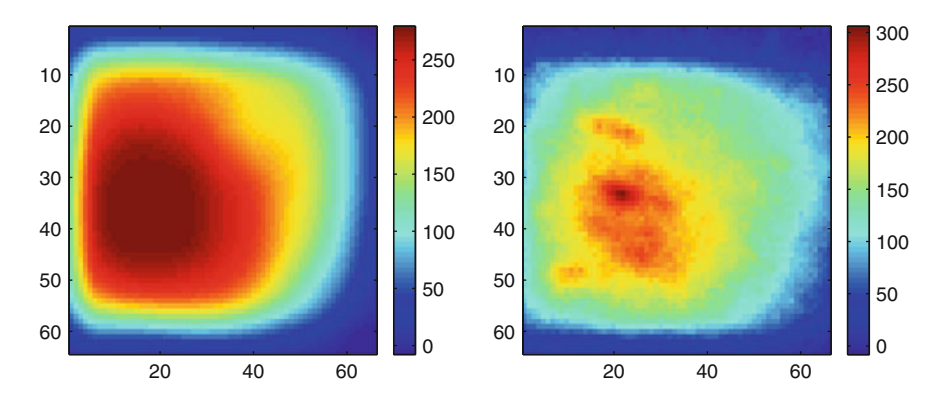


Fig. 3.22 Computed background illumination using as a structure element a disk of radius 10 pixels (*left*) and smoothed, and the measured background illumination after averaging 1200 frames (*right*)

3.2.2.4 Background Illumination

By inspection of the data it appears that the background illumination is common and very similar for all the baselines, indicating that the source of it might be the CHIP itself. For this reason a measurement of a CHIP scene where all the pixels are in 'off' position is performed. Figure 3.22 shows the computed background illumination using as a structure element a disk or radius 10 pixels (left) and the measured background illumination after averaging 1200 frames (right), both after subtraction of the averaged dark frame. It can be observed that the number of counts and shape is similar. However, as the process of data acquisition with WIIT requires the selection of the area of interest of the CCD (for data volume purposes) a direct match between the previous analyzed data and the measured background illumination would be inaccurate, meaning this data cannot be used a posteriori.

From the day of this experiment, the data acquisition process has been modified. Not only a set of dark frames is acquired before the data, also a set of background frames is acquired for a reliable background illumination subtraction. Note that the peak of the measured background illumination is consistent with the position of the source number 12 of the 5×5 point sources array which presented a drop of visibility of $50 \,\%$.

3.2.2.5 An Example: The Pyramid

The 5×5 point sources array data is a good set for validation and calibration of the WIIT system. However, one of the objectives of WIIT is to observe astronomically representative test scenes, which can be binary sources.

Figure 3.23 (left) shows the distribution of sources with CHIP for a source rotation of -90° . 4 reference sources are placed at the corners (1, 2, 3 and 4), sources 5–9 are double point sources separated 0, 1, 2, 4 and 8 CHIP pixels respectively, forming

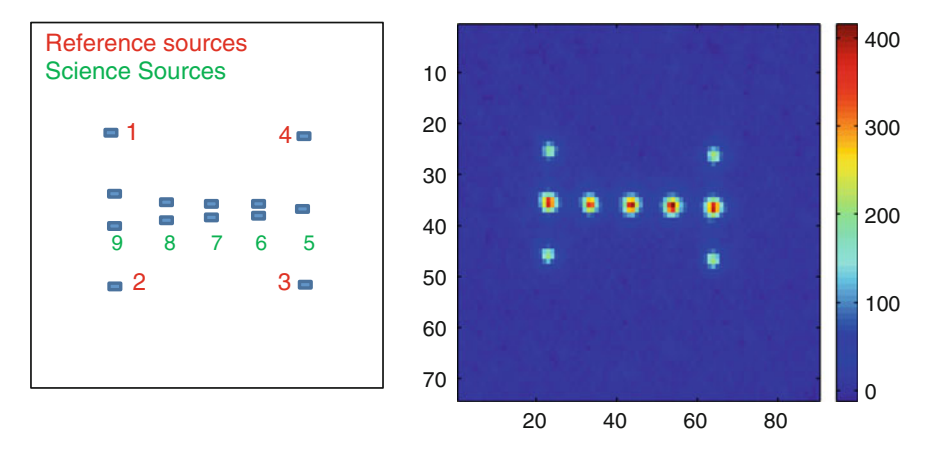


Fig. 3.23 Pyramid distribution of sources with CHIP for a source rotation of -90° . Numbers assigned to the sources (*left*) and one of the frames of the data cube (*right*)

a 'pyramid'. The separation between double sources is 128 CHIP pixels. One of the frames of the measured data is shown in Fig. 3.23 (right).

Figure 3.24 shows the interferograms recorded for the pyramid for different baseline separations. The interferograms for sources 5–9 are clearly separated because for this position of the source (rotation -90°), the axis of the pyramid is parallel to the baseline, so each angle corresponds to a ZPD displacement of $d_{ZPD} = b_0 \sin \theta$. However, in this configuration the interferograms corresponding to the reference sources 1 and 2 overlap with the interferogram of source 9, and the interferograms corresponding to the reference sources 3 and 4 overlap with the interferogram of source 5. The instrument 'sees' the sources in the same position. By using widefield imaging interferometry the interferograms corresponding to different sources are recorded in different pixels and can therefore be distinguished.

However, for this data set the scanned optical path difference is not scanning the ZPD for all the sources of the scene. More specifically, after the baseline length of 70 mm no ZPD of any source is scanned. As the WIIT plate scale has not yet been redefined, a way to predict the ZPD evolution is by data fitting. Figure 3.25 shows the predicted ZPD (*) for all the baselines from the measured ZPD (o) for the science sources (left) and the reference sources (right).

As the interferograms are not perfectly symmetric, it is recommended to scan a range of $120\,\mu m$ around the ZPD. For the current configuration the last ZPD, corresponding to the longest baseline for reference sources 1 and 2 and science source 5, will appear for an OPD of $-387.6\,\mu m$, so the scanning length should be of approximately $450\,\mu m$.

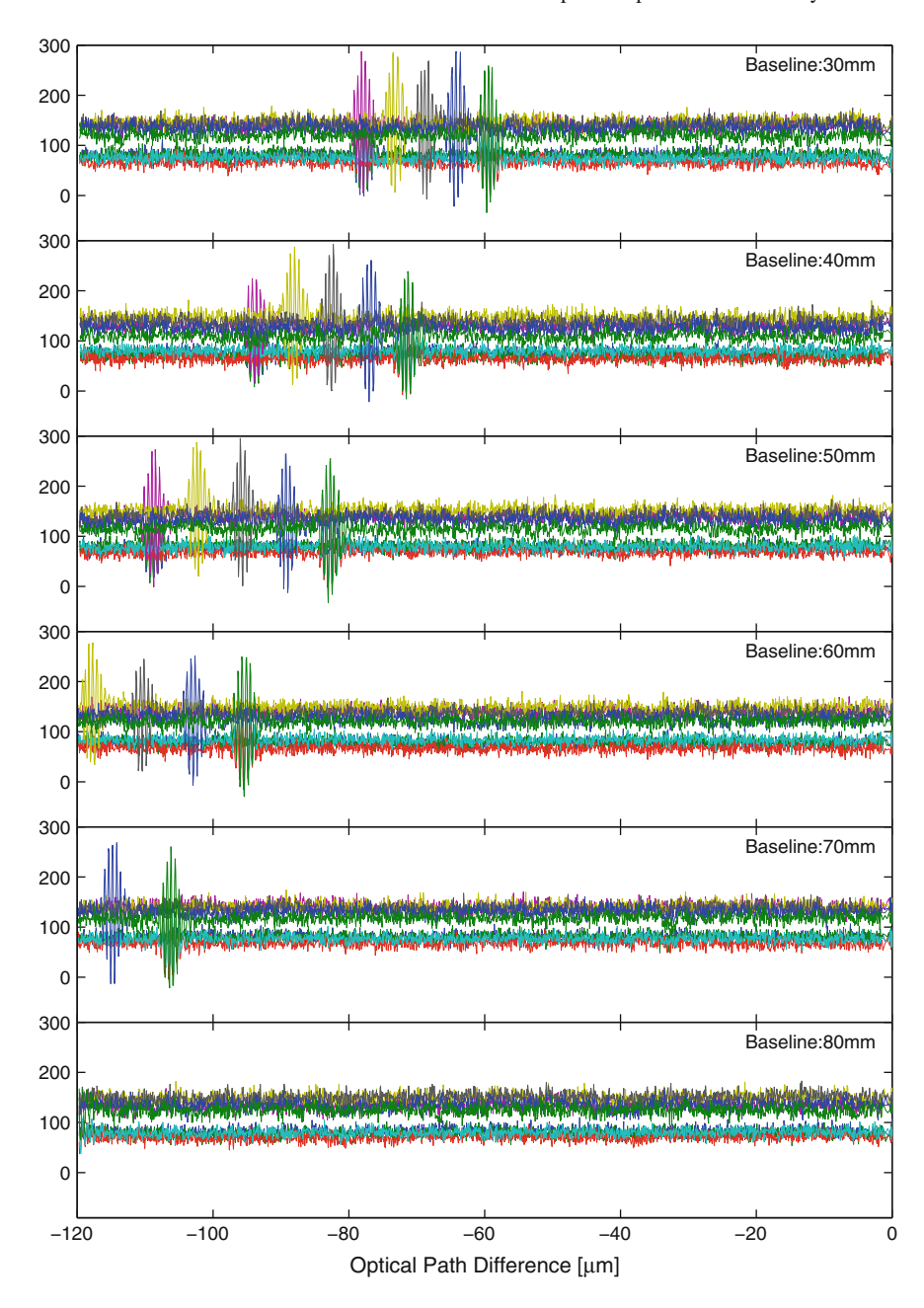


Fig. 3.24 Interferograms recorded for the pyramid test scene for baseline separations from 30 to $80\,\mathrm{mm}$ with baseline steps of $10\,\mathrm{mm}$. Purple, yellow, black, dark blue and green correspond to sources 5, 6, 7, 8 and 9 from Fig. 3.23, respectively. Turquoise corresponds to the reference source 1 and is overlapping with the interferogram corresponding to the reference source 2 (red). Light green corresponds to the reference source 3 and is overlapping with the interferogram corresponding to the reference source 4 (blue)

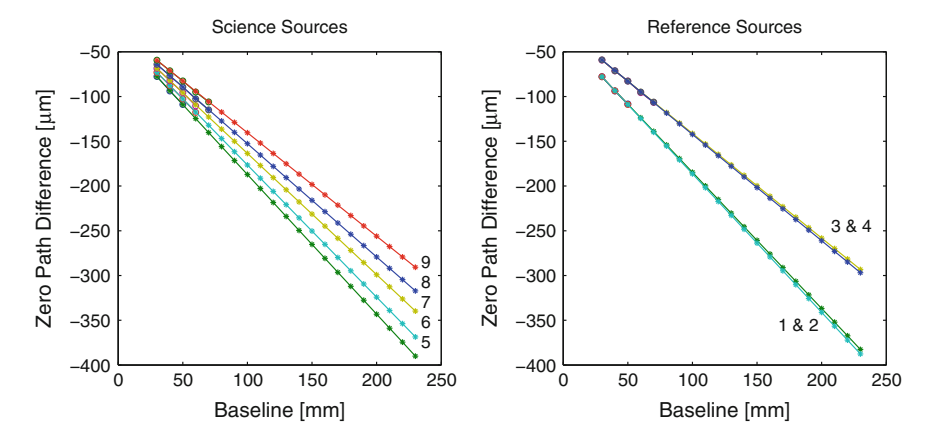


Fig. 3.25 Predicted ZPD (*) for all the baselines from the measured ZPD (o) for the science sources (left) and the reference sources (right)

3.2.3 Data Synthesis and Simulation

The WIIT team at NASA's Goddard Space Flight Center has developed the Spatio-spectral Synthesis Software (Lyon et al. 2008) (S4). This software processes the interferometric data cubes to produce a single spatial-spectral cube with 2-dimensional high resolution images along a third spectral dimension. The output spatial-spectral cube is an integral-field spectroscopic representation of the observed modelled scene. Input to S4 comprises as many interferometric data cubes as desired, where each cube corresponds to a unique interferometric baseline measurement (length and position angle).

To compare the synthesised data they have also developed a computational optical model of WIIT with the non-sequential optical system modelling software FRED from Photon Engineering, LLC, called Spatio-spectral Interferometer Computational Optical Model (SsICOM). Output data files from SsICOM are identical in format to the FITS files that come from WIIT but with simulated data. SsICOM has the capability of activating or deactivating imperfections associated with each individual optical element and of adding shot noise to model photon-counting statistics. With all imperfections activated, SsICOM models WIIT, while with all imperfections deactivated, SsICOM predicts the performance of an ideal system.

3.2.4 Current Issues and Next Steps

As described above one of the main issues is regarding the WIIT plate scale. Although it does not affect the quality of the data, it is required for the data synthesis process. This problem has been addressed and new data includes information about this para-

meter. It must be mentioned that every time the optics system is modified, this value will need to be measured.

The AIM lab where WIIT is housed is a temperature controlled laboratory. However, during measurements corresponding to the data presented here the temperature control system was turned off to avoid air turbulence. Currently an enclosure has been positioned around WIIT to be able to operate the system with cooled temperatures. This allows to reduce issues like drifts in the baseline source separations, which does not affect the visibility analysis but is very important for the data synthesis.

3.3 Chapter Summary

In this chapter the two Spectro-Spatial Interferometry Testbeds in which I have been involved during my programme have been presented: the FIRI laboratory testbed and WIIT, the Wide-field Imaging Interferometry Testbed. Both testbeds demonstrate the theory of Double Fourier Spatio-Spectral Interferometry or the application of a Fourier-transform spectrometer (FTS) to aperture synthesis interferometry presented in the previous chapter, at far infrared wavelengths and optical wavelengths, respectively.

The knowledge acquired by working with these systems has been applied in the development of the instrument simulator FIInS described in the next chapter, as well as for its validation. In Chap. 5 a more detailed validation of FIInS via the FIRI testbed is presented.

References

- P.A.R. Ade, G. Pisano, C. Tucker, S. Weaver, A review of metal mesh filters, in Society of Photo-Optical Instrumentation Engineers (SPIE) Conference Series, Presented at the Society of Photo-Optical Instrumentation Engineers (SPIE) Conference, vol. 6275, July 2006. doi:10.1117/12. 673162
- M.R. Bolcar, D.T. Leisawitz, S.F. Maher, S.A. Rinehart, Demonstration of the wide-field imaging interferometer testbed using a calibrated hyperspectral image projector, in *Society of Photo-Optical Instrumentation Engineers (SPIE) Conference Series, Society of Photo-Optical Instru*mentation Engineers (SPIE) Conference Series, vol. 8445 (2012)
- W.F. Grainger, R. Juanola-Parramon, P.A.R. Ade, M. Griffin, F. Liggins, E. Pascale, G. Savini, B. Swinyard, Demonstration of spectral and spatial interferometry at THz frequencies. Appl. Opt. 51(12), 2202–2211 (2012). doi:10.1364/AO.51.002202, http://ao.osa.org/abstract.cfm?URI=ao-51-12-2202
- D.A. Harper, R.H. Hildebrand, R. Winston, R. Stiening, Heat trap—an optimized far infrared field optics system. Appl. Opt. 15, 53–60 (1976). doi:10.1364/AO.15.000053
- F.P. Helmich, R.J. Ivison, FIRI a far-infrared interferometer. Exp. Astron. 23, 245–276 (2009). doi:10.1007/s10686-008-9100-2
- D.T. Leisawitz, M.R. Bolcar, R.G. Lyon, S.F. Maher, N. Memarsadeghi, S.A. Rinehart, E.J. Sinukoff, Developing wide-field spatio-spectral interferometry for far-infrared space applications, in *Soci-*

References 71

ety of Photo-Optical Instrumentation Engineers (SPIE) Conference Series, Society of Photo-Optical Instrumentation Engineers (SPIE) Conference Series, vol. 8445 (2012)

- D.T. Leisawitz, B.J. Frey, D.B. Leviton, A.J. Martino, W.L. Maynard, L.G. Mundy, S.A. Rinehart, S.H. Teng, X. Zhang, Wide-field imaging interferometry testbed I: purpose, testbed design, data, and synthesis algorithms, in *Society of Photo-Optical Instrumentation Engineers (SPIE) Conference Series, Society of Photo-Optical Instrumentation Engineers (SPIE) Conference Series*, vol. 4852, ed. by M. Shao, Feb 2003, pp. 255–267. doi:10.1117/12.460704
- D.B. Leviton, B.J. Frey, D.T. Leisawitz, A.J. Martino, W.L. Maynard, L.G. Mundy, S.A. Rinehart, S.H. Teng, X. Zhang, Wide-field imaging interferometry testbed 3: metrology subsystem, in Society of Photo-Optical Instrumentation Engineers (SPIE) Conference Series, Society of Photo-Optical Instrumentation Engineers (SPIE) Conference Series, vol. 4852, ed. by M. Shao, Feb 2003, pp. 827–838. doi:10.1117/12.460948
- R.G. Lyon, S.A. Rinehart, D.T. Leisawitz, N. Memarsadeghi, Wide-field imaging interferometry testbed (WIIT): image construction algorithms, in *Society of Photo-Optical Instrumentation Engineers (SPIE) Conference Series, Society of Photo-Optical Instrumentation Engineers (SPIE) Conference Series*, vol. 7013, July 2008. doi:10.1117/12.789833
- D.A. Naylor, B.G. Gom, SCUBA-2 imaging Fourier transform spectrometer, in Society of Photo-Optical Instrumentation Engineers (SPIE) Conference Series, Presented at the Society of Photo-Optical Instrumentation Engineers (SPIE) Conference, vol. 5159, ed. by S.S. Shen, P.E. Lewis, Dec 2003, pp. 91–101. doi:10.1117/12.506395
- E. Pascale, P.A.R. Ade, J.J. Bock, E.L. Chapin, J. Chung, M.J. Devlin, S. Dicker, M. Griffin, J.O. Gundersen, M. Halpern, P.C. Hargrave, D.H. Hughes, J. Klein, C.J. MacTavish, G. Marsden, P.G. Martin, T.G. Martin, P. Mauskopf, C.B. Netterfield, L. Olmi, G. Patanchon, M. Rex, D. Scott, C. Semisch, N. Thomas, M.D.P. Truch, C. Tucker, G.S. Tucker, M.P. Viero, D.V. Wiebe, The Balloon-borne large aperture submillimeter telescope: BLAST. Astrophys. J. 681, 400–414 (2008). doi:10.1086/588541
- G. Pisano, G. Savini, P.A.R. Ade, V. Haynes, Metal-mesh achromatic half-wave plate for use at submillimeter wavelengths. Appl. Opt. 47(33), 6251–6256 (2008). doi:10.1364/AO.47.006251, http://ao.osa.org/abstract.cfm?URI=ao-47-33-6251
- M. Pozar David, Microwave Engineering (Wiley, 2005)
- S.A. Rinehart, D.T. Leisawitz, M.R. Bolcar, K.M. Chaprnka, R.G. Lyon, S.F. Maher, N. Memarsadeghi, E.J. Sinukoff, E. Teichman, Recent progress in wide-field imaging interferometry, in Society of Photo-Optical Instrumentation Engineers (SPIE) Conference Series, Society of Photo-Optical Instrumentation Engineers (SPIE) Conference Series, vol. 7734, July 2010. doi:10.1117/12.857108
- J. Serra, Image Analysis and Mathematical Morphology (Academic Press Inc., Orlando, 1983). ISBN 0126372403
- QMC Instruments Ltd. Cryogenic Composite Bolometer System Operating Manual, April 2005

Chapter 4 Far-infrared Interferometer Instrument Simulator (FIInS)

The Far-infrared Interferometer Instrument Simulator, FIInS, is an instrument simulator for a Far-infrared Spectro-Spatial Interferometer. The main goal is to simulate both the input and the output of such a system, and compare the input sky map with the synthesised one after data processing algorithms have been applied. With a modular design, intermediate outputs are also available. In this chapter the different modules created to build FIInS are described, from the sky map generator to the raw data on the detectors module. In Chap. 5 the data processing algorithms are presented and the simulator is verified via the Cardiff-UCL FIRI testbed described in Chap. 3.

4.1 FIInS Overview

FIInS has been developed using MATLAB ®. The selection of this software is due to its user friendly environment. Eventually some of the heavy routines can be written in c/c++ to increase the simulation speed. The simulator presents a modular design for the testing of individual steps of the spectro-spatial interferometry technique. From a global point of view, the simulator is divided in a sky generator module, an instrument group of modules, and a data processing module (see Chap. 5), which is currently tuned with the Cardiff-UCL FIRI testbed. However, these modules are not fully independent as will be explained in the following sections. For the selection of parameters, the user is provided with two Microsoft Excel files: one corresponding to the parameters for the sky map definition, the other one for the definition of the different instrument parameters (i.e. baseline range and configuration, spectral parameters, efficiencies, among others).

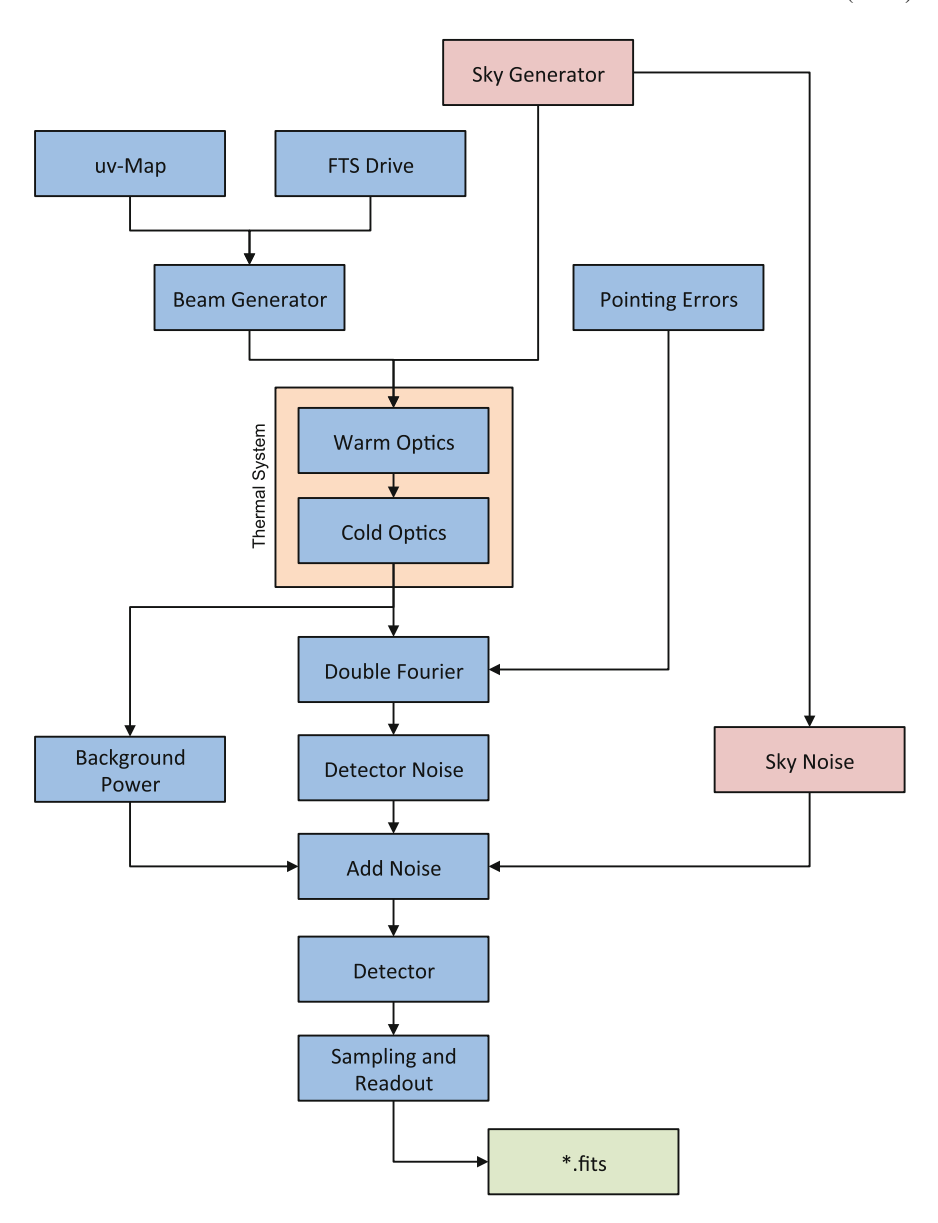


Fig. 4.1 Flow diagram of FIInS. *Pink boxes* indicate the sky simulator modules, *blue boxes* indicate modules in the instrument model, the *green box* indicates the output of the simulator

4.2 FIInS Architecture 75

4.2 FIInS Architecture

FIInS is a modular simulator, and each module is activated in a sequential way to recreate a spectro-spatial measurement via a core program. The easiest way to understand how FIInS works is through a flow diagram, as shown in Fig. 4.1. Each box in the flow diagram indicates a FIInS Module. Pink boxes correspond to the Sky Simulator, blue boxes indicate modules inside the Instrument Model, and the green box represents the output of the simulator.

The first step is to generate a Sky Map to be fed to the subsequent modules in the Sky Generator Module and the corresponding photon noise, computed in the Sky Photon Noise Module. In parallel, given the parameters defined by the user for the instrument, an interferometric *uv*-map is created at the *uv*-Map Generator Module from the position of the two telescopes. The FTS Drive module calculates the spectrometer scan parameters. Once a *uv*-map and the scan parameters are defined, the instrument beam is calculated at the Beam Generator Module. The sky map and the beam are then combined to recreate the observed sky map.

The thermal system includes the Warm Optics Module and the Cold Optics Module, which given the optical set-up and the optical parameters of the different optical elements calculates the transmission of the sky map through the instrument. At this point the physical properties of the instrument are defined and the Double Fourier Modulation can be performed at the Double Fourier Module. Here is where the interferograms are computed analytically for different baseline positions. If pointing errors are selected, the Pointing Errors Module generates them and they are fed to the Double Fourier Module.

At the Detector Noise Module, the Noise Equivalent Power (NEP) associated to the detectors and the 1/f noise are calculated. In parallel, with the physical properties of the system defined, the Background Power Module calculates the background power noise due to the instrument and the Cosmic Microwave Background (CMB), Cosmic Infrared Background (CIB) and Zodiacal Light.

Once all the simulated noises are computed, they are added to the interferograms at the Add Noise Module to simulate more realistic measurements. The simulated interferograms are then sent to the Detector Module, where the interferograms are distorted according to the detector effects such as the time response. This interferograms are then sampled and readout at the Sampling and Readout Module, which also stores the data for the data reduction and processing.

4.3 FIInS Parameters

FIInS user parameters are defined in two Microsoft Excel files, FIInS_Instrument.xlsx and SkyParams.xlsx. FIInS_Instrument.xlsx contains the parameters that define the instrument itself, and are organised in sheet. In FTSectrograph the spectral band where the instrument operates is defined, as well as the spectral resolution and the sampling.

FTSMecanical contains the drive speed and the number of scans to perform by the spectrograph. In Interferometer the baseline parameters and the baseline configuration are selected. At Telescope the diameter, temperature, and emissivity of the apertures are introduced. Combining the Interferometer and Telescope parameters, the ForSkyParams sheet is updated in order to guide the user to define the sky map. For example, the field of view is calculated so the user can place the sources in a position inside the field of view of the instrument. The data cube size is also calculated for an estimation of the simulation time. Warm Optics and Cold Optics contain information regarding temperatures, emissivities and transmissions of the optics of the system. In Background the emissivity and temperature of the CMB, CIB and Zodiacal light are stored. Finally, in Detectors the user can select the detector time constant, optical efficiency, knee frequency for the 1/f noise and acquisition frequency.

In *SkyParams.xlsx* the user defines the sky map to be created if no science input map is used. The first sheet in the file is the one that the simulator reads, so different configurations can be stored in the same file. The first option is the Full Width Half Maximum (FWHM): if empty, a point source is created, if full, a Gaussian source is simulated with this FWHM. The user may input the source position in the sky at *x_pos* and *y_pos*. If empty the simulator will display a sky grid where the user selects the position or a source by clicking on that position. *Temp* is for the temperature in Kelvin of a Blackbody spectrum. *cut-on* and *cut-off* will filter the Blackbody spectrum at the wavenumbers given at these parameters. For verification purposes, if the user inputs 1 the spectrum for that given source will be the one measured with the Cardiff-UCL FIRI testbed. If the user inputs 0 the spectrum will consist of a single wavenumber tone, defined at *tone wl*.

4.3.1 Control Flags

For simulation speed purposes and comparison between an ideal instrument or a more realistic one, a series of effects within the simulator can also be activated or deactivated by the user. The current control flags are

TimeEffects, that allows the computation of the interferograms in a way that time effects such as the drive velocity errors can be included in the simulation.

DetectorEffects, to create a set of interferograms including all the detector effects (otherwise the simulator returns the raw interferograms, which is described later in this chapter).

CalculateBeam activates the computation of the instrument beam.

PointingErrors allows pointing errors to be included in the Double Fourier Modulation.

4.4 Sky Simulator 77

4.4 Sky Simulator

The Sky Simulator consists of two modules: the Sky Generator Module and the Sky Photon Noise Module. The Sky Generator Module creates the input data cube to which a Double Fourier Modulation will be applied. Once the data cube is created, the Sky Photon Noise Module calculates the corresponding photon noise, that will be added to the interferograms at the Add Noise Module.

4.4.1 Sky Generator Module

The Sky Generator Module is the module that generates the datacube to be fed to the subsequent blocks. This data cube consists of series of 2-dimensional images of a Sky. These 2-dimensional images are defined by the field of view (FOV_x and FOV_y) of the instrument. Along the 3rd dimension of the Sky and where a source has been positioned, the spectrum of this source is stored. The number of samples N defines the number of the images and is determined such that there is no aliasing.

Figure 4.2 shows the structure of the sky datacube (left) and the spectrum for two pixels of the sky datacube (right) indicated as A (purple) and B (green) along the wavenumbers axis ν . The axis θ_x and θ_y represent the position of the sources on the sky grid, and $\Delta\theta_x$ and $\Delta\theta_y$ are the pixel size or angular resolution.

The Sky map module is capable of placing point sources or gaussian sources on a sky grid defined by the FOV and the pixel resolution. Each source has its own spectrum, which can be loaded from data (i.e. the spectrum measured with the Cardiff-UCL testbed) or can be a black body of a given temperature and modified by

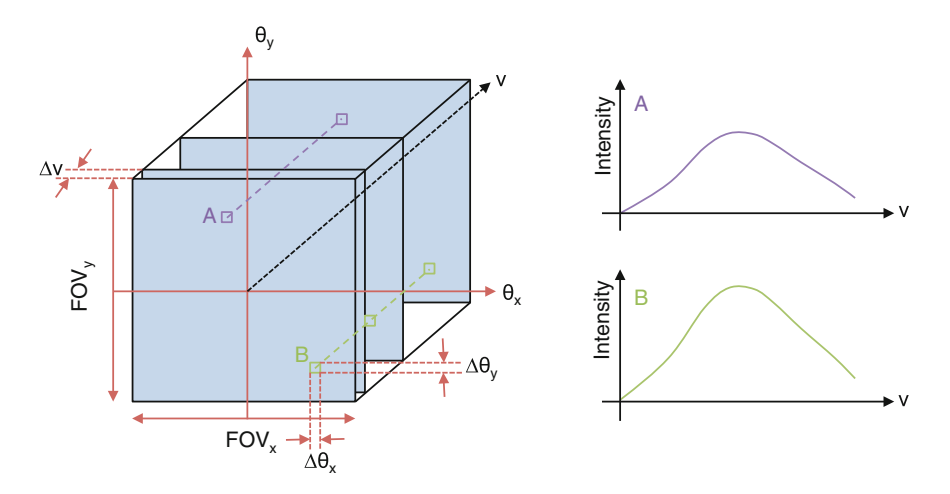


Fig. 4.2 Sky datacube structure (left) and spectra stored in two pixels of the sky datacube (right)

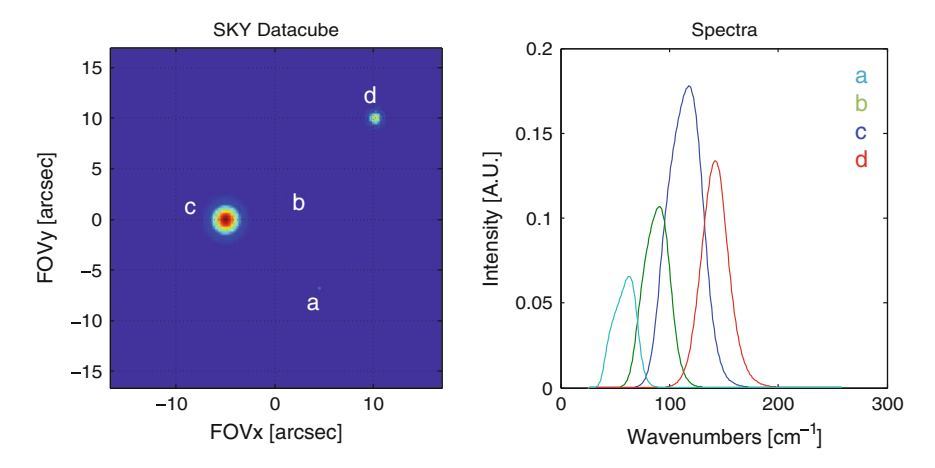


Fig. 4.3 Simulated sky datacube where 2 point sources (a, b) and 2 gaussian sources (c, d) with different spectra have been placed on a sky grid

filters. A sky map consisting of 3 circular sources the position and diameter of which is pseudo-random in a way that there are not spatial harmonics or beats present is also available.

Figure 4.3 shows an example of a simulated datacube, where 4 sources have been positioned on the sky grid (left): two gaussian sources, and two point sources. The spectra of these sources are different, corresponding to blackbodies of different temperatures which have been multiplied by filters with different cut-on and cut-off wavenumbers (right). For the loading of more complex sky map data cubes such as science datacubes the simulator will interpolate or decimate to meet the instrument parameters.

4.4.2 Sky Photon Noise Module

Once the sky map reaching the system is determined, one can compute the associated photon noise that will reach the detector. The fundamental limit of any ideal photon integrating sub-mm detector is the noise associated with the Bose-Einstein fluctuations in photon arrival rate (Lamarre 1986) which results in a photon noise limited NEP

$$NEP_{ph} = \sqrt{2Qhf(1+mB)} \approx \sqrt{2Qhf}$$
 (4.1)

where Q is the sky power loading the detector at a frequency f from the sub-mm source. B is the photon occupation number per mode and m the efficiency from emission to detection of one mode. The (1+mB) term is the correction to Poisson statistics due to wave bunching (Boyd 1982; Baselmans 2012). Here we consider no wave bunching, as the detector is considered single mode and so the dominant noise

4.4 Sky Simulator 79

is the shot noise as before. Given the fact that the input sky map is a datacube of considerable dimensions, it is computationally heavy to compute and integrate the photon noise NEP for each position of the sky, for each baseline. For this reason, the following approximation has been used. The number of photons for each sky position per frequency is

$$N(\theta_{x,i}, \theta_{y,j}, f_k) = \frac{SkyS(\theta_{x,i}, \theta_{y,j}, f_k)}{hf_k}$$
(4.2)

then the noise equivalent power associated to the number of photons per frequency is

$$NEP_{ph}(v_k) = \sum_{i=0}^{N_{FOV_x}} \sum_{i=0}^{N_{FOV_y}} \sqrt{2N(\theta_{x,i}, \theta_{y,j}, f_k)} h v_k$$
 (4.3)

Finally, the total data cube NEP is

$$NEP_{ph,sky} = \sum_{k=0}^{N} NEP(f_k)df$$
 (4.4)

4.5 Instrument Model

As shown in Sect. 4.2 the instrument model is comprised of a sequence of semiindependent modules. In this section the different modules are described and the connections between them shown.

4.5.1 uv-Map Generator Module

The uv-Map Generator Module calculates the baseline configuration according to the user parameters. The user selects the minimum and maximum baseline length (b_{min} and b_{max} , respectively) for each configuration and the spacing between baselines, b_{step} . The minimum baseline will always be equal or bigger than the single dish telescope diameter to perform interferometry. The geometric configurations available are Fixed Arc Length, Fixed Angle, Spiral, Random and Single and are shown in Fig. 4.4 for a single wavelength.

4.5.1.1 Fixed Arc Length Configuration

In this configuration the distance between consecutive baseline positions for a given baseline length is constant. Figure 4.4 top-left shows the *uv*-map in this situation.

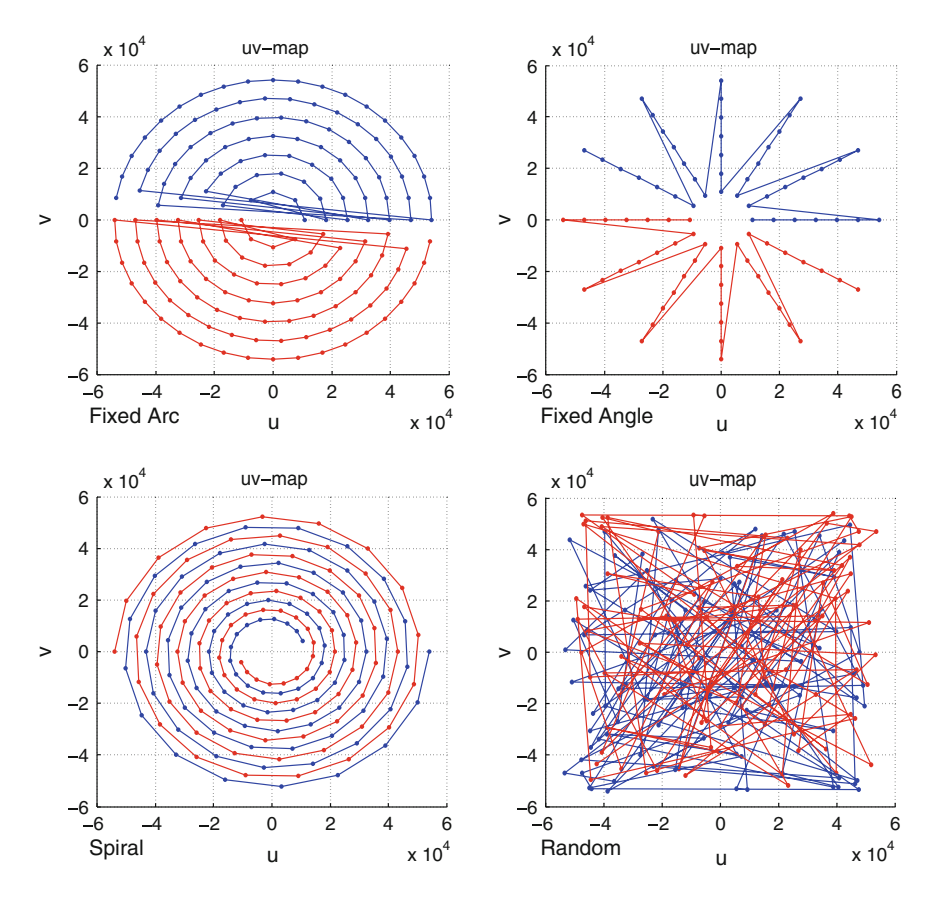


Fig. 4.4 Simulated *uv*-map for different baseline configurations for a fixed wavelength. *Red* and *blue dots* represent the *uv*-positions corresponding to the baselines between telescopes. The simulated baselines configurations are Fixed Arc Length (*top-left*), Fixed Angle (*top-right*), Spiral (*bottom-left*) and Random (*bottom-right*)

The blue and red colours represent the two telescopes conforming the interferometer. The simulator creates a vector of telescope positions. Given the angle between two consecutive baseline positions at b_{min} (user defined in degrees, α_{arc}), this module calculates the arc length

$$L_{arc} = \frac{b_{min}}{2} \frac{\alpha_{arc} \pi}{180} \tag{4.5}$$

Following baseline positions are calculated to maintain the distance L_{arc} between consecutive positions. Selecting the baseline length step similar to L_{arc} generates a regular grid-like uv-map.

4.5.1.2 Fixed Angle Configuration

When a Fixed Angle configuration is selected, in addition to the main baseline parameters the user also defines the maximum angle the baseline vector is going to rotate α_{max} , and the number of steps within this angular range where the instrument is going to stop and perform spectroscopy measurements, N_{α} . Figure 4.4 top-right shows the uv-map in this situation.

4.5.1.3 Spiral Configuration

The Spiral configuration is the more realistic one in terms of telescope motion, and it recreates a variation of an Archimedean spiral. The simulator first calculates the number of turns of the spiral, $N_{turns} = (b_{max} - b_{min})/b_{step}$. The user also defines the number of baselines to be created, N_b . The baseline vector is then created in polar coordinates as

$$\phi_i = \frac{i}{N_b} 2\pi N_{turns} \tag{4.6}$$

$$\rho_i = \frac{\phi_i}{2\pi} b_{step} + b_{min} \tag{4.7}$$

where i is an integer from 1 to N_b . Figure 4.4 bottom-left shows the uv-map in this situation.

4.5.1.4 Single Baseline Configuration

The Single Baseline configuration is the most simple one and is available for testing purposes. It is simulated by setting a maximum baseline length b_{max} and a baseline angle, α .

4.5.1.5 Random Configuration

This configuration is for testing purposes only. Given a maximum baseline b_{max} and a number of baselines N_b the simulator calculates a randomly-generated baseline vector. Figure 4.4 bottom-right shows the uv-map in this situation.

4.5.2 FTS Drive Module

The FTS Drive Module generates the time-line, physical and optical position vectors for the spectrometer scan. The user defines a band of operation for the instrument

with the minimum and maximum wavelength (λ_{min} and λ_{max}), the resolving power R and the number of points per Nyquist sampling, N_{Nyq} . To avoid aliasing according to the Nyquist criterion, the sampling frequency or wavenumber is greater than or equal to twice the bandpass of the system, this is, $v_{Nyq} \ge 2v_{max}$.

The first derived parameter is the spectral resolution, Δv , defined as

$$\Delta v = \frac{v_{min}}{R} \tag{4.8}$$

The maximum required optical path difference δ_{max} is then given by the spectral resolution $\Delta \nu$

$$\delta_{max} = \frac{1}{2\Delta\nu} \tag{4.9}$$

and the optical delay is $\Delta \delta = (2\nu_{max}N_{Nyq})^{-1}$. Once the maximum optical path difference and the optical delay are defined, the number of sampling points is defined as

$$N = \frac{\delta_{max}}{\Delta \delta} \tag{4.10}$$

which, for $N_{Nvq} = 1$, is equivalent to

$$N = \frac{\nu_{max}}{\Delta \nu} \tag{4.11}$$

If $N_{Nyq} > 1$, which results on a finer optical delay, the maximum wavenumber of the system is then $v'_{max} = N_{Nyq}v_{max}$ and the spectral resolution is conserved.

The optical path difference vector δ is a vector of N samples from 0 to δ_{max} sampled every $\Delta\delta$. Depending on the optics design, the physical position vector will range from 0 to $x = \delta_{max}/2$ (Martin-Pupplet configuration) or from 0 to $x = \delta_{max}/4$ (modified Mach-Zehnder design).

The time-line vector is then defined by the optical position and the optical velocity V as $t = \delta/V$. The optical velocity is derived from the driver velocity V_{scan} and the Optical System Level (OSL), which depends on the band of interest and is described in Sect. 4.5.5.2. With these parameters, the optical velocity is $V = 2V_{scan}OSL$, and the factor 2 is because of the selected Martin-Pupplet configuration.

4.5.3 Beam Calculator Module

The Beam Calculator Module generates the instrument beam as a function of the FTS and interferometric input parameters selected by the user, and the telescope parameters. The first derived parameter required is the interferometric angular resolution, $\Delta\theta_I$. For an interferometer with a maximum baseline b_{max} , the maximum

angular resolution is $\Delta\theta_I \approx \lambda_{min}/b_{max}$. Thus the required sky grid angular resolution $\Delta\theta_{max} = \Delta\theta_I/2$ at the spatial domain (θ_x, θ_y) . The beam has to be calculated such that the angular resolution remains constant for each wavelength.

For a single dish with a diameter D_{Tel} the angular resolution is $\Delta\theta_S \approx 1.22\lambda_{min}/D_{Tel}$, and the field of view at a given wavelength is $FOV = 2.44\lambda/D_{Tel}$. The number of pixels required per FOV is

$$N_{FOV} = \frac{FOV}{\Delta\theta_I} = 2.44 \frac{\lambda_{max}}{D_{Tel}} \frac{1}{\Delta\theta_I}$$
 (4.12)

The beam profile is a function of the wavelength and the required angular resolution $\Delta\theta_{max}$, which defines the spatial span for the calculation of the illumination profile in (x, y). The telescope illumination can be written as

$$f(x, y; \nu) = \begin{cases} 1 & \text{if } (x^2 + y^2) < (D_{Tel}/2)^2 \\ 0 & \text{otherwise} \end{cases}$$
 (4.13)

where $-\lambda/\Delta\theta_{max} < (x, y) < \lambda/\Delta\theta_{max}$. By performing the calculation of the telescope profile at each wavelength by changing the spatial span, the spatial sky grid remains constant. The software also allows a gaussian profile illumination function to be used for the computation of the instrument beam. The instrument beam is then calculated by performing a 2-dimensional Discrete Fourier Transform of the illumination

$$Beam(\theta_x, \theta_y; \nu) = DFT2\{f(x, y)\} = \sum_{n=0}^{N-1} \sum_{m=0}^{M-1} f(x_n, y_m; \nu) e^{-j2\pi(\frac{\theta_x n}{N} + \frac{\theta_y m}{M})}$$
(4.14)

where $N = M = N_{FOV}$. The normalised beam profile is

$$Beam(\theta_x, \theta_y; \nu) = \frac{|beam(\theta_x, \theta_y; \nu)|^2}{|beam(0, 0; \nu)|^2}$$
(4.15)

This computed beam is then multiplied by the sky map. In order to avoid the interpolation or decimation of the sky map, these parameters can be used as an input for the simulation of the sky map itself.

As an example, Fig. 4.5 shows the calculated normalised beam profile (right) for a given wavenumber and for a telescope diameter $D_{Tel} = 3$ m illuminated uniformly (left).

An alternative to calculating the telescope beam profile is to use the Hankel transform, valid for an ideal and circularly symmetric aperture. The calculation of beam profiles using Hankel transforms is detailed in Appendix A.

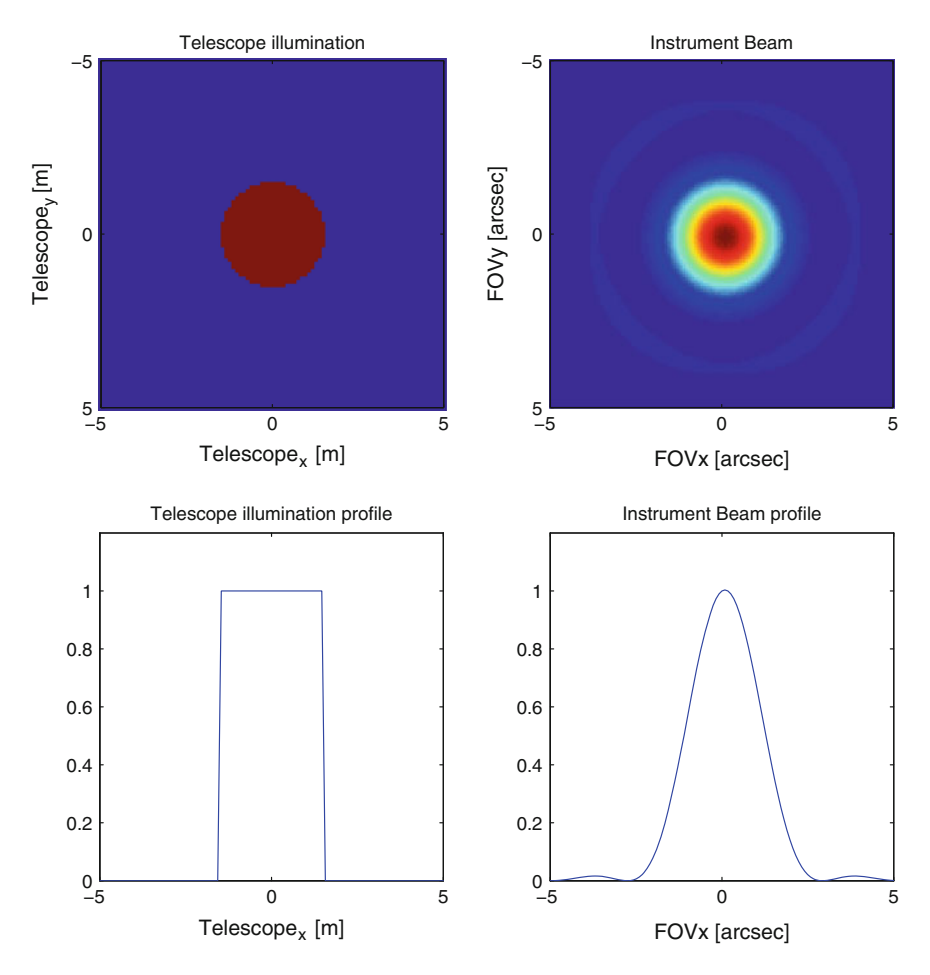


Fig. 4.5 Calculated beam for a given telescope diameter, D_{Tel} . Telescope illumination (top-left) and its profile (bottom-left) and normalised beam profile (top-right) and its corresponding profile (bottom-right)

4.5.4 Pointing Errors Module

In FIInS two types of pointing errors are considered: pointing errors affecting the whole spacecraft (PES), and pointing errors relative to each of the telescopes of the interferometer (PET1 and PET2). The pointing errors affecting the whole spacecraft are considered as a tilt of the baseline vector with respect to the sky map vector, while pointing error relative to each of the telescopes are computed as a shift of the instrument beam with respect to the sky map.

Figure 4.6 is a schematic of the pointing of the telescopes. If a perfect instrument is simulated, each of the telescopes sees the same source with the same intensity

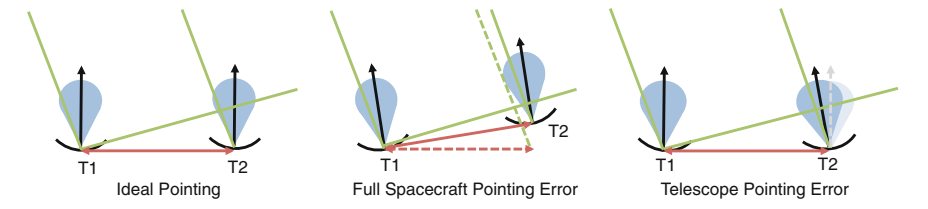


Fig. 4.6 Pointing of a two-telescope interferometer. If the pointing is ideal, the light coming from a given direction will see the same telescope beam (*left*) with a given delay. If the telescope baseline is tilted, light coming from a given direction will see the same telescope beam, but the delay will have changed (*centre*). If the pointing of one of the telescopes is different with respect to the other telescope, the light coming from a given direction will see a different telescope beam (*right*)

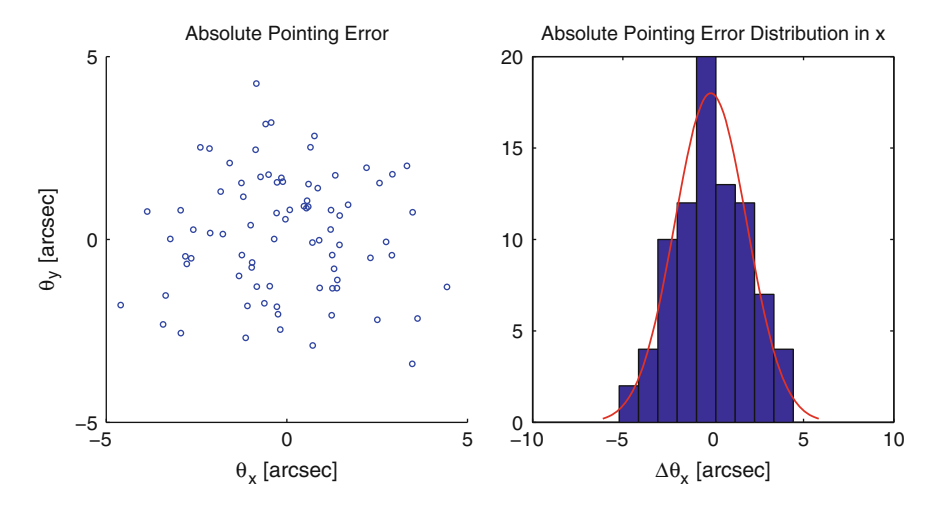


Fig. 4.7 Simulated pointing position with an absolute pointing error (*left*) and the absolute pointing error distribution in the x direction (*right*) including a gaussian fit to the data with $\sigma_p = 2$ arcsec

and with a given delay. However if there is a tilt of the baseline vector with respect to the sky map plane, the same source is seen with the same intensity but with a different delay respect the ideal position. FIInS applies both types of pointing error simultaneously.

Each type of pointing error has an absolute and a relative component. The absolute pointing error is defined as the measurable pointing error, which can be used at the data reduction and processing. The relative pointing error is the non-measurable pointing error and can not be corrected. The absolute pointing error follows a Gaussian noise distribution with a 2 arcsec standard deviation, σ_p , according to Herschel Space Observatory pointing data (Pilbratt et al. 2010). The relative pointing error follows a Gaussian noise distribution with a standard deviation corresponding to the 10% of the absolute pointing error.

Figure 4.7 shows the simulated pointing position with an absolute pointing error (left) in the θ_x and θ_y space and the corresponding distribution (right, only in the

x direction). The standard deviation for the absolute pointing error, as well as the percentage for the relative pointing error, are user defined parameters and can be modified

4.5.5 Instrument Thermal System

The Instrument Thermal System is divided in two parts, the Warm Optics Module and the Cold Optics Module. In the Warm Optics module the emissivity and transmission of the optics external to the cryostat are modelled. In the Cold Optics Module the emissivities and transmissions of the optics from the cryostat window to the detectors are modelled. The current cold optics design is based on a FIRI design presented at the CDF Report (ESA Concurrent Design Facility 2006). The warm optics consists of a two telescope interferometer.

4.5.5.1 Warm Optics Module

Figure 4.8 shows the collecting telescopes configuration. Each consists of a pair of focal parabolas (primary M1, secondary M2) used in a Cassegrain configuration, plus a fold flat used for coarse beam steering (M3). The design is based in NASA's SPIRIT proposal (Wilson et al. 2007). After the beam steering mirror the light is directed to the windows (W) of the cryostat in order to enter the cold optics box.

The purpose of this module is to compute the emissivity and transmission of the 3 components of each telescope. The emissivity of the primary (M1) and secondary (M2) is assumed to be the same and is based on Herschel mirror sample measurements, with a wavelength-dependent emissivity based on the results of Fischer (Fischer et al. 2004) who give the following equation for the best fit to the

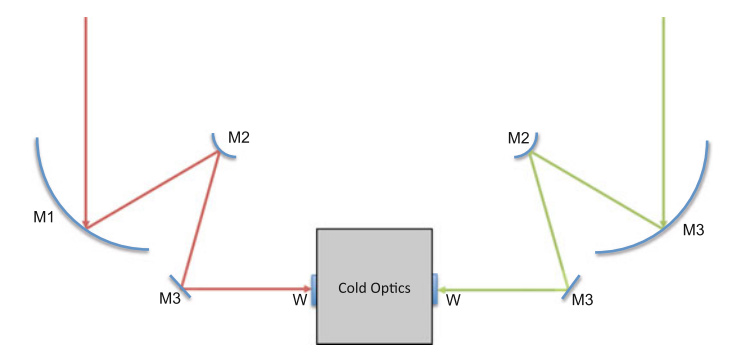


Fig. 4.8 Collecting telescopes configuration consist of a pair of focal parabolas (primary M1, secondary M2) used in a Cassegrain configuration and a fold flat used for coarse beam steering (M3). Light is then directed to the cold optics box through the windows (W)

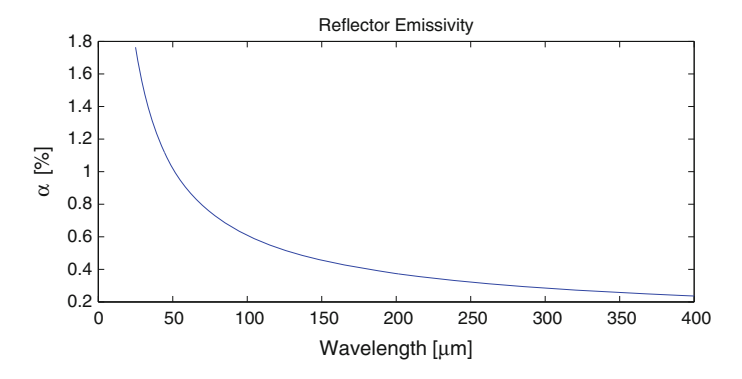


Fig. 4.9 Reflector emissivity as a function of the wavelength

absorptivity α (or emissivity ε_{ref}) of a dusty Herschel mirror sample

$$\alpha = 0.0336\lambda^{-0.5} + 0.273\lambda^{-1} \tag{4.16}$$

where the wavelength is given in μ m. Figure 4.9 shows the corresponding emissivity per reflector as a function of the wavelength. Each reflector is assumed to have a transmission $t = 1 - \varepsilon$.

For the beam steering mirror, the emissivity is assumed to be constant in the FIRI band and is a user defined parameter. In this module the stray light component is also modelled and assumed to have an emissivity proportional to the telescope emissivity, $\varepsilon_{stray} = 0.2\varepsilon_{tel}$, where for this situation ε_{tel} is a user defined parameter.

4.5.5.2 Cold Optics Module

The incoming light from the two telescopes enters the cryostat through the windows (W) from the left (red) and from the right (green) as shown in Fig. 4.10. The first optical component is a NIR-FIR dichroic (NFD) that rejects the NIR radiation. The light then goes through the delay lines and each dichroic (D) selects the band of interest per each set of detectors (Det). The incoming light from the two sides of the system then interferes at the beam splitter (BS) and one detector records the interferogram and the other detector records the inverted interferogram. A filter (F) before the beam splitter further selects the band that the dichroic selected. The current configuration consists of 4 bands.

The Cold Optics Module computes the transmission of each side of the system per band as a function of the transmissions of the individual elements, which are user defined parameters, as well as the emissivities. Two parameters are defined, t_L and t_R , which correspond to the left side transmission and the right side transmission, respectively:

$$t_L = t_W t_{NFD} (1 - \varepsilon_M)^{N_{ML}OSL - (OSL - 1)} t_D t_F t_{BS}$$
(4.17)

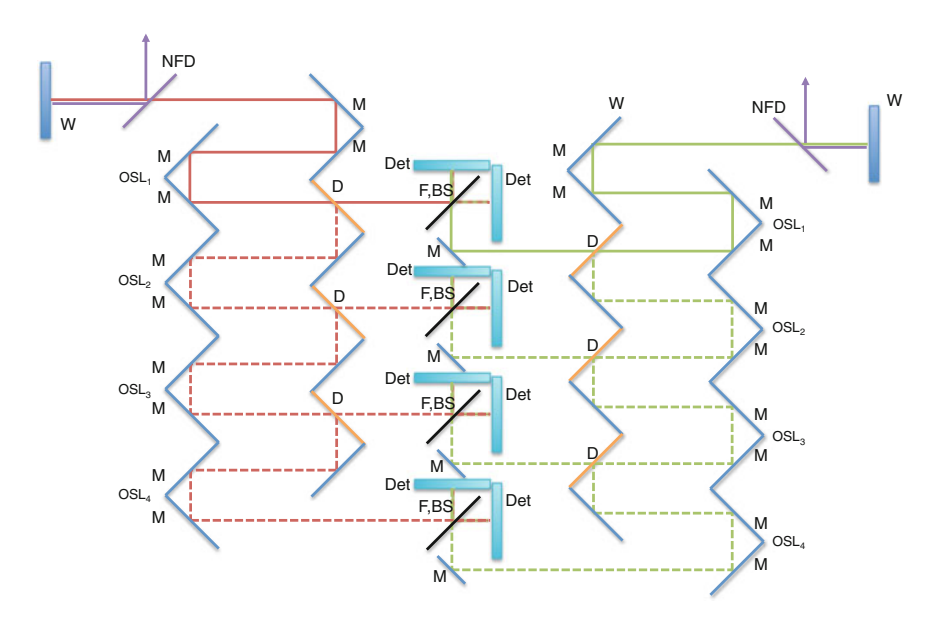


Fig. 4.10 Instrument cold optics model for a proposed FIRI system. The incoming light from the two telescopes enters the cryostat through the windows (W) from the left (red) and from the right (green). A NIR-FIR dichroic (NFD) rejects the NIR radiation. Light travels through the delay lines and a dichroic (D) selects the band of interest. The reflected light travels to the next delay line for the measurement of another band of interest. OSL_1 to OSL_4 indicate the Optical System Level or band of interest. The transmitted light from the dichroic (D) travels to the beam splitter (BS) through a filter (F), where it interferes with the light coming from the other arm of the system. Interferograms are recorded at the detectors (Det)

$$t_R = t_W t_{NFD} (1 - \varepsilon_M)^{N_{MR}OSL - 2(OSL - 1)} t_D t_F \rho_{BS}$$
(4.18)

where t_W is the window efficiency, t_{NFD} is the NIR-FIR dichroic transmission, ε_M is the mirror emissivity, N_{ML} and N_{MR} are the number of mirrors at the left and right side, respectively, OSL is the optical system level used to select the band of interest, t_D is the dichroic transmission, t_F is the filter transmission and t_{BS} and ρ_{BS} are the beam splitter transmission and reflection, respectively. For the inverted interferogram t_{BS} and ρ_{BS} need to be exchanged. Although in this current version all the transmissions of the different components are constant, the simulator accepts measured transmissions as a function of the wavelength as an input parameter. In FIInS, the OSL also defines the filter for the band of interest for the calculation of the background power.

Temperature	Transmission	Transmission to detector	Emissivity
T_{tel}	$ t_1 $	$td_{0L,R} = t_1 t_2 t_{BSM} t_{L,R}$	$\varepsilon_1 = \varepsilon_{ref}$
T_{tel}	t_2	$td_{1L,R} = t_2 t_{BSM} t_{L,R}$	$\varepsilon_2 = \varepsilon_{ref}$
T _{tel}	t_{BSM}	$td_{2L,R} = t_{BSM}t_{L,R}$	$\varepsilon_3 = \varepsilon_{BSM}$
T _{box}	$t_{L,R}$	$td_{4L,R} = 1$	$\varepsilon_5 = 1 - t_{L,R}$
	T_{tel} T_{tel} T_{tel}	T_{tel} t_1 T_{tel} t_2 T_{tel} t_{BSM}	T_{tel} t_1 $t_2 t_{BSM} t_{L,R}$ t_{tel} t_2 $t_3 t_{BSM} t_{L,R}$ $t_4 t_{tel}$ $t_5 t_{BSM}$ $t_5 t_{tel}$ $t_7 t_{tel}$ $t_8 t_7 t_{tel}$ $t_8 t_7 t_7 t_8$

Table 4.1 Transmission to the detectors for the different elements

L and R indicate the left and right side of the system

4.5.6 Background Power Module

Once the transmission of the different optical elements has been computed, the Background Power Module calculates the photon noise associated to the system from the emission of all the elements between the sky and the detector. The system is defined by four elements at different temperature stages. The primary mirror, the secondary mirror and the beam steering mirror at T_{tel} temperature, and the cold optics box or cryostat at T_{box} temperature. Both T_{tel} and T_{box} are user defined.

The first step is the computation of the transmission to the detectors td for the different elements. Again the left and right side of the system are considered. Table 4.1 shows the list of elements and their properties, where L and R indicate the path of the system.

The stray light contribution is calculated as the product of the blackbody emission from the Sun multiplied by the scattering coefficient (user defined), transmitted through the full instrument $(td_{0L,R})$.

Once the individual transmissions and emissivities are known for each element i, the background power level on detector, Q is computed.

$$Q_{i_{L,R}} = \eta_{det} \int_{\nu_{min}}^{\nu_{max}} \varepsilon_i(\nu) t d_i(\nu) A\Omega(\nu) B(T_i, \nu) d\nu$$
 (4.19)

where η_{det} is the detector efficiency, A is the collecting area and Ω is the solid angle, computed at the Beam Calculator Module for each wavenumber. ν_{min} and ν_{max} are the cut-on and cut-off wavenumbers for each band. $B(T_i, \nu)$ is the Blackbody emission at the element temperature. The total background power on the detector is the sum of the contributions of the two arms of the system

$$Q_{total} = Q_{total,L} + Q_{total,R} = \sum_{i} Q_{i_R} + \sum_{i} Q_{i_L}$$
 (4.20)

The simulator also takes into account the emission from the Cosmic Microwave Background (CMB), the Cosmic Infrared Background (CIB) and Zodiacal light (Zodi), at the respective temperatures T_{CMB} , T_{CIB} and T_{Zodi} . From internal communication, the emissivites for these three components are

$$\varepsilon_{CMB}(v) = 1 \tag{4.21}$$

$$\varepsilon_{CIB}(\lambda) = \varepsilon_{CIB} \frac{200 \times 10^{-6}}{\lambda} \tag{4.22}$$

$$\varepsilon_{Zodi}(\lambda) = \varepsilon_{Zodi} \sqrt{\frac{30 \times 10^{-6}}{\lambda}}$$
 (4.23)

The contribution from these sources is transmitted through all the elements in the system. As an example, the background power on the detectors for the CMB is

$$Q_{CMB_{L,R}} = \eta_{det} \int_{\nu_{min}}^{\nu_{max}} \varepsilon_{CMB}(\nu) t d_{0L,R} A\Omega(\nu) B(T_{CMB}, \nu) d\nu$$
 (4.24)

These calculations allow us to have an idea of the background power level at the detectors. However, to include these contributions to the simulator the Noise Equivalent Power (NEP) is calculated following Lamarre's derivations (Lamarre 1986).

$$NEP_{ph}^{2} = 2 \int h \nu Q_{\nu} d\nu + \int \frac{c^{2} Q_{\nu}^{2}}{U \nu^{2}} d\nu$$
 (4.25)

where U is the throughput. The first term on the right-hand side is the shot noise produced by a Poisson process where the detected photons are not correlated, and it dominates for most of the sources at short wavelengths (visible and near-infrared). The second term is the excess noise which dominates at radio wavelengths and is proportional to the square of Q_{ν} . For this reason, we cannot always consider the different sources contributing to Q_{ν} as statistically independent and simply add the power of the sources of noise. Rearranging Eq. 4.25, the Noise Equivalent Power for each element can be written as

$$NEP_{ph,k}^{2} = \frac{4h^{2}}{c^{2}} \int \left(1 + \varepsilon_{k}td_{k} \frac{\eta_{det}}{e^{\frac{h\nu}{k_{b}T_{k}}} - 1}\right) \left(\frac{A\Omega(\nu)\varepsilon_{k}td_{k}\eta_{det}\nu^{4}}{e^{\frac{h\nu}{k_{b}T_{k}}} - 1}\right) d\nu \qquad (4.26)$$

where k indicates the source of the noise being computed. Finally, the total background NEP (in units of W/\sqrt{Hz}) is the addition of all the contributions from the instrument plus the CMB, CIB, and Zodiacal light

$$NEP_{ph,background}^{2} = NEP_{ph,instrument}^{2} + NEP_{ph,CMB}^{2} + NEP_{ph,CIB}^{2} + NEP_{ph,Zodi}^{2}$$

$$(4.27)$$

4.5.7 Double Fourier Module

This module is the analytical module that performs the Double Fourier Modulation as the application of Fourier Transform Spectroscopy and Interferometry

simultaneously. Given the sky map SkyS a set of interferograms Ig are computed, one for each interferometric baseline b.

$$Ig(\delta, b) = I_1 + I_2 + 2\sum_{i=0}^{N_{FOV}} \sum_{j=0}^{N_{FOV}} \sum_{k=0}^{N} |SkyC(\theta_{x,i}, \theta_{y,j}; \nu_k)| \cos[2\pi \nu_k \delta - 2\pi \nu_k (\mathbf{b} \cdot \boldsymbol{\theta}) + \phi_{\mathbf{BS}}]$$
(4.28)

where $SkyC(\theta_x, \theta_y; \nu) = SkyS(\theta_x, \theta_y; \nu)Beam(\theta_x, \theta_y; \nu)td_0(\nu)$, I_1 and I_2 are the total intensity of the sky map on each of the telescope dishes, and $\mathbf{b} \cdot \boldsymbol{\theta}$ is the projection of the sky map vector (θ_x, θ_y) on the baseline vector (b_x, b_y) , this is

$$\mathbf{b} \cdot \boldsymbol{\theta} = |\mathbf{b}||\boldsymbol{\theta}| \cos[\arctan(b_{v}/b_{x}) - \arctan(\theta_{v}/\theta_{x})] \tag{4.29}$$

By observing Eq. 4.28, it can be noted that the FTS contribution and the interferometer contribution at the cosine arguments: the spectroscopic modulation is due to the term $2\pi \nu \delta$ and the interferometric delay is due to $2\pi \nu_k(\mathbf{b} \cdot \boldsymbol{\theta})$. The longer the baseline separation, the longer the delay between cosine modulations, the more separated the interferograms corresponding to different sources will appear. ϕ_{BS} is the phase delay introduced by the beam splitter which, if ideal and symmetric, is $\pi/2$ and the cosine interferograms become sine interferograms.

4.5.8 Detector Noise Module

The Detector Noise Module calculates the Noise Equivalent Power (NEP) and the 1/f noise of the selected detection system. This module is flexible and different types of detectors will require the computation of different parameters. The detector selected for further development is the Lumped Element Kinetic inductance Detector (Doyle et al. 2008), LeKID, as it presents the most promising solution high sensitivity spectro-spatial interferometry. For the current version of the simulator, a single pixel and single mode detector is assumed for simplicity and computational reasons.

4.5.8.1 Lumped Element Kinetic Inductance Detectors

Kinetic Inductance Detectors (KIDs) are the most promising candidate for future space and ground based spectroscopy at sub-millimetre wavelengths (Mazin 2009; Zmuidzinas 2012; Baselmans 2012). They provide a promising solution to the problem of producing large format arrays of ultra sensitive detectors for astronomy. Traditionally KIDs have been constructed from superconducting quarter-wave resonant elements capacitively coupled to a co-planar feed line.

The principal of operation for any KID device is to measure the change in quasiparticle population within the volume of a superconducting film upon photon absorption and is shown in Fig. 4.11. Any photon with an energy $hf > 2\Delta$, where Δ is

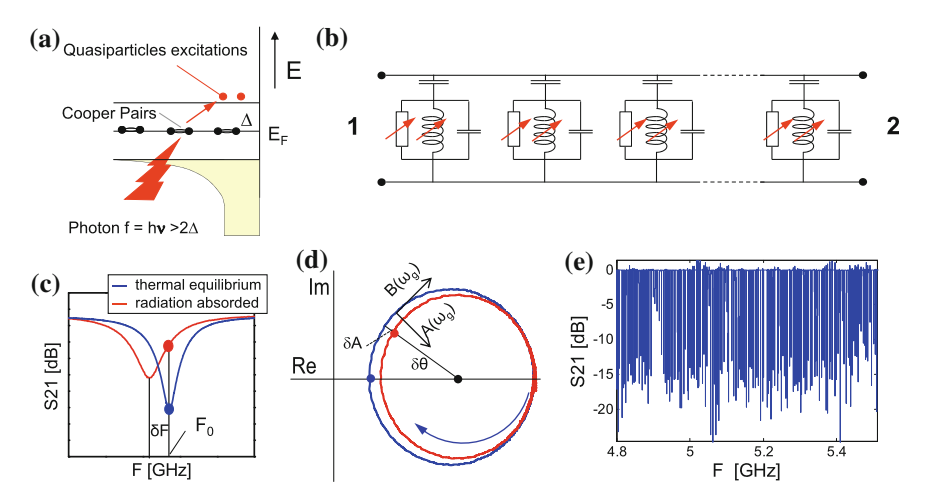


Fig. 4.11 Kinetic Inductance Detector principle of operation. An absorbed photon breaks apart a Cooper pair resulting in an excess quasi-particle population (**a**). The complex impedance of the film is altered by increasing the kinetic inductance L_k and a microwave resonance circuit is used to sense this variation (**b**). A fixed tone microwave probe signal centred on the resonant frequency changes in phase and amplitude (**c**, **d**) and is readout via a frequency comb (**e**) if an array of detectors is used. (Figure extracted from Baselmans 2012)

the energy gap of the semiconductor, if absorbed will break apart Cooper pairs (Fig. 4.11a) resulting in an excess quasi-particle population (n_{qp}) . The result of this event is to alter the complex impedance of the film by increasing the kinetic inductance (L_k) . In practice the variance in L_k with change in quasi-particle density is very small and requires the film to be fabricated into a high Q, microwave resonance circuit to sense this variation (Fig. 4.11b). In this regime the change in phase or amplitude of a fixed tone microwave probe signal centred on the resonant frequency can be monitored (Fig. 4.11c, d) and readout via a frequency comb (Fig. 4.11e) if an array of detectors is used.

Traditional KIDs arrangement requires the quasi-particles generated by photon absorption to be concentrated at positions of high current density in the resonator. This is usually achieved through antenna coupling or quasi-particle trapping. For these detectors to work at wavelengths shorter than around 500 μ m where antenna coupling can introduce a significant loss of efficiency, then a direct absorption method needs to be considered.

One way of solving the problem of optical coupling THz radiation to a KID device is to use a Lumped Element KID (LeKID), which unlike its distributed counterpart shows no current variation across the device. This means the device itself can act as the absorber as well as the sensing element in a detector system. The device is based on a series LC circuit inductively coupled to a microstrip feed line.

Regarding the optical coupling to a LeKID, simulations show (Doyle et al. 2008) that in the absence of a substrate and by tuning the thickness of the meander alone

an absorption of >50% can be achieved over a broad range of frequencies. With the presence of a substrate and ground plane behind the meander, in conjunction with a low loss anti-reflection coating, a quasi-optical analysis approach shows that the optical coupling can reach values close to 100% (more than 90% absorption is achieved in the band from 1 to 2 THz) (Doyle et al. 2007). However, for this simulation the coupling of radiation to these devices shows a strong polarization response.

For the readout of an array of KIDs, one must generate a comb of frequencies with a sine wave at the resonant frequency of each individual resonator. This comb is then sent through the device, where each detector imprints a record of its illumination on its corresponding sine wave. The comb is then amplified with a cryogenic amplifier and brought outside the cryostat. The comb is then digitised, and the phase and amplitude modulation of each individual sine wave is recovered in room temperature electronics.

As a first order approach, the responsivity of Kinetic Inductance Detectors can be considered linear (Day et al. 2006). For this reason it is not simulated in this version of FIInS, but can be implemented in future versions.

4.5.8.2 KIDs Generation-Recombination Noise

For Kinetic Inductance Detectors the fundamental noise source is the quasiparticle generation-recombination noise (Visser et al. 2012; Baselmans et al. 2008). To integrate this source of noise in the simulation, the first step is to compute the density of quasiparticles per unit volume in a superconductor in thermal equilibrium, this is

$$n_{qp} = 2N_0 \sqrt{2\pi k_B T \Delta} \exp(-\Delta/k_B T)$$
 (4.30)

valid at $k_BT < \Delta$, with N_0 the single spin density of states at the Fermi level and Δ the energy gap of the semiconductor. The number of quasiparticles is then $N_{qp} = n_{qp}V$, with V the volume of the system. Assuming a thermal distribution of quasiparticles and phonons, the average quasiparticle recombination time is given by

$$\tau_r = \frac{\tau_0}{\sqrt{\pi}} \left(\frac{k_B T_c}{2\Delta} \right)^{5/2} \sqrt{\frac{T_c}{T}} \exp(\Delta/k_B T)$$
 (4.31)

where T_c is the critical temperature of the superconductor and τ_0 a material dependent, characteristic electron-phonon interaction time.

The simulator default parameters correspond to aluminium. Figure 4.12 shows the theoretical quasiparticle lifetime or recombination time τ_r (right), and the number of quasiparticles N_{qp} (left) as a function of temperature. However, measurements show that for temperatures below 160 mK the number of quasiparticles saturates to around 30000 (300 μ m⁻³) and the quasiparticle recombination time to 2.2 ms.

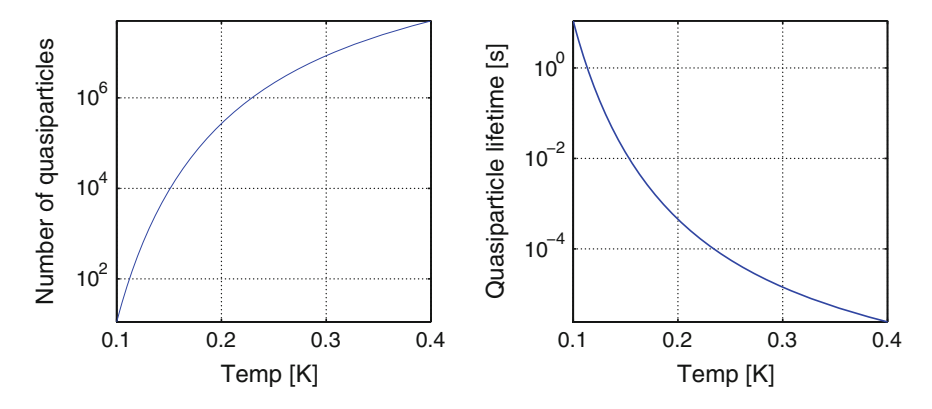


Fig. 4.12 Theoretical number of quasiparticles N_{qp} (left) and quasiparticle lifetime (right) as a function of the temperature for a KID

The power spectral density of the quasiparticle number fluctuations is

$$S_N(\omega) = \frac{4N_{qp}\tau_r}{1 + (\omega\tau_r)^2} \tag{4.32}$$

and the power spectral density due to quasiparticle number fluctuation in the resonator amplitude is given by

$$S_A(\omega) = S_N(\omega) \frac{(dA/dN_{qp})^2}{1 + (\omega \tau_{res})^2}$$
(4.33)

where $\tau_{res} = Q/(\pi f_0)$ is the resonator ringtime. The amplitude responsivity to quasiparticles, dA/dN_{qp} , is determined experimentally. Finally, the noise spectra are converted into noise equivalent power (NEP_{g-r}) through

$$NEP_{g-r}(\omega) = \sqrt{S_A} \left(\frac{\eta \tau_r}{\Delta} \frac{\delta A}{\delta N_{qp}} \right)^{-1} \sqrt{1 + \omega^2 \tau_r^2} \sqrt{1 + \omega^2 \tau_{res}^2}$$
(4.34)

where $\omega = 2\pi v$.

4.5.8.3 1/f noise

Also included in the Detector Module is the 1/f noise or pink noise. It is defined by the knee frequency, f_k , at which the noise level has increased by a factor of $\sqrt{2}$ compared to the white noise level, e_n . Figure 4.13 shows a typical 1/f noise power spectrum for different values of the knee frequency.

Although the 1/f noise is computed within the Detector Module, it is included in the simulated interferograms at the Add Noise Module along with the other sources of noise.

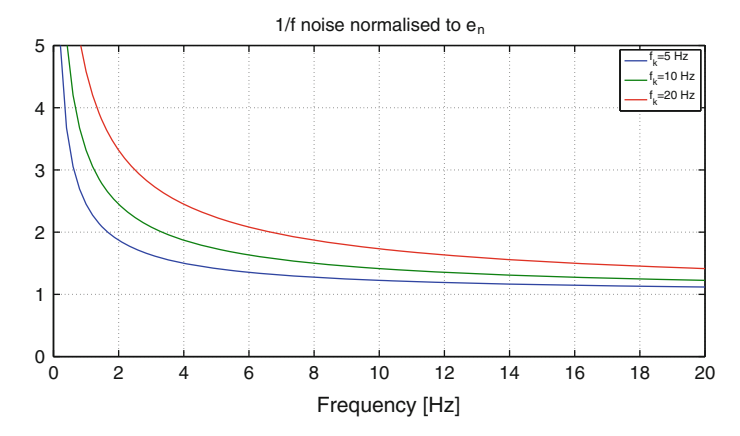


Fig. 4.13 Typical 1/f noise power spectrum for a knee frequency f_k of 5 Hz (blue), 10 Hz (green) and 20 Hz (red), normalised to the white noise level e_n

4.5.9 Add Noise Module

Once a set of interferograms $Ig(\delta, b)$ has been computed as the power incident on the detectors, the Add Noise Module determines the actual signal measured by the system, by integrating the detector response and noise to the simulated interferograms.

To add the photon noise contribution to the interferograms generated by the simulator, Ig_{raw} , the dominant term of the NEP considered is the shot noise. In this situation, photon noise follows Poisson statistics and it can be approximated by a Gaussian probability distribution. The generation-recombination contribution to the NEP is assumed to follow also Poisson statistics. The total NEP is calculated as

$$NEP_{total}^{2} = \frac{NEP_{ph,background}^{2} + NEP_{ph,sky}^{2} + NEP_{g-r}^{2}}{\eta_{det}}$$
(4.35)

In this situation, the standard deviation of the noise is $\sigma_N = NEP_{total}/\sqrt{\Delta t}$, where Δt is the time interval or the inverse of the acquisition frequency f_{acq} . The acquisition frequency is defined as $f_{acq} = 1/(n_\tau \tau)$ where n_τ is the user defined number of time constants per acquisition. This σ_N value is then multiplied by a random number generated vector, $rand(\delta)$ and added to the raw interferograms as

$$Ig_{noisy}(\delta, b) = Ig_{raw}(t, b) + \sigma_N rand(\delta)$$
 (4.36)

If the spectrometer is set to perform multiple scans (N_s , user defined parameter) for the same measurement, this process is performed N_s times.

If the Instrument Simulator is set to include 1/f noise, it is added to the simulated interferograms along with the calculated NEP, as the white noise level e_n is effectively

the standard deviation of the NEP. It is included in the simulated interferograms via a Fast Fourier transform as

$$Ig_{noisy,1/f} = Ig_{raw} + iFFT \left\{ FFT \{ \sigma_N rand(\delta) \} \left(1 + \frac{f_k}{f} \right)^{1/2} \right\}$$
(4.37)

where FFT and iFFT stand for Fast Fourier Transform and Inverse Fast Fourier Transform, respectively. A typical value of the knee frequency for KIDs detectors is $f_k = 10$ Hz (Baselmans 2011) although recent results show this value can be improved (Roesch et al. 2012).

In this module the detector efficiency η_{det} (user defined) is applied to the interferograms via multiplication, as it affects both the signal and the noise.

4.5.10 Detector Module

This module accounts for the detector response to the time constant, which is common for all kinds of detectors. A detector's time resolution is limited by its response to an instantaneous change of the input signal. In the simulator, the detected interferograms are calculated as

$$Ig_{detected}(t,b) = Ig(t,b) * e^{\frac{-t}{\tau}}$$
(4.38)

where τ is the thermal time constant of the detector (user defined), and * indicates convolution. In a real scenario, this time constant could be measured via cosmic rays for instrument calibration. Also, a more detailed MTF (Modulation Transfer Function) could be obtained during calibration phase with a variable chopper in front of a source. Figure 4.14 shows the effects of an exaggerated time constant $\tau = 50\,\mathrm{ms}$, which can be observed at the shift between the raw interferogram and the detected one. Both interferograms have been normalized to their maximum value

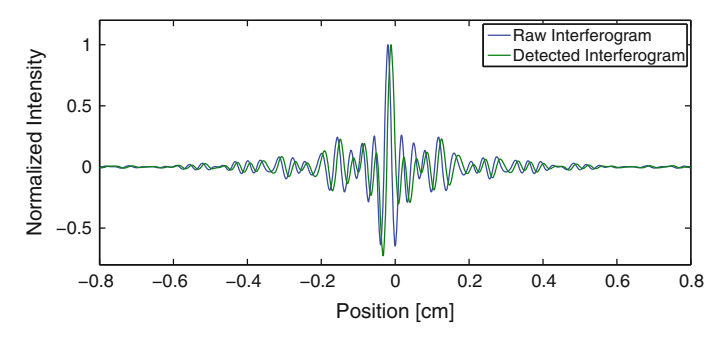


Fig. 4.14 Simulated raw interferogram (*blue*) and detected interferogram (*green*) for a detector with an exaggerated time constant of $\tau = 50 \, \text{ms}$

4.5 Instrument Model 97

to make this effect more noticeable. However, the time response of a detector also affects the detected power. In practice, the detector time constant is smaller than the time required by the delay line to move one sampling step.

4.5.10.1 Cosmic Rays

Although it has yet to be modelled in FIInS, cosmic ray strikes on the detector are relatively common and create a spike in an interferogram, and it can take several time constants for the detector to return to normal operation.

It is important to remove cosmic ray spikes from the interferograms before the data processing, because Fourier transforming an interferogram containing a cosmic ray spike will result in a high frequency sinusoidal modulation added to the recovered spectra.

4.5.11 Sampling and Readout Module

This module samples the interferometric data at the rate specified by the user, f_{acq} , this acquisition frequency being lower than the simulator frequency. Also in this module mechanical errors at the FTS drive are included, as in a real situation the sampling will not be perfect. In general, an internal metrology system can be used to mitigate the effects of imperfect motions. In this module, the starting point is the set of interferograms measured in watts and sampled at equal increments of time (or position) for each baseline and including the corresponding noise and detector effects. This module then simulates an asynchronous sampling, and by interpolation the signal is distorted to recreate a more realistic interferogram.

Finally, to facilitate data reduction and analysis each interferogram is recorded in the astronomical standard FITS (Flexible Image Transport System) format. All the data from a single FTS scan are recorded in a single FITS file, including metrology data for both the FTS drive and pointing errors. The header includes all the information needed to calculate the baseline vector.

Although the simulator is set to operate with a single pixel detector and simple ASCII files could be used to store the data, if a detector array is used this data storage format is more adequate.

4.6 Sensitivity

Once the set of interferograms has been generated a sensitivity calculation can be performed. The sensitivity ΔS of given optical system gives us information about the minimum flux density detectable in a given integration time, Δt . Assuming the signal to noise ratio, SNR, in the spectrum is the same as that in the interferogram,

and that the degradations in performance due to non-ideal effects are negligible, the Noise Equivalent Flux Density, NEFD, in units of Jy \cdot Hz^{-1/2} is defined as

$$NEFD(\nu, \Delta\nu) = \frac{2NEP_{total}}{\eta_{total}(\nu)A_{tel}\sqrt{Ntel(Ntel-1)}\Delta\nu}$$
(4.39)

where A_{tel} is the telescope area, $\Delta \nu$ is the bandwidth, N_{tel} is the number of telescopes and η_{total} is the total system efficiency, this is $\eta_{total}(\nu) = td_0(\nu)\eta_{det}$. The instrument sensitivity is then defined as

$$\Delta S = \frac{NEFD}{\sqrt{2t}} \tag{4.40}$$

where t is the integration time and the units are Jy.

4.7 Chapter Summary

In this chapter the Far-infrared Interferometer Instrument Simulator has been described as a sequence of modules comprising the sky simulator and the instrument model. The sky simulator generates the input datacube, including the corresponding photon noise, and is fed to the instrument model. The instrument model can operate as an ideal instrument or a more realistic one if the control flags are activated. It is in the instrument model that the Double Fourier Modulation is performed and the interferograms are generated, and physical quantities such as different sources of noise are modelled. The output of the system is a set of FITS files containing the interferograms to be processed. FIInS allows the user to output not only the set of interferograms, also independent outputs as *uv*-maps or transmission profiles are available. Once the interferograms are stored, they are sent to the data reduction and analysis modules, described in the next chapter. Also in Chap. 5 the simulator is verified using the knowledge acquired with the Cardiff-UCL FIRI Testbed. Once the simulator is verified, a more detailed example of its capabilities is described in Chap. 6.

References

- J.J.A. Baselmans, Background limited antenna coupled mkid arrays for ground based imaging, in 4th Workshop on the Physics and Applications of Superconducting Microresonators, Grenoble, France, July 2011
- J. Baselmans, Kinetic inductance detectors. J. Low Temp. Phys. 167(3-4), 292–304 (2012). ISSN 0022-2291. doi:10.1007/s10909-011-0448-8
- J. Baselmans, S.J.C. Yates, R. Barends, Y.J.Y. Lankwarden, J.R. Gao, H. Hoevers, T.M. Klapwijk. Noise and sensitivity of aluminum kinetic inductance detectors for sub-mm astronomy. J. Low Temp. Phys. 151(1–2), 524–529 (2008). ISSN 0022-2291. doi:10.1007/s10909-007-9684-3

- R.W. Boyd, Photon bunching and the photon-noise-limited performance of infrared detectors. Infrared Phys. **22**(3), 157–162 (1982). ISSN 0020-0891. doi:10.1016/0020-0891(82)90034-3. http://www.sciencedirect.com/science/article/pii/0020089182900343
- P.K. Day, H.G. Leduc, A. Goldin, T. Vayonakis, B.A. Mazin, S. Kumar, J. Gao, J. Zmuidzinas, Antenna-coupled microwave kinetic inductance detectors. Nuclear Instrum. Methods Phys. Res. Sect. A 559(2), 561–563 (2006). ISSN 0168-9002. doi:10.1016/j.nima.2005.12.057. http://www.sciencedirect.com/science/article/pii/S0168900205024824. Proceedings of the 11th International Workshop on Low Temperature Detectors, 11th International Workshop on Low Temperature Detectors
- S. Doyle, J. Naylon, P. Mauskopf, A. Porch, C. Dunscombe. Lumped Element Kinetic Inductance Detectors, ed. by A. Karpov. Eighteenth International Symposium on Space Terahertz Technology, p. 170 (2007)
- S. Doyle, P. Mauskopf, J. Naylon, A. Porch, C. Duncombe, Lumped element kinetic inductance detectors. J. Low Temp. Phys. 151(1–2), 530–536 (2008). ISSN 0022-2291. doi:10.1007/s10909-007-9685-2
- ESA Concurrent Design Facility. Far Infrared Interferometer—CDF Study Report. CDF-49(A), 1–294 (2006). http://sci.esa.int/future-missions-office/40738-firi-cdf-study-report/
- J. Fischer, T. Klaassen, N. Hovenier, G. Jakob, A. Poglitsch, O. Sternberg, Cryogenic far-infrared laser absorptivity measurements of the herschel space observatory telescope mirror coatings. Appl. Opt. 43(19), 3765–3771 (2004). doi:10.1364/AO.43.003765. http://ao.osa.org/abstract.cfm?URI=ao-43-19-3765
- J.M. Lamarre, Photon noise in photometric instruments at far-infrared and submillimeter wavelengths. Appl. Opt. 25(6), 870–876 (1986). doi:10.1364/AO.25.000870. http://ao.osa.org/abstract.cfm?URI=ao-25-6-870
- B.A. Mazin, Microwave Kinetic Inductance Detectors: The First Decade, eds. by B. Young, B. Cabrera, A. Miller. *American Institute of Physics Conference Series*, volume 1185 of American Institute of Physics Conference Series, pp. 135–142 (2009). doi:10.1063/1.3292300
- G.L. Pilbratt, J.R. Riedinger, T. Passvogel, G. Crone, D. Doyle, U. Gageur, A.M. Heras, C. Jewell, L. Metcalfe, S. Ott, M. Schmidt, Herschel space observatory. Astron. Astrophys. 518, L1 (2010). doi:10.1051/0004-6361/201014759
- M. Roesch, A. Benoit, A. Bideaud, N. Boudou, M. Calvo, A. Cruciani, S. Doyle, H.G. Leduc, A. Monfardini, L. Swenson, S. Leclercq, P. Mauskopf, K.F. Schuster, for the NIKA collaboration. Development of Lumped Element Kinetic Inductance Detectors for NIKA. ArXiv e-prints, December 2012
- P.J. Visser, J.J.A. Baselmans, P. Diener, S.J.C. Yates, A. Endo, T.M. Klapwijk. Generation-recombination noise: The fundamental sensitivity limit for kinetic inductance detectors. J. Low Temp. Phys. 167(3–4), 335–340 (2012). ISSN 0022-2291. doi:10.1007/s10909-012-0519-5
- M.E. Wilson, D. Leisawitz, A.J. Martino, S. Rinehart, J. Crooke, J. Tveekrem, J. Budinoff, T. Hyde, The space infrared interferometric telescope (spirit): optical system design considerations. vol. 6687, pp. 66870B–66870B–11 (2007). doi:10.1117/12.738562
- J. Zmuidzinas, Superconducting microresonators: physics and applications. Ann. Rev. Condens Matter Phys. 3(1), 169–214 (2012). doi:10.1146/annurev-conmatphys-020911-125022. http://www.annualreviews.org/doi/abs/10.1146/annurev-conmatphys-020911-125022

Chapter 5 FIInS Data Processing and Verification

In this chapter the Data Processing of spectro-spatial data is presented, as well as the instrument simulator verification via the Cardiff University-UCL FIRI testbed.

In Sect. 5.1 the process that converts the recorded interferograms to the 'dirty' data cube is described through a master simulation, and possibilities for the correction of the instrumental artifacts are shown. In Sect. 5.3 the validation of FIInS is presented following the description of the FIRI testbed shown in Chap. 3. In this case, a one dimensional analysis is given.

5.1 Datacube Reconstruction from Detected Interferograms

The output of the instrument simulator FIInS is a set of FITS files where the interferograms corresponding to each baseline and to each FTS scan are stored for a given input sky datacube, Sky_{in} . These FITS files also include the metrology data for the FTS drive and pointing of the telescope, as well as all the information needed to calculate the baseline vector.

Once the data has been loaded, if noise has been selected to be included in the simulation, the first step will be the noise reduction to increase the dynamic range (DR) and the signal to noise ratio (SNR). Next the reconstruction of the dirty datacube is achieved by extracting the spectral and spatial properties detailed below. To illustrate the data reduction process a master sky map is used.

The Master Sky Map

To run a FIInS simulation the first step is to select the instrument parameters which define the size of the sky grid. For a pseudo-realistic simulation, the baseline range

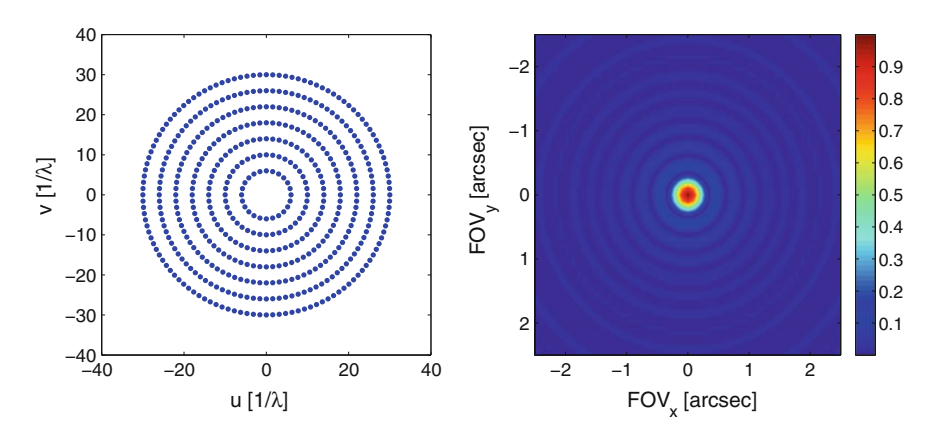


Fig. 5.1 uv-map coverage for a Fixed Arc Length baseline configuration ranging from 6 to 30 m, with a baseline step of 4 m (*left*). Fourier transform of the uv-map coverage at $v = 118 \text{ cm}^{-1}$ (right)

is set from $b_{min} = 6 \text{ m}$ to $b_{max} = 30 \text{ m}$, with a $b_{step} = 4 \text{ m}$ and a fixed arc length configuration. The uv-map normalised to the wavelength is shown in Fig. 5.1 (left). The telescope size is set to $D_{tel} = 3 \text{ m}$. These parameters could be the ones for a boombased interferometer, providing the physical space for the central hub. Figure 5.1 (right) shows the Fourier transform of the uv-map for a wavenumber $v = 118 \text{ cm}^{-1}$.

The instrument parameters define the beam size. Setting up the spectrograph to work in the 25–400 μ m range (400–25 cm⁻¹), the minimum beam size is $\Delta\theta_{tel}=2.097$ arcsec and the spatial angular resolution $\Delta\theta_{int}=0.086$ arcsec. To prove the principles of interferometry, the astronomical sources on the sky grid must be positioned inside the beam.

Three different types of sources are positioned in the sky grid: a point source, a gaussian source and an elliptical source, as shown in Fig. 5.2 (left).

Spectrally, the gaussian source is a blackbody with a brightness temperature of $100 \,\mathrm{K}$ and an emission line at $60 \,\mathrm{cm}^{-1}$. The point source corresponds to a blackbody at $2000 \,\mathrm{K}$, and the elliptical source is a blackbody at $50 \,\mathrm{K}$ and an absorption line at $80 \,\mathrm{cm}^{-1}$. The spectra of the three sources is shown in Fig. 5.2 (right).

The elliptical source could correspond to a circumstellar disk with an envelope size of \sim 200 AU at \sim 150 pc. The gaussian source can also be a circumstellar disk of \sim 80 AU at \sim 300 pc but with a different orientation with respect to the observer plane. The point source can be considered a protostar at \sim 50 pc and with a radius \sim R_{Sun} . As the point source size is smaller than the pixel size on the sky grid, an emissivity parameter ε has to be introduced, this is

$$\varepsilon = \frac{\Omega_{point}}{\Omega_{pixel}} \tag{5.1}$$

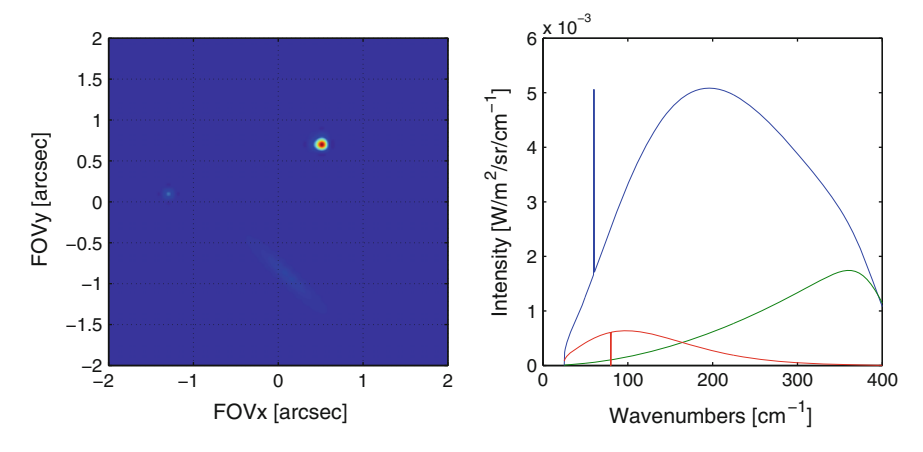


Fig. 5.2 The Master sky map. A gaussian source, a point source and an elliptical source are positioned on the sky grid (*left*). Spectrally (*right*) the gaussian source is a blackbody with a brightness temperature of $100 \, \text{K}$ and an emission line at $60 \, \text{cm}^{-1}$ (*blue*); the point source corresponds to a blackbody at $2000 \, \text{K}$ (*green*), and the elliptical source is a blackbody at $50 \, \text{K}$ and an absorption line at $80 \, \text{cm}^{-1}$ (*red*)

where Ω_{point} is the point source solid angle and Ω_{pixel} is the pixel solid angle. With the current configuration and with the defined astronomical distances, for this simulation $\varepsilon \simeq 10^{-3}$.

5.1.1 Noise Reduction and Time Domain Interpolation

To improve the dynamic range (DR) achievable in an interferogram, signal-averaging techniques must be used. The dynamic range is defined as

$$DR = \frac{S_{pp}}{N_{rms}} \tag{5.2}$$

where S_{pp} is the peak to peak power of the signal at the zero path difference, and N_{rms} is the root-mean-square value of the noise, computed as

$$N_{rms} = \sqrt{\frac{1}{n} \sum_{i=1}^{n} [N(\delta_i)]^2}$$
 (5.3)

where n is the number of samples.

Given the number of scans N_{scans} for a given baseline and assuming that the signal and noise are uncorrelated, by averaging them the DR is increased by $\sqrt{N_{scans}}$.

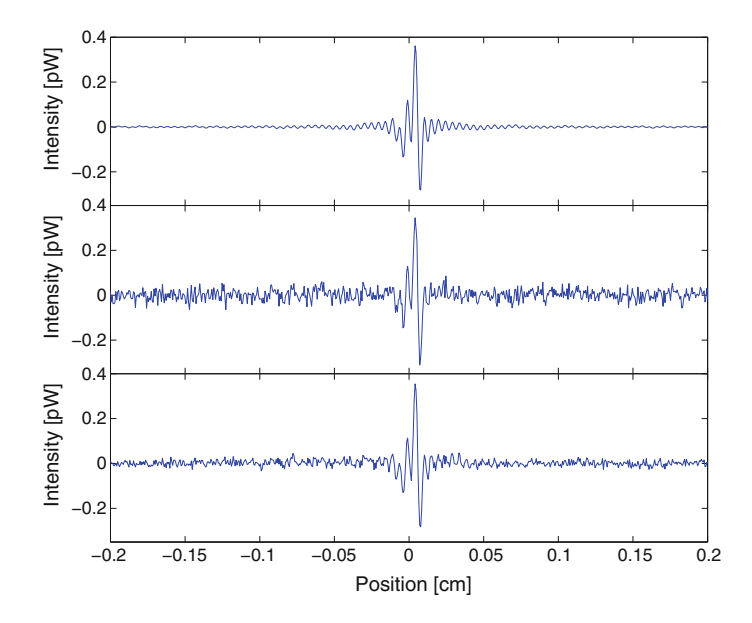


Fig. 5.3 Interferograms generated by FIInS for the Master simulation with a baseline length of 18 m: the raw or ideal interferogram Ig_{raw} (top), the noisy interferogram Ig_{noisy} (centre) and the averaged interferogram $Ig_{noisy,av}$ (bottom)

Figure 5.3 shows interferograms generated by FIInS for the Master simulation with a baseline length of 18 m: the raw or ideal interferogram Ig_{raw} (top), the noisy interferogram Ig_{noisy} (centre) which is the result of the addition of the instrumental, background and detector noise, and the averaged interferogram $Ig_{noisy,av}$ (bottom) for 4 scans at the given baseline. For this simulation, the calculated dynamic ranges are $DR_{noisy} = 32.2$ and $DR_{noisy,av} = 62.6$ for 4 scans, which is consistent with the expected increase in DR by a factor of 2.

The signal to noise ratio (SNR) can be calculated at the spectral domain after the image synthesis as

$$SNR = \frac{S}{N} = \frac{S\sqrt{\Delta t}}{NEP}$$
 (5.4)

where S is the detected power and Δt is the time interval (described in Sect. 4.5.9). If the interferograms have been distorted due to errors in the FTS drive, at this point it is necessary to interpolate the interferograms to a continuous optical delay line. Figure 5.4 shows the effects of errors in the velocity of the drive (bottom) and the ideal interferogram (top) for the previous simulation. A disproportionate velocity error of 30% has been applied to increase the visual effect. It can be observed that the sampling points are not equidistant, which without correction will alter the detected spectrum.

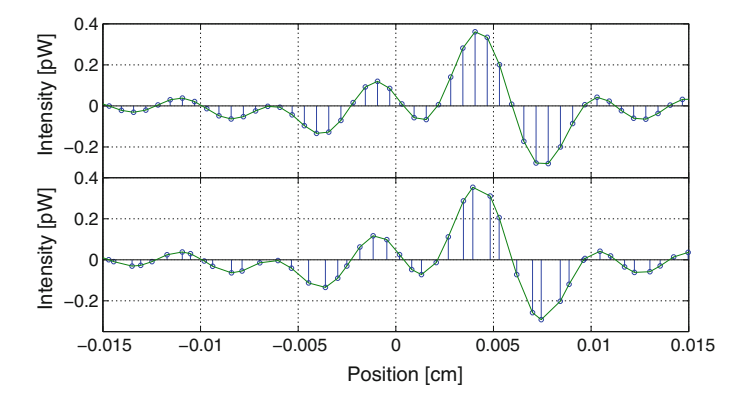


Fig. 5.4 Effect of errors in the velocity of the drive (*bottom*) and the ideal interferogram (*top*) for the Master simulation

5.1.2 Extracting the Spectra

Once the interferograms have been preprocessed to reduce the noise and the distortions, one can proceed to the extraction of the spectra. In order to avoid aliasing, the spectral band of operation of the detectors is set from 25 to $212\,\mathrm{cm}^{-1}$.

The first step is to perform the Inverse Fourier Transform. Given the set of interferograms $Ig(\delta, b)$ the 'dirty' spectra Sp is extracted for each baseline as

$$Sp(v, b_j) = \sum_{i}^{N} Ig(\delta_i, b_j) \exp(-i2\pi v \delta_i) d\delta$$
 (5.5)

where ν is the wavenumber vector and b_j indicates a given baseline position. The result of this operation is a set of spectra corresponding to the source spectra modulated by a cosine. This cosine is dependent on the baseline of interest.

Figure 5.5 shows the recovered spectra for 3 baselines, $22 \,\mathrm{m}$ (left), $26 \,\mathrm{m}$ (centre) and $30 \,\mathrm{m}$ (right), with an orientation of $\sim 40^{\circ}$. The selection of the orientation is because at this position the interferometer 'sees' 2 sources, as the elliptical source and the point source have the same position with respect to the projected baseline on the sky (see Fig. 5.2 (left)). For this reason, the modulation introduced by the baseline position has a cosine shape as for the binary system shown in Sect. 2.2.2. It can be observed that the longer the baseline, the higher the frequency of the cosine modulation, as expected.

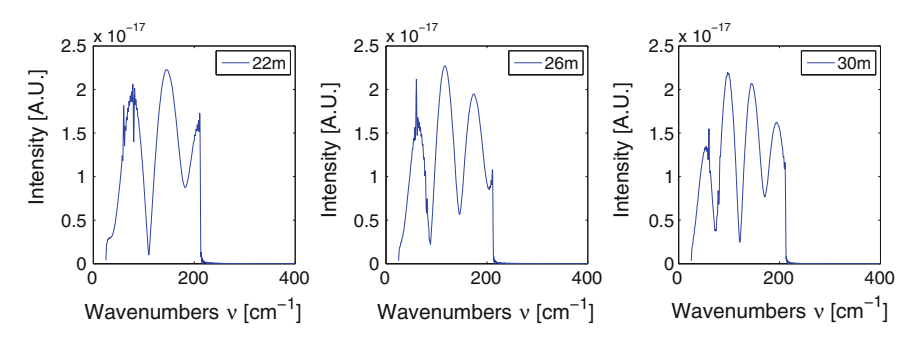


Fig. 5.5 Recovered spectra for the Master sky map for a 22 m baseline (*left*), a 26 m baseline (*centre*) and 30 m baseline (*right*), with an orientation of \sim 40° (with respect to the axis FOV_y = 0, anticlockwise)

5.1.3 Interferometric Image Synthesis: The Dirty Data Cube

The next step is the extraction of the spatial features of Sp, this is the dirty datacube, Sky_d . To extract the spatial features one has to perform the 2-dimensional Fourier Transform of the uv-map. Combining each baseline position b_j and each wavenumber v_k the dirty datacube is calculated as

$$SkyA_{s}(\theta_{x}, \theta_{y}; \nu_{k}) = \sum_{j=1}^{N_{b}} |Re\{Sp(\nu_{k}, b_{j})\}\cos(2\pi(u_{j,k}\theta_{x} + \nu_{j,k}\theta_{y})) - Im\{Sp(\nu_{k}, b_{j})\}\sin(2\pi(u_{j,k}\theta_{x} + \nu_{j,k}\theta_{y}))|$$
 (5.6)

where $u_{j,k} = b_{x,j} v_k$ and $v_{j,k} = b_{y,j} v_k$ are the spatial frequencies. In this operation the previous knowledge of the sky grid (θ_x, θ_y) has to be used. If pointing errors have been included in the simulation, the sky grid is modified accordingly for each baseline position.

Figure 5.6 (top row) shows three spatial layers of the dirty data cube for the Master simulation, corresponding to the minimum wavenumber $(25\,\mathrm{cm^{-1}}, \mathrm{left})$, central wavenumber $(118\,\mathrm{cm^{-1}}, \mathrm{centre})$ and maximum wavenumber $(212\,\mathrm{cm^{-1}}, \mathrm{right})$, and the telescope beam for each of these wavenumbers is displayed on the bottom row. Outside the area corresponding to the central lobe of the telescope beam, the dirty data cube presents some modulations due to the discrete data processing and should not be taken into account. It can be observed that the spatial size of the sources is not the same for the three wavenumbers, which is due to the fact that the interferometric beam is wavelength-dependent and must be corrected. This beam is also responsible for the ripples present in the dirty data cube, as it presents a sinc-like shape. This interferometric beam is the so-called *dirty beam* which is shown in Fig. 5.1 (right), and it is the 2-dimensional Fourier transform of the *uv*-map sampling function Fig. 5.1 (left).

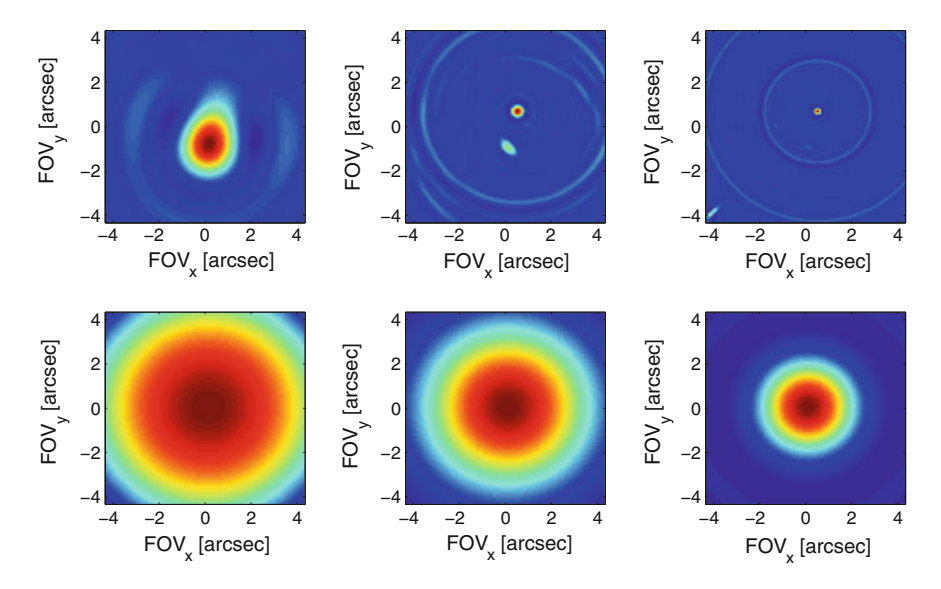


Fig. 5.6 Spatial layers of the dirty data cube for the Master simulation, corresponding to the minimum wavenumber (25 cm⁻¹, *left*), central wavenumber (118 cm⁻¹, *centre*) and maximum wavenumber (212 cm⁻¹, *right*) (*top*). Telescope beam for each of these wavenumbers (*bottom*)

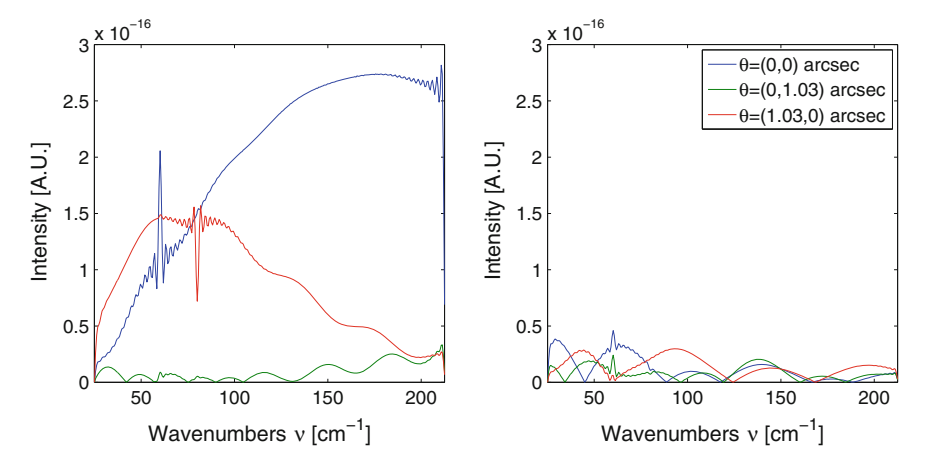


Fig. 5.7 Spectral results of the Master simulation for the central pixel of the gaussian source (*blue*), the point source (*green*) and the central pixel elliptical source (*red*) (*left*). Detected spectra for three positions in the sky where no source intensity is expected (*right*)

The spectral results of the simulation are shown in Fig. 5.7 (left) for the central pixel of the gaussian source (blue), the point source (green) and the central pixel of the elliptical source (red). It can be observed that the emission and absorption line positions are detected but present a sinc-shape: this is due to the boxcar function

that defines the scanning of the FTS. Comparing with the input spectra (see Fig. 5.2 (right)) one expects the power of the gaussian source to be higher than the power of the elliptical source for the full spectral range, but this differs from the results. The reason is that the spatial size of the dirty beam at lower frequencies or wavenumbers is bigger than the source separation on the sky and there is a transfer of power from source to source. Also, as the spatial size of the elliptical source is bigger than the gaussian source, there is more power at the spatial position of the elliptical source because of the fact that the detected dirty data cube is the result of the convolution of the sky map with the dirty beam.

Also present in the detected spectra is a modulation clearly noticeable for the point source (green). For comparison, Fig. 5.7 (right) shows the detected spectra for three positions in the sky, where a similar modulation appears. Again, this is due to the dirty beam, which is wavelength dependent: as the frequency (or wavenumber) increases, the dirty beam narrows and so do the side lobes. By selecting a spatial position and increasing the frequency, the variation of size of the dirty beam causes a spectral modulation.

Although for a binary system it is easy to model and correct this fact, when the number of sources increases or when extended sources are present on the sky, the correction of the modulation is not straightforward because in each spatial position there is the contribution of the dirty beam generated by each source present on the sky. For this reason, more complex data synthesis algorithms are required.

By integrating the dirty data cube over wavenumber one can extract the spatial features of the sky, because the dirty beam ripples at different frequencies or wavenumbers cancel and hence the ratio between the power of the central lobe and the secondary lobe increases. However, this is only useful if the sources on the sky have similar size and power.

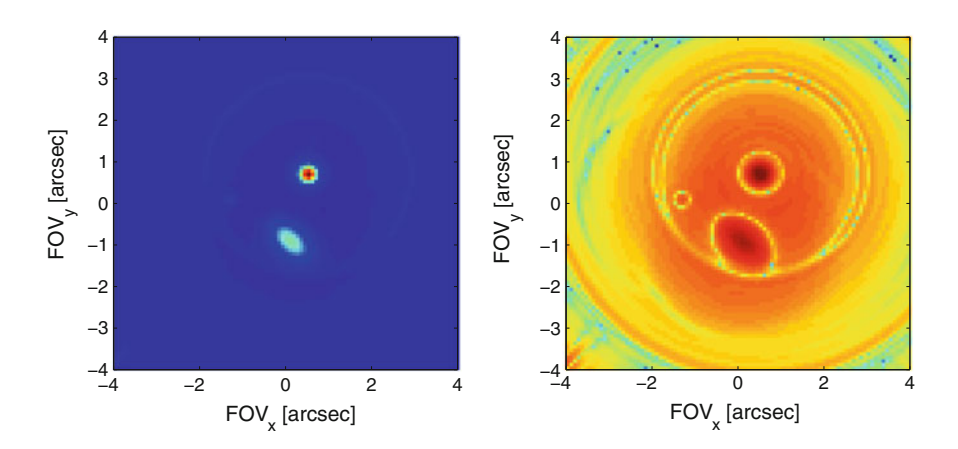


Fig. 5.8 Result of the wavenumber integration (left) and its logarithm (right)

Figure 5.8 (left) shows the result of the wavenumber integration. It can be observed that the spatial features for the gaussian source and the elliptical source are recovered, but the point source is difficult to detect because the integrated power is much lower than that for the elliptical or gaussian source. Figure 5.8 (right) shows the logarithmic version of the wavenumber integration. In this case, the positions of the three sources are recovered. The location of the sources on the sky can be useful for forward data processing.

5.2 Data Synthesis Algorithms

In this section forward processing of the dirty datacube Sky_s is presented. First, a blind deconvolution algorithm commonly used in image deblurring is applied to the datacube, where no knowledge or little knowledge of the instrument beam is assumed. Secondly, the CLEAN algorithm widely used in radio interferometry synthesis is modified for Double Fourier Modulation.

5.2.1 Blind Deconvolution

In image processing, blind deconvolution is a technique used to correct blurred images when the system Point Spread Function (PSF) is unknown or poorly known. The PSF is then estimated from the image. This technique has been used for decades (Ayers and Dainty 1988; Levin et al. 2009) and in this section a blind deconvolution iterative algorithm is applied to spectro-spatial data to study its applicability.

The blind deconvolution algorithm used here is the one integrated in MATLAB®, more specifically the Damped Richardson-Lucy method (Lucy 1974; Richardson 1972; White 1994). This algorithm restores both the image and the PSF simultaneously by deconvolving the image using the maximum likelihood algorithm. One can input system characteristics to define the PSF, in this case this is the Full-Width Half-Maximum (FWHM) of the interferometric dirty beam. Another input parameter is the number of iterations, and for the current Master simulation it is set to 1, 2 and 5 iterations.

To apply this algorithm to the dirty datacube one has to loop along the wavenumber dimension. For each wavenumber or dirty datacube layer, a deblurred version of the layer is recovered as well as the corresponding PSF. The blind deconvolution algorithm has been applied to the Master simulation dirty datacube and as an example the results for 1 iteration are shown in Fig. 5.9, for 2 iterations in Fig. 5.10 and for 5 iterations in Fig. 5.11. In the top row of each of these figures the synthesised datacube layer corresponding to the minimum wavenumber (25 cm⁻¹, left), central wavenumber (118 cm⁻¹, centre) and maximum wavenumber (212 cm⁻¹, right) is presented. The bottom row corresponds to the restored PSF at each of the previous wavenumbers.

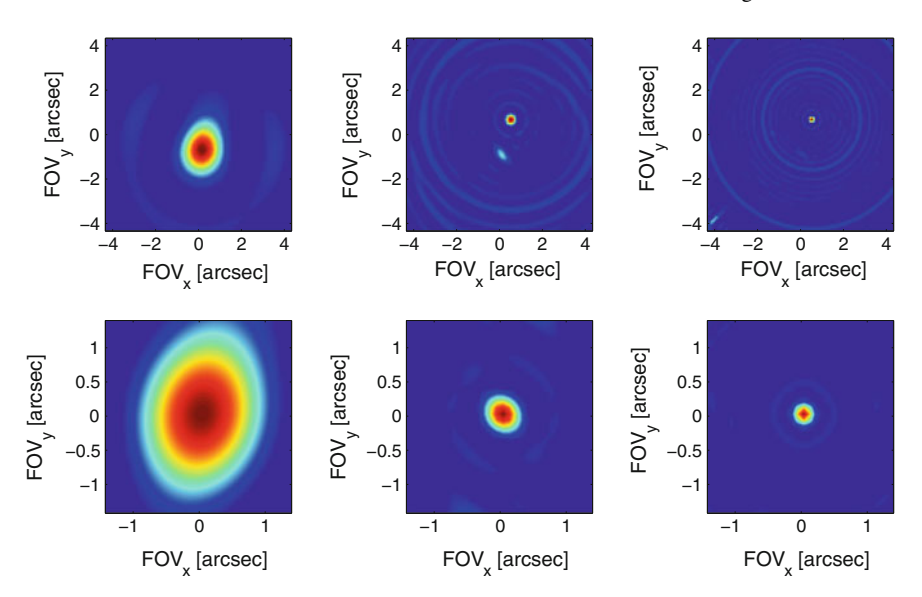


Fig. 5.9 Synthesised datacube layer after 1 iteration of the blind deconvolution algorithm for the minimum wavenumber (25 cm⁻¹, *left*), central wavenumber (118 cm⁻¹, *centre*) and maximum wavenumber (212 cm⁻¹, *right*) (*top*). Restored PSF at each of the previous wavenumbers (*bottom*)

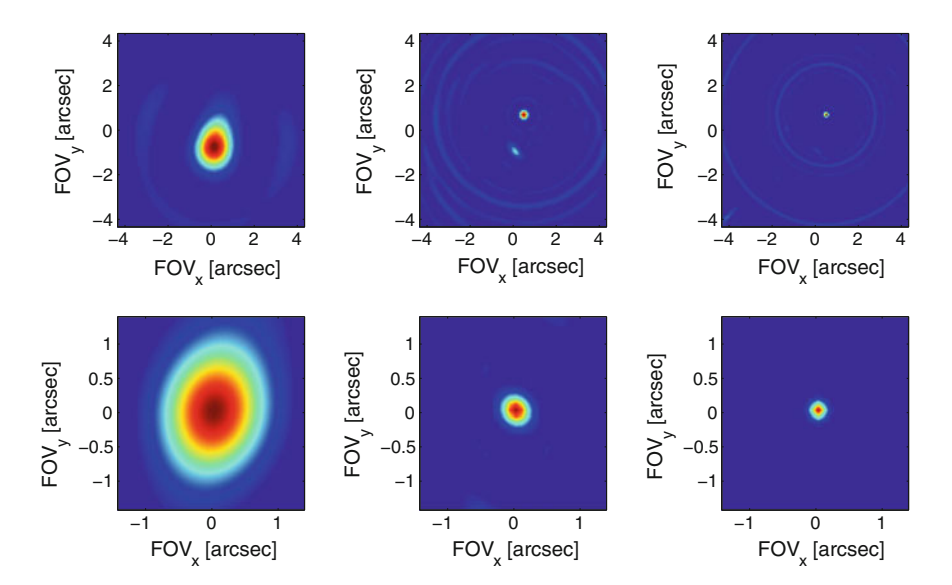


Fig. 5.10 Synthesised datacube layer after 2 iterations of the blind deconvolution algorithm for the minimum wavenumber ($25 \,\mathrm{cm}^{-1}$, left), central wavenumber ($118 \,\mathrm{cm}^{-1}$, centre) and maximum wavenumber ($212 \,\mathrm{cm}^{-1}$, right) (top). Restored PSF at each of the previous wavenumbers (bottom)

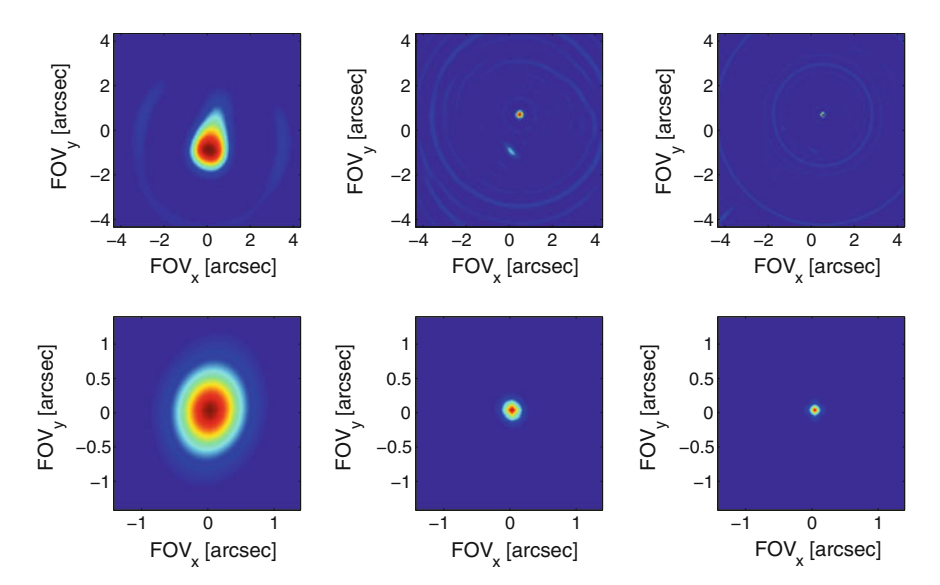


Fig. 5.11 Synthesised datacube layer after 5 iterations of the blind deconvolution algorithm for the minimum wavenumber $(25\,\mathrm{cm}^{-1}, left)$, central wavenumber $(118\,\mathrm{cm}^{-1}, centre)$ and maximum wavenumber $(212\,\mathrm{cm}^{-1}, right)$ (top). Restored PSF at each of the previous wavenumbers (bottom)

In the case of one iteration of the blind deconvolution algorithm (Fig. 5.9) it can be observed that around the sources the background level has decreased slightly and hence the contrast has been increased. The detected PSF size is comparable to the theoretically expected, this is λ/b_{max} and the spatial size of the sources has slightly decreased compared to the dirty image (Fig. 5.6 top row). However, although the PSF includes some of the ripples expected from the dirty beam these ripples have not been removed in the deconvolution itself.

For a 2-iteration blind deconvolution, the results do not improve. Although the PSF beam size is still consistent with the one expected from theory, the ripples have vanished from the PSF and are still present in the recovered datacube. The spatial size of the gaussian source approximates to a point source for the maximum wavenumber image (right) and does not correspond to the expected spatial size.

When 5 blind deconvolution iterations are applied to the dirty data cube, the beam size does not correspond to the one expected from theory anymore, from which one can infer that the recovered datacube is unrealistic.

Spectrally, applying a blind deconvolution algorithm does not improve the recovery of the sources spectra. Figure 5.12 (left) shows the spectra for the central spatial point for each of the sources on the sky. The presence of ripples indicates that there are still instrument systematics in the recovered datacube. Also, the spectral power for the point source (green) appears to be reduced, because this kind of algorithm has been developed to account for non uniform image quality (e.g. bad pixels) and a point source can be considered as such. In Fig. 5.12 (right) the detected spectra for

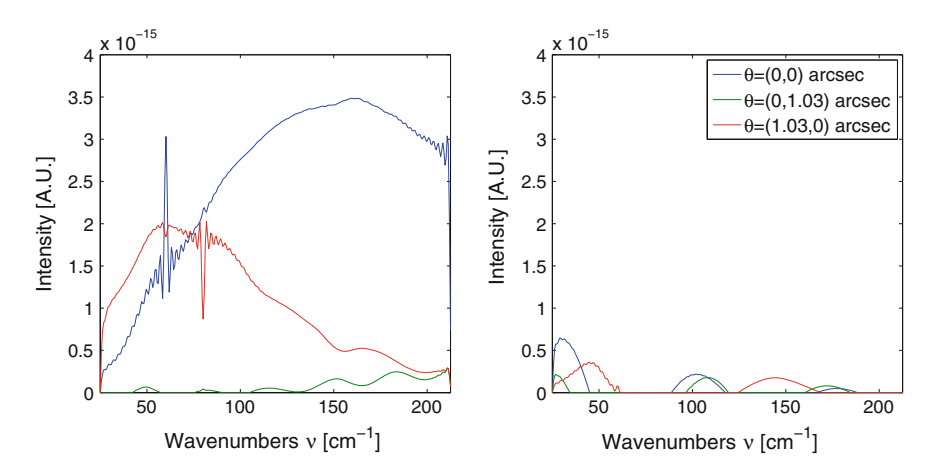


Fig. 5.12 Spectral results of the Master simulation after 1 iteration of the blind deconvolution algorithm for the central pixel of the gaussian source (*blue*), the point source (*green*) and the central pixel elliptical source (*red*) (*left*). Detected spectra for three positions in the sky where no source intensity is expected (*right*)

three positions in the sky where no power is expected is shown. The zero power (i.e. red curve from approximately $60-120\,\mathrm{cm}^{-1}$) is due to a positivity constrain of the blind deconvolution algorithm, for which negative values are considered 0.

In conclusion, a blind deconvolution algorithm is not suitable for DFM dirty datacubes because for a proper restoration, more information regarding the dirty beam has to be applied. As the information of the dirty beam can be extracted from the known *uv*-map, previous knowledge of the dirty beam can be used. One algorithm that makes use of a known dirty beam is the interferometric CLEAN algorithm.

5.2.2 Interferometic CLEAN Algorithm

The CLEAN algorithm (Högbom 1974) is essentially a brute force deconvolution. The starting point is the fact that the measured dirty image $I_D(\theta_x, \theta_y)$ is the convolution of the true intensity or sky map $I(\theta_x, \theta_y)$ with the dirty beam $B(\theta_x, \theta_y)$, this is

$$I_D(\theta_x, \theta_y) = I(\theta_x, \theta_y) * B(\theta_x, \theta_y)$$
(5.7)

Although working in the Fourier domain seems like an option to recover the sky map by dividing the Fourier transfer of $I_D(\theta_x, \theta_y)$ by the Fourier transform of $B(\theta_x, \theta_y)$ which is the uv-map, in practice the Fourier transform of $B(\theta_x, \theta_y)$ contains areas where it is zero and thus this is not an option (Thompson et al. 1986). The problem arises from the fact that the uv-map is sparse.

Interpolating the uv-map can also arbitrarily generate information which is not present in the initial sky map. Basically, one wants the visibility at non-sampled uv-map positions to take values consistent with the most reasonable or likely intensity distribution while minimising the addition of arbitrary detail.

The CLEAN algorithm is vastly used and is one of the most successful iterative deconvolution algorithms which attempts to obtain an image compatible with the data assuming it is made of point-like sources.

It works as follows: given the dirty image, the location of the brightest source is searched and the response to a point source, this is the dirty beam, is subtracted from the dirty image and the intensity and position subtracted are recorded. This procedure is repeated for the new residual dirty image which is searched for evidence of another point-like source. The number of iterations is user defined, the aim being to stop when the noise level is reached. Finally, the image created from the recorded positions and intensities is convolved with the *clean beam* (usually a Gaussian shaped PSF) to have a resolution in agreement with the extension of the *uv*-map coverage, this is, a beam of the same dimensions as the central lobe of the dirty beam.

CLEAN is aimed for point sources or compact sources. However, once the point sources from a dirty beam have been removed, the residual dirty image is essentially due to the extended sources which may be smooth enough to not be too distorted by the convolution with the dirty beam. For this reason, the residual dirty image can be added to the clean image to create the final image.

5.2.2.1 The Dirty Beam

As presented before, the dirty beam is the Fourier transform of the uv-map coverage function. For the Master simulation, the dirty beam and the uv-map coverage function were shown in Fig. 5.1 (right) and (left), respectively, for a given wavenumber. The number of uv-map points is 256.

For Double Fourier Modulation, the reality is that there is a scaled version of the dirty beam for each wavenumber, increasing the overall *uv*-coverage. Figure 5.13 shows the spatial coverage of the Master simulation as an addition of individual wavenumbers covered. It can be observed that the *uv*-coverage is increased, hence the spatial restoration as an integration over wavenumber as presented earlier in this chapter is suitable given the object's shape is achromatic with regards to the wavelength.

The problem of ground based interferometry is that although the *uv*-coverage can be increased by making use of the Earth rotation, the fixed position of the antennas will always limit the performance capabilities of such a system. This will not be a problem for space based interferometry, because even if operating a boom-based interferometer one will have the freedom to move the full spacecraft and sample the *uv*-map according to the target requirements.

Every *uv*-map has its own dirty beam, according to the position of the telescopes. As presented in Chap. 4, different baselines configurations are available in FIInS.

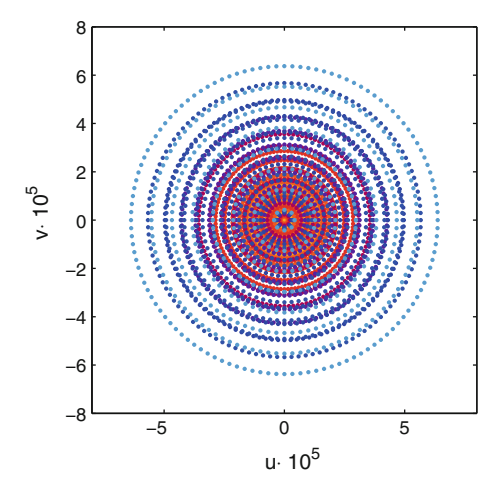


Fig. 5.13 *uv*-map coverage for a Fixed Arc Length baselines configuration for a range of wavelengths (from *red*, long wavelength, to *blue*, short wavelength)

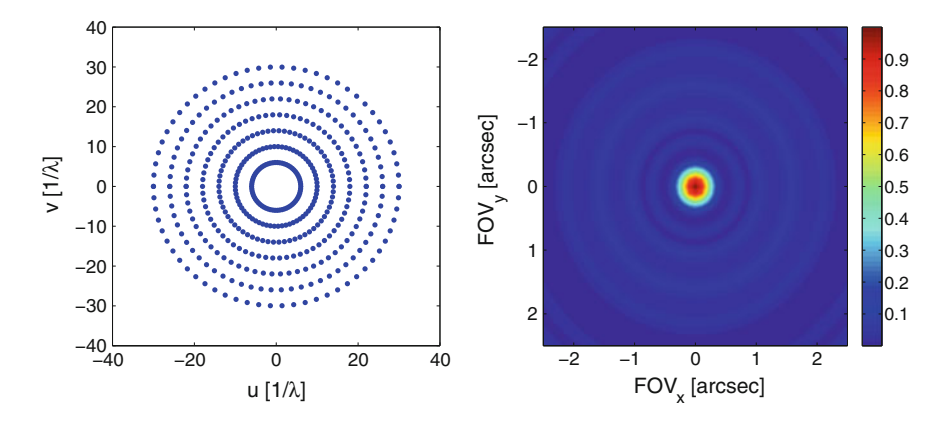


Fig. 5.14 *uv*-map coverage for a Fixed Angle baselines configuration (*left*) and the corresponding normalised dirty beam (*right*)

Figure 5.14 shows the *uv*-map converge for a Fixed Angle baselines configuration (left). The number of baselines is 238, thus of the order of the Fixed Arc Length configuration. The baseline parameters remain unchanged with respect to the Fixed Arc Length configuration. Looking at the normalised dirty beam (right) it can be appreciated that although the size of the central lobe is maintained because it is defined by the maximum baseline, the width of the other lobes (or the position of the function zeroes) has been increased.

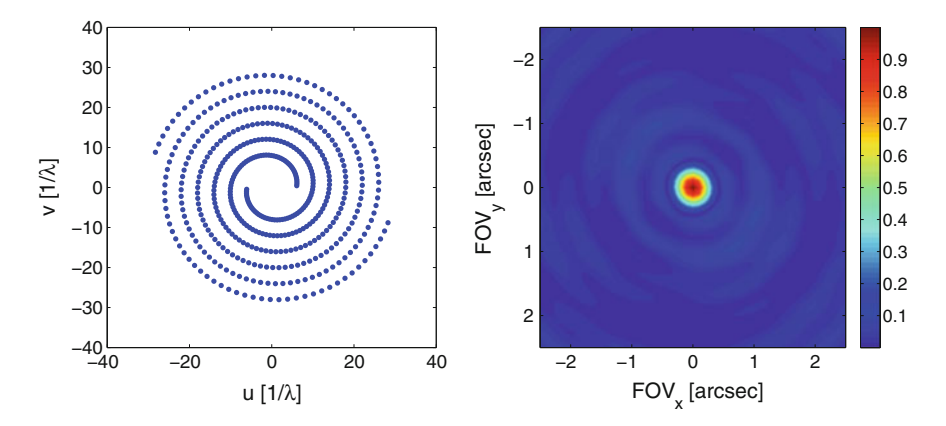


Fig. 5.15 *uv*-map coverage for a Spiral baselines configuration (*left*) and the corresponding normalised dirty beam (*right*)

Figure 5.15 presents the Spiral baselines configuration (left) for 250 baseline positions. Again, the size of the central lobe of the normalised dirty beam (right) remains unchanged, but the circular symmetry has been lost. This feature could be useful in the case of sources positioned in spatial harmonics, this is, when the ripples of the interferometric beams corresponding to two or more different sources interfere constructively and hence a strong modulation appears in the dirty image.

In general, if possible one selects the uv-map coverage to create a beam suitable for a given observation.

5.2.2.2 Master Sky Map Restoration with CLEAN

The restoration of the Master sky map has been kindly performed by Dr. Danielle Fenech from UCL using the Astronomical Image Processing System AIPS (Greisen et al. 2003). AIPS is a package to support the reduction and analysis of data acquired with radio telescopes and radio interferometers. The software, originally developed by NRAO (National Radio Astronomy Observatory) in Charlottesville (Virginia, US) in the seventies, has improved to be the standard software package in radio astronomy.

The input to AIPS is the dirty image (in this case the dirty data cube) and the dirty beam. After applying the CLEAN algorithm for each spectral channel, the CLEAN data cube is obtained.

Figure 5.16 shows the obtained results for three layers of the datacube corresponding to the wavenumbers 25, 118 and 212 cm⁻¹ (top), and the corresponding interferometric dirty beam (bottom). It can be observed that for the minimum wavenumber CLEAN can not separate the sources due to the size of the interferometric dirty

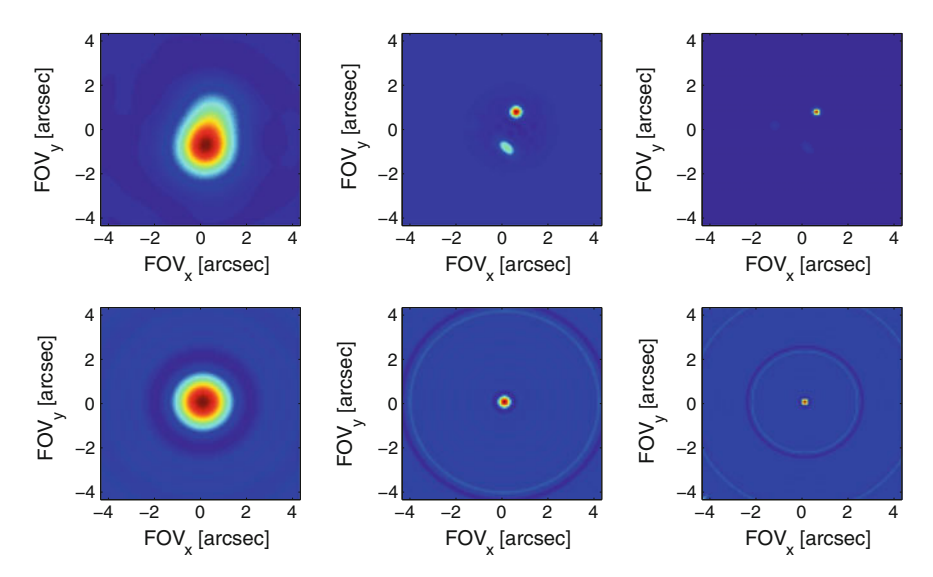


Fig. 5.16 Synthesised datacube layer after restoration with the CLEAN algorithm for the minimum wavenumber (25 cm⁻¹, *left*), central wavenumber (118 cm⁻¹, *centre*) and maximum wavenumber (212 cm⁻¹, *right*) (*top*). Corresponding interferometric dirty beam at each of the previous wavenumbers (*bottom*)

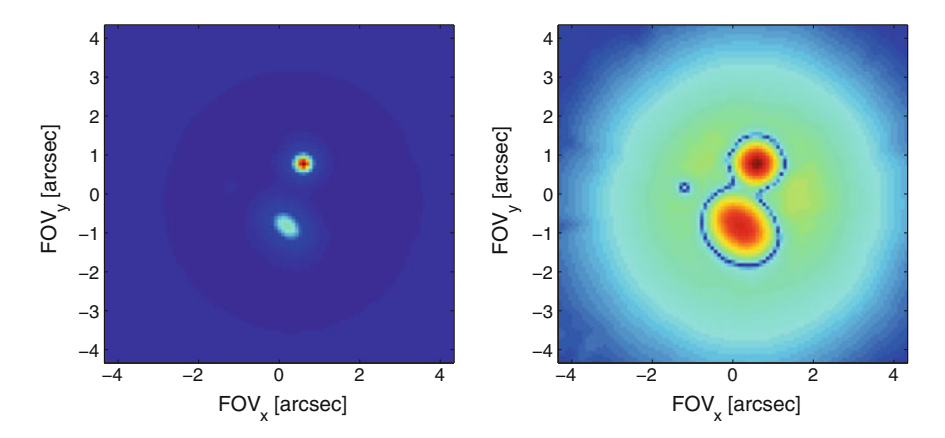


Fig. 5.17 Result of the wavenumber integration of the CLEAN datacube (*left*) and its logarithm (*right*)

beam compared to the separation of the sources. As the size of the beam reduces with wavenumber, the three sources can be differentiated.

By performing a wavenumber integration of the CLEAN data cube, it is easier to detect the three sources of the Master sky map. The results are shown in Fig. 5.17 (left). By representing the logarithm of the integration (right) the three sources are

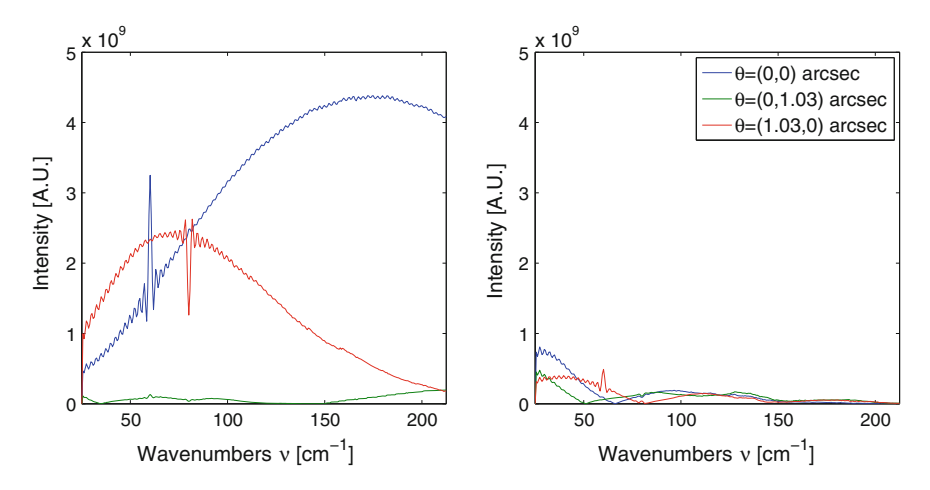


Fig. 5.18 Spectral results of the Master simulation after restoration with the CLEAN algorithm for the central pixel of the gaussian source (*blue*), the point source (*green*) and the central pixel elliptical source (*red*) (*left*). Detected spectra for three positions in the sky where no source intensity is expected (*right*)

easily observed. As expected, the point source is being detected with a diameter smaller than the interferometric dirty beam.

Finally, in Fig. 5.18 (left) the detected spectra for the central pixel of the gaussian source (blue), the point source (green) and the central pixel of the elliptical source (red) is shown. One can observe that the ripples due to the interferometric dirty beam have vanished and the detected spectra is in concordance with the input Master sky map. Again, for comparison, Fig. 5.18 (right) presents the detected spectra for three positions in the sky where no signal is expected. The presence of power in the low wavenumbers is due to the interferometric beam size. From $\sim 60\,\mathrm{cm}^{-1}$ the sources are resolved, the power in those pixels reduces and the modulation present in the dirty datacube (see Fig. 5.7) disappears because there are no ripples from the interferometric beam.

The sinusoidal modulation present in the spectra in the shape of small ripples with high frequency is due to the instrumental line shape (ILS) of the FTS. It has a period of $2.3 \,\mathrm{cm}^{-1}$, which corresponds to an optical distance of 4 mm, this is the maximum optical path difference δ_{max} of this simulation.

In conclusion, these results suggest that the CLEAN algorithm is valid for Double Fourier Modulation data. Applying some FTS algorithms (i.e. phase correction algorithms) in localised areas where there is only one source or the sources are unresolved could be included to further improve the results in the spectral domain.

5.3 FIInS Validation via FIRI Testbed

In this section the performance of FIInS is evaluated through the Cardiff-UCL FIRI testbed data. First, the input sky map for FIInS is defined according to the testbed specifications, including the spatial geometry of the source and its spectra. Three cases will be studied: (a) the single slit aperture, (b) the double slit aperture and (c) the double slit aperture with one of the slits spectrally filtered. Secondly, the corresponding interferograms are generated. Finally, the spectral and spatial information is recovered. As the set of baseline positions of the Cardiff-UCL FIRI testbed is unidimensional, in this chapter a one dimensional analysis is presented. This allows an increase in the simulation speed of the software.

5.3.1 Input Sky Map

To define the input sky map the starting point is the geometry of the slit placed in front of the mercury arc lamb (MAL) described in Sect. 3.1.1.1.

From the Zemax simulation presented in Chap. 3 it is known that the focal plane scale is 0.027 degrees/mm. The slit width is 1 mm, which converts to 97.2 arcsec. The slit separation for the case of the double slit is 5.5 mm, this is 534.6 arc sec. The FIInS spatial resolution is set to $\Delta\theta=25$ arcsec, three times better than the required resolution at the maximum wavenumber, $35\,\mathrm{cm}^{-1}$, and with the maximum baseline, $b_{max}=392\,\mathrm{mm}$. This spatial resolution represents 4 pixels per slit in the sky map. The slit separation converts to 21 pixels. Figure 5.19 shows the spatial map simulated with the Sky Simulator included in FIInS for a single slit (left) and a double

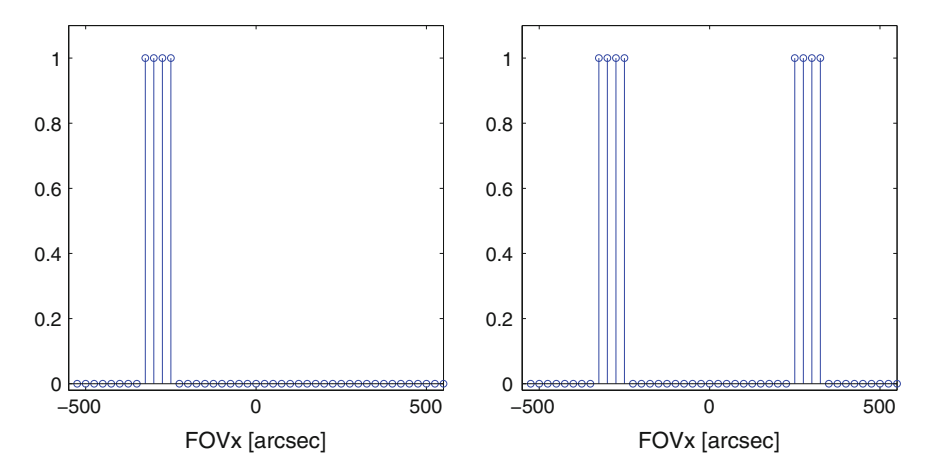


Fig. 5.19 Spatial map generated with the Sky Simulator for a single slit (*left*) and a double slit (*right*)

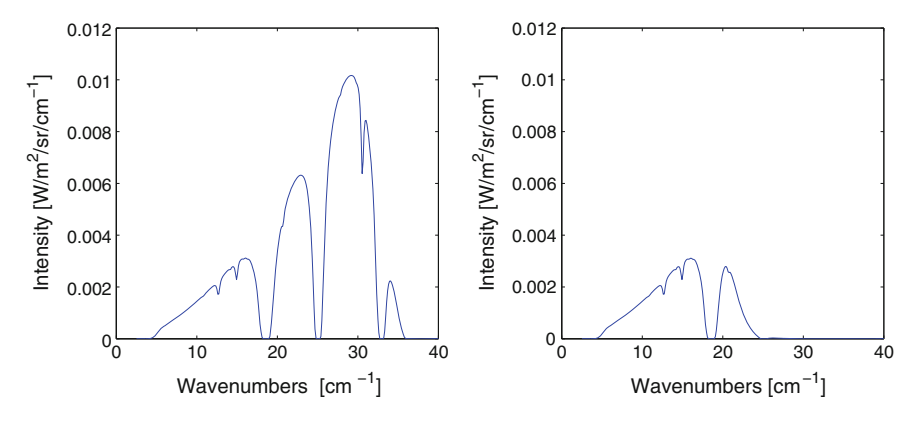


Fig. 5.20 Spectra generated with the Sky Simulator for the source consisting of a blackbody at $1800 \,\mathrm{K}$ with cut-on and cut-off wavenumbers of $5 \,\mathrm{cm}^{-1}$ and $33 \,\mathrm{cm}^{-1}$ respectively and attenuated by the atmosphere (left) and the same source with the $21 \,\mathrm{cm}^{-1}$ low-pass filter (right)

slit (right). Increasing the spatial resolution will not change the results, because the maximum spatial resolution is limited by the maximum baseline.

Spectrally, the MAL is a blackbody at 1800 K. The cut-on and cut-off wavenumbers are 5 cm⁻¹ and 33 cm⁻¹ respectively, and are defined by the Winston cone and the filters at the bolometer. All such relevant parameters are set in the SkySparams.xlsx file. In this case, as the testbed is set in a laboratory, the atmospheric transmission has also to be applied.

Figure 5.20 shows the simulated spectra for the source without filtering (left) and with the $21\,\text{cm}^{-1}$ low-pass filter in front of the slit (right).

5.3.2 Instrument Parameters and Generation of Interferograms

Once the sky map has been defined both spatial and spectrally, the Double Fourier Modulation can be applied. For this simulation, the baselines are set from $b_{min} = 142 \,\mathrm{mm}$ to $b_{max} = 392 \,\mathrm{mm}$, with a baseline separation of $b_{step} = 5 \,\mathrm{mm}$, giving a total of 51 baselines.

Figure 5.21 shows the simulated interferograms for the double slit aperture in front of the MAL for 3 baselines: 217 mm (top), 292 mm (centre) and 367 mm (bottom). No instrumental errors have been applied to this simulation except for the telescope beam. It can be observed that as the baseline length increased, the separation between the peaks that corresponds to the interferogram generated for each of the apertures, increases accordingly. The simulated interferograms are in agreement with the testbed data shown in Fig. 3.7: the separation between the peaks of the interferograms is approximately 200 samples, 250 samples and 300 samples respectively, which for an

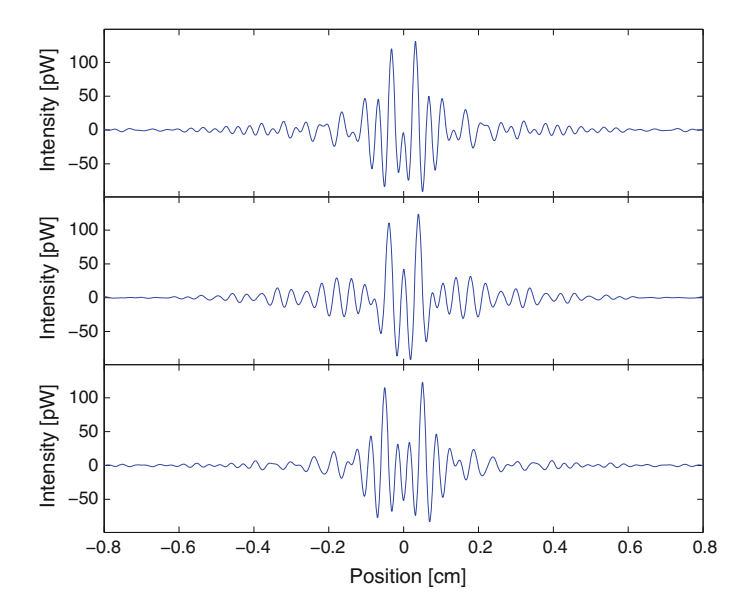


Fig. 5.21 Simulated interferograms for the double slit aperture in front of the MAL for 3 baselines: 217 mm (*top*), 292 mm (*centre*) and 367 mm (*bottom*)

optical step size of $32\,\mu m$ and an oversampling rate of 10 it corresponds to an optical path difference of $0.64\,mm$, $0.8\,mm$ and $0.96\,mm$, respectively. In the simulation, the separation between peaks of the interferograms for the three baselines shown is 0.63, 0.78 and $1.00\,mm$.

Once the interferograms have been generated, one can proceed to extract the spectral and spatial features of the datacube using the algorithms described earlier in this chapter.

5.3.3 Recovering the Spectral and Spatial Information

After the three sets of interferograms have been generated for the single slit aperture, the double slit aperture and the double slit with one of the apertures spectrally filtered, the simulated interferograms are processed to extract the spatial and spectral information. The next figures show the results obtained for each of these scenarios for an ideal instrument.

Figure 5.22 shows the results obtained for the single slit aperture in front of the MAL. Spatially, the wavenumber integration of the dirty image (left) presents a peak at the spatial position $\theta = -275$ arcsec, consistent with the input sky map. The width of the aperture cannot be recovered because at the maximum wavenumber of the power spectrum $(35\,\mathrm{cm}^{-1})$ and for the maximum baseline, the resolution of the interferometer is $\Delta\theta = 150$ arcsec and thus bigger than the source width. In this case,

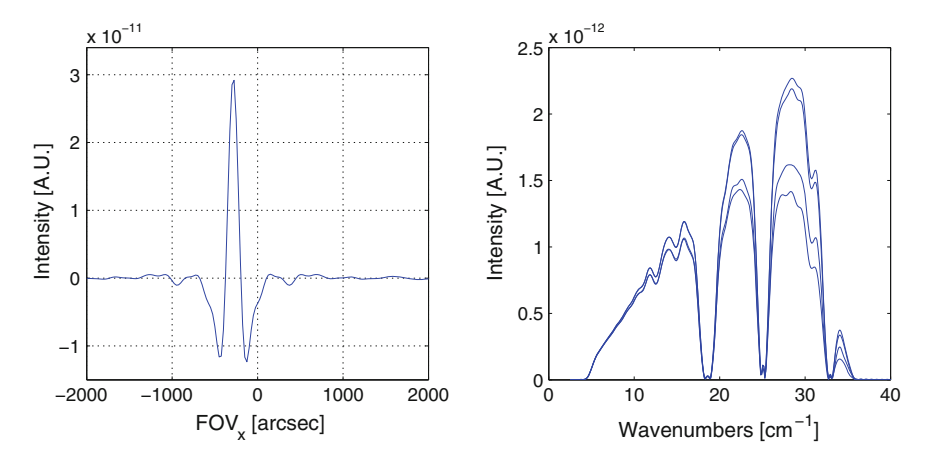


Fig. 5.22 Ideal case results obtained for the single slit aperture in front of the MAL. Integration of the dirty image over wavenumber (*left*) and recovered spectral data for the 4 pixels that define the aperture (*right*)

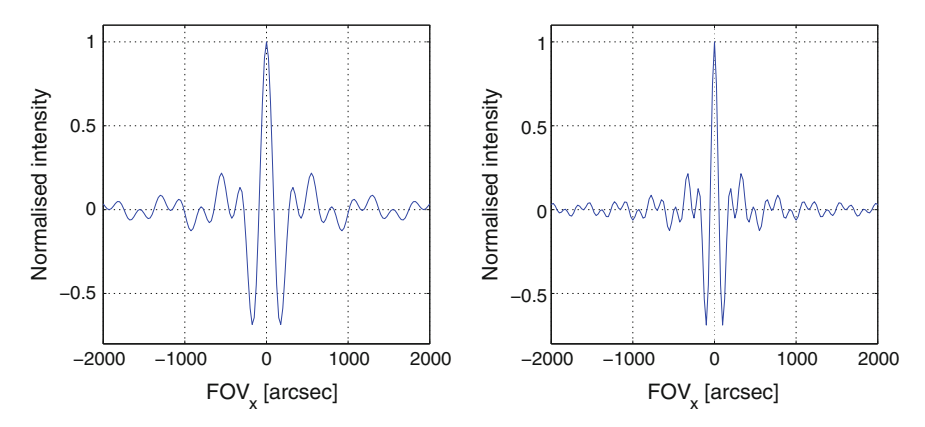


Fig. 5.23 Normalised dirty beam at 21 cm⁻¹ (*left*) and 35 cm⁻¹ (*right*)

the source remains unresolved. The shape of the recovered spatial map corresponds to the interferometric dirty beam convolved with the source. The spectral data from the 4 pixels that define the aperture is plotted (right). The amplitude variation between the 4 pixels is due to the interferometric dirty beam: if we consider the aperture as 4 independent point sources, the spatial size of the dirty beam is bigger than the source separation and there is a transfer of power from source to source.

For comparison, in Fig. 5.23 the normalised dirty beam at 21 cm⁻¹ (left) and 35 cm⁻¹ (right) is shown. In Fig. 5.22 (left) the width of the detected spatial map is bigger than the width of the dirty beam at 21 cm⁻¹ due to the convolution of the beam with the spatial map.

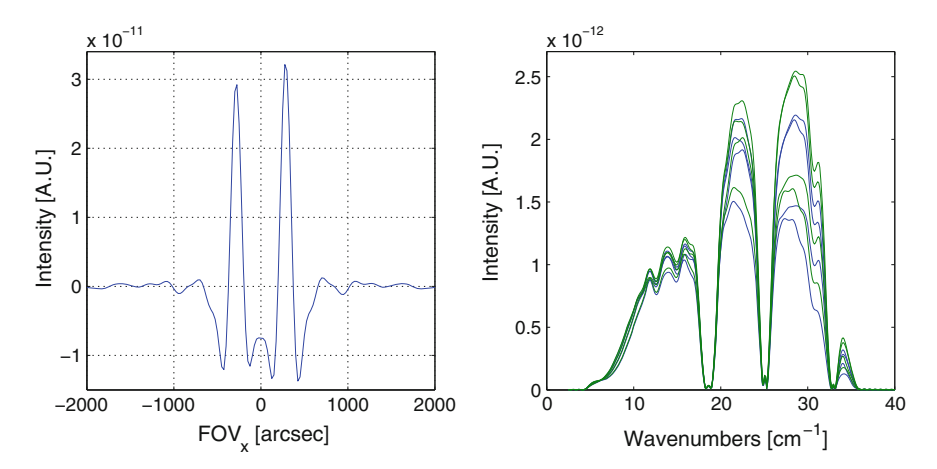


Fig. 5.24 Ideal case results obtained for the double slit aperture in front of the MAL. Integration of the dirty image over wavenumber (*left*) and recovered spectral data for the 8 pixels that define the aperture (*dark green* for *right* slit, *dark blue* for *left* slit)

For the case of the ideal double slit aperture presented in Fig. 5.24, the spatial position of the two apertures (left) is recovered. Again, the sources are unresolved and so the shape of the spatial map is the sum of the two dirty beams. The recovered spectra (right) for the aperture situated at the negative part of the FOV (blue) and for the aperture at the right part of the FOV (green) is consistent with the input spectrum. The amplitude variation between the 4 pixels that define each aperture is due to the interferometric dirty beam, as in the previous case.

When a low-pass filter is positioned in front of one of the slits, in this simulation in front of the slit situated on the right (FOV_x > 0), the spatial position of the slits is recovered. In this situation, the wavenumber integration of the dirty image shown in Fig. 5.25 (left) presents some differences with respect to the simple double slit case: the width of the dirty beam corresponding to the non-filtered spectra is smaller than the width of the dirty beam corresponding to the filtered spectra. The reason is that by integrating over wavenumber, the spatial dirty beam is the sum of the dirty beam corresponding to each wavenumber, the width of which decreases with the wavenumber. As the wavenumber band of the filtered slit is smaller, the width of the integrated dirty beam is bigger (in this case by a factor \sim 2, proportional to the decrease in wavenumber band). In Fig. 5.23 (left) the dirty beam at 21 cm⁻¹ is shown, with a beam width bigger than the dirty beam width at 35 cm⁻¹ (right).

The results just presented correspond to a simulation where no errors have been introduced, which is the ideal case scenario. The next plots correspond to the same simulations (single slit aperture, double slit aperture and double slit with a low-pass filter on one of the slits) when instrumental errors are introduced.

Specifically, the sources of errors implemented are the system NEP extracted from laboratory measurements, with a value of NEP = $2.8 \, pW/Hz^{1/2}$, the bolometer time

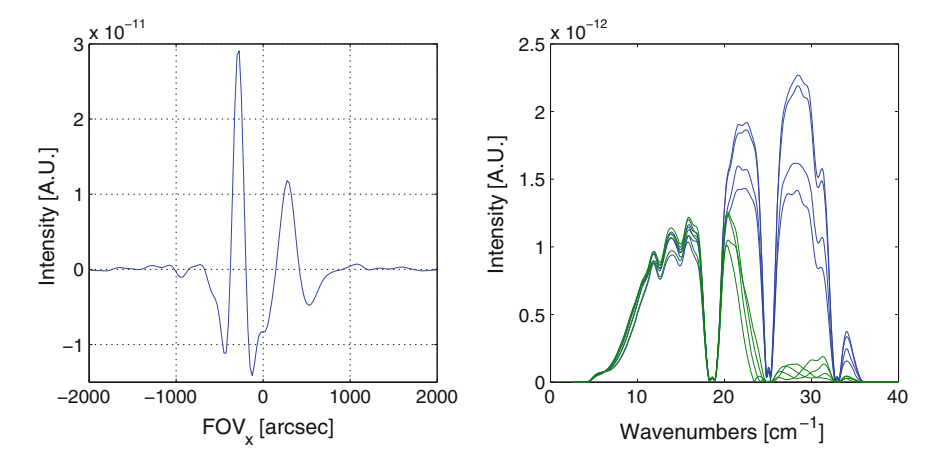


Fig. 5.25 Ideal case results obtained for the double slit aperture in front of the MAL, with one of the slits covered with a low-pass filter. Wavenumber integration of the dirty image (*left*) and recovered spectral data for the 8 pixels that define the aperture (*dark green* for *right* slit, *dark blue* for *left* slit)

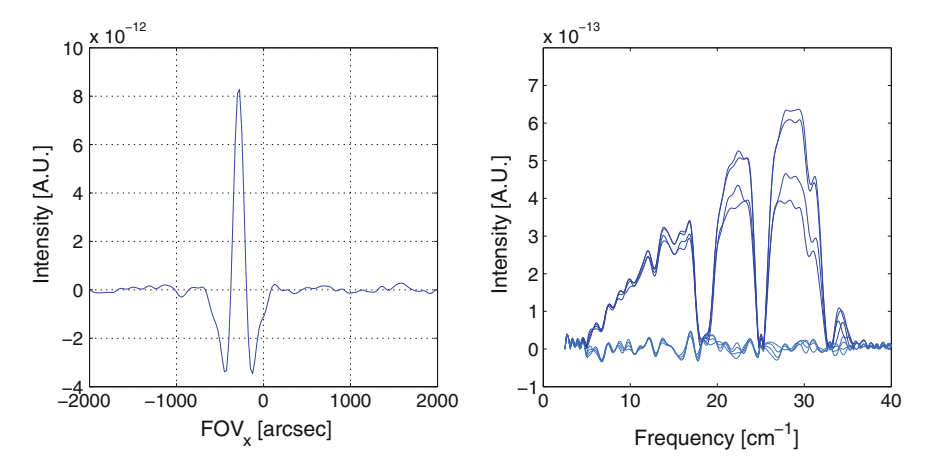


Fig. 5.26 Realistic case results obtained for the single slit aperture in front of the MAL. Integration of the dirty image over wavenumber (*left*) and recovered spectral data for the 4 pixels (*dark blue*) that define the aperture and the residual differences with the ideal instrument (*light blue*) (*right*)

constant, $\tau = 2.5$ ms, and the 1/f noise, with a knee frequency of $f_{knee} = 30$ Hz. For each baseline position 5 interferograms are acquired and averaged afterwards.

For the three simulations shown in Figs. 5.26, 5.27 and 5.28 (single slit, double slit, and double slit with filter, respectively) it can be observed that the results are consistent both with the previous ideal simulations and with the testbed data. The residual differences have been calculated as the difference between the normalised detected spectra in the ideal case and the normalised detected spectra in the realistic

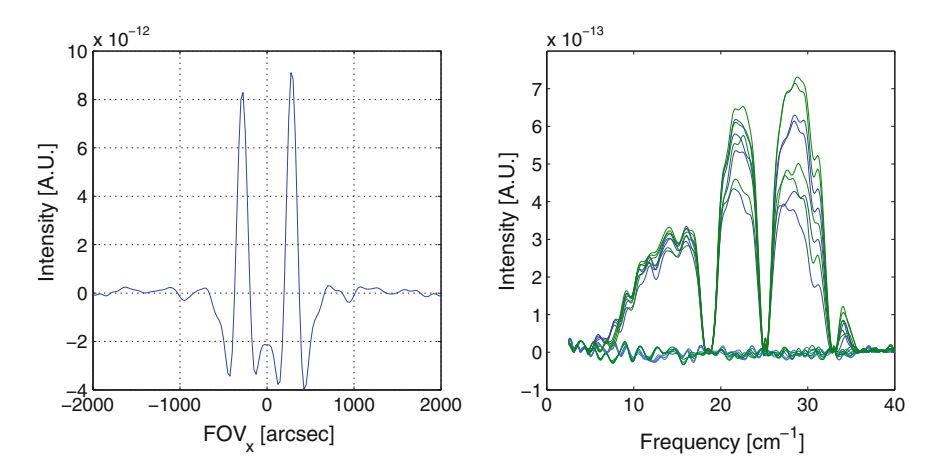


Fig. 5.27 Realistic case results obtained for the double slit aperture in front of the MAL. Integration of the dirty image over wavenumber (*left*) and recovered spectral data for the 8 pixels that define the aperture (*dark green* for *right* slit, *dark blue* for *left* slit) and the residual differences with the ideal instrument (*light green* for *right* slit, *light blue* for *left* slit) (*right*)

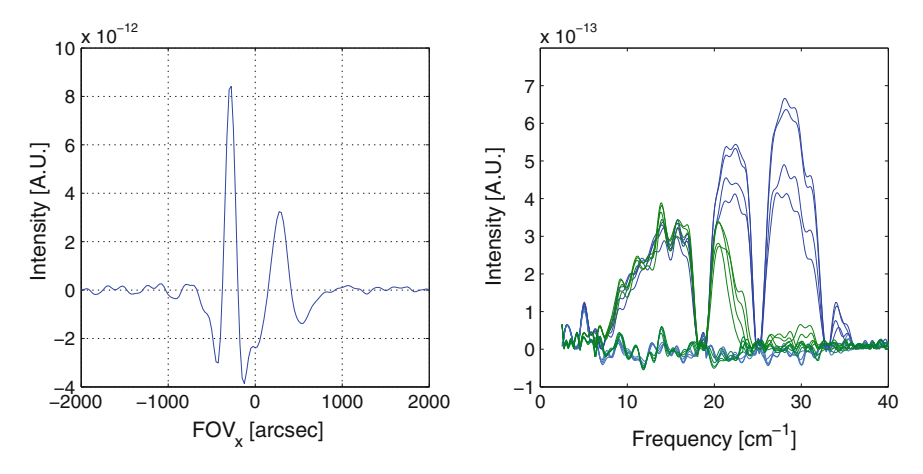


Fig. 5.28 Realistic case results obtained for the double slit aperture in front of the MAL, with one of the slits covered with a low-pass filter. Integration of the dirty image over wavenumber (*left*) and recovered spectral data for the 8 pixels that define the aperture (*dark green* for *right* slit, *dark blue* for *left* slit) and the residual differences with the ideal instrument (*light green* for *right* slit, *light blue* for *left* slit) (*right*)

case. In all three cases the standard deviation of the noise represents approximately a 2% of the maximum value of the spectra. The spatial position of the sources is recovered (left) as is the spectra (right). The higher frequency modulation present in the spectra is due to the addition of the photon noise via the NEP of the system. At low frequencies (corresponding to wavenumbers $<5\,\mathrm{cm}^{-1}$) there is now power,

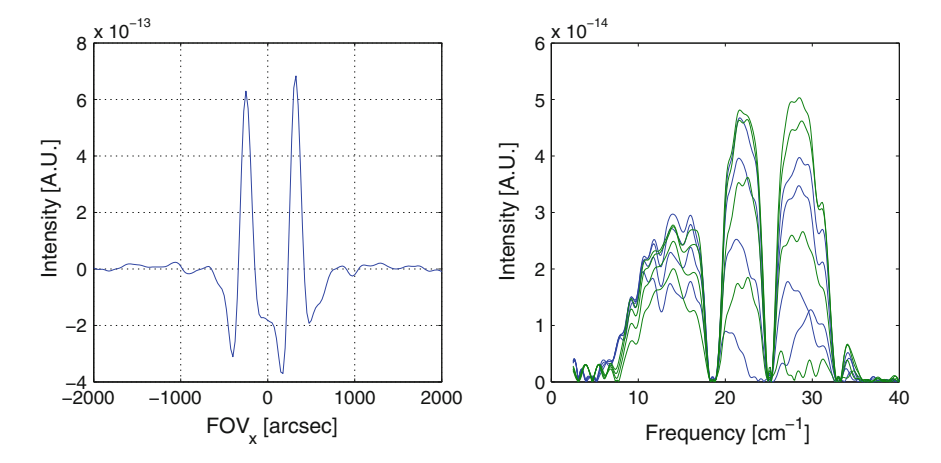


Fig. 5.29 Realistic case results obtained for the double slit aperture in front of the MAL with an exaggerated bolometric time constant of 2.5 s. Integration of the dirty image over wavenumber (*left*) and recovered spectral data for the 8 pixels that define the aperture (*dark green* for *right* slit, *dark blue* for *left* slit) (*right*)

which is explained by the addition of the 1/f noise. In this case, the time constant of the bolometer doesn't affect the obtained results because it is much faster than the sampling speed.

For longer time constants (bigger than the sampling interval), the detector acts as a low pass filter smoothing the recorded interferograms, which can be useful for high frequency noise. However, as a result high frequency components or the signal are filtered as well and the spectrum can not be properly recovered. Figure 5.29 shows the effects of an exaggerated time constant of 2.5 s (approximately 7 times longer than the sampling interval).

5.4 Chapter Summary

In this Chapter the FIInS data processing of spectro-spatial data has been presented through the Master simulation and the instrument simulator has been verified via the Cardiff-UCL FIRI testbed.

The datacube reconstruction from detected interferograms has been performed. Initial steps consist of the noise reduction and time domain interpolation when instrument errors have been included in the simulation. Once the data has been reduced, the dirty datacube is calculated in two steps: first through Fourier transforming in the wavenumber domain and second through two dimensional Fourier transforming in the spatial domain.

It has been observed that instrumental artifacts appear at the dirty datacube. To reduce them, one can use interferometric data synthesis algorithms. Brute force

blind deconvolution is not suitable for this kind of data because the dirty beam corresponding to the Fourier transform of the *uv*-map sampling is complex. However, it could be useful when the baseline selection is not as regular causing the dirty beam to be a gaussian-like beam. In general, the selection of the *uv*-map coverage has to be consistent with the intended observation, because it defines the dirty beam. The CLEAN algorithm, vastly used in radio interferometry, has been applied to the dirty image, and the results presented show that with small modifications it could be the designated algorithm for spectro-spatial data cubes.

Finally, a one dimensional approach of the FIInS capabilities has been presented for verification with the Cardiff-UCL FIRI testbed. The results obtained show that FIInS is capable of performing an accurate simulation of interferograms given the system parameters and by processing the simulated data one can recover both the spatial and spectral features of the input map.

References

- G.R. Ayers, J. Christopher, Dainty. Iterative blind deconvolution method and its applications. Optics Lett. 13(7), 547–549 (1988)
- E.W. Greisen et al., Aips, the vla, and the vlba. Astrophys. Space Sci. Libr. 285, 109-126 (2003)
- J.A. Högbom, Aperture synthesis with a non-regular distribution of interferometer baselines. Astron. Astrophys. Suppl. 15(1974), 417–426 (1974)
- R.L. White. Image restoration using the damped richardson-lucy method. *The restoration of HST images and Spectra II*, pp. 104–110 (1994)
- A. Levin, Y. Weiss, F. Durand, W.T. Freeman. Understanding and evaluating blind deconvolution algorithms, in *IEEE Conference on Computer Vision and Pattern Recognition*, 2009. CVPR 2009 (IEEE, 2009), pp. 1964–1971
- L.B. Lucy, An iterative technique for the rectification of observed distributions. Astron. J. **79**, 745 (1974)
- W.H. Richardson, Bayesian-based iterative method of image restoration. JOSA **62**(1), 55–59 (1972) A.R. Thompson, J.M. Moran, G.W. Swenson. *Interferometry and synthesis in radio astronomy*

Chapter 6 Simulated Observations with FIInS

In the Introduction of this thesis the potential science cases that could be assessed by a Far-Infrared Spectro-Spatial Space Interferometer were introduced. This chapter focuses on one of these science cases, the Circumstellar Disks, because it is one of the major areas of focus in ground-based infrared interferometry observations.

There is an extensive bibliography regarding protoplanetary disks and their evolution (Williams and Cieza 2011), structure (Dullemond and Monnier 2010) and composition (Wood 2008). For this reason, in Sect. 6.1 a brief introduction of the science behind the circumstellar disks focusing on the disk properties around the far infrared frequency range is given. In Sect. 6.2 a simulation of a circumstellar disk is presented. This simulated disk is fed to the instrument simulator FIInS, and the obtained results are described in Sect. 6.3 for both an ideal instrument and for a more realistic instrument.

6.1 Protoplanetary Disks—Birthplaces of Planets

To understand how planetary systems and habitable planets are formed, it is essential to study objects in a variety of evolutionary states. The planet formation process starts when stars accrete material through disks, created when the massive protostellar envelopes collapse. When the protostars make their way towards the main sequence, the remainder of this protostellar disk is what constitutes a protoplanetary disk. These protoplanetary disks are the birthplaces of planets. An interesting type of a protoplanetary disk is the transition disk, in which forming planets close to the star have cleared out gaps in the dust in the inter disk, which if observed could mean the observation of signatures of planet formation. Disks exhibit a range of temperatures (hot near the star and cooler further away) thus radiating strongly at a range of wavelengths from microns to millimeters.

6.1.1 Protoplanetary Disk Evolution

The process of star and planet formation begins with the collapse of a molecular cloud, which consists in an exchange of mass: the mass is initially all in the core but it is processed through an accretion disk inward onto the protostar and outward through an outflowing material in a jet or wind, allowing the formation of a rotating flat disk, the protoplanetary disk, due to conservation of angular momentum.

Originally, the protoplanetary disk contains gas and dust with a composition similar to the parental molecular cloud. During the course of evolution, this material turns into larger bodies such as comets, asteroids, and planets. Because these disks are very opaque in their youngest phase, it is difficult to observe this process directly. However, the stellar radiation is absorbed by the gas and dust in the disk and heats the matter to typical temperatures of a few 1000 K in the inner disk regions to 10 K in the outer regions.

After about one million years (for solar-mass stars, this process is much faster for higher masses), the combination of outflow and infall disperses the majority of the envelope and the star is optically revealed, although a circumstellar disk is still present. For solar-mass stars, this is the T Tauri phase, while for intermediate masses, these stars are referred to as Herbig Ae/Be stars (Hillenbrand et al. 1992). Several million years after the primordial disk has almost disappeared.

6.1.1.1 Pre-main-Sequence Classification

Disks are generally associated with the "Class II" spectral energy distributions (SED) from the pre-main-sequence (PMS) infrared spectral classification of Young Stellar Objects (YSO) (Lada 1987). This initial classification was based on whether the emitted energy from YSOs was rising in the mid-IR or with negligible IR excess.

Currently there are four classes to the PMS classification. Classes 0, I, II and III spectra are seen as an evolutionary sequence with Class 0 being the youngest sources embedded in natal material, the collapse phase. Class I corresponds to the accreting protostar. Class II is the stage when the properties of the disks and their central stars first become optically visible. Finally, Class III YSO spectra represents the dissipation of circumstellar material prior to the protostar reaching the main sequence.

However, it must be noticed that SED classification does not give a unique description of the amount and distribution of circumstellar material. For instance, when a YSO has a highly extinct edge-on disk it can be mis-interpreted as a more embedded, hence, less evolved object.

In order to distinguish these ambiguities, resolved images, ideally at multiple wavelengths, are required to fully characterise the evolutionary state of any individual YSO. Objects exhibiting Class II spectra have many clear lines of sight to the central star and produce the classic infrared signatures of star plus disk systems.

6.1.2 Protoplanetary Disk Structure

The protoplanetary disks, or circumstellar disks around young stars, have a very rich structure, made up of several regions where different physics apply and hence different wavelength ranges need to be observed. For this reason, the techniques used to observe these regions vary with the characteristic temperatures and scale sizes involved.

Figure 6.1 shows a representation of a protoplanetary disk. In general, these disks are relatively large, from a few tens of astronomical units up to 1000 AU or more, while the inner gap disk radius is typically of the order of 0.03AU.

A protoplanetary disk contains gas and dust. The chemistry is dominated by freeze out and low temperature ion-molecule reactions. Outflows and UV radiation clear out most of the envelope, leaving a protoplanetary disk with the inner gap between the disk and the star. Close to the dust inner rim temperatures are high and X-rays heat dust and gas, which in turn excite molecular lines such as H_2 , fine-structure lines, and H_2O , among others. The middle planes are cold and gas is frozen out on dust grains. The outer disk is irradiated by UV light from the star showing mostly molecular rotational lines in the form of ions and radicals.

The thermal emission from the protoplanetary disks can be observed, as well as the scattered light from the dust grains in the surfaces of these disks which is comparable to the light received from stars. This disk radiation appears in the spectral energy distribution of a young star as an excess of infrared radiation.

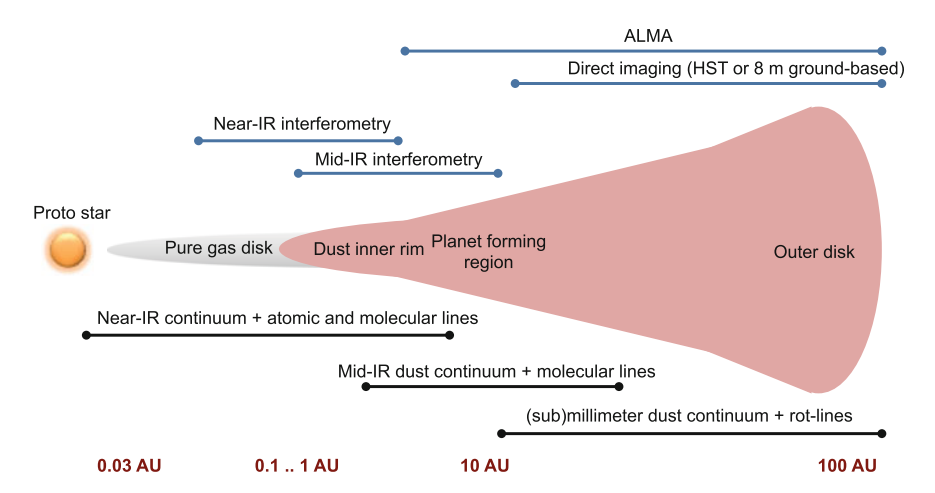


Fig. 6.1 Representation of the structure and spatial scales of a typical protoplanetary disk, adapted from Dullemond and Monnier (2010), including the techniques that allow the resolution of the spatial scales

6.1.3 Far Infrared Interferometry for the Observation of Disks

The physical properties of circumstellar disks in terms of spatial scale, density and temperature require to use different observational techniques for different regions of the disks (Akeson 2008). Also, their basic building blocks are gas, dust and ice, which radiate predominantly in the far-infrared wavelength range.

In general, for thermally emitted radiation from a disk, far-infrared systems can probe the outer ring of a disk (from 10 to a few 100 AU), while mid-infrared telescopes and near-infrared telescopes can observe intermediate radii (about a few AU) and inner rims, respectively. Optical and UV systems can observe regions very close to the stellar surface.

Spatially, the process of observing a circumstellar disk is not straightforward. To measure disk sizes is difficult because the outer parts are cool and emit weakly. Also, due to their small angular scales in nearby star-forming regions, interferometry is required. For this reason, a far-infrared interferometric system is required.

Thanks to Herschel and ALMA, the progress on the study of all phases of circumstellar, proto-planetary and debris discs has increased remarkably (Wolf and DAngelo 2005). However, Herschel spatial resolution is not high enough to resolve relevant spatial scales. Regarding ALMA, although the spatial resolution requirement is met, it is limited by the fact of being a ground-based facility. As it is affected by the transmission of the atmosphere, spectral analysis is limited, for example, the detection of water is not possible.

Basically, for a full characterisation of stars surrounded by protoplanetary disks in order to understand their evolution, the only solution to meet the spatial and spectral requirements is interferometry from space at the far-infrared wavelength range combined with spectroscopy.

6.2 Numerical Simulation of a Circumstellar Disk

In the previous chapter a simulation of a Master sky datacube for FIInS was presented. However, this sky simulation was generated within the simulator itself.

In the case concerning this chapter, a science sky datacube is the input to FIInS: a simulation of a circumstellar disk around a Herbig Ae star kindly generated by Dr. Catherine Walsh at Leiden Observatory (Walsh et al. 2014).

To input an external science datacube, FIInS first loads and extracts the sky grid parameters from the science datacube. Depending on the frequency range of the science datacube, FIInS operates at the required band and selects the corresponding Optical System Level (OSL). The sky grid is then created to compute the corresponding telescope beam. Once the FIInS sky grid is matching the science sky grid no further modifications have to be performed to run FIInS.

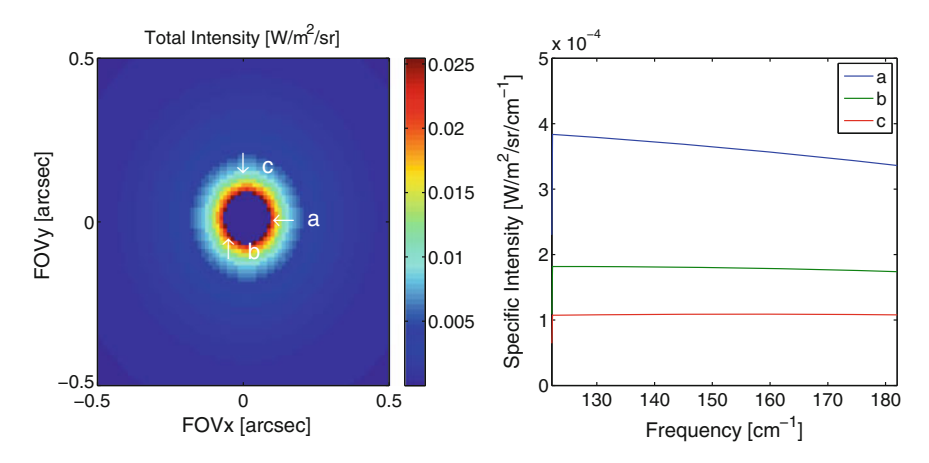


Fig. 6.2 Science datacube consisting of a circumstellar disk model. Wavenumber integration of the science datacube (*left*) and spectral content for 3 selected pixels (*right*)

The science datacube selected for the next simulations corresponds to a protoplanetary disk surrounding a Herbig Ae star ($T_{eff} \sim 10,000 \, \text{K}$). As presented earlier in this chapter, Herbig Ae/Be stars are pre-main-sequence stars. The main difference with T Tauri stars is the mass, this being $M_* \gtrsim M_{\odot}$. Spectrally, their SED shows strong infrared radiation excess due to the presence of the circumstellar accretion disk (Hillenbrand et al. 1992), this is, the thermal emission of circumstellar dust.

Spatially, the science datacube is a disk model with a diameter of approximately 400 AU and with a gap of radius = 10 AU situated 130–140 parsecs from our Solar System, where the nearest regions of ongoing star formation are. At this distance, 1 AU subtends an angle of 7 milliarcseconds.

Figure 6.2 shows the provided science datacube. Spatially, it consists of a face-on disk decreasing in intensity from its centre (left), while spectrally it contains the dust continuum only (right) which is the predominant at Far Infrared wavelengths. Three pixels (a, b and c in the picture) have been selected to show the intensity variation over wavenumber for comparison with the detected spectra later in this chapter.

6.3 A Circumstellar Disk as Seen by a Spectro-Spatial Space Interferometer

To perform a simulation with FIInS of an observation, in this case a circumstellar disk, the first step is to define the instrument parameters that will define the simulation. Given the distance to the target and its size, first one has to select the range of interferometric baselines.

For this given case, the interesting observation is the shape of the disk, this is, the radius of the inner gap and the diameter of the disk. To achieve the spatial

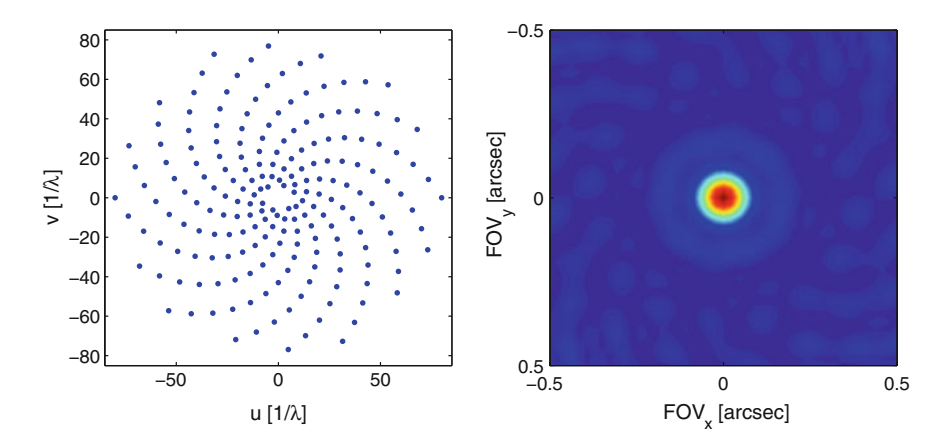


Fig. 6.3 uv-map coverage for the Spiral baseline configuration (left) and the corresponding normalised dirty beam (right)

resolution required, here decided to be approximately an order of magnitude better than the size of the inner gap (0.7 arcseconds), a maximum baseline of 80 m has been selected, which gives us a diffraction limited angular resolution of 0.065 arcseconds at $200\,\mathrm{cm}^{-1}$ and hence enough to resolve the inner gap radius. The telescope diameter has been set to 3m.

It is assumed that the interferometer is operating in a boom-based system, and for this reason the Spiral baseline configuration has been selected.

Figure 6.3 shows the *uv*-coverage for the Spiral baselines configuration (left) and the corresponding dirty beam (right).

6.3.1 Ideal Instrument

The first simulation with FIInS consists of an ideal instrument, meaning no noise or errors have been applied to the measured signal. A set of 100 interferograms has been acquired, one corresponding to each baseline.

Figure 6.4 shows the detected spatial maps corresponding to six different wavenumbers, this is, the dirty image. It can be observed that the detection of the inner gap is more pronounced for higher wavenumbers, as expected: at those wavenumbers the interferometric beam allows us to resolve the size of the inner radius. One can also see the effects of the dirty beam due to the regular spiral nature of the baseline configuration, because as the wavenumber increases the telescope beam size decreases, and the spatial noise in the image reconstruction outside the beam area is higher.

Figure 6.5 (left) shows the profile of the dirty image in the FOV_x direction (for FOV_y = 0) for the previous wavenumbers. As presented before, the higher the wavenumber the higher the contrast in the detection of the inner gap radius.

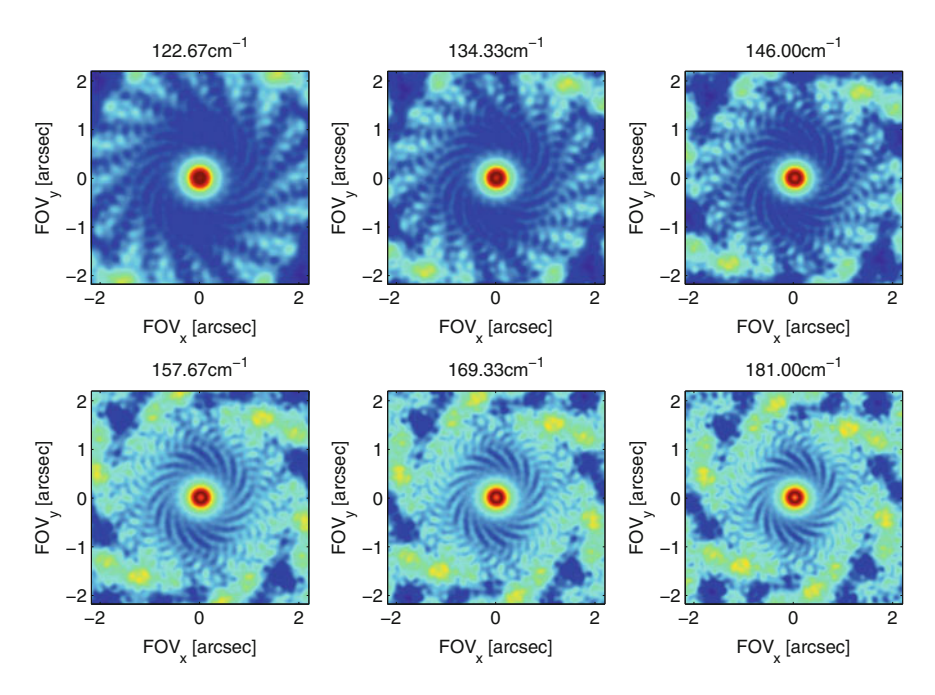


Fig. 6.4 Spatial layers of the reconstructed dirty data cube corresponding to six different wavenumbers (shown on *top* of each image) in the band of operation of the system for an ideal instrument simulation

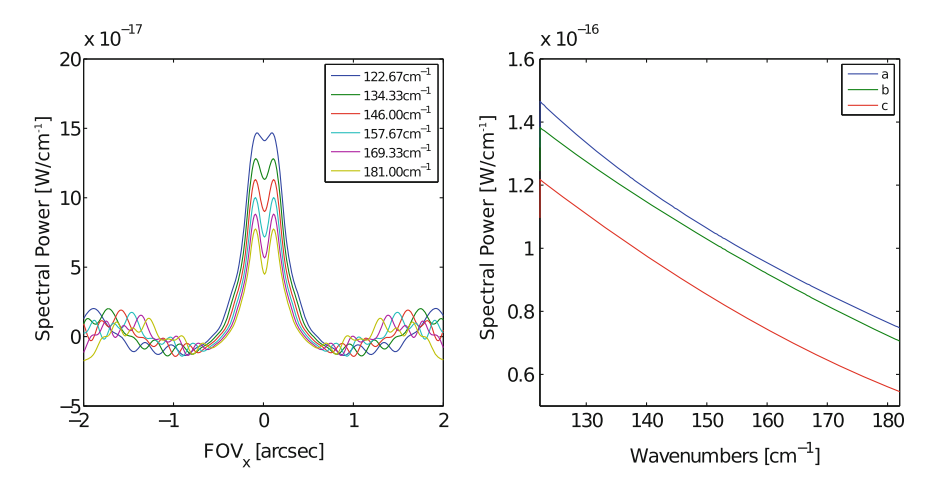


Fig. 6.5 Ideal instrument simulation. Profile of the dirty image in the FOV_x direction (for FOV_y = 0) corresponding to six different wavenumbers in the band of operation of the system (*left*). Detected spectra for the three selected pixels (*right*)

Figure 6.5 (right) shows the detected spectra for the three pixels shown in Fig. 6.2 (right). Although the relative power of the three pixels is consistent with respect to the input map a new effect appears in the detection which is a decrease of the power as a function of the wavenumber much more pronounced than in the input map. This effect is due to the extended nature of the source: if we consider the extended source as an addition of point sources, the convolution of the interferometric beam with each of the point sources will increase the power to the point sources nearby, this increase will depend on the interferometric beam size. This is why for lower frequencies or wavenumbers, as the interferometric beam size is bigger, more power is distributed to the nearby point sources. For higher frequencies or wavenumbers the interferometric beam size is smaller and thus the power is concentrated around the point source being convolved. For an ideal instrument, this effect could be modelled and corrected easily.

6.3.2 Realistic Instrument

The next simulation performed consists of FIInS operating as a more realistic instrument, this is, noise and detector effects are included. The instrument physical parameters are maintained. The effects included in this simulation are the background noise (instrument photon noise and sky background power photon noise, with a calculated $NEP_{ph,background} = 1.20 \times 10^{-18} \text{ W/Hz}^{1/2}$), the detector noise (photon noise and 1/f noise, with an $NEP_{g-r} = 2.66 \times 10^{-18} \text{ W/Hz}^{1/2}$), the source photon noise and the time constant $\tau = 200 \,\mu s$ of the detector. The acquisition frequency is set to $f_{aca} = 1/10\tau$, which if compared to the optical Nyquist sampling yields a mechanical scanning speed of v = 3.125 mm/s equivalent to an optical velocity of $v_{opt} = 1.25$ cm/s because the instrument band of operation corresponds to the Optical System Level 2 (see Sect. 4.5.2). As the maximum OPD is 1.5 cm and the acquisition is set to double sided interferograms, the time for a scan is 2.4 s. The number of scans selected for a given baseline position is 100, meaning for a point in the uv-map a 240s observation is needed. As the number of baselines is 100, the total observing time will be 400 min, which does not include the time to move the telescopes in such position, also referred to as telescope slewing time', which is to be simulated in future versions of FIInS.

Figure 6.6 shows the dirty image for different wavenumbers for this simulation. Although by acquiring 100 scans for each *uv*-point the signal to noise ratio has been increased by a factor 10, the presence of noise is still high. However, spatial features can be easily recovered.

As in the ideal instrument simulation, Fig. 6.7 (left) shows the profile of the dirty image in the FOV_x direction (for FOV_y = 0) for the previous wavenumbers. The presence of noise and errors in the simulation have reduced the contrast of the spatial detection considerably. Spectrally, as presented in Fig. 6.7 (right) one can observe that the spectra contained in the source presents a strong continuum component, but

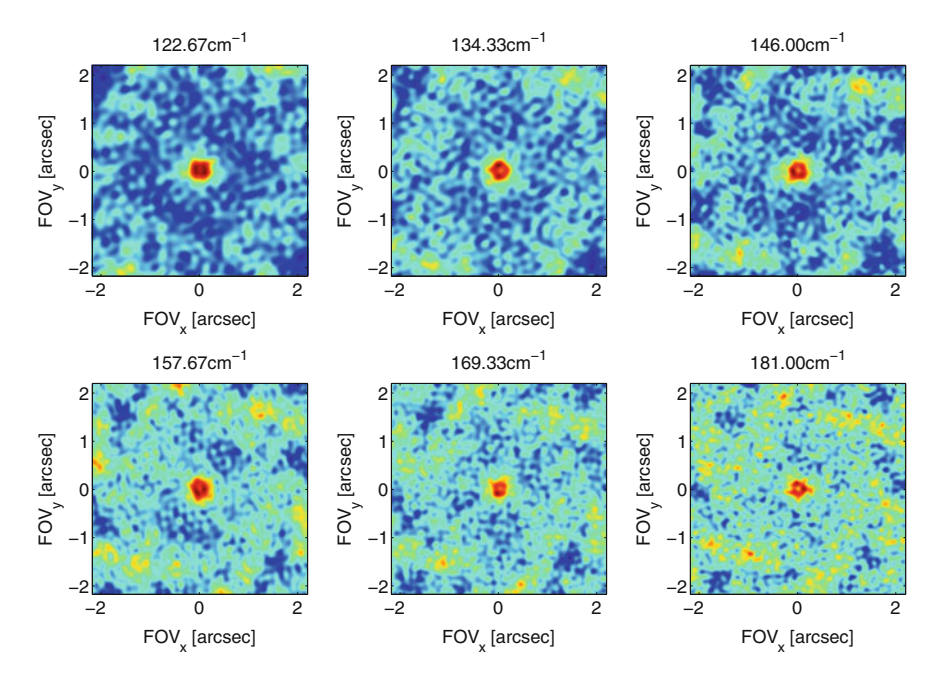


Fig. 6.6 Spatial layers of the reconstructed dirty data cube corresponding to six different wavenumbers in the band of operation of the system for a realistic instrument simulation

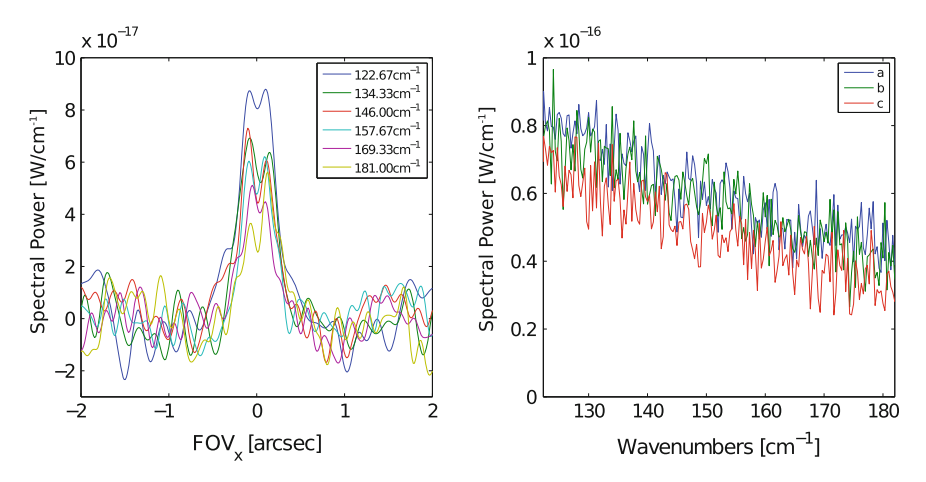


Fig. 6.7 Realistic instrument simulation. Profile of the dirty image in the FOV_x direction (for $FOV_y = 0$) corresponding to six different wavenumbers in the band of operation of the system (*left*). Detected spectra for the three selected pixels (*right*)

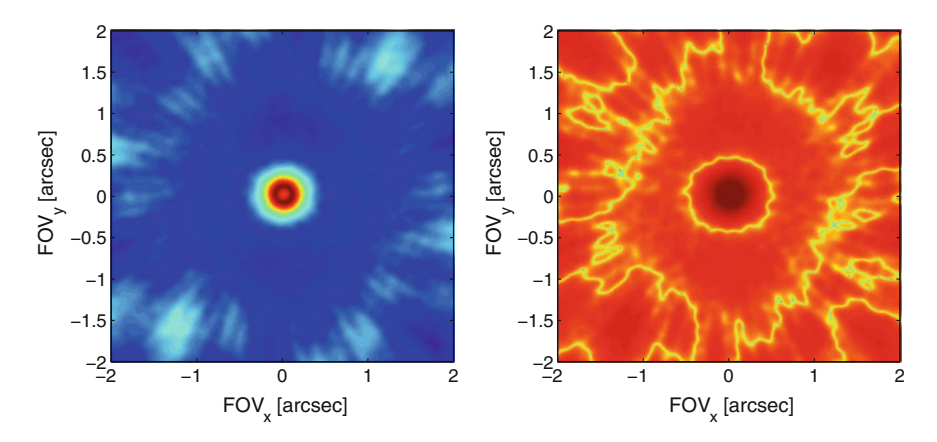


Fig. 6.8 Result of the wavenumber integration (*left*) and its logarithm (*right*) for a realistic instrument simulation

it is difficult to discern whether in some position of the circumstellar disk the power is higher than in other positions. The reason is that the noise level is higher than the signal difference between regions of the circumstellar disk.

Spatially, one way to increase the contrast to detect the inner gap of the disk is by integrating over wavenumber.

Figure 6.8 shows the result of the wavenumber integration (left) and its logarithm (right), where it can be observed that the radius of the inner gap is retrievable. The logarithmic image intensifies the circular shape of the target.

By looking at the interferograms shown in Fig. 6.9, which correspond to the averaging of 100 interferograms per *uv*-point for five different baselines, one can explain the obtained results.

For baselines longer than at least $36\,\mathrm{m}$ the interferogram fringes wash out due to the extended nature of the source and thus the dynamical range decreases considerably (DR \sim 10). Although spatially one can recover the target by integration over wavenumber, spectrally it is more complicated. Without changing the observation parameters, a partial solution consists of applying the data reduction and reconstruction algorithms to the shorter baselines.

Figure 6.10 shows the results obtained when applying the data reduction and image reconstruction algorithms to the baselines from 6.74 to 28.98 m with values of Dynamical Range (DR) \sim 80 to 15, respectively. Spatially (left) the inner gap radius cannot be measured, as expected: the interferometric beam is bigger than the radius at these baselines. Spectrally, however, one can extract that different points of the extended source present different levels of continuum.

In general, one has to select the parameters to account for all the described effects. Although acquiring more scans would increase the DR and SNR by a factor \sqrt{N} , the corresponding increase in observing time would limit the number of observations with the instrument. For this current observation, if previous knowledge of the source

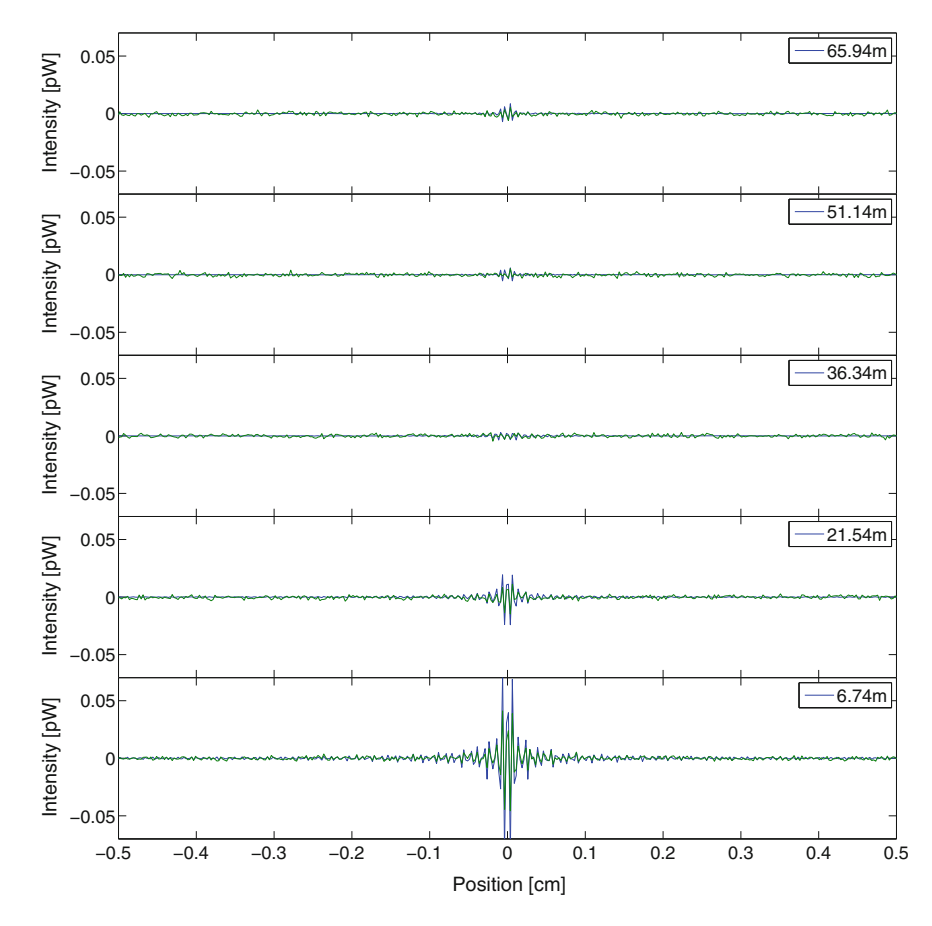


Fig. 6.9 Result of the average of 100 simulated interferograms for five different baseline lengths for a realistic instrument simulation (*green*), and an ideal instrument simulation (*blue*) for comparison

existed (i.e. the circular symmetry), a baseline configuration limited to a one dimension baseline configuration (such as the available Fixed Angle configuration without rotation, see Sect. 4.5.1) would have been enough because the projected baselines on the sky would measure the same source structure.

Finally, another source of errors that has been simulated are the pointing errors. In FIInS, the pointing errors are implemented as a measurable quantity corresponding to a Gaussian distribution with a standard deviation equivalent to half the smallest telescope beam, for this simulation this is 1.72 arcseconds, plus a non-measurable quantity equivalent to a 10% of the previous standard deviation, this is 0.172 arcseconds.

Without pointing errors, the zero optical path difference (ZPD) of the interferogram generated by an on-axis source ($\theta_x = \theta_y = 0$) appears at the scan position 0 cm. The effect of pointing errors in the acquisition of an interferogram can be easily observed from the evolution of the ZPD.

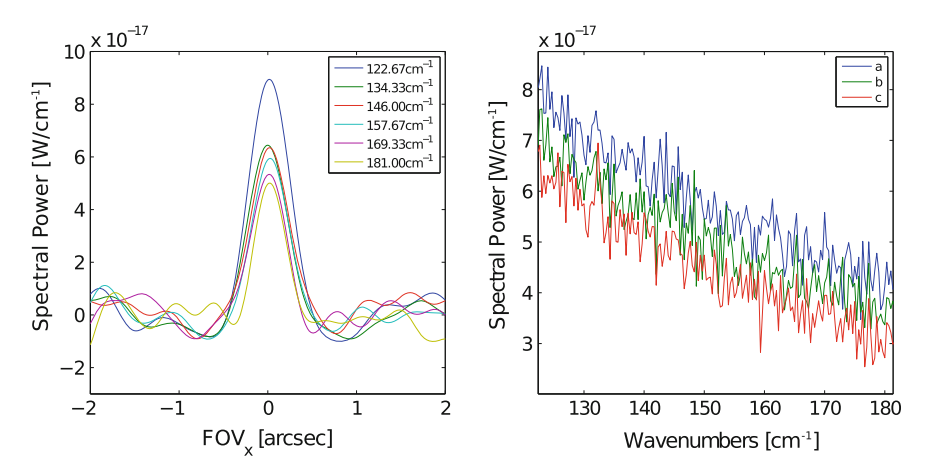


Fig. 6.10 Realistic instrument simulation. Profile of the dirty image in the FOV_x direction (for $FOV_y = 0$) corresponding to six different wavenumbers in the band of operation of the system (*left*), and detected spectra for the three selected pixels (*right*) when a short baseline range is used in the image reconstruction

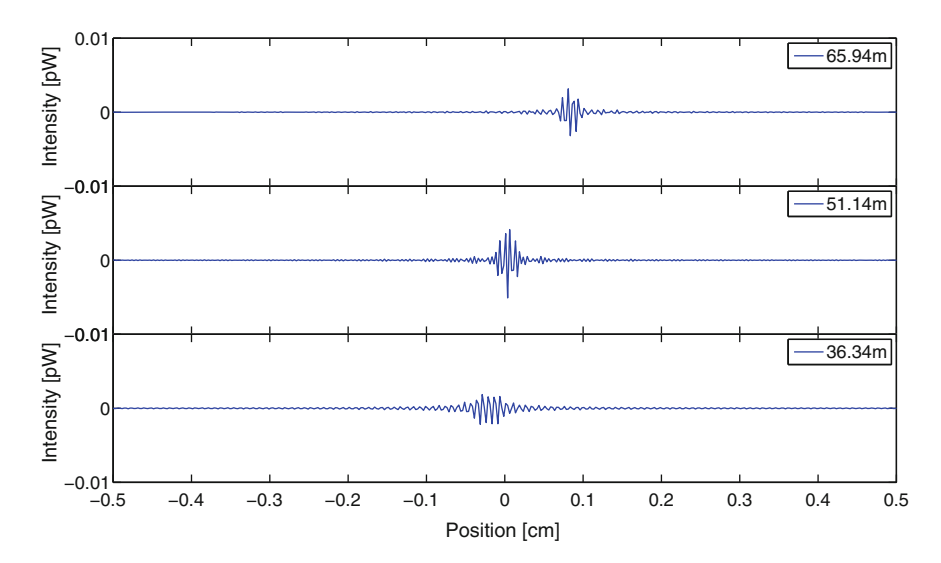


Fig. 6.11 Simulated interferograms when pointing errors are applied to the ideal instrument simulation for three different baseline lengths

Figure 6.11 shows the interferograms corresponding to three baselines. The selection of the baselines is because pointing errors affect more evidently longer baselines. It can be observed that the ZPD of the interferograms has shifted away from 0 cm.

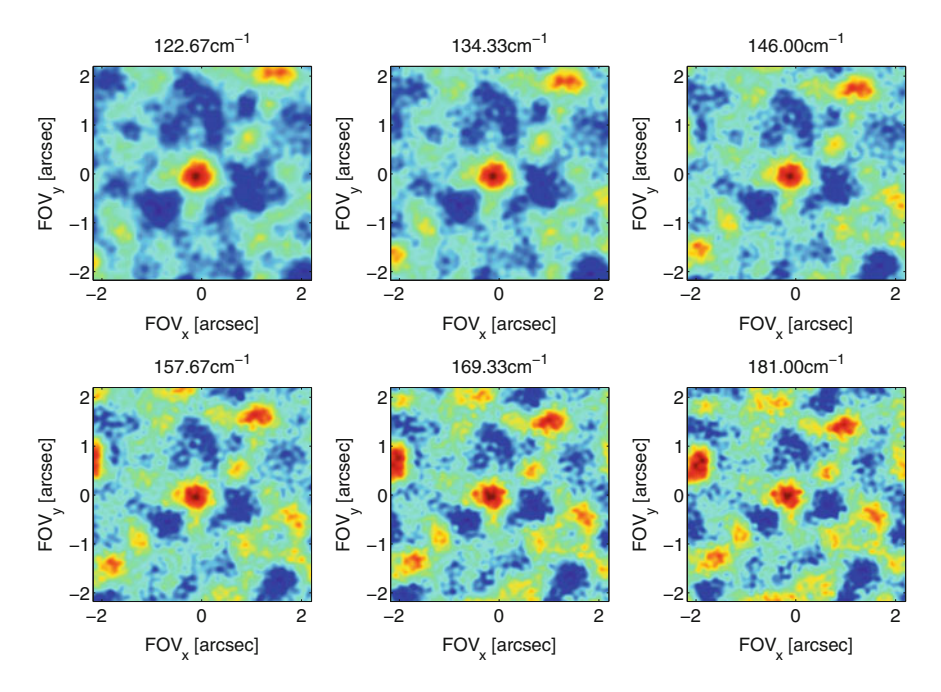


Fig. 6.12 Spatial layers of the reconstructed dirty data cube corresponding to six different wavenumbers in the band of operation of the system for an ideal instrument simulation when pointing errors have been applied

The measurable pointing errors are corrected at the dirty image reconstruction by compensating the sky grid for each baseline, this is (θ_x, θ_y) from Eq. 5.6. However, this is not possible for the non-measurable pointing errors.

Figure 6.12 shows the reconstructed dirty image for six wavenumbers. The radius of the inner gap cannot be measured, because the non-measurable pointing errors are bigger than the inner gap radius, which is 0.1 arcseconds.

If the non-measurable pointing errors are not included in the simulation, the detection is equivalent as for the ideal instrument, because technically what is done is the calculation of a slightly modified *uv*-map.

Currently the pointing errors are implemented in FIInS spatially, not spectrally, meaning that it is assumed the pointing does not change during a FTS scan. Implementing pointing errors during a FTS scan requires the computation of the beam for each spectral bin, for each telescope, and for each baseline, thus increasing the simulating time resulting in a computationally heavy routine. After optimisation of the software, future versions of FIInS will include the effect of pointing errors within a FTS scan.

6.4 Chapter Summary

In this chapter the capabilities of FIInS for the simulation of an observation of an external science datacube have been presented. The science case selected and presented in Sect. 6.1 has been a circumstellar disc because of its importance in the understanding of how planetary systems and habitable planets are formed. Also, due to the nature of their structure and composition, cirumstellar disks can only be measured using interferometric systems at the Infrared wavelength range.

In Sect. 6.2 the numerical simulation of the circumstellar disk has been presented alongside the FIInS procedure to convert the external map to a FIInS validated map. In Sect. 6.3 the results of a simulated observation have been shown for two cases: an ideal instrument and a realistic instrument.

For the ideal instrument, the capabilities of a Far Infrared Interferometer from space to extract the spatial and spectral contents of a circumstellar disk have been proved. Due to the extended nature of the source, the importance of the selection of the baseline configuration and range has been shown, as it defines the interferometric dirty beam which is then convolved with the sky map.

In the realistic instrument case, different sources of noise and effects have been applied to the simulated interferograms. It has been shown how the selection of instrument and observation parameters is crucial to maintain a sufficient signal to noise ratio which allows the detection of the spectral and spatial features of the target. However, this selection should not be arbitrary and both science product implications and observational constraints must be taken into account, for example, the required observation time. Also different observations will require different parameters: longer baselines allow us to extract the small spatial features of a circustellar disk but degrade the detection of the spectral continuum, while short baselines are useful for the detection of the spectral features but limit the spatial resolution. Finally, pointing errors affect widely the detection of small spatial structures, but with a properly designed metrology system they can be corrected.

In summary, this first version of FIInS allows the simulation and study of some instrumental effects during a simulated observation of a science datacube. Future versions of FIInS will include more instrumental errors and noise, such as pointing errors during an FTS scan which have not yet been included here for computational reasons. Future work on the software will be performed prior to its release to the scientific community to include additional instrumental effects and configurations.

References

R. Akeson, Observations of circumstellar disks with infrared interferometry. New Astron. Rev. 52(2), 94–104 (2008)

C.P. Dullemond, J.D. Monnier, The inner regions of protoplanetary disks. Annu. Rev. Astron. Astrophys. 48, 205–239 (2010) References 141

L.A. Hillenbrand, S.E. Strom, F.J. Vrba, J. Keene, Herbig ae/be stars-intermediate-mass stars surrounded by massive circumstellar accretion disks. Astrophys. J. 397, 613–643 (1992)

- C.J. Lada, Star formation-from ob associations to protostars, in *Star Forming Regions*, vol. 115, pp. 1–17 (1987)
- C. Walsh, T.J. Millar, H. Nomura, E. Herbst, S. Widicus Weaver, Y. Aikawa, J.C. Laas, A.I. Vasyunin, Complex organic molecules in protoplanetary disks. Astron. Astrophys. 563, A33 (2014). doi:10. 1051/0004-6361/201322446
- J.P. Williams, L.A. Cieza, Protoplanetary disks and their evolution. Annu. Rev. Astron. Astrophys. 49, 67–117 (2011)
- S. Wolf, G. D. Angelo, On the observability of giant protoplanets in circumstellar disks. Astrophys. J. **619**(2), 1114 (2005)
- K. Wood, Infrared signatures and models of circumstellar dust disks. New Astron. Rev. **52**(2), 145–153 (2008)

Chapter 7 Conclusions and Future Work

In this Thesis an instrument simulator for a Far Infrared space interferometer has been presented, as well as a testbed implementation of the technique intended to be used to achieve high spectral and spatial resolutions from space.

In the Introduction a general view of Far Infrared astronomy and possible science cases for high angular resolution observations was given, through the past and present Far Infrared instruments to FIRI, the concept of a space based Far Infrared Interferometer, a system required because of the need for such observations in the wavelength range between JWST and ALMA. To achieve such angular resolution at those wavelengths interferometry from space is the only plausible solution. One of the techniques that could be used to perform spectro-spatial interferometry was presented: Double Fourier Modulation.

In Chap. 2 the theoretical background underpinning Double Fourier Modulation was presented, this is the combination of Fourier Transform Spectroscopy and Stellar Interferometry. Fourier Transform spectroscopy is based on the Michelson interferometer, concept in which one can generate an interferogram by dividing the light from a source and recombining it on a beam splitter after delaying one of the optical paths. For a correct detection of the spectral information the sampling of the interferogram is of great importance, because it defines the spectral resolution and the spectral band coverage. Stellar Interferometry, based on the Young's two slit experiment, combines the light from two apertures to create interference to measure the complex visibility. One can recover the brightness distribution on the plane of the source by Fourier transforming the complex visibility. The baseline length defines the angular resolution of the interferometer. Finally, the Double Fourier Modulation technique is the combination of Fourier Transform Spectroscopy with Stellar Interferometry. With this technique measurements of the source brightness distribution and spectrum are performed simultaneously.

Chapter 3 focused in the spectro-spatial interferometer testbeds in which I have been involved during my programme: the FIRI laboratory testbed (based at Cardiff University) and WIIT, the Wide-field Imaging Interferometry Testbed (based at NASA's Goddard Space Flight Center). Both testbeds have demonstrated the theory of Double Fourier Spatio-Spectral Interferometry or the application of a Fourier

transform spectrometer (FTS) to aperture synthesis interferometry, the FIRI at Far Infrared wavelengths, while WIIT at optical wavelengths.

The first version of the instrument simulator FIInS was described in Chap. 4. With a modular architecture, divided in the Sky Simulator and the Instrument model, its operation was shown through the different modules of the software. The sky simulator generates the input datacube, including the corresponding photon noise, and is fed to the instrument model. The instrument model (where Double Fourier Modulation is performed) can operate as an ideal instrument or a more realistic one if the control flags are activated. The output of the system is a set of FITS files containing the interferograms to be processed. FIInS allows the user to output not only the set of interferograms, but also independent outputs such as *uv*-maps or transmission profiles if available.

The current status of FIInS allows to perform simulations of what we call first order errors. For example, the simulation of the FTS drive response, non-linearities that occur in a real system (for example a vibrational frequency due to the mechanical motion involved) need to be modelled. By performing the Double Fourier Modulation via the cosine co-addition one can introduce these errors easily.

The data-processing of FIInS data has been presented in Chap. 5 through a Master simulation, and its performance has been verified via the Cardiff-UCL FIRI testbed. For the datacube reconstruction, initially one needs to perform the noise reduction and time domain interpolation if instrument errors have been included in the simulation. Once the data has been reduced, the dirty datacube is calculated in two steps: first through Fourier transforming in the frequency domain and second through two dimensional Fourier transforming in the spatial domain. However, instrumental artifacts appeared at the dirty datacube.

To reduce them, interferometric data synthesis algorithms have been proposed. Brute force blind deconvolution was proven non suitable for this kind of data because the dirty beam corresponding to the Fourier transform of the *uv*-map sampling is complex. However, it could be useful when the baseline selection is not as regular causing the dirty beam to be a Gaussian-like beam. In general, the selection of the uv-map coverage has to be consistent with the intended observation, because it defines the dirty beam. The CLEAN algorithm, vastly used in radio interferometry, has been applied to the dirty image, and the results presented have shown that with small modifications it could be the designated algorithm for spectro-spatial data cubes.

Also in Chap. 5, a one dimensional approach of the FIInS capabilities has been presented for verification with the Cardiff-UCL FIRI testbed. The results obtained show that FIInS is capable of performing an accurate simulation of interferograms given the system parameters and by processing the simulated data one can recover both the spatial and spectral features of the input map.

For all the simulations with FIInS absolute knowledge of the sky grid with respect to the baseline projections has been assumed, which is not the case in a real system and calibration sources are required.

Finally, in Chap. 6 the capabilities of FIInS for the simulation of an observation of an external science datacube were presented. The selected science case was a circumstellar disk because of its importance in the understanding of how planetary

systems and habitable planets are formed, as well as the nature of their structure and composition, making them ideal for interferometric observations. The first step was to convert the external map to a FIInS validated map. Then two scenarios were simulated: an ideal instrument and a realistic instrument.

For the ideal instrument, the capabilities of a Far Infrared Interferometer from space to extract the spatial and spectral contents of a circumstellar disks were proved. Due to the extended nature of the source, the importance of the selection of the baseline configuration and range was shown, as it defines the interferometric dirty beam which is then convolved with the sky map.

In the realistic instrument case, different sources of noise and effects were applied to the simulated interferograms. The obtained results proved the importance in the selection of instrument and observation parameters, crucial to maintain a sufficient signal to noise ratio which then allows the detection of the spectral and spatial features of the target. However, this selection should not be arbitrary and both science product implications and observational constraints must be taken into account, for example, the required observation time. Also different observations will require different parameters: longer baselines allow us to extract the small spatial features of a circumstellar disk but degrade the detection of the spectral continuum, while short baselines are useful for the detection of the spectral features but limit the spatial resolution. Finally, pointing errors were seen to affect widely the detection of small spatial structures, but with a properly designed metrology system they could be corrected.

7.1 Future Work

Because of the nature of the work presented in this Thesis, the suggested future work is divided in the work to be performed with the FIRI testbed, the intended improvements of the instrument simulator FIInS and the possible solutions for the synthesis of Double Fourier Modulation data.

7.1.1 About the Cardiff-UCL FIRI Testbed

The Cardiff-UCL FIRI testbed can undergo improvements in the modelling of the testbed itself as well as hardware upgrades.

Regarding the hardware, the beam walk-off or vignetting in the spectral arm of the interferometer, could be reduced by using beam focusing optics. Also, the mechanical construction of the aperture mask is not robust, and if we are to move to higher frequencies, the uniformity of the slit edges and parallelism need to be more carefully controlled by utilising photolithographic-made aperture masks. In further work, more robust scenes will be used, as well as tunable sources. Finally, there exists the possibility of unbalanced spectral throughput in each interferometer arm, which

can lead to phase errors. The latter can be monitored by examining both output ports at the beam splitter.

The use of a step and sample scan method is inefficient compared with rapid scan techniques for the spectral drive. At the time of writing, this change has already been performed. More specifically, the fast scan drives have been upgraded to a higher specification to allow finer monitoring of the position.

As we explore more complex scenes, more sophisticated data-processing techniques must be considered. The current forward modelling is limited to the knowledge of the single slit spectral information. These requirements include observations of known point-like sources to calibrate the instrument or taking advantage of techniques such as self-calibration, where a known point source in a complex scene is used to calibrate the system. However, the instrument simulator FIInS has proved to be able to detect the spatial and spectral features without prior knowledge of the source spectral information, and the data reduction and processing of simulated data can be applied to testbed data.

To study more complex scenes with the FIRI testbed there exist two possibilities: first, to develop tunable sources which can be calibrated with standard FTS instruments, and second, following the concept of the apertures in front of the Mercury Arc Lamp, to photolithographically build a complex scene. To recreate the sampling of the *uv*-map, this complex scene can be rotated as the scenes generated by CHIP for WIIT.

7.1.2 About the Instrument Simulator FIInS

The work presented in this thesis is the first version of the instrument simulator FIInS and, although proved valid for relatively simple simulations, more instrumental effects need to be implemented in order to approach the simulation of the performance of a real spectro-spatial interferometer in space.

In the *uv*-map generator module, accounting for the slewing time of the telescopes will be interesting in order to compute the total observation time, as well as fuel calculations. Related to this, the pointing errors of the telescope need to be simulated not only for the different telescope positions, but also the pointing errors during an FTS scan will need to be modelled. To model these some software optimisation is required because this process is computationally heavy.

The FTS drive is delicate, and the effect of errors in the velocity of the drive is included in FIInS. However other effects like vibrations during the scan, metrology errors, temperature variations, among others must be taken into account because it can affect the readout of the position of the drive, and hence distort the recovered datacube.

The telescope beam has been modelled in two ways: from the Fourier transform of the telescope aperture, and from the Hankel transform of the radial profile of the telescope, both for a uniform illumination. In both cases different illuminations of

7.1 Future Work 147

the telescope can be included and simulated. A future step is to include telescope obscurations profiles, i.e. due to telescope supports, in which case the Fourier transform calculation will need to be used.

The thermal system (optics modules) in FIInS has been modelled according to the FIRI-CDF Study Report (ESA Concurrent Design Facility 2006). Variations of this optical setup will require to perform some minimal modifications in FIInS. Currently the cold optics emissivities and transmission (and hence reflection) are constant along the band of operation of the instrument. To input transmission profiles from the different optical elements will narrow the gap between an ideal simulator and a much more realistic one.

Diffraction due to optical components, non-ideal beam splitters (i.e. errors in the beam splitter phase), among other effects, can be included in FIInS via a Zemax simulation of the optical system. To do this one option is to project these effects in the direction of the collecting telescopes and apply them to the calculated telescope beam. Current efforts are focused in the Zemax simulation of this FIRI system.

The detector module in FIInS has been tailored to LeKIDs detectors, which are still under development. To this date, very little is known on the noise properties and non-linearities of these detectors where substantial research is taking place. With publication of such results, appropriate modification of the detector module can take place. Also, an extension to a detector array simulation is planned, as well as the inclusion of the electronics readout. Due to the modular design of FIInS, other detector technologies can also be simulated.

Finally, a full sensitivity model will need to be created for the different observing modes available.

7.1.3 About the Synthesis of DFM Data

The synthesis of Double Fourier Modulation data has been performed with a blind deconvolution algorithm and with the CLEAN algorithm via AIPS (Greisen et al. 2003). Only the second one has been proved robust enough for DFM data.

The next step will be to perform some modifications on the CLEAN algorithm by coding a DFM specific one, in order to include some FTS algorithms such as phase correction and apodization. Apodization requires a unique zero path difference (ZPD), and research would need to be performed to design tailored apodization filters for DFM data.

Current FTS phase correction algorithms are also dependent on a unique ZPD. However, the instrumental phase errors, if linear, will affect in the same way different regions of an interferogram. This fact can be used to redesign some of the existing phase correction algorithms, for example the Forman phase correction one.

7.2 Closing Remarks

In this Thesis the work performed during my PhD programme has been presented. During the first year, my efforts focused in the Cardiff-UCL FIRI testbed data analysis and forward modelling, which resulted in the publication of the article 'Demonstration of spectral and spatial interferometry at THz frequencies' (Grainger et al. 2012) in the journal Applied Optics.

The second and third year have focused in the development and testing of the Far Infrared Interferometer Instrument Simulator FIInS, and preliminary results have been presented at international Conferences (Juanola-Parramon et al. 2012; Juanola-Parramon and Savini 2013).

This work presented here provides, for the first time, an end to end simulator of a Double Fourier Modulation Far Infrared Interferometer. It is intended to be a tool for the astronomical community to explore the limits of a space interferometer, as well as to test the performance and technical limits of such a system.

References

- ESA concurrent design facility. Far infrared interferometer—CDF study report. **CDF-49**(A), 1–294 (2006). http://sci.esa.int/future-missions-office/40738-firi-cdf-study-report/
- W.F. Grainger, R. Juanola-Parramon, P.A.R. Ade, M. Griffin, F. Liggins, E. Pascale, G. Savini, B. Swinyard, Demonstration of spectral and spatial interferometry at THz frequencies. Appl. Opt. 51(12), 2202–2211 (2012). doi:10.1364/AO.51.002202. http://ao.osa.org/abstract.cfm?URI=ao-51-12-2202
- E.W. Greisen et al., AIPS, the VLA, and the VLBA. Astrophys. Space Sci. Libr. 285, 109-126 (2003)
- R. Juanola-Parramon, P.A. Ade, W.F. Grainger, M. Griffin, E. Pascale, G. Savini, L. Spencer, B. Swinyard, A space-based far infrared interferometer (FIRI) instrument simulator and test-bed implementation, in SPIE Optical Systems Design (International Society for Optics and Photonics, 2012), pp. 85501Y–85501Y
- R. Juanola-Parramon, G. Savini, FIInS The far-infrared interferometer instrument simulator, in *Fourier Transform Spectroscopy* (Optical Society of America, 2013)

Appendix A

Telescope Beam Profiles Calculation

In mathematics, the Hankel transform (Goodman 2005; Bracewell and Bracewell 1986) of order zero is an integral transform equivalent to a two-dimensional Fourier transform with a radially symmetric integral kernel. It is also called the Fourier-Bessel transform.

Given a function f(r), the Hankel transform pairs are

$$F(q) = 2\pi \int_0^\infty f(r)J_0(2\pi q r)rdr \tag{A.1}$$

$$f(r) = 2\pi \int_0^\infty F(q)J_0(2\pi q r)qdq \tag{A.2}$$

where $J_0(x)$ is a zeroth order Bessel function of the first kind.

The two-dimensional Fourier transform is defined as

$$g(u,v) = \int_{-\infty}^{\infty} f(x,y)e^{-2\pi(ux+vy)}dxdy$$
 (A.3)

and it is equivalent to Eq. A.1 for $x + iy = re^{i\theta}$ and $u + iv = qe^{i\phi}$.

If the telescope illumination is uniform, this is f(r) = 1 from 0 to the radius of the telescope in units of wavelength, this is $r_{Tel} = \frac{D_{Tel}}{2} \frac{1}{\lambda} = \frac{D_{Tel}}{2} \nu$, one can write

$$F(q) = 2\pi \int_0^{r_{Tel}} J_0(2\pi q r) r dr$$
 (A.4)

Applying a coordinate transformation $w = 2\pi qr$ yields

$$F(q) = 2\pi \int_0^{2\pi q r_{Tel}} \frac{w}{2\pi q} J_0(w) \frac{dw}{2\pi q}$$

$$= 2\pi \frac{1}{(2\pi q)^2} \int_0^{2\pi q r_{Tel}} w J_0(w) dw$$
(A.5)

© Springer International Publishing Switzerland 2016

149

 ${\bf R.\ Juanola-Parramon}, A\ Far-Infrared\ Spectro-Spatial\ Space\ Interferometer,$

Springer Theses, DOI 10.1007/978-3-319-29400-1

One can then apply the well known recurrence relation

$$\frac{d}{dx} \left[x^{n+1} J_{n+1}(x) \right] = x^{n+1} J_n(x) \tag{A.6}$$

giving, for n = 0, on integration

$$\int_0^x x' J_0(x') dx' = x J_1(x) \tag{A.7}$$

where $J_1(x)$ is a Bessel function of the first kind, order 1. With $x = 2\pi q r_{Tel}$, Eq. A.5 can be written as

$$F(q) = 2\pi \frac{1}{(2\pi q)^2} 2\pi q r_{Tel} J_1(2\pi q r_{Tel})$$
 (A.8)

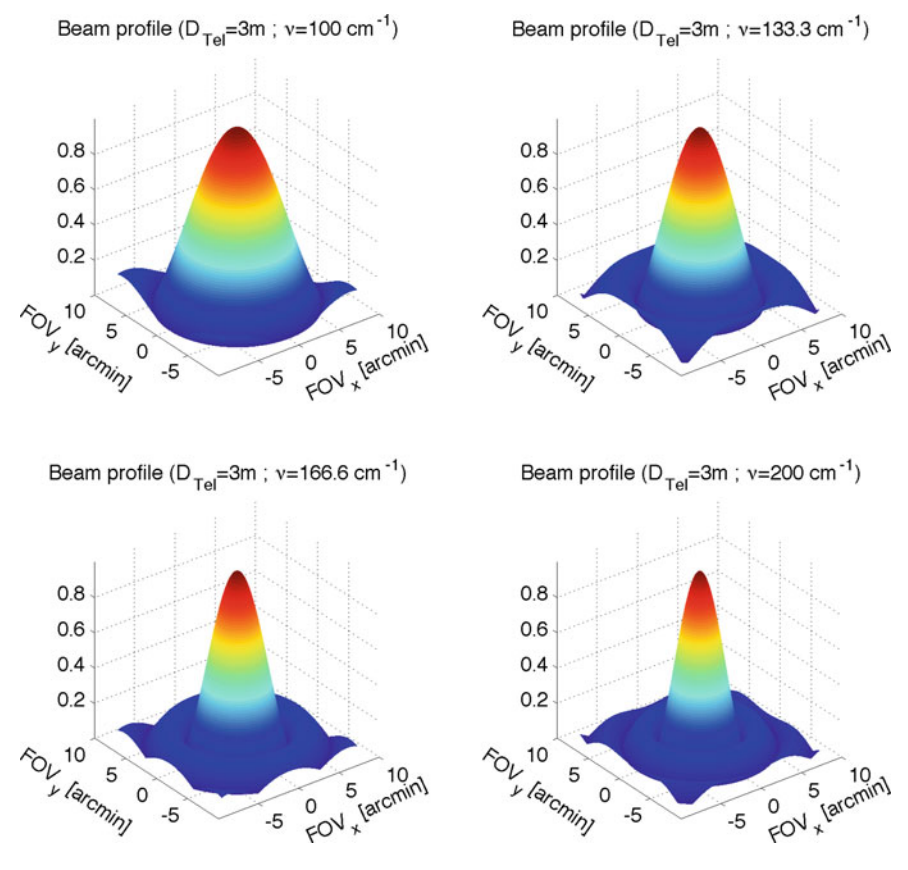


Fig. A.1 Beam profile for a circular aperture of $D_{Tel} = 3$ m and uniform illumination at $\nu = 100 \text{ cm}^{-1}$ (top-left), $\nu = 133 \text{ cm}^{-1}$ (top-right), $\nu = 166 \text{ cm}^{-1}$ (bottom-left) and $\nu = 200 \text{ cm}^{-1}$ (bottom-right)

Rearranging Eq. A.8 one obtains the beam profile as

$$F(q) = 2\frac{J_1(2\pi q r_{Tel})}{2\pi q r_{Tel}} \pi r_{Tel}^2$$
 (A.9)

In the centre of the beam profile, properties of the Bessel function give

$$\lim_{x \to 0} \frac{J_1(x)}{x} = \frac{1}{2} \tag{A.10}$$

Finally, the normalised beam profile is

$$Beam(q) = \frac{|F(q)|^2}{|F(0)|^2} = \left(2\frac{J_1(2\pi q r_{Tel})}{2\pi q r_{Tel}}\right)^2$$
(A.11)

Figure A.1 shows the computed beam profile from Eq. A.9 normalised to the telescope area πr_{Tel}^2 for a telescope of $D_{Tel} = 3$ m at the wavenumbers 100, 133, 166 cm⁻¹ and 200 cm⁻¹.

References

- 1. J.W. Goodman. Introduction to Fourier optics. (2005).
- 2. Ronald Newbold Bracewell and RN Bracewell. *The Fourier transform and its applications*, volume 31999. McGraw-Hill New York, (1986).

Appendix B FIInS Quick Start Guide

In this appendix a brief guide to perform a simulation with FIInS is provided. When performing a simulation, this document should be read in parallel with Chap. 4.

B.1 Preparing a Simulation with FIInS

Before performing a simulation of an observation with FIInS, the user must open the two Microsoft Excel files provided, *FIInS_Instrument.xlsx* and *SkyParams.xlsx*, where the simulation parameters can be tailored.

B.1.1 FIInS_Instrument.xlsx

In *FIInS_Instrument.xlsx* the user will find the predefined instrument parameters, organised in sheets. In the *FTSpectrograph* sheet the four predefined bands of operation of the FIRI system are shown, which are also presented in Table B.1.

To select the band of operation, the user needs to switch to the *ColdOptics* sheet. In this sheet the basic parameters of the Cold Optics module are shown. By selecting the Optical System Level (OSL) the band of operation is automatically selected (shown in red in the FTSpectrograph sheet).

The sheets *Telescope*, *WarmOptics*, *Background* and *Detector* contain the predefined parameters such as emissivity, transmission and temperature of the different elements. The user may modify them according to the preferred observation. In the sheet *Interferometer* one selects the baseline configuration and range. In *FTSmechanical* the number of FTS scans is selected.

Once all the parameters have been modified accordingly to the user preferences, one needs to display the *ForSkyParams* sheet. This sheet contains the derived parameters and it is intended to be a guide for the definition of the input datacube. The derived parameters are separated in Spatial parameters and Spectral parameters.

Band	λ _{min} (μm)	λ_{max} (µm)	Resolving Power	Points per Nyq
1	25	50	300	1
2	50	100	300	1
3	100	200	300	1
4	200	400	300	1

Table B.1 Predefined bands of operation in FIInS

The Spatial parameters show the pixel resolution (derived from the maximum baseline and the band of operation), the field of view (derived from the telescope size and the band of operation), and the corresponding number of spatial pixels (N_x and N_y).

The Spectral parameters show the derived maximum optical path difference and its increment, the spectral resolution, and the corresponding number of spectral pixels (N).

In *ForSkyParams* one can also find the datacube size, both in number of points and in bytes. The user must account for the size when performing a simulation. To make use of the Parallel Computing Toolbox in Matlab, the datacube size must not exceed 1 GByte as each Matlab worker (or processor) only accepts up to 2 GBytes of data (1 GByte for the sky datacube, 1 GByte for the beam datacube).

B.1.2 SkyParams.xlsx

In *SkyParams.xlsx* the user can design a sky datacube. Following the guidelines in *ForSkyParams* from *FIInS_Instrument.xlsx*, the user must place the sources within the field of view.

Three different sources are available: point source, gaussian source and elliptical source. The common parameters are x_pos and y_pos (in arcseconds), the temperature (in Kelvins), the cut-on and cut-off wavenumbers, the emission wavenumber (to place an emission line across the spectrum) and the absorption wavenumber (to place an absorption line across the spectrum). The specific parameters are:

Point source The FWHM must be left empty, the user has to include the emissivity. *Gaussian source* The user inputs the FWHM (in arcseconds).

Elliptical source The FWHM must be 0, the user then inputs the x-width, y-width (all in arcseconds) and tilt of the ellipse (in degrees).

The user has also the option to leave the x_pos and y_pos empty. In this case, the simulator will prompt a sky grid and the user selects the position of the sources by clicking. Once the parameters have been selected, the user must move the corresponding sheet to the beginning of the sheets list: Matlab will read the first sheet to create the sky datacube.

B.2 Running FIInS

Once the instrument and the sky datacube parameters have been modified according to the desired observation, the user can run FIInS. A preliminary step is to activate or deactivate the control flags. To do this, one must open FLAGS.m from MATLAB® or from a text editor.

The FIInS folder must then be opened from MATLAB®. By typing FIInS core on the command line, the simulation will start, MATLAB® will prompt the simulator progress, as shown in Listings B.1.

Listing B.1 Example of the FIInS command line output.

```
1:02:19.663 PM Loading instrument parameters...
 1:02:21.238 PM Calculating uv-map...
Spiral baselines computed!
1:02:21.248 PM Calculating FTS derived parameters...
1:02:21.268 PM Generating instrument beam...
1:02:21.899 PM Starting sky generator module...
Gaussian source positioned in Sky Map...
Point source positioned in Sky Map...
Elliptical source positioned in Sky Map...
1:02:22.391 PMSky map generated correctly!
1:02:22.531 PM Calculating warm optics derived
    parameters...
 1:02:22.548 PM Calculating cold optics derived
    parameters...
1:02:22.571 PM Calculating background power...
1:02:22.703 PM Calculating sky noise...
1:02:22.753 PM Starting Double Fourier Module...
Computing interferograms...Please wait.
Starting matlabpool using
the 'local' profile ... connected to 4 workers.
1:03:11.253 PM Interferogram computed..
 1:03:11.895 PM Interferogram computed..
1:03:12.420 PM Interferogram computed..
1:03:12.968 PM Interferogram computed..
 1:03:49.845 PM Interferogram computed..
1:04:27.450 PM Interferogram computed..
1:03:50.839 PM Interferogram computed..
1:03:51.397 PM Interferogram computed..
1:04:28.679 PM Interferogram computed..
1:03:52.062 PM Interferogram computed..
 1:04:28.488 PM Interferogram computed..
1:05:02.003 PM Interferogram computed..
1:04:28.721 PM Interferogram computed..
1:05:02.592 PM Interferogram computed..
1:05:03.597 PM Interferogram computed..
1:05:31.830 PM Interferogram computed..
1:05:02.316 PM Interferogram computed..
 1:05:31.892 PM Interferogram computed..
 1:05:32.220 PM Interferogram computed..
```

```
1:05:33.586 PM Interferogram computed..
1:05:33.607 PM Interferograms computed!
Sending a stop signal to all the workers ... stopped.
1:05:36.946 PM Calculating detector noise ...
1:05:36.989 PM Adding noise to the interferograms ...
1:05:37.416 PM Applying detector effects ...
1:05:37.663 PM Sampling and readout ...
1:05:39.854 PM FIIns simulation finished!
Elapsed time is 200.256837 seconds.
```

When the simulation is finished, the user may access the output interferograms, summarised in Table B.2, where N is the number of samples per interferogram, N_b is the number of baselines and N_s is the number of scans per baseline. For each of these interferograms the position vector and the time vector are also recorded.

Table B.2 Available output interferograms from FIInS

Variable	Size	Description
Variable	SIZE	Description
Ig	$N \times N_b$	Raw interferogram
IgD	$N \times N_b$	Raw interferogram, time constant
IgDN	$N \times N_b \times N_s$	Raw interferogram, detector time constant, photon noise
IgDNS	$N \times N_b \times N_s$	Raw interferogram, detector time constant, photon noise, sampling
IgDNf	$N \times N_b \times N_s$	Raw interferogram, detector time constant, photon noise, 1/f noise
IgDNfS	$N \times N_b \times N_s$	Raw interferogram, detector time constant, photon noise, 1/f noise, sampling
IgN	$N \times N_b \times N_s$	Raw interferogram, photon noise
IgNS	$N \times N_b \times N_s$	Raw interferogram, photon noise, sampling
IgNf	$N \times N_b \times N_s$	Raw interferogram, photon noise, 1/f noise
IgNfS	$N \times N_b \times N_s$	Raw interferogram, photon noise, 1/f noise, sampling
IgS	$N \times N_b$	Raw interferogram, sampling
IgDS	$N \times N_b$	Raw interferogram, detector time constant, sampling